ornl

NUREG/CR-3471
ORNL/TM-8906

OAK RIDGE
NATIONAL
LABORATORY

MARTIN MARIETTA

Pressure Suppression Pool Thermal Mixing

D. H. Cook

Prepared for the U.S. Nuclear Regulatory Commission
Office of Nuclear Regulatory Research
Under Interagency Agreements DOE 40-551-75 and 40-552-75

OPERATED BY
MARTIN MARIETTA ENERGY SYSTEMS, INC.
FOR THE UNITED STATES
DEPARTMENT OF ENERGY

Printed in the United States of America. Available from
National Technical Information Service
U.S. Department of Commerce
5285 Port Royal Road, Springfield, Virginia 22161

Available from

GPO Sales Program
Division of Technical Information and Document Control
U.S. Nuclear Regulatory Commission
Washington, D.C. 20555

NUREG/CR-3471
ORNL/TM-8906
Dist. Category RX, 1S

Engineering Technology Division

PRESSURE SUPPRESSION POOL THERMAL MIXING

D. H. Cook

Manuscript Complete — August 20, 1984
Date Published — October 1984

Prepared for the
U.S. Nuclear Regulatory Commission
Office of Nuclear Regulatory Research
Under Intergency Agreements DOE 40-551-75 and 40-552-75

NRC FIN No. B0452

Prepared by the
OAK RIDGE NATIONAL LABORATORY
Oak Ridge, Tennessee 37831
operated by
MARTIN MARIETTA ENERGY SYSTEMS, INC.
for the
U.S. DEPARTMENT OF ENERGY
Under Contract No. DE-AC05-840R21400

ABSTRACT

A model is developed and verified to describe the thermal mixing that occurs in the pressure suppression pool (PSP) of a commercial BWR. The model is designed specifically for a Mark-I containment and is intended for use in severe accident sequence analyses. The model developed in this work produces space and time dependent temperature results throughout the PSP and is useful for evaluating the bulk PSP thermal mixing, the condensation effectiveness of the PSP, and the long-term containment integrity. The model is designed to accommodate single or multiple discharging T-quenchers, a PSP circumferential circulation induced by the residual heat removal system discharge, and the thermal stratification of the pool that occurs immediately after the relief valves close.

The PSP thermal mixing model is verified by comparing the model-predicted temperatures to experimental temperatures that were measured in an operating BWR suppression pool. The model is then used to investigate several PSP thermal mixing problems that include the time to saturate at full relief valve flow, the temperature response to a typical stuck open relief valve scenario, and the effect of operator rotation of the relief valve discharge point.

ACKNOWLEDGEMENTS

It is impossible to acknowledge here all the people who have provided help to this dissertation effort. Many people have offered suggestions on how to satisfy the dissertation objectives.

There are two individuals who have provided guidance throughout the work: the first is my major professor, Dr. H. L. Dodds, Jr., and the second is Dr. S. A. Hodge, who is manager of the Severe Accident Sequence Analysis (SASA) program at Oak Ridge National Laboratory.

There are two organizations that provided support for my work. The Oak Ridge National Laboratory provided funds for a research assistantship to The University of Tennessee Nuclear Engineering Department which provided this graduate student the opportunity to work on a state-of-the-art research program. The Containment Systems Research Branch of the Division of Accident Evaluation of the research arm of the Nuclear Regulatory Commission supplied the experimental data that was used to verify my work, and ultimately provided all the financial support to the SASA program to fund my research.

I am very thankful for the help of my brother Daniel in the construction and performance of the flow visualization experiments and in the drawing of the figures.

TABLE OF CONTENTS

CHAPTER PAGE

CHAPTER PAGE

CHAPTER I

INTRODUCTION

A. BACKGROUND

There are 24 boiling water reactors (BWRs) now operating in the United States. The overall safety of each of these nuclear power plants depends on the performance of a pressure suppression pool (PSP). The PSP is designed to provide two key safety functions. The first and most important safety function is to prevent any significant pressure increase from occurring in the small primary containment that surrounds the BWR reactor vessel. The second PSP safety function is to scrub and contain any fission products that might be present in the reactor vessel discharge.

Ordinarily, the PSP will function as designed. If the pressure in the reactor vessel becomes too high, steam is piped to the PSP through safety relief valves (SRVs) located on the main steam lines. The steam is condensed in the pool and the pressure increase in the reactor vessel is mitigated. If fission products are present in the discharge to the PSP (discharge from either the SRV or the vent system), scrubbing of the fission products occurs as the steam is condensed in the subcooled water. Most of the fission products remain in the water and the primary containment walls isolate the radioactivity from the secondary containment and environment.

In very rare situations, the PSP may not perform as designed. During accidents at two foreign plants,[1] the primary containment was broken at the PSP; both of these events resulted in radioactive water leaking into the reactor building. During transients at five domestic plants,[1] the PSP bulk temperature reached elevated levels before the events were ended. If the transients had continued, and additional safety system failures had occurred, there was a small chance that the primary containment could have failed due to overpressurization.

All the field experience with suppression pools has resulted in major design changes in the safety relief valves, steam discharge device, PSP support structures, and PSP instrumentation, and in changes to reactor operational procedures. The principal cause of most of the problems is high water temperature near the steam discharge device. The principal reason for all this design and analysis activity is to improve the overall performance of the PSP.

Any reactor safety analysis that is performed on a BWR plant requires a model of the pressure suppression pool. The model is used to predict the temperature of the water that feeds the steam condensation and to predict the evaporation rate from the water surface. The local

water temperature* and pool evaporation are two key inputs for the primary containment integrity analysis.

In most of the current pool models, the PSP is treated as a single, well-mixed node.[2,3,4] These models in essence treat the entire PSP as a large, well-mixed pot of water, which is adequate if the energy is added to the pool at many locations or if the steam mass flux from a single location is large enough to ensure thorough mixing throughout the pool.

In many accident scenarios the well-mixed requirements are not met. This is particularly true during many of the postulated severe accidents.[5,6] One such severe accident is the station blackout accident (SBA).

A SBA is initiated by the loss of all offsite and onsite power except for the unit batteries. During the early stages of the accident, control power exists, and the reactor operator can follow the procedure for controlling the reactor pressure by sequentially opening SRVs that discharge to different locations around the PSP. The energy added to the PSP is distributed uniformly, and local - to - bulk temperature differences remain small. A well-mixed pool model is adequate for the early stages of a station blackout.

When control power fails due to battery exhaustion, a very different scenario unfolds. Instead of many SRVs opening and discharging steam to different points around the pool, a single SRV would repeatedly cycle and deposit the decay-heat generated by the reactor into just one part of the PSP. The bulk pool temperature would still increase slowly, but the temperature of the water immediately surrounding the relief valve tailpipe would rapidly increase.

As the SRV continued to open and close, more and more energy would be deposited near the steam discharge, and the water temperature there would monotonically increase. As the water temperature approached the saturation temperature corresponding to the pressure in the containment, steam bubbles would detach from the discharge device, rise, and break through the pool surface, thus causing the containment pressure to increase. If the scenario continued, the containment would eventually reach the failure pressure.

The possibility exists for the containment to fail due to overpressurization before any core damage occurs and before the bulk pool temperature reaches saturation. Clearly, a single-node analysis could not model the station blackout accident correctly.

For the SBA and other situations in which the single node model is inadequate, a model that produces more detailed information about space and time dependent pool temperatures is needed. Currently, there is no model available in the open literature for calculating detailed PSP thermal mixing.

---

*The phrase "local water temperature" is currently used in the reactor safety field to denote the temperature of the water feeding the steam condensation.

B. GENERAL STATEMENT OF THE PROBLEM

The purpose of this work is to develop and verify a model for calculating PSP local temperatures* versus time. The emphasis in the work is on the PSP temperature response to a single SRV discharging to the pool. An important part of the model is to correctly predict the velocity field in the PSP that is induced by a single safety relief valve discharge. The resulting velocity distribution is then used to predict the temperature distribution in the pool. The temperature distribution in turn feeds back into the velocity field and affects the condensation source.

The results of the model will have several practical applications. The model will be useful for predicting the interactions between the PSP and the rest of the plant during severe accidents. This includes: (1) providing the pool surface temperature input for a containment pressurization calculation, (2) evaluating the steam condensation stability, and (3) providing input to a fission product transport analysis. Another use of the model will be to predict local-to-bulk temperature differences in the PSP: this will supplement and possibly eliminate the need for expensive in-plant testing.

The model provides some fundamental benefits also. The significant new contributions expected from this work are as follows.

1. The PSP system behavior is identified. The thermal-hydraulic phenomena of importance are described in Chapter two.

2. A set of detailed models are developed for the fluid flow in the PSP. This includes the flow in the highly turbulent region near the steam discharge and the very slow moving flow in the part of the PSP located far away from the steam discharge. The models are developed based on the existing knowledge in the areas of steam jet condensation, turbulent plume and jet transport, density currents, hydraulic channel theory, and thermal stratification. The flow models are described in Chapter four.

3. A thermal mixing model of the PSP is developed and verified. The model produces temperatures versus time throughout the PSP. The thermal mixing model is presented in Chapter four and the model verification is described in Chapter six.

The thermal mixing model is designed specifically for a Mark-I containment system, which is the most common BWR containment. Although the model is designed for a particular system, the methodology should be extendable to other containment geometries. The remainder of this chapter describes the Mark-I system in detail.

---

*Local temperature for the purposes of this dissertation is defined as the temperature of a given node in the domain. That node can consist of the small region near the steam discharge, or a region at the water surface, or any other part of the domain for which an energy balance is written.

C. DESCRIPTION OF THE MARK I PRESSURE SUPPRESSION CONTAINMENT SYSTEM

The Mark I containment system consists of the drywell, the pressure suppression pool, a vent system connecting the drywell and PSP, a containment cooling system, isolation valves, and various service equipment. The arrangement of the drywell, PSP, and vent system is shown in Fig. 1.

The drywell is a steel pressure vessel with a spherical lower portion and a cylindrical upper portion. It is designed to withstand an internal pressure of 56 psig at a temperature of 281 F.* The normal environment in the drywell during plant operation is an inert atmosphere of nitrogen at atmospheric pressure and a temperature of about 135 F.

The vent system consists of eight circular vent pipes which connect the drywell to the PSP. The vent pipes are designed to conduct steam flow from the drywell to the PSP (in the event of a LOCA) with minimum resistance, and to distribute this flow uniformly in the pool. The vent pipes are designed for an internal pressure of 56 psig at a temperature of 281 F; however, their design will withstand an external pressure of only 2.0 psi above internal pressure.

The pressure suppression pool is contained in the wetwell, which is a toroidal shaped steel pressure vessel located below the drywell. The torus is constructed of 16 cylindrical sections joined at 22.5° angles. Each 22.5° section of the torus is called a "bay" of the PSP. The PSP contains about 135,000 ft^3 of water and there is an air space in the wetwell above the water pool of 119,000 ft^3. Inside the wetwell, extending around the circumference of the torus above the pool, is a 4.75 ft diameter vent header, to which the eight drywell vents connect. Projecting down from the vent header are 96 downcomer pipes of 2.0 ft diameter which terminate about 4.0 ft below the surface of the water.

At 13 approximately evenly distributed positions around the PSP, discharge lines from the reactor vessel safety relief valves extend through the vent pipes and terminate in a T-quencher device located near the bottom of the pool. Figure 2 shows a cross section of the PSP and the relative locations of the vent pipe, vent header, downcomer, SRV discharge line, and the T-quencher, which has been rotated 90° for the purpose of illustration. Outside the wetwell near the bottom of the torus, a 2.5 ft diameter suction header (ring header) circumscribes the torus and connects to the pool at four locations. At most BWRs, the RHR, HPCI, core spray, and RCIC systems can be supplied from this header.

The torus that contains the pressure suppression pool is designed to essentially the same requirements as the drywell liner, i.e., a maximum internal pressure of 56 psig at 281 F, but neither the drywell nor the torus is designed to withstand the stresses that would be created by

---

*All of temperatures, pressures, and dimensions in this section apply to the Browns Ferry Unit I PSP.

a significant internal vacuum. To ensure that a significant vacuum cannot occur in the drywell, twelve 26-inch vacuum breaker valves are installed on the vent pipes: the vacuum breakers will open to permit flow from the torus airspace above the PSP into the drywell whenever the suppression pool pressure exceeds the drywell pressure by more than 0.5 psi. Additional vacuum breaker valves with the same setpoints are installed to permit flow from the Reactor Building into the torus airspace, to prevent a significant vacuum there.

The T-quencher device at the relief valve terminus consists of two horizontal pipes connected to the SRV discharge line to form a "T". The horizontal pipes have arrays of holes in each side through which the SRV steam discharges in a roughly horizontal fan of small jets. The actual T-quencher design is shown in Fig. 3. The T-quenchers are distributed fairly evenly around the torus, as shown in Fig. 4.* During an accident when remote - manual operation of the SRVs is needed, emergency operating instructions require the operator to open oppositely located valves in a specific order, so that the energy input to the PSP is evenly distributed.

---

*The safety relief valve distribution presented in Fig. 4 is from Brown's Ferry Unit I.

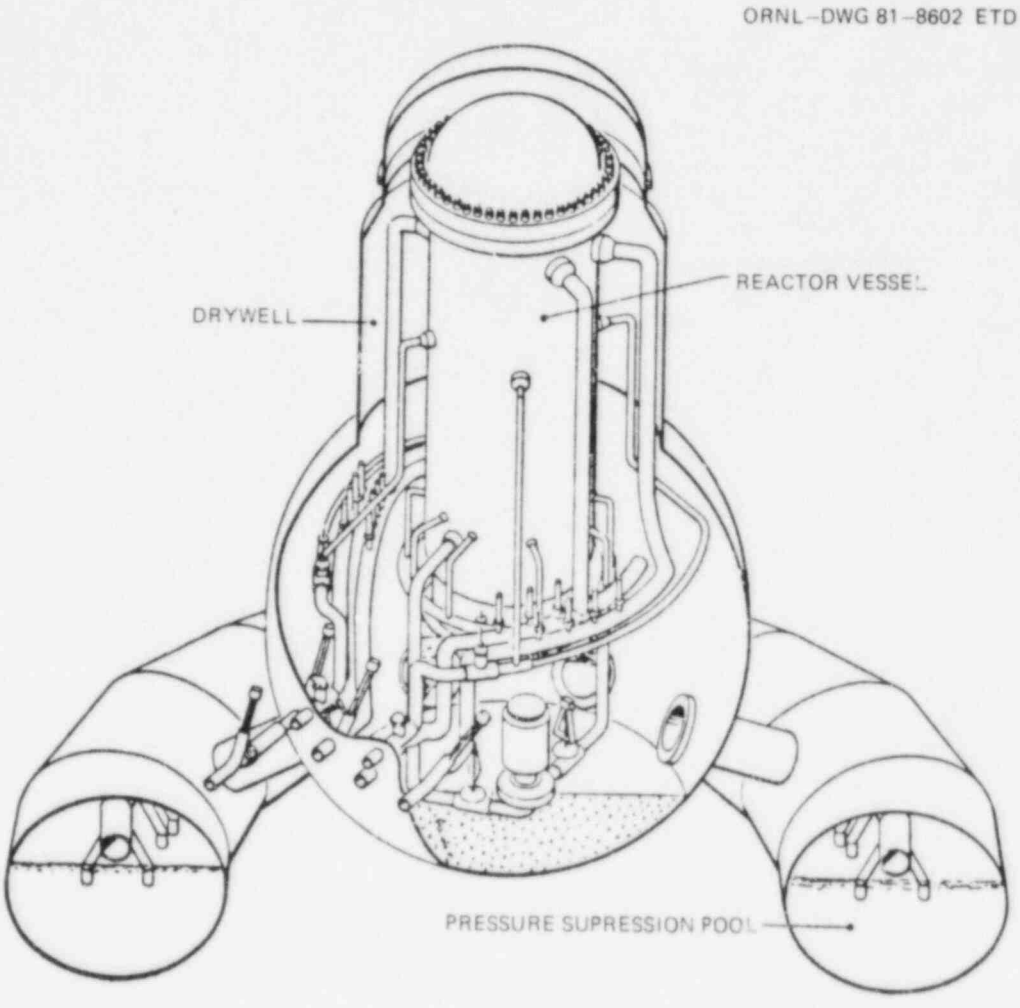

Fig. 1. Arrangement of drywell and torus.

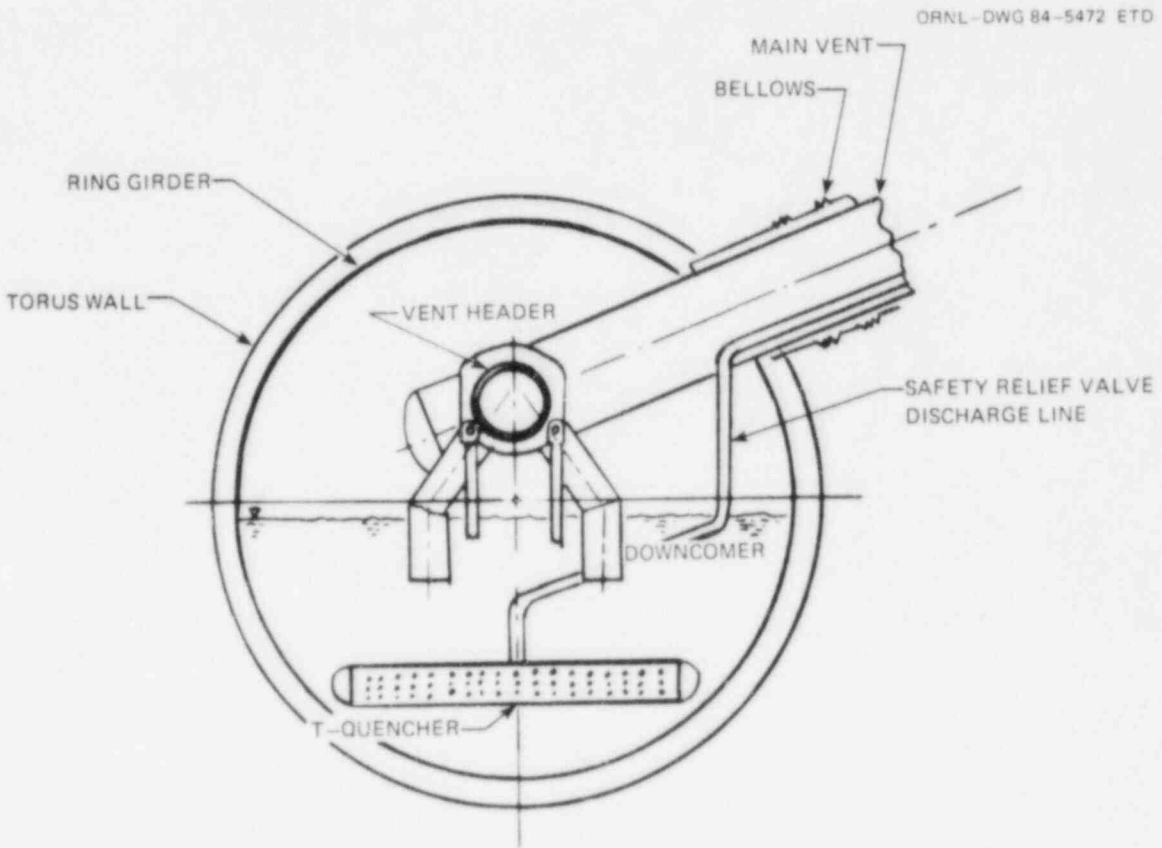

Fig. 2. Suppression pool cross section.

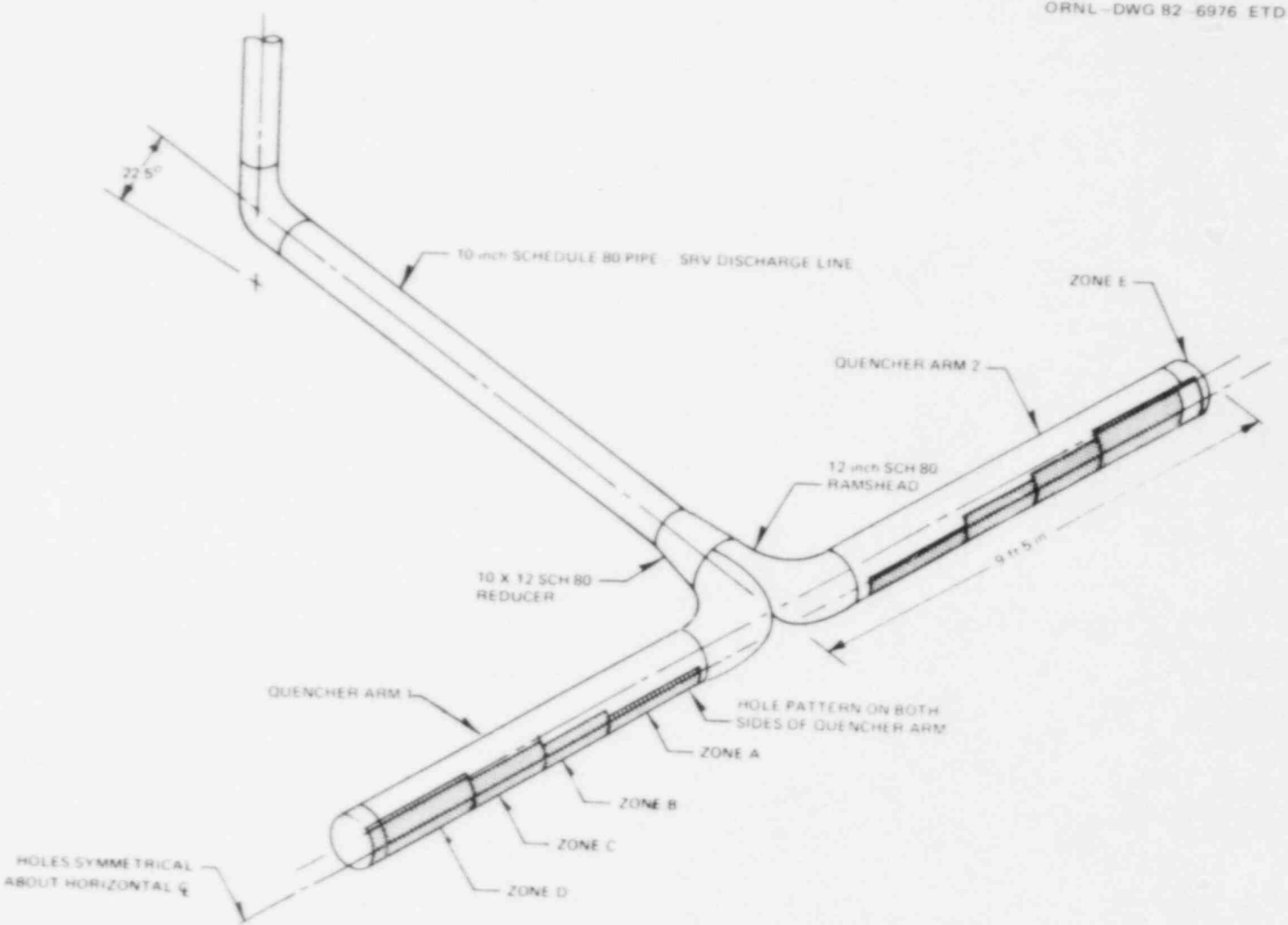

Fig. 3. Typical T-quencher (from Ref. 25).

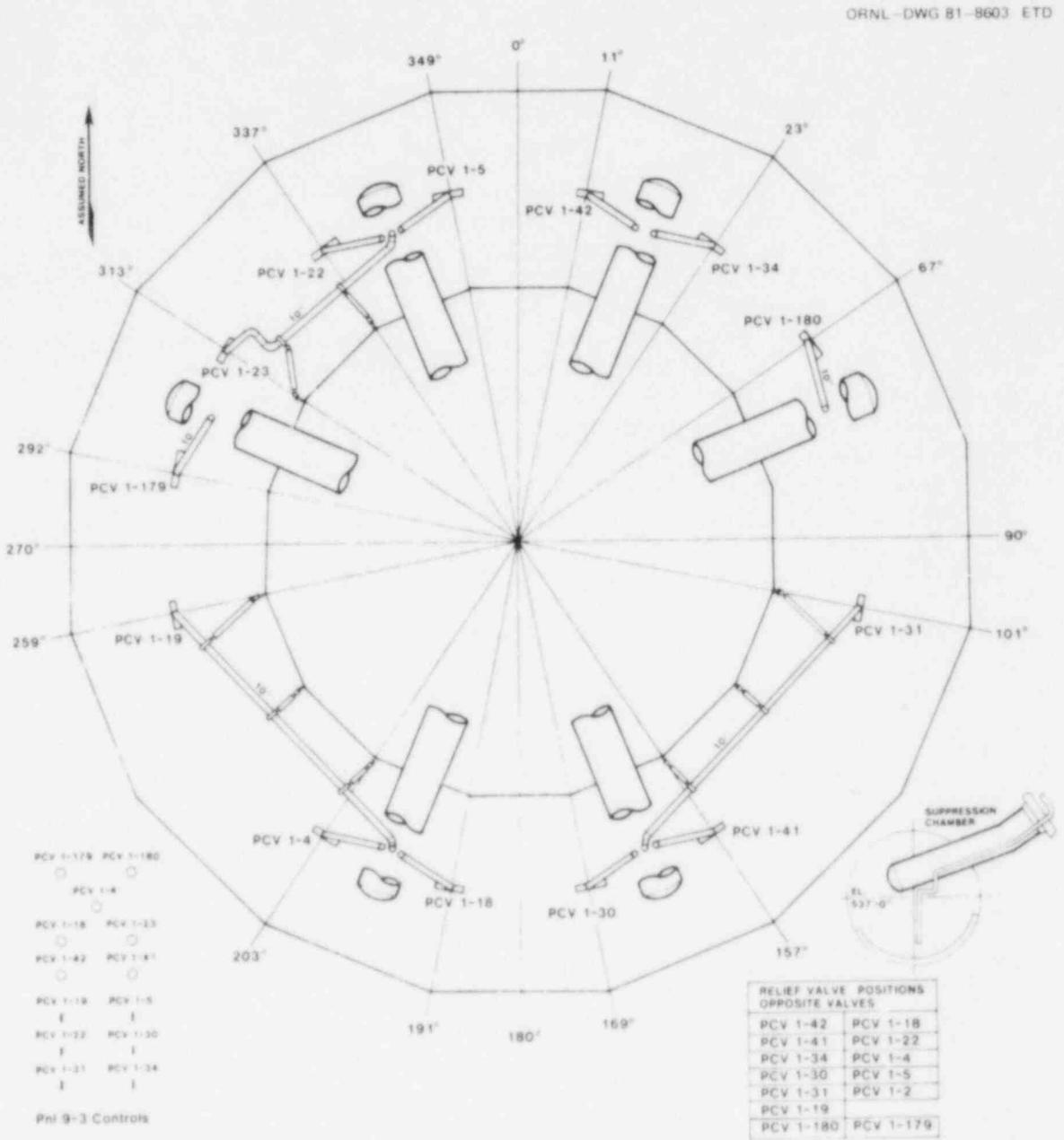

RELIEF VALVE POSITIONS OPPOSITE VALVES	
PCV 1-42	PCV 1-18
PCV 1-41	PCV 1-22
PCV 1-34	PCV 1-4
PCV 1-30	PCV 1-5
PCV 1-31	PCV 1-2
PCV 1-19	
PCV 1-180	PCV 1-179

Fig. 4. Relief valve discharge locations.

CHAPTER II

A COMPENDIUM ON PRESSURE SUPPRESSION POOL THERMAL-HYDRAULICS

A. INTRODUCTION

A complete analysis of pressure suppression pool (PSP) dynamics requires an understanding of the thermal-hydraulic phenomena that occur in the pool. The purpose of this chapter is to identify the phenomena that are relevant to a PSP thermal mixing study and to describe the methods that exist for modeling them.

In general, the phenomena can be separated into two broad categories: loss of coolant accident (LOCA)-related phenomena and safety relief valve (SRV)-discharge phenomena.

Suppression pool LOCA-related phenomena have been studied in detail for many years as part of BWR design basis accident analyses.[7] The goal of these analyses was to ensure that the containment pressure remained below the design pressure during a large break LOCA and to ensure that the containment survived the intense localized loads induced during various phases of the blowdown. The LOCA-related phenomena that have received the most attention are pool swell, condensation oscillation, and chugging. These three phenomena are described in Section B of this chapter.

SRV-discharge phenomena have also been studied for many years. The objective of these studies was to ensure that (1) the steam flowing into the PSP was completely condensed while (2) maintaining acceptable loads on the structures in the pool.

Both of the SRV-discharge objectives have been achieved through a difficult history of changing the steam discharge device. The original discharge device was simply a vertical pipe submerged in the PSP. This design had problems associated with the chugging phenomenon. The second discharge device consisted of a ramshead attached to the vertical pipe. This design eliminated the chugging problems. However, excessive loads occurred during the air clearing phase of the SRV discharge and during condensation oscillations that occurred at high water temperatures.

The third (and current) SRV steam discharge device is the T-quencher. The T-quencher is essentially a ramshead with a section of perforated pipe welded to each side. The T-quencher hole patterns are designed to provide complete condensation over a wide temperature range so that small containment loads are induced.

The success of the T-quencher design has eliminated much of the concern about localized containment loads near the steam discharge. However, the T-quencher does not provide enough circumferential momentum to ensure thorough and rapid thermal mixing throughout the torus. Thus, a concern exists about the amount and rate of thermal mixing in the pool during SRV discharge.

The phenomena that control the bulk circumferential mixing and the phenomena that affect the steam condensation at the T-quencher are described in Section C. Sections D through F constitute a literature review of several basic physical processes that underlie all PSP dynamics. These processes include the behavior of steam jets in water, the dynamics of density currents, and the dynamics of gravity-induced thermal stratification. Finally, a description of some elementary PSP flow visualization studies performed as a part of this work is presented in Section G.

B. LOCA-RELATED PHENOMENA

Immediately following the pipe break in a hypothetical LOCA, the drywell pressure and temperature increase very quickly. The pressure increase forces water standing in the downcomers to accelerate rapidly into the PSP and impinge on the torus wall. Following the slug of water, air that was in the vent pipes and drywell is forced into the PSP. This forms a bubble of air at the downcomer exit which expands into the suppression pool and causes the pool to swell. As the air bubble rises into the torus airspace, the water will fall back due to gravity.

The pool swell transient described above lasts about 3 to 5 seconds.[8] It has been studied by many researchers, with both experimental[9-11] and numerical methods.[12,13] The consensus is that the pool swell impingement and drag loads during a LOCA are conservatively estimated and acceptable. Nevertheless, the downcomer submergence at many BWR plants has been conservatively reduced in order to decrease the estimated pool swell loads.[14]

Following the pool swell transient, an air-steam mixture will flow into the PSP. Early in this process, when the mass flow is high, the injected steam condenses at an unsteady rate causing periodic oscillations in the pressure and flow. Since the mass flow is high enough to maintain the steam/water interface outside the downcomer, the overall condensation proceeds at a regular rate. This phenomenon is known as condensation oscillation, and is characterized by a steady, periodic variation in the pressure which forces local structures within the torus to vibrate in phase with the oscillations. Condensation oscillations have been studied experimentally[15,16] and analytically;[17] however, the basic driving mechanism for the pressure resonance has not been identified.[18]

When the air-steam flow through the downcomer decreases to the point where the condensation rate outside the pipe exceeds the steam flow exiting the pipe, the steam bubble collapses very rapidly. This results in a large drop in the steam pressure and the steam/water interface rushes up into the downcomer. Once there, the interface is warmed by condensing steam and the condensation rate decreases. At some point, the steam pressure will rise and the interface is pushed out of the downcomer to form an irregularly shaped bubble at the pipe exit. The bubble begins to collapse and the entire process, known as chugging,

repeats. Chugging is characterized by rapid, irregular interface accelerations and pressure oscillations that cause large loads on the torus structures.

Like the condensation oscillation problem the chugging phenomenon has also been studied in detail with analyis methods that range from manometer-like models that attempt to predict the gross motion of the interface to probabilistic models that attempt to predict internal chugging.[19-21] The central problems that plague analysis of the chugging phenomenon are (1) high uncertainty in the basic condensation rates involved and (2) lack of understanding of the triggering mechanism for the bubble collapse.

For the purpose of modeling the PSP thermal mixing, the LOCA-related phenomena can generally be considered to induce a well-mixed pool. The LOCA flow path is from the drywell, through the downcomers, and into the PSP. This flow is uniformly distributed around the torus with enough momentum to distribute the energy evenly throughout the water.

C. SAFETY RELIEF VALVE-RELATED PHENOMENA

1. T-Quencher Discharge Phenomena

Each of the SRVs is designed to open automatically when the main steam line pressure exceeds the pressure set point of the valve. When a SRV actuates, high pressure steam enters the discharge line from the reactor vessel. Initially, the pipe contains water up to its submerged length and nitrogen in the remainder. The initial pressure in the line is the same as the drywell pressure — normally about 15 psia. As steam enters the line and mixes with the nitrogen, the line pressure increases and the water slug below is accelerated out the holes in the T-quencher. High speed water jets exit the T-quencher until all the water is cleared. As soon as the water is expelled, nitrogen will flow out the T-quencher and form a swarm of bubbles that rises to the surface of the pool. High velocity steam jets follow the nitrogen and condense in the subcooled water surrounding the quencher. As the steam condenses in the nitrogen saturated water, the dissolved, noncondensible gas comes out of solution to form millions of small (~1 mm dia) nitrogen bubbles that slowly move to the PSP surface. If the surrounding water is at the saturation temperature, the steam jets will break up and form steam bubbles that will also rise to the surface. When the SRV closes, steam remaining in the discharge line condenses, and vacuum breakers installed on the discharge line open to equalize the pressure between the drywell and the discharge line.

The SRV discharge phenomena associated with the steam exiting the T-quencher have been studied in detail by General Electric Company analysts. The emphasis in their work was to obtain good analytical models for the loads induced on the structures in the wetwell by a SRV discharge. The first work[22,23] was aimed at modeling the compressible flow in the discharge line upstream of the T-quencher. The pipe dynamics were coupled to the equations for bubble dynamics to produce pressure-time histories for the PSP. More recent work on T-quencher discharge

phenomena[24] has been focused on estimating the loads on the wetwell structure caused by the water jet flow. Reference 24 contains detailed models for the T-quencher water jet mixing and penetration distance, but does not deal with the nitrogen or steam jet flow.

Any PSP thermal mixing model must have a description of the discharging T-quencher. The T-quencher model comprises the mass, momentum, and energy source for the problem. Unfortunately, the development of a complete and correct model of a discharging T-quencher is presently impossible. Too little is known about the basic condensation process, the effects of the noncondensibles, and the behavior of multiple condensing jets. Nevertheless, for severe accident studies, an adequate T-quencher model is constructed based on the following assumptions.

1. The discharge line dynamics are decoupled from the T-quencher discharge. That is, the flow through the T-quencher is dependent on the nominal pressure in the line.
2. The presence of noncondensibles is neglected--both on the steam and on the water side of the condensation front.
3. The behavior of one T-quencher jet characterizes all of the jets.
4. Steady state, equilibrium thermodynamic conditions exist.

These four assumptions are used in constructing the T-quencher steam condensation model discussed in Chapter 4. In the work that is done there the steam condensation model is more than adequate.

2. PSP Flow Phenomena

When the SRV discharge begins, the bay containing the T-quencher experiences a small pool swell event. The pool swell is due to two effects: (1) the geometry of the T-quencher directs the momentum of the steam jets slightly upward toward the surface and (2) voids near the T-quencher displace water upward. The net pool swell is a superposition of both these effects.

The pool swell creates a surface wave that travels out of the discharge bay, impacts the downcomers, and moves around the torus. The major effect of the wave is to set up fluid motion in the upper layers of the pool moving from the discharge bay outward in both directions to the rest of the torus.

When steam flow begins at the T-quencher, the hot water created by the steam condensation moves toward the PSP surface in the form of turbulent, buoyant, forced plumes. The plumes are accelerated by buoyancy and decelerated by entrainment of the surrounding cold water. The entrainment also decreases the plume temperature. If the momentum of the plume is large compared to the buoyancy, the plume will behave very much like a jet: it will strike the torus wall and be deflected upward. If the momentum is small compared to the buoyancy, the forced plume will behave like a pure plume: it will flow vertically from the T-quencher and move to the PSP surface.

Whether the forced plume behavior is jet-like, plume-like, or somewhere in between, the heated water will reach the surface of the PSP in

the discharge bay. At the surface, or in a region near the surface, the plume flow will split, and part of the hot water will flow downward as the plume momentum reflects off the free surface. This downward flow remains in the discharge bay and provides some of the water that feeds steam condensation near the T-quencher and some of the water entrained in the plumes above the T-quencher. The downflow of the hot water in the discharge bay is defined as the local recirculation flow.

The remainder of the heated plume reaching the PSP surface flows out of the discharge bay and moves around the circumference of the torus in both directions. Since the water is hot relative to the PSP water located away from Bay D, the outflow tends to remain on the surface. The hot water layer is buoyed up by the vertical temperature difference and driven by the circumferential temperature difference.

For conservation of mass, cold water must flow into the lower layers of Bay D to replace the hot water outflow at the top. This lower layer backflow (a countercurrent flow located beneath the hot water layer) is created by the down-welling of the horizontally moving hot water as it decelerates due to friction and by the effect of a symmetry plane located 180° from the centerline of the discharging T-quencher. The symmetry plane at 180° is the point at which the two hot water outflows meet head-on. The collision of the surface flows causes the upper layers coming from both directions to turn down, thereby forming the origin of the lower layer backflow.

The combination of the hot water flow on the top and the countercurrent cold layer flow on the bottom is defined as the whole pool recirculation flow. This terminology is used to stress that the entire PSP participates in the thermal mixing — not just the Bay D region around the T-quencher.

The PSP flow field described above is depicted in Figure 5. The flow field is effectively two large, alternating convection cells. The cells consist of hot water moving up to the surface in Bay D, around and across the PSP, together with colder water that is moving down and back toward the T-quencher.

It is the whole pool recirculation flow that keeps the discharge bay cool. Experimental evidence* indicates that this flow is quite strong, involving bulk pool velocities on the order of 0.5 to 1 ft/s. Correctly modeling the recirculation flow is essential to determining the transient local PSP temperatures.

The last flow phenomenon of interest is the gravity-induced thermal stratification of the PSP that occurs very quickly after SRV closure. As soon as the valve closes, hot water moves to the upper layers and cold water moves to the lower layers of the pool. The driving mechanism for the motion is internal density differences. Thermal stratification is important because experiments have shown that its effect remains long after the SRV closes,[25] it serves as an initial condition for subsequent

---

*The experimental evidence referred to is data from the Monticello tests, which are described in Chapter 6.

SRV discharge events, it is important for calculating BWR primary containment pressurization (through evaporation), and because it is important to fission product transport analyses.*

A model does not exist that will describe all the PSP flow phenomena of interest. However, there have been many studies on the individual phenomena that are important to the pool mixing. For example, the behavior of plumes and thermals has been studied for many years.[26-28] The knowledge that exists concerning plumes can be used to model the thermal mixing in the discharge bay. The behavior of an energy source in a confined region has been studied,[29-31] and this research can also be used to characterize the thermal mixing in the discharge bay. The flow of density currents has been modeled (a summary of this literature is provided in Section E), and can be used to construct a model for the whole pool recirculation flow. Thermal stratification has been studied (described in Section F), and can be used as a basis for a model of the PSP thermal mixing and stratification after SRV closure.

A complete PSP thermal mixing model can be constructed by coupling several of the individual models into a single, large model. The details of the construction, and of the individual models, are provided in Chapter 4.

D. STEAM JETS IN WATER

Almost all of the practical boiling water reactor PSP thermal mixing problems of interest involve the question of adequate steam condensation in the PSP water.

Despite the attention from many researchers, surprisingly little detail is known about steam jets condensing in water. Only macroscopic phenomena, such as the jet penetration length, are well understood. The research that has been performed is limited to studies at atmospheric pressure, studies of single jets, and studies without noncondensibles present in the receiving flow.

The effect of water temperature on the steam jet condensation is well established.[32-34] As the water temperature increases, the length of the steam jet increases because more surface area is required to absorb the thermal energy. The length of the steam jet, known as the penetration length, has been studied in detail. Several correlations exist for the penetration length as a function of the hole exit conditions and the bulk water conditions.[35-37]

Macroscopic steam jet studies rely on steady state analysis of the unsteady condensation process. Very few researchers[38,39] have dealt with the dynamic character of steam jet condensation.

The difficulty in dynamic analysis of steam jet condensation is the uncertainty that exists in the interfacial condensation rates. There

---

*Under the conditions of core degradation that would occur in a BWR severe accident, most of the fission products released would exit from the T-quencher.

are two extremes: the condensation rate can be kinetically limited by mass transfer on the steam side, or heat transfer limited by turbulence on the water side. An excellent review on the interfacial condensation rates is presented by Catton.[39]

For the purpose of calculating PSP thermal mixing, the steady state jet penetration length correlations will provide enough information to form a starting point for the discharge bay analysis presented in this work.

E. DENSITY CURRENTS

When a SRV is discharging through a T-quencher into the PSP, the flow in the region away from the discharge bay has the characteristics of a density current. A density current is a flow that is set in motion and sustained by density gradients in the fluid. Density currents are commonly referred to as "gravity currents."

In the PSP, the density gradients are due to temperature differences in the water. As a result of steam condensation, the water in the discharge bay is hot relative to the water in the rest of the torus. A horizontal pressure difference is produced by the density difference, and the pressure difference drives a density current.

The density current in the BWR Mark I containment design is depicted in Fig. 6. It consists of a hot water layer that moves out across the top of the PSP combined with a cold layer underneath that moves back toward the discharge bay. The combination of the hot and cold layer flows was termed the whole pool recirculation flow earlier in this chapter.

There are many important examples of density currents. Some are man-made, such as the flow of hot water across the top of a cooling pond from a conventional power plant main condenser cooling water discharge. Another example is the intrusion of salt water under fresh water when a lock is opened at the mouth of a river. There are naturally occurring density currents, such as the flow from the main body of a lake into a sidearm of the lake caused by evaporation in the shallow sidearm. As an example on a large scale, the meteorological "cold front" advancing into warmer air is a density current.

Several researchers have studied density currents analytically; the earliest work being by von Kármán.[40] Benjamin[41] clarified some of the early work, and presented an analytical result for the average propagation velocity of the density current based on a momentum balance and application of Bernoulli's equation.

Density current flow in a channel is sometimes treated as a two layer stratified flow.[42-44] The change in the layer thicknesses with distance along the channel is often neglected because the buoyant force on the upper layer strongly inhibits vertical mixing of the fluid.

An excellent two layer approach developed by Sturm[45,46] consists of a boundary layer-type approximation to the governing equations for the 2-D fluid velocities and temperature. The vertical shape of the horizontal velocity is fitted to a fourth order polynomial. This is the

classic Kármán-Polhausen approximation.[47] The approximation was substituted into the governing partial differential equations. The equations were then integrated over the fluid depth, and the resulting ordinary differential equations were solved numerically. A limitation of Sturm's method is that it applies to very long hydraulic channels.

Sturm's general method is appropriate for modeling the thermal mixing in the very large part of the PSP located away from the discharge bay. However, several improvements to the method are necessary for adaptation to the PSP geometry. These improvements are presented in Chapter 4, along with the model for the whole pool recirculation flow.

F. THERMAL STRATIFICATION

The subject of thermal stratification is relevant to this PSP thermal mixing study because the pool is known to stratify very quickly after any active source of thermal mixing, such as T-quencher discharge, is suddenly terminated. Furthermore, the stratification in well-defined horizontal layers is known to remain for a long time unless enough kinetic energy is subsequently supplied to the pool to thoroughly mix the discrete layers and break up the stratification.*

Thermal stratification falls into the category of internal mixing processes.[48] The mechanisms responsible for the internal mixing in a stratified fluid can be roughly divided into two groups: internal wave motion and interfacial mixing. Internal wave motion contributes to thermal mixing primarily in the horizontal direction. Interfacial mixing contributes to thermal mixing in the vertical direction. Very little detail is known about either of these mechanisms and what is known is qualitative in nature.

Internal wave motion contributes appreciably to the mixing in stratified fluids through the breaking of large amplitude interfacial waves.[49] An internal wave is similar in many ways to a surface wave. The highest point on the wave moves with the largest velocity which forces the wave to steepen, break, and then disperse. When this phenomenon occurs in the interior of the PSP, the resulting turbulence eliminates temperature differences in the horizontal direction to produce a stack of well-mixed layers.

Figure 7 is a sketch of the internal wave mixing in the PSP. The rectangular regions in Fig. 7 represent one half of a PSP in which one T-quencher is discharging steam. The top of the rectangle represents the water surface, the bottom represents the PSP floor, the left side

---

*A small radial thermal stratification is known to exist when the PSP water is moving. As part of his peer review of this work, Earl Worley of Los Alamos National Laboratory mentioned that the radial thermal stratification is important when installing plant temperature sensors. The three dimensional mixing induced by the radial stratification is a small effect when considering the overall mixing in the entire PSP.

represents the centerline of the discharge bay, and the right side represents the symmetry plane located 180° from the T-quencher. The shaded region represents water that has been heated by the condensing steam. When the T-quencher is turned off, the hot water is distributed as in Fig. 7a. This is an unstable distribution because the hot water in the discharge bay is in effect below colder water in the PSP interior. The fluid moves toward dynamic equilibrium by internal density waves that move across the pool, interact with each other, and possibly break. The movement of the waves is sketched in Fig. 7b. The wave motion slows as the kinetic energy of the PSP dissipates into small scale turbulence. Finally, all horizontal motion ceases and a series of layers forms in the vertical direction.

Interfacial mixing occurs between the layers as fluid moves vertically across the density interfaces and becomes entrained in the adjacent layers. The vertical mixing is strongly inhibited by buoyancy effects. If a packet of hot water moves downward into the colder water, it is quickly "pushed" upward by the buoyant force. Similarly, if a packet of cold water moves upward into warmer water, it is quickly "pushed" downward.

The mixing that occurs in a stratified fluid due to internal wave-breaking has been studied.[50,51] The emphasis in past work was on the effect that a passing internal wave has on an already stratified section of fluid. No work has been done to analyze the internal wave formation and movement, nor has any work been done to predict the nature of the initial layers that are formed as the waves break down.

The mixing that occurs vertically across the layers in a stratified fluid has been studied as part of research on the upper layer wind and wave mixing in the ocean. Most of the work has focused on two layer systems in which the upper layer is artificially stirred.[52,53] For systems in which no external source of turbulence is present, the entrainment across a density interface is primarily influenced by molecular diffusion.[54] This is a very weak transport mechanism; thus it is typical for a system to form many well-mixed layers separated by sharp density interfaces.

The literature concerning thermal stratification in fluids provides very little information that can be used in a PSP thermal mixing study. The internal wave studies that have not been performed (on formation and breakdown of the internal waves) are precisely the ones that are needed. Given a PSP temperature distribution at the time of SRV closure, a model is needed for the formation, movement, and breakup of internal waves. Since no model exists, and since no experimental data exists, a very simple model is all that can be developed. The thermal stratification model is described in Chapter 4.

G. PSP FLOW VISUALIZATION STUDIES

1. Introduction

Some very elementary flow visualization experiments were performed as part of this work in order to observe the phenomena that are relevant

to the PSP thermal mixing study. The purpose of these experiments was simply to observe the phenomena. No data were recorded. No measurements were made.

Three very simple experiments were performed. They are: (1) the behavior of density currents in a confined circular channel, (2) the flow in a confined circular channel with a line energy source, and (3) the flow in a confined circular channel from a steam condensing diffuser.

2. Density Currents in a Confined Circular Channel

The flow in the upper layers of the PSP away from the discharge bay is identified as a density current. It is instructive to isolate this density current from the discharge bay turbulence and to make observations based upon a simple experiment.

The facility that was built to study the density current is sketched in Fig. 8. It consists of a circular plexiglass channel that ends in a solid sheet of plexiglass on the right, and to which an entrance/exit region is attached on the left. The entrance/exit region is designed to introduce hot water into the top of the channel, allow an equal amount of cold water to exit from the bottom of the channel, and to maintain a constant water level inside the channel. The flow is separated at the left end of the channel by a plastic flow divider. The water level is maintained by a moveable weir at the back of the entrance/exit region. The hot and cold water volumes are contained in separate, insulated plenums inside the entrance/exit region.

The facility was designed to operate as a steady flow device. Any hot water introduced into the hot plenum causes an equal amount of cold water to flow into the cold plenum and out across the weir.

The facility is designed to crudely mimic the PSP flow when one T-quencher is discharging. The left side introduces the flow that is set up away from the discharge bay. The right side simulates the symmetry plane located 180° from the discharging T-quencher. The channel itself corresponds to a torus that has a very large major radius.

The flow of a density current in the channel is shown in Figs. 9 and 10. The density current was made visible with red dye dissolved in the hot water. In Fig. 9(a), the hot water is introduced into the channel. The rounded nose of the density current profile is evident in Fig. 9(b), and the density current approaches the solid wall in Fig. 9(c). In Fig. 10(a), the density current has reached the wall, and is turning downward. In Fig. 10(b), the countercurrent flow located underneath the density current carries some of the heated water back toward the left end of the channel. The front part of the countercurrent flow in Fig. 10(b) shows the internal wave structure of the returning density current. After a short time, the wave structure is dissipated, and the steady flow of Fig. 10(c) exists.

3. Density Currents from a Line Energy Source in a Confined Circular Channel

The second flow visualization experiment was designed to eliminate the entrance/exit section that was used in the first experiment, replacing it with a method of forming the density current that resembles the thermal plume behavior in the discharge bay of the PSP. The facility shown in Fig. 8 was modified by replacing the entrance/exit region with a plexiglass plate through which an ordinary household water heater element was inserted. The modified facility is shown in Fig. 11.

The water heater element resembles a T-quencher in effect, by creating a turbulent, buoyant rectangular plume that flows vertically to the surface of the channel. A complicated surface impingement region exists at the surface in which some of the heated water recirculates downward to feed the plume entrainment, and some of the water flows horizontally to form the density current.

The density current formed by the line energy source is shown in Fig. 12. As in the first experiment, red dye was injected near the source to make the flow visible. This density current is much less turbulent than the density current shown in Figures 9 and 10. It even exhibits laminar characteristics in the center portion of the channel. Instead of being formed abruptly at an artificial boundary (as in the first experiment), this density current is formed gradually as the hot water near the heater moves to the surface, turns, and then flows horizontally across the top of the channel. Although this is not a scaled experiment, the flow field in Fig. 12 is similar to the expected flow in a PSP because the density current is formed by the interaction of a very turbulent region near a line energy source with an almost laminar flowing region very far away from the source.

4. Density Currents from a Steam Condensing Diffuser in a Confined Circular Channel

The last flow visualization experiment was designed to study a density current from a steam condensing diffuser. The facility used in the second experiment was modified by replacing the heater rod with a steel tube that had a row of holes drilled along both sides. The modified facility is shown in Fig. 13. Steam is injected into the channel through the steel tube.

The density currents produced by steam condensing at the diffuser are shown in Fig. 14. Dye was unnecessary in these experiments because the very small air bubbles that come out of solution at the condensation site act as a tracer. Figure 14(a) shows the density current formed by a low steam flow; Fig. 14(b) shows the density current formed by a high steam flow.

Several photographs were made showing an end view of the quencher. Two of these photographs are shown in Fig. 15. The pictures in Fig. 15 were made looking through the channel. The pictures were made after the apparatus was run for a long time--almost completely degassing the water.

The pictures in Fig. 15 are confusing until one realizes that the center portion of each frame is the true end view. The upper part of each picture is a reflection off the underside of the free surface.

Figure 15(a) shows the quencher operating at a relatively low steam flow; Fig. 15(b) was at a much higher steam flow. The buoyancy effect on the steam jets is apparent by comparing the jet trajectories in Figures 15(a) and 15(b).

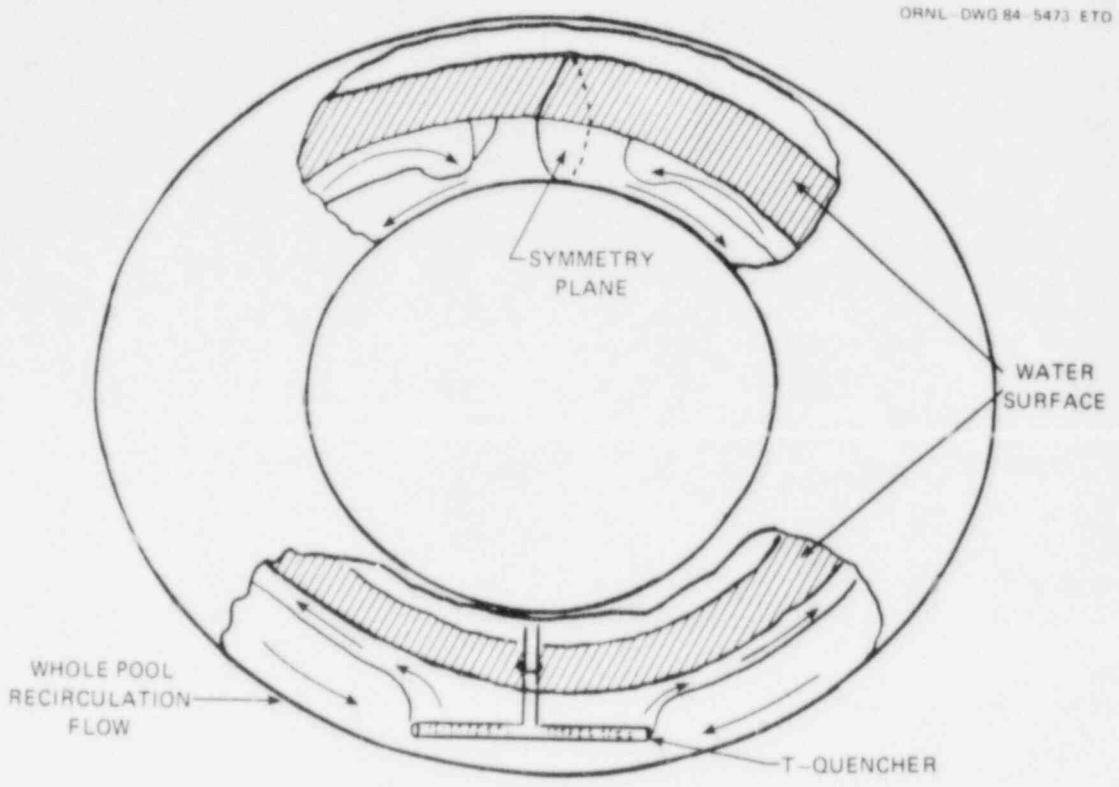

Fig. 5. Qualitative description of the PSP flow induced by a single discharging T-quencher.

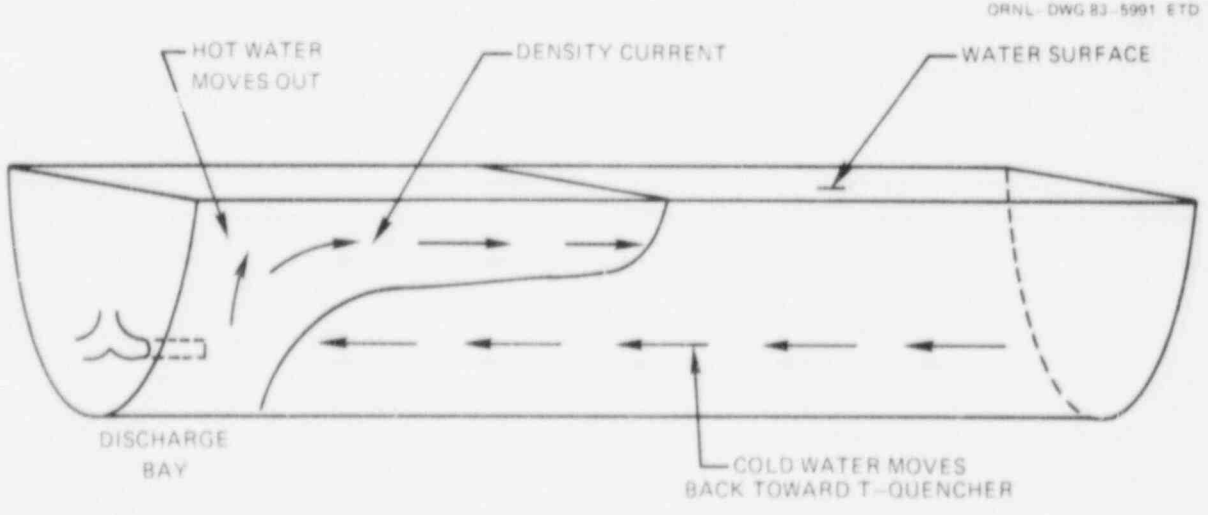

Fig. 6. Sketch of the PSP density current flow.

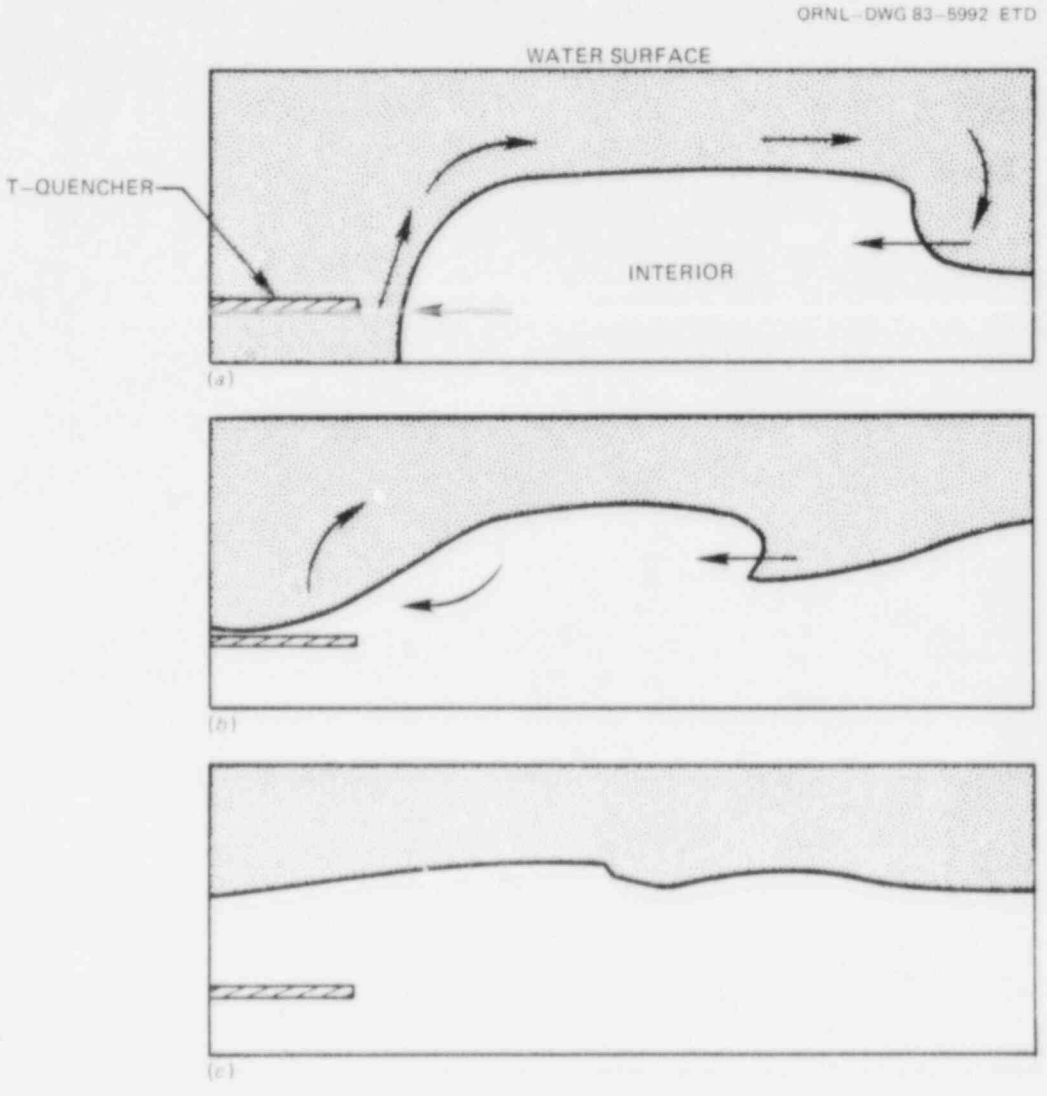

Fig. 7. Sketch of PSP internal wave mixing.

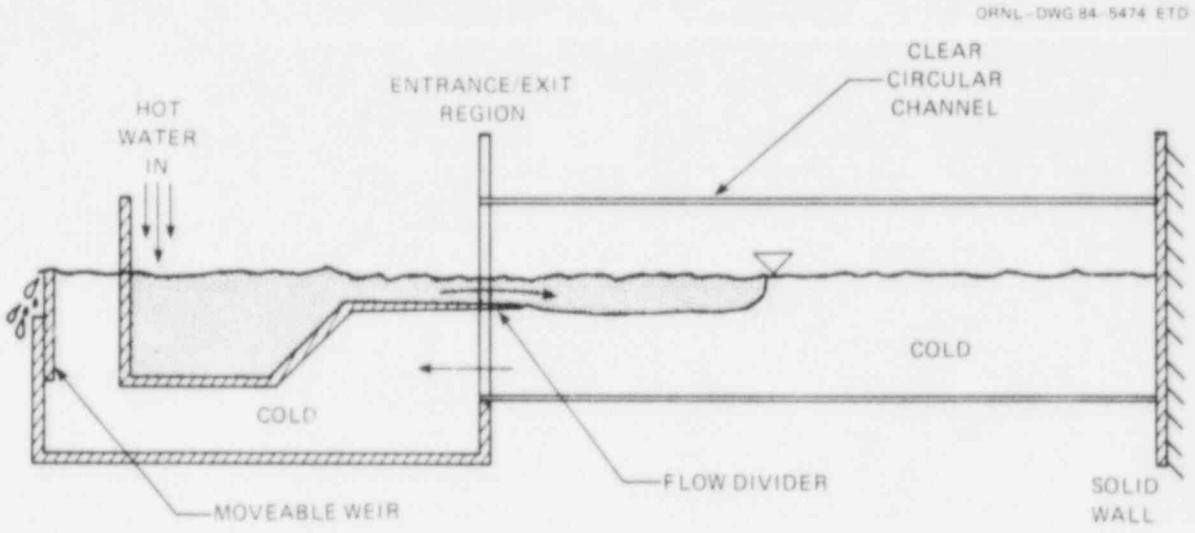

Fig. 8. Density current experimental facility.

ORNL PHOTO 4587-84

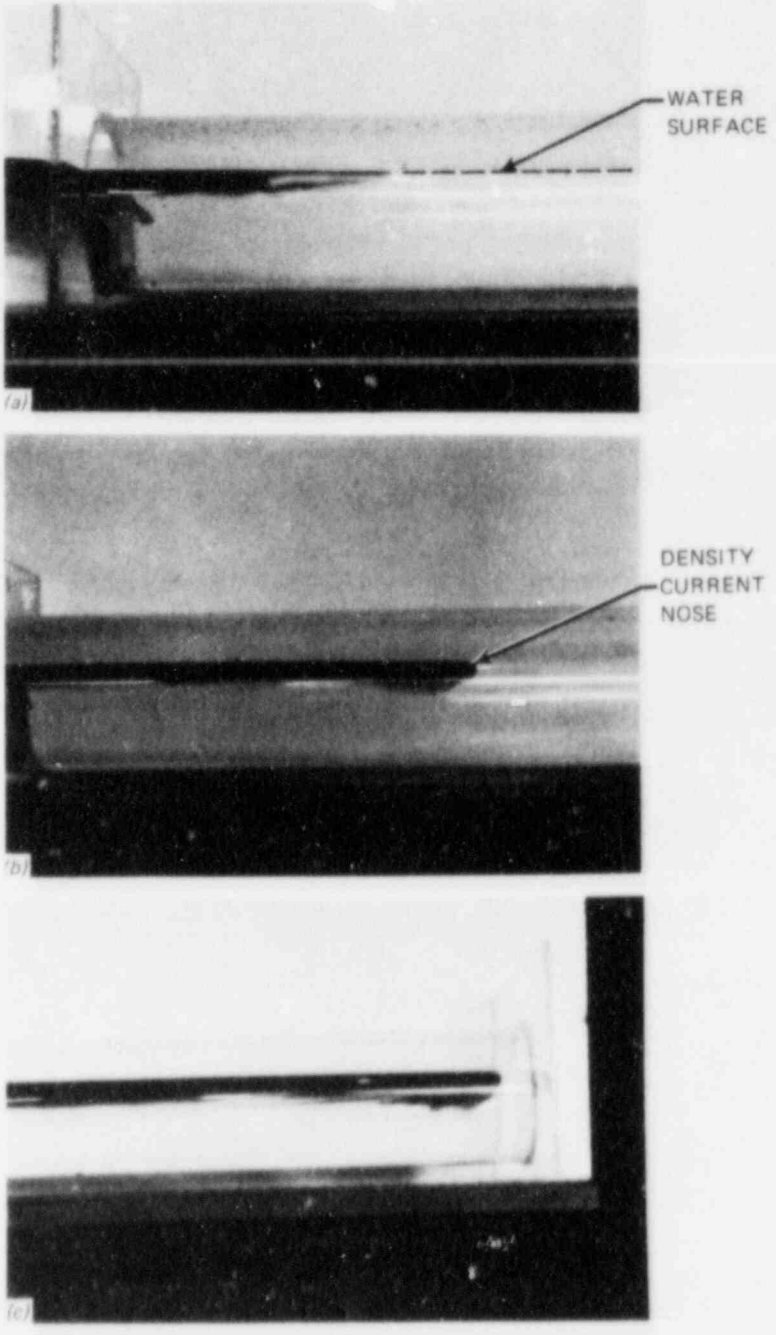

Fig. 9. Density current flow in a circular channel.

ORNL PHOTO 4586-84

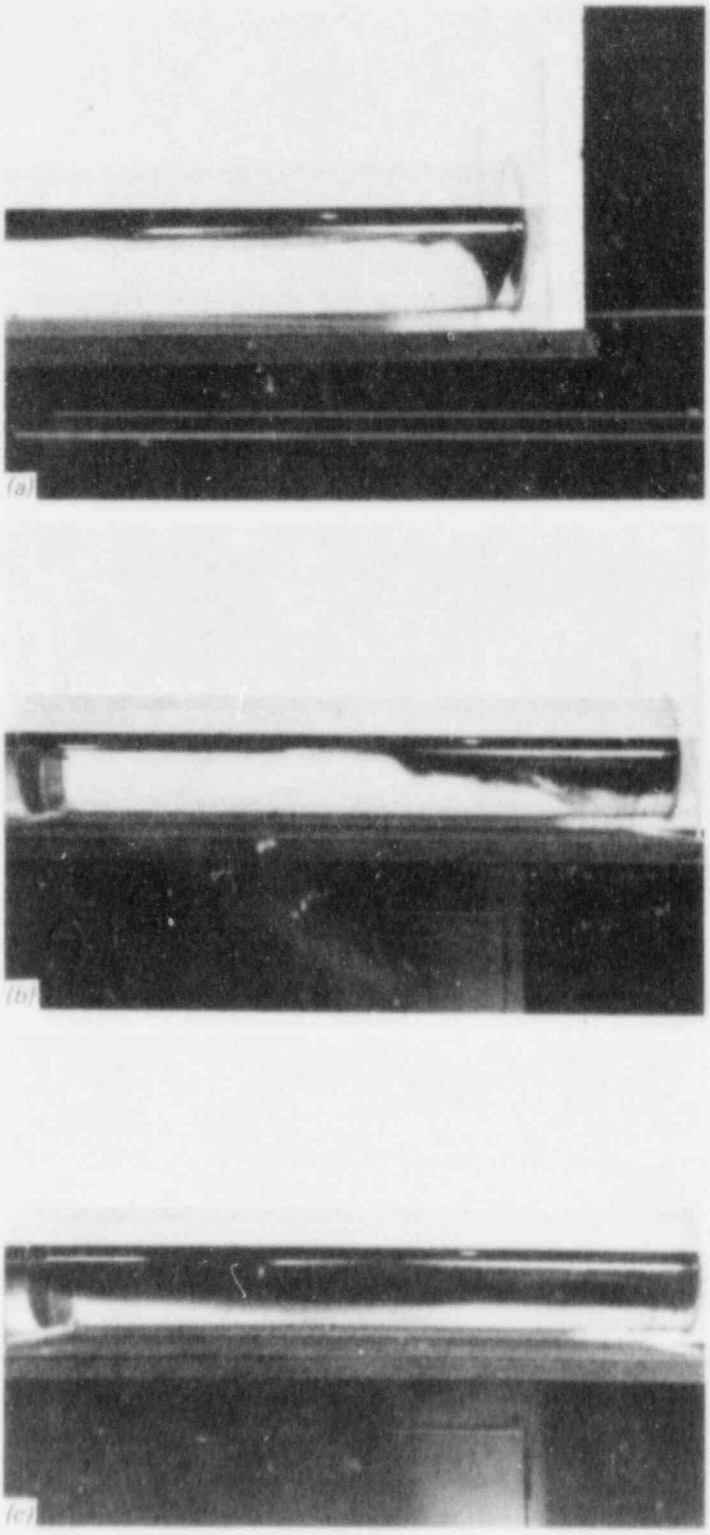

Fig. 10. Continued density current flow in a circular channel.

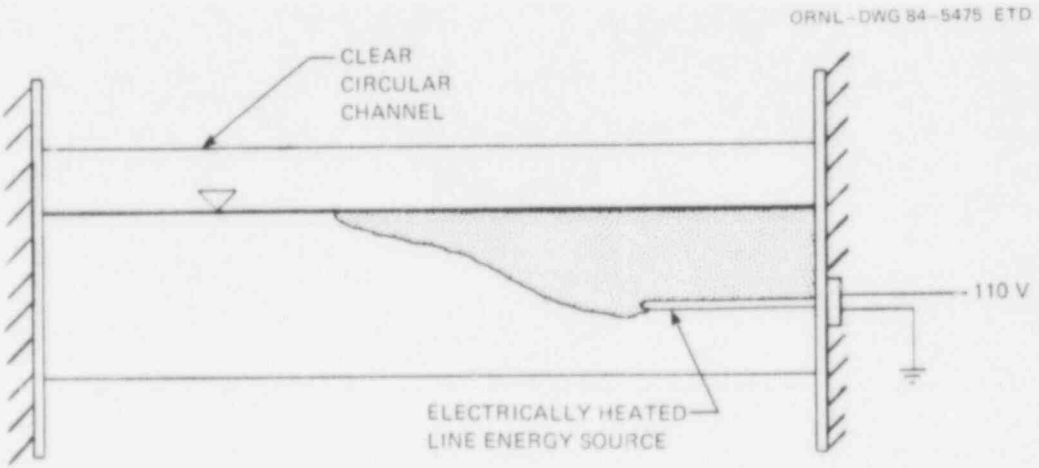

Fig. 11. Line energy source facility.

ORNL PHOTO 4588-84

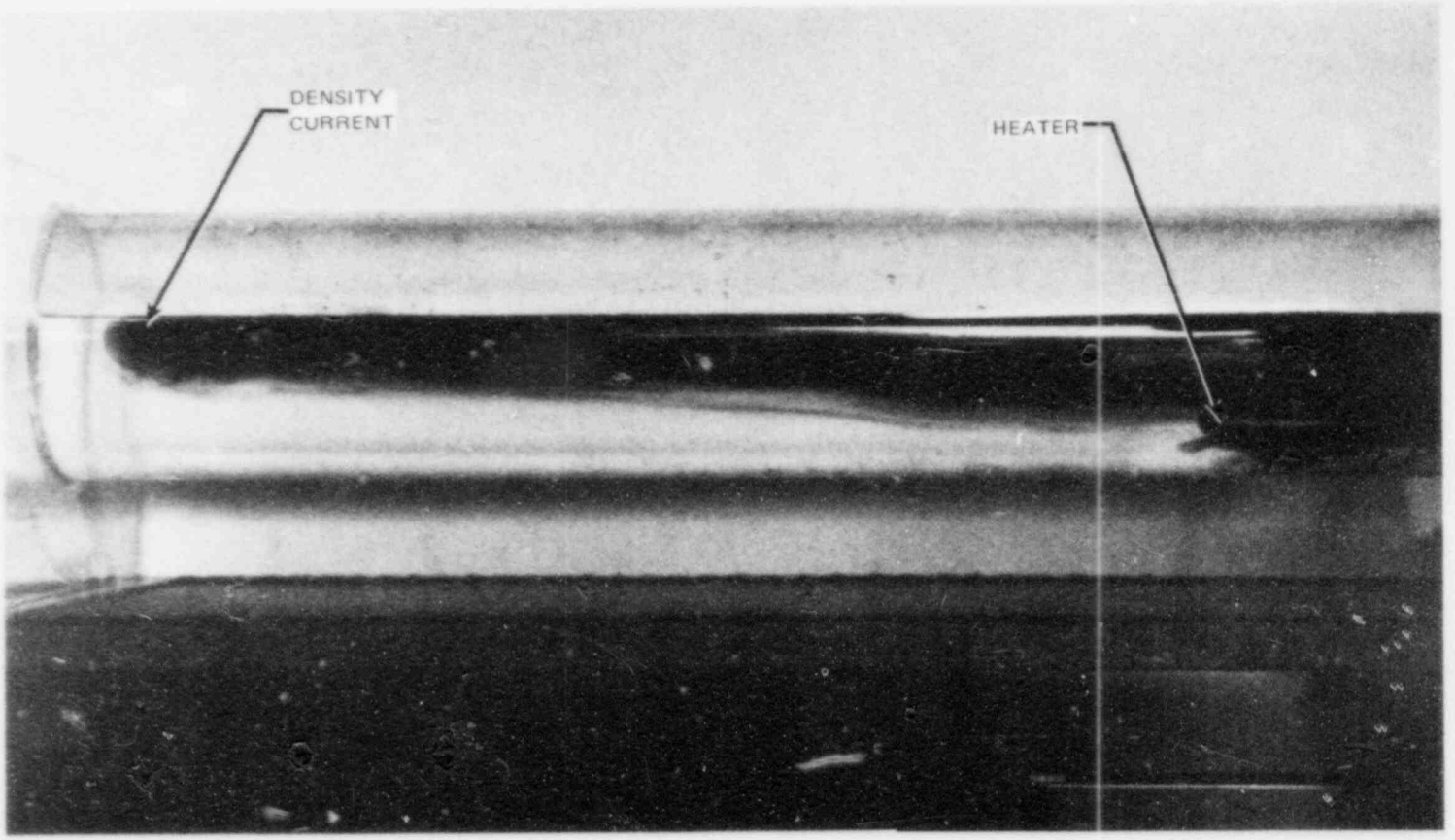

Fig. 12. Density current flow from a line energy source.

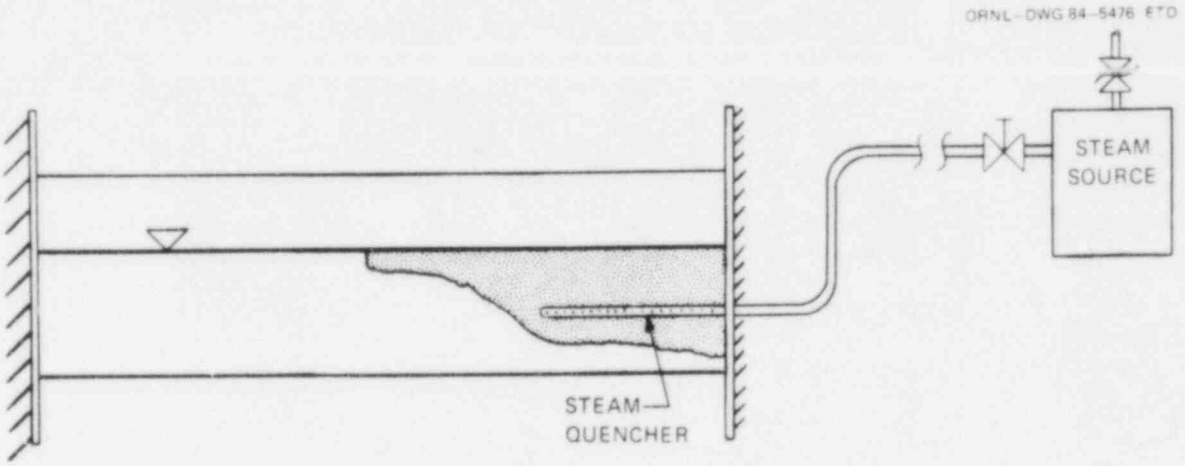

Fig. 13. Steam condensing diffuser facility.

ORNL PHOTO 4589-84

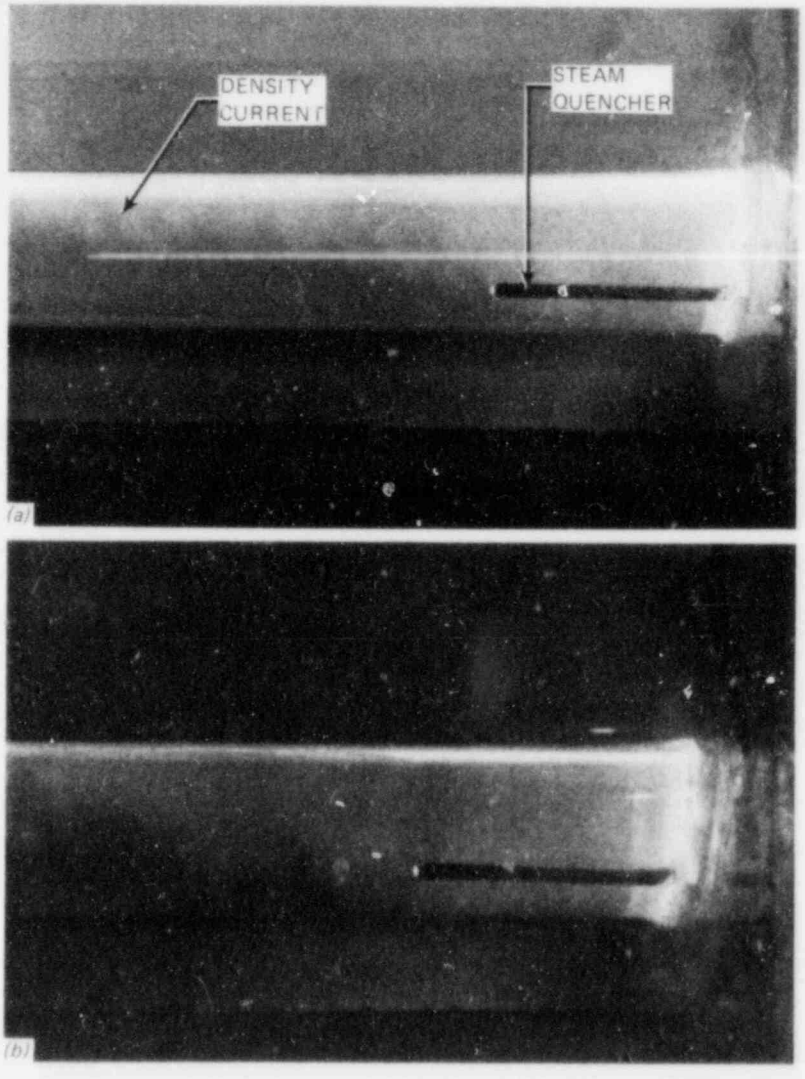

Fig. 14. Density currents from a steam condensing diffuser.

ORNL PHOTO 4590–84

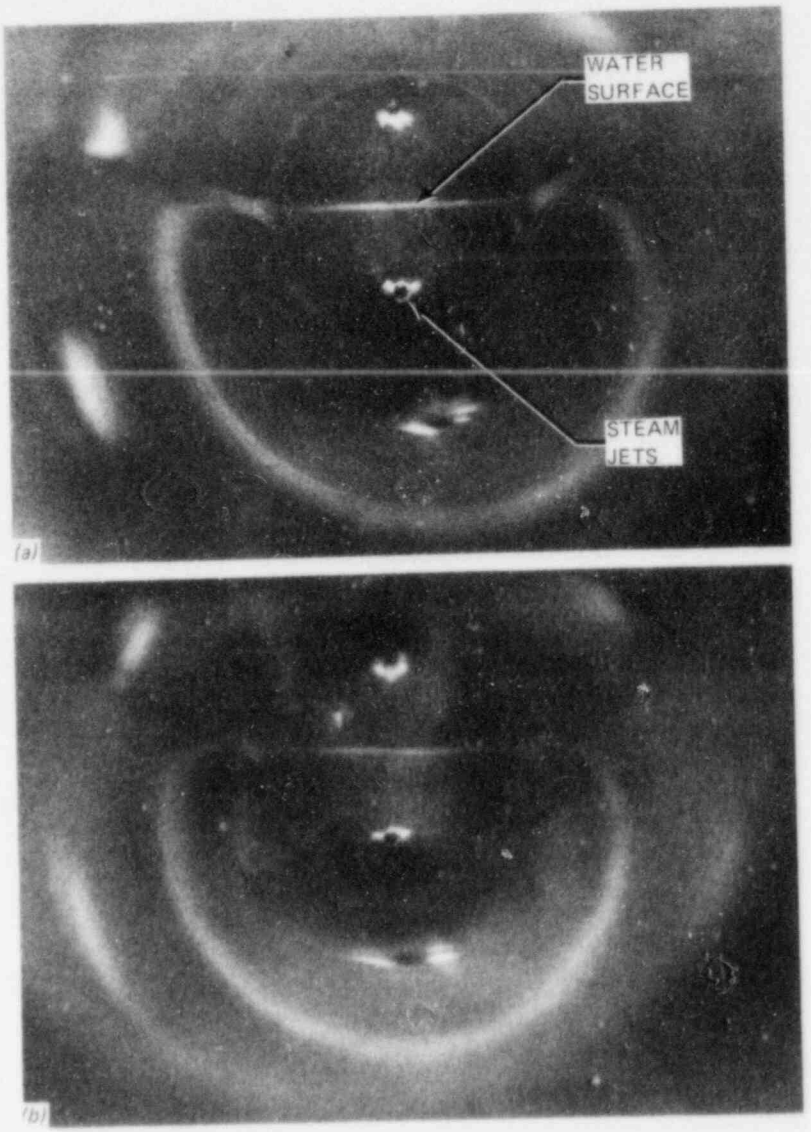

Fig. 15. End view of the discharging quencher.

CHAPTER III

DISSERTATION OBJECTIVES

A. MODELING REQUIREMENTS

There are many requirements that a PSP model must fulfill. Ideally, the model would be capable of simulating transient, three dimensional mass, momentum, and energy transport over a long period of time in a toroidal coordinate system. The ideal model would accomodate a free water surface and allow for internal flow obstructions. It would predict the velocity distributions in the highly turbulent shear flow near the energy source while at the same time coupling to the very slow buoyancy-driven flow in the part of the domain located far away from the source. The ideal model would describe the flow in the PSP immediately following a SRV closure. It would accomodate internal wave motions and the ensuing thermal stratification of the pool.

Besides the above phenomenological requirements, there are also practical requirements that any PSP model must meet. When implemented on a computer, the model must execute quickly, because the transients of interest often involve many hours of real time. In addition, the model must be simple enough to allow coupling to other computer models that describe the reactor, primary containment, and secondary containment.

It is economically impossible to construct an "ideal" PSP model. However, a "good" PSP model can be built by meeting as many of the ideal modeling requirements as possible.

An implicit objective of this dissertation is to build a PSP model that is as close as possible to the ideal model described above.

B. SPECIFIC OBJECTIVES

The primary objective of this dissertation is to develop and evaluate a computational model for PSP thermal mixing. The focus will be the PSP temperature response to a single safety relief valve discharge.

During the course of this dissertation effort, it was found that improvements and extensions of the PSP model beyond the primary objective were easily performed. In order to provide a more complete PSP thermal mixing model, these improvements were made, and are listed below as secondary objectives. The secondary objectives of this dissertation are

1. to extend the PSP model to include the capability of modeling an arbitrary number of SRVs discharging steam through T-quenchers into the PSP,
2. to extend the PSP model capability past the point in time when the water near the T-quencher saturates,

3. to provide the capability to model the PSP thermal mixing when a large circumferential velocity is induced in the pool by the RHR system,
4. to provide the capability to model a well mixed PSP, and
5. to show applications of the PSP model to some current BWR pressure suppression pool safety studies.

CHAPTER IV

MATHEMATICAL MODEL OF THE PRESSURE SUPPRESSION POOL

A. OVERALL DESCRIPTION OF THE THERMAL MIXING MODEL

The BWR pressure suppression pool (PSP) thermal mixing model is not an individual mathematical prescription or a single computational fluid dynamics algorithm for determining the PSP thermal mixing. Rather, it is an ensemble of four separate flow models and one thermal model for the purpose of determining the transient temperature distribution throughout the pool. The flow models are (1) a thermal convection cell model, (2) a thermal stratification model, (3) a bulk pool circulation model and (4) a well-mixed pool model.

The four modeling groups are designed to accomodate as broad a range of PSP transients as possible. Group 1 consists of the flow phenomena that exist when one or more SRVs is discharging through a T-quencher. The flow field is characterized by large, alternating convection cells that are formed by an outflow from the top of the discharge bay (Bay D), a downflow in the region away from Bay D, and a countercurrent inflow to the bottom of Bay D. The thermal convection cell model applies to group 1. Group 2 consists of the flow phenomena that exist when the SRVs are turned off or when energy is added to the PSP with very small initial momentum. The flow field in this group is characterized by complicated internal buoyancy effects that create a thermal stratification in the pool. The thermal stratification model applies to group 2. Group 3 consists of the mixing phenomena induced by a bulk circumferential circulation in the PSP. The flow field in this group is described by a 1D, circumferential variation of velocity and temperature. The bulk pool circulation model applies to group 3. Group 4 consists of uniform whole-pool mixing. The flow field in this group is a highly turbulent, 3D motion. The well-mixed pool model applies to group 4.

All of the models have a common goal: to determine the PSP temperature distribution at a new time $t + \Delta t$, given the temperature distribution at time t and the total energy input to the pool. In addition, all of the models have a common approach to the temperature calculations. That approach is outlined in the steps below.

1. The PSP is broken into N user-determined lumped nodes. The nodes are defined by a grid in the vertical and circumferential direction. There are arbitrary (user input) nodes in both directions.
2. Energy balances are written for all the nodes in the form of first order ordinary differential equations (ODEs) for the rate of change of the nodal temperatures. The coefficients of the equations are determined from the flow field.
3. The flow field (at the current time t) is determined by one of 4 models for the PSP thermal mixing.

4. The coupled set of N ODEs is solved for the temperature distribution at the new time t + Δt.

There are three major assumptions included in the above modeling scheme. The first assumption is that the pool can be modeled using a limited, 2D, transient approach to the energy transport. The two dimensions are z, the vertical direction, and θ , the circumferential direction.

This assumption is based on a study of the Monticello data,[55] which is described in Chapter six, and on a study of the basic physical phenomena, which are described in Chapter two.

Figure 16 is a schematic of the 2D "unwrapping" of the PSP from a 3D torus to a 2D z-θ model.

The second major assumption is that the flow field in the torus can be evaluated at the current time t and assumed fixed over the time step Δt. Furthermore, the flow field is assumed to be calculable based on steady state analyses of the pool temperature distribution at t and the characteristics of the energy source. This method is denoted as the quasistatic approach.*

The third major assumption in the PSP model is that lumped parameter energy balances are an adequate representation of the energy equation.

The implications of the above assumptions are discussed in Appendix B.

Figure 17 is a schematic of a general node i, of uniform temperature T_i, bounded on the right by node i+1 and on the left by node i-1. Above is node $i+N_\theta$ and below is node $i-N_\theta$. The bounding nodes are also of uniform temperature. The inflow from the right side FIR carries with it energy $(C_pT)_{i+1}$.† The outflow to the right, FOR, carries with it energy $(C_pT)_i$. The left, top, and bottom sides behave similarly.

In order to simulate the energy addition due to the T-quencher, a uniform volumetric mass source for node i, S_i, is added to the discharge bay nodes. This source exists only for those nodes which include the T-quencher. The construction of S_i is discussed in Section C of this chapter.

A general energy balance on node i is given by

$$\frac{dU_i}{dt} = \Sigma(h\dot{m})_{in} - \Sigma(h\dot{m})_{out} + S_i \qquad (1)$$

---

*The term quasistatic comes from the neutron kinetics field. There, the spatial shape of the neutron flux is assumed constant over a time step in a time dependent flux calculation. The comparison between that work and this dissertation is that the flux shape is analogous to the PSP flow field and the amplitude of the flux is analogous to the PSP temperature.

†In this work the enthalpy of the PSP water is expressed as the product of an average specific heat, Cp, and the temperature T, above a reference. The reference temperature is 32°F.

where

U_i = the internal energy of node i,
h, δm = the enthalpy and mass flow, respectively, of water that crosses the node boundary (does not include the mass crossing the boundary at the T-quencher since this is included in S_i).

If node i is assumed to be a fixed, incompressible volume of water, then equation (1) may be written as

$$M_i C_p \frac{dT_i}{dt} = (FIL)C_p T_{i-1} + (FIR)C_p T_{i+1} + (FIB)C_p T_{i-N_\theta}$$

$$+ (FIT)C_p T_{i+N_\theta} - (FOL + FOB + FOR + FOT)C_p T_i + S_i \ , \qquad (2)$$

where

FIL, FIR, FIT, FIB = flow into the left, right, top, and bottom faces of node i, respectively,
FOL, FOR, FOT, FOB = flow out the left, right, top, and bottom faces of node i, respectively.

The diffusion terms have been neglected in writing equation (1). In the circumferential direction, the density driven convection dominates the turbulent thermal diffusion part of the transport. In the vertical direction, the diffusion is strongly inhibited by the thermal stratification.

When equation (2) is applied to each node in the domain, the result is a set of N ODEs. The coupled set of ODEs can be arranged in matrix form as

$$\frac{d\underset{\sim}{T}}{dt} = \underset{\sim}{A}\underset{\sim}{T} + \underset{\sim}{S} \qquad (3)$$

with initial conditions

$$\underset{\sim}{T}(0) = \underset{\sim}{T}_i$$

The vector S contains all the source terms in equation (1). The matrix A contains all the flow field information. A changes at each time step due to changes in the flow field.

The system of ODEs, (3), is solved for the PSP nodal temperatures T at time $t+\Delta t$. The details of the solution method are described in Chapter five.

The remainder of this chapter describes the four flow models in detail. Emphasis is placed on the convection cell model (described in sections B, C, and D) and the thermal stratification model (section E) because these two models satisfy the primary goal of this dissertation. The bulk pool circulation model described in section F and the well mixed pool model described in section G are very simple models that were added in order to have a comprehensive PSP modeling package. The utility of these extra models is described in Appendix C where use of the models is discussed.

B. THERMAL CONVECTION CELL MODEL--GENERAL DESCRIPTION

The thermal convection cell model is designed for transients where one or more safety relief valves is discharging steam through a T-quencher into the PSP. As discussed in Chapter 2, the discharging T-quencher creates a very turbulent, shear mixing in the immediate vicinity of the T-quencher (the near field) and a much slower, buoyancy driven flow in the remainder of the torus (the far field). The near field/far field density difference determines the strength of the far field circulation. The far field circulation slowly feeds back into the near field mixing by changing the near field density and the momentum source (the condensation).

The purpose of the convection cell model is to determine the flow field in the highly turbulent near field (using the near field theory which is described in section C) and in the slower moving far field region (using the far field theory which is described in section D). In addition, the model must couple the two regions to determine a 2D flow distribution for the entire PSP that conserves mass and momentum. The 2D flow field can then be integrated over the cell faces to produce the coefficients for the lumped parameter temperature calculations. Figure 18 illustrates the discharging T-quencher, the near field, and the far field region.

The fluid motion in the near field is plume-like, with an impingement zone at the water surface. The vertical component of the near field flow forms the left side of a large convection cell, as shown in Fig. 19. The top of the cell is made up of the hot water outflow from the near field. The outflow decelerates to zero horizontal velocity as it moves along the top of the far field toward a symmetry plane. The deceleration produces a downflow, corresponding to the right side of the convection cell. The downflow feeds a countercurrent flow at the bottom of the PSP that moves back toward the T-quencher. The backflow forms the bottom of the convection cell.

The convection cell is bounded on either side by a symmetry plane. One plane passes through the center line of the T-quencher, the other plane is located half-way between the T-quencher under study and the next discharging quencher. If only one T-quencher is discharging, the second symmetry plane is 180° from the discharging T-quencher's center line.

C. THERMAL CONVECTION CELL MODEL--NEAR FIELD ANALYSIS

1. Description of the Near Field Region

The near field is broadly defined as the region of the PSP containing the T-quencher. Since the T-quencher is about as long as one bay of the suppression pool, the theta boundaries of the near field are conveniently chosen to be the theta boundaries of the discharge bay. If the T-quencher is centered at the intersection of two bays, the theta boundaries become the center lines of the adjacent bays. The theta boundaries of the near field are shown in Fig. 20.

The near field is assumed to be symmetric about the center line of the T-quencher. All of the near field analyses apply to one half of the discharge bay.

There are two reasons for performing a detailed analysis of the near field. First, a near field analysis is necessary because the thermal mixing model of the entire PSP is incapable of describing the 3D mixing in the discharge bay. The fluid motion in the discharge bay is primarily in the direction that is neglected in the z-θ model. This flow is modeled in the near field analysis by starting with the steam condensation and following the hot water as it moves away from the T-quencher. Any detail about the thermal mixing in the discharge bay must come from the near field models.

The second reason for performing the near field analysis is to control the distribution of the extraneous source terms in the thermal energy balances that describe the whole pool.

In the z-θ model, the energy deposited by the T-quencher must be distributed among several large fluid cells. The question is, "How is the energy distributed?" The answer to the question is found by writing (and solving) special energy balances on the near field region. The detailed near field solutions are then used to construct the source terms that are required in the large cells that overlap the near field region in the thermal model of the whole pool.

In essence, the procedure used to construct the T-quencher source terms in the z-θ model of the whole pool involves using a small, very detailed model of the near field to drive a large, simpler model of the entire PSP.

The highly turbulent, 3D flow in the near field can be separated into four zones: a steam condensation zone, a plume transport zone, a surface spreading zone, and a local recirculation zone. The zones are illustrated in Fig. 21.

Each zone of Bay D is analyzed separately. The zones couple to form a lumped model for the near field region, as shown in Fig. 22.

The zonal analyses are performed in an order that is designed to follow the fluid motion. The steam condensation analysis is performed first; it provides the initial conditions for the plume transport analysis and determines the mass flow of the Bay D water that feeds the condensation. The plume transport analysis is performed second; it determines the entrainment from the surrounding water and the total energy at the end of plume zone. The surface spread analysis is third; it determines the layer thickness, h, and determines the amount of Bay D

water that leaves the near field region. The local recirculation analysis is performed last; it is a simple mass balance that recirculates in Bay D the difference between the plume flow that is input to the surface region and the far field outflow.

A lumped parameter energy balance (separate from the balances described in section A) is written for both the surface spreading zone and the local recirculation zone. This procedure is necessary for correct modeling of the source terms in the energy balances of the whole pool. The two coupled ODEs are solved analytically for the temperature of the surface and recirculation zones at the new time; the known solution, together with the plume energy transport, is then used to distribute the energy of the steam among the large, lumped nodes in the whole pool model. These special energy balances and their solution are described in part 8 of this section.

The remainder of this section describes the individual parts of the near field analysis.

2. T-Quencher steam condensation model

The steam condensation zone is defined by a control volume that encloses the T-quencher and the condensing steam. The steam usually exits from the T-quencher holes in a fan of small jets, as shown in Fig. 23.

The purpose of the condensation zone analysis is to determine a set of initial conditions for input to the plume transport analysis. Also determined is the amount of cold water feed, W_{cnd}, that flows into the condensation zone from the local recirculation zone.

There are three steps in the condensation zone analysis: (1) calculate the thermodynamic conditions in a typical quencher hole, (2) determine the steam condensation regime, and (3) calculate the plume initial conditions using conservation of momentum and energy.

A typical quencher hole is shown in Fig. 24. Two types of steam jet profiles are shown in Fig. 24: a sonic and a subsonic jet profile.

The flow at the quencher hole is sonic or subsonic depending on the mass flow into the quencher and the Bay D pressure. If the flow is sonic, the exit velocity, U_e, is given approximately as

$$U_e = \sqrt{\gamma P_e / \rho_e} \quad , \tag{4}$$

where

P_e = the exit plane pressure
ρ_e = the exit plane density.

Equation (4) treats the steam as an ideal gas (with $\gamma = 1.3$). Over the range of pressures and enthalpies of interest (Bay D pressures from 18 psia to 150 psia and enthalpies close to 1200 Btu/lbm), equation (4) is a fairly accurate approximation to the choked quencher hole velocity.[56] Although it is strictly incorrect to treat steam as an ideal gas, equation (4) nevertheless produces reasonable estimates of the sonic velocity. In Kerney's[56] study of submerged steam jets, the

vapor velocities found using (4) matched those from a Fanno flow solution to within 1 % under most conditions.

If adiabatic flow is assumed from the reactor vessel to the T-quencher, then

$$h_o = h_e + U_e^2/2g_cJ \ , \tag{5}$$

where

h_o = reactor vessel stagnation enthalpy,
h_e = quencher hole exit enthalpy,
U_e = quencher hole exit velocity.

Assuming uniform velocity over the hole exit area, A_e,

$$\dot{m}_e = \rho_e A_e U_e \tag{6}$$

Given $\dot{m}_e/A_e$ and h_o as input, the choked flow conditions at the quencher exit plane (U_e, P_e, ρ_e, h_e) are determined by a simple iterative procedure using the ASME steam tables. The solution results for the standard T-quencher are shown in Figure 25 in the form of quencher hole exit plane pressure, P_e, as a function of the quencher mass flow and the reactor stagnation enthalpy.

The curves of figure 25 are correlated by

$$P_e = a + b\ \dot{m}_Q \ , \tag{7}$$

where

$$\begin{aligned} a &= -0.5, \\ b &= 0.08 + 0.0001\ h_o, \\ P_e &= \text{exit plane pressure, psia,} \\ \dot{m}_Q &= \text{total flow through the T-quencher, Lbm/s.} \end{aligned} \tag{8}$$

For subsonic flow through the quencher holes, the exit plane pressure approximately equals the ambient pressure, i.e.,

$$P_e = P_\infty \tag{9}$$

and equations (5) and (6) still apply.

Given $\dot{m}_e/A_e$, h_o, and P_∞, an iterative procedure produces the subsonic conditions at the quencher exit plane. The solution is presented in Fig. 26 as the subsonic quencher hole exit plane velocity, U_e, versus the quencher total mass flow and the Bay D local pressure. The curves in Fig. 26 are correlated by

$$U_e = c\ \dot{m}_Q + d\ \dot{m}_Q^2 \tag{10}$$

where

$$
\begin{aligned}
U_e &= \text{exit plane velocity, Ft/s,} \\
c &= c_1 P_\infty^{c_2}, \\
d &= c_3 P_\infty^{c_4}, \\
c_1 &= 371.6,\ c_2 = -1.013 \\
c_3 &= -29.77,\ c_4 = -2.347\ , \\
P_\infty &= \text{local pressure, psia.}
\end{aligned}
\tag{11}
$$

The model for determining the thermodynamic conditions at the quencher hole exit plane is summarized by the following steps.

1. Given the quencher mass flow and the stagnation enthalpy, calculate the choked flow exit plane pressure using equation (7).
2. If the Bay D pressure is greater than P_e, go to the subsonic steam jet section (step 5).

Sonic steam jets

3. Calculate ρ_e using equations (6) and (4).
4. Calculate U_e using equation (6); h_e using (5).

Subsonic steam jets

5. $P_e = P_\infty$ for subsonic flow.
6. Calculate U_e using equation (10).
7. Calculate ρ_e using equation (6); h_e using (5).

The second step in the steam condensation zone analysis is to determine the condensation regime for the T-quencher. A detailed condensation map does not exist for a steam diffuser submerged in water (a T-quencher). Therefore, a map is constructed based on a combination of (1) previous studies of single steam jet behavior in water, and (2) engineering judgement.

Chan[57] has presented a flow regime map for steam injected through a vertical pipe into a pool. He identifies three zones of chugging, three zones of steam jet behavior, one zone of bubble oscillation, and one zone in which steam passes uncondensed through the surface. The separation of the condensation behavior into many distinct zones and subzones is appropriate for a single, isolated steam jet. However, it is improper to apply this map directly to the complicated interactions of the numerous steam jets that exit the T-quencher. The purpose of using Chan's map is to roughly identify the condensation regime boundaries. Figure 27 is an approximation to Chan's map for application to T-quenchers.

A difficult part of determining the steam condensation regime is determining the effect of PSP overpressure on the flow map. The PSP overpressure determines the local saturation temperature near the T-quencher. In addition, the overpressure has a strong effect on the density of the steam that exits the T-quencher holes. These two effects make the PSP overpressure an important parameter in identifying the condensation regime.

Unfortunately, the effect on the condensation of varying the local pressure has not been studied experimentally. Virtually all of the steam — water condensation studies on jets have been performed at atmospheric pressure.

A guess at the effect of PSP overpressure on the condensation regime map is to assume that transitions from one regime to another occur at the same average steam velocity. This assumption is based on the way the boundary between the sonic and the subsonic regime varies in Fig. 26. As the local pressure is increased from 15 to 50 psia, the sonic velocity remains approximately constant (~1550 Ft/s). The boundary between the subsonic jets and bubble oscillation, and between bubble oscillation and chugging are also assumed to be flat. From Chan's data, these boundaries are estimated to be at 800 Ft/s and 400 Ft/s, respectively. Thus, the flow regime map for arbitrary PSP overpressure is developed, and shown in Fig. 28.

The third step in the T-quencher condensation zone analysis is to determine the plume initial conditions (width, velocity, and temperature) using the thermodynamic properties in the quencher hole and knowledge of the condensation regime.

The plume initial conditions are found by solving a bulk horizontal momentum and a conservation of energy equation that are written over the condensation zone boundaries. The side boundaries are shown in Fig. 29. The left hand boundary is a curved surface that passes through the steam jet exit planes. The right hand boundary is a vertical plane located X_c distance from the centerline T-quencher jet. X_c is the condensation length. R_Q is the T-quencher outside radius. Θ_z is the total angle subtended by all the quencher jets. As shown in Fig. 3 there are 4 zones of holes on the T-quencher, each with a different Θ_z.

The conservation equations are written for a typical column of holes on the T-quencher. As shown in Fig. 30 , the column spacing is L_1. The flow area at plane 1 is A_c:

$$A_c = 2L_1 (R_Q + X_c) \tan \Theta_z \ . \qquad (12)$$

A horizontal momentum balance between surface 0 and plane 1 is

$$g(N) \{A_e \rho_e U_e^2 + (P_e - P_\infty) A_e\} = A_c \rho_\ell U_\ell^2 \ , \qquad (13)$$

where

A_e = area of an individual quencher hole,
U_e = hole exit velocity,
ρ_e = hole exit density,
P_e = hole exit pressure,
P_∞ = Bay D local pressure,
ρ_ℓ = average density of hot water at plane 1,
U_ℓ = average velocity of hot water at plane 1,
$g(N)$ = initial x - momentum component. This function gives the fraction of the initial steam momentum that is imparted in the x - direction.

An energy balance over the same region is

$$N \dot{m}_e h_o + (\dot{m}_c - N\dot{m}_e) h_\infty = \dot{m}_c h_\ell \qquad (14)$$

where

N = number of holes in the column,
h_o = initial total enthalpy of the steam,
h_∞ = Bay D local enthalpy,
h_ℓ = hot water enthalpy at plane 1.

The initial flow into surface 0 is

$$\dot{m}_e = \rho_e A_e U_e \ . \tag{15}$$

The flow at plane 1 is

$$\dot{m}_c = \rho_\ell A_c U_\ell \ . \tag{16}$$

The total water entrained by the condensing steam is

$$\dot{m}_{ent} = \dot{m}_c - N\dot{m}_e \tag{17}$$

Given the conditions inside the quencher holes, the condensation length, X_c, is calculated using a correlation by Kerney[56] which gives the steam jet penetration length in terms of the initial mass flux, G_o, and a condensation potential, B_κ, defined by

$$B_\kappa = \frac{h_{s\ell} - h_\infty}{h_s - h_{s\ell}} \tag{18}$$

where

$h_{s\ell}$ = saturated liquid enthalpy
h_∞ = ambient enthalpy
h_s = initial enthalpy after the external expansion in a sonic jet. The external expansion region is shown in Fig. 24.

Kerney's correlation is

$$\frac{X_c}{r_o} = \frac{35.5 \sqrt{G_o/G_s}}{\sqrt{\rho_\infty/\rho_s}\ B_\kappa} \tag{19}$$

where

G_s, ρ_s = mass flux and steam density, respectively, at the end of external expansion
r_o = steam jet hole radius.

Equation (19) applies to sonic jets. For subsonic quencher jets and condensation oscillation at the T-quencher, Kerney's correlation is used to obtain an average X_c by eliminating the external expansion region.

For a sonic jet, subsonic jet, or condensation oscillation jet, the procedure for determining the plume initial conditions at each zone on the T-quencher is given by the following steps.

1. Calculate X_c, the condensation penetration length.
2. Calculate A_c using equation (12).
3. Assume a temperature T_ℓ for the plume initial temperature and calculate ρ_ℓ.
4. Calculate U_ℓ using (13).
5. Calculate $\dot{m}_\ell^c$ using (16), $\dot{m}_e$ using (15).
6. Calculate h_ℓ^c using (14).
7. Determine $T_\ell(h_\ell)$ from steam table data.
8. If T_ℓ(tables) - T_ℓ(assumed) is small, quit. If not, go back to step 2 with T_ℓ(assumed) = T_ℓ(tables).
9. The amount of cold water to feed the condensation is found using equation (17).

The above procedure is included in subroutine CONDNS, as described in the next chapter.

If chugging exists at the T-quencher, very little horizontal momentum is imparted to the Bay D water. The plumes that form due to chugging start directly above the T-quencher instead of out to the side. The plume initial conditions for this case are determined by assuming that just enough cold water is entrained to condense the steam. Furthermore, the flow area is assumed equal to the T-quencher pipe diameter multiplied by the length of the condensation zone. These assumptions are based on a study of Kerney's[56] steam jet work and Liseth's[58] merging plume work.

With the above two assumptions, the plume initial conditions for chugging are

$$U_\ell = \frac{N \dot{m}_e (1 + 1/B_\kappa)}{\rho_{s\ell} R_Q L_1} \tag{20}$$

with

$\rho_{s\ell}$ = saturated liquid density,
$T_\ell = T_{sat}$,
R_Q = T-quencher radius.

The initial plume width is 2 R_Q.

The plume initial conditions for chugging are included in subroutine CONDNS, as described in the next chapter.

3. Plume Transport Dynamics

An important part of the near field mixing is the vertical hot water transport from the T-quencher upward to the surface of the pool. The hot water is forced to the surface by the combined action of the condensation momentum source and the buoyancy of the hot water relative

to the colder Bay D water. As it moves upward, the plume cools by entraining the surrounding water. Figure 31 illustrates the plume transport region of the near field.

The objective of the plume transport analysis is to determine the entrainment from the discharge bay into the plume, and to determine the plume temperature near the PSP surface. The entrainment and plume terminal temperature will provide enough information to construct the sources and sinks that drive the energy balances of the near field.

The plume transport problem begins a short distance away from the T-quencher where steam has condensed and a rectangular jet of hot water is formed. At this point, the water temperature, velocity, density, and jet thickness are known. To model the behavior from this initial condition upward, a set of one dimensional conservation equations for mass, momentum, and energy are written for the forced plume transport. The equations are written along the plume trajectory, s.

In essence, the equations are formulated as an initial value problem for numerical solution. The march will begin near the T-quencher and end near the water surface. The following development starts with the conservation equations and ends with a coupled set of one ODE and two algebraic equations for the solution. A solution method is then outlined for obtaining the plume temperature, width, and velocity as a function of position in the discharge bay.

A rectangular jet of thickness b_o and width M originates at the origin of the rectangular coordinate system in Fig. 32. At the origin the plume has initial temperature T_o (which is greater than the ambient temperature, T_∞) and velocity U_{po}. At any point along s (the plume centerline trajectory), a tangent to s makes an angle Ψ with the horizontal. The plume flow is assumed to be steady state, and the properties across the width and thickness are assumed constant. In addition, the following assumptions are made.

1. Viscous dissipation is negligible, and
2. the plume entrains water from the ambient at a rate linearly proportional to the local velocity, i.e., U_{ent} = entrainment velocity = αU_p. α is the entrainment coefficient.

Assumptions (1) and (2) are common to almost all plume analyses performed in the past.[59-61] The constant α has a numerical value determined by numerous experiments[62,63] to be in the range 0.08 - 0.16. A best estimate for α is 0.10 (Ref. 64).

The set of equations to solve (in dimensional form) is

$$\frac{d}{ds}(\rho U_p b) = 2 \alpha \rho_\infty U_p , \tag{21}$$

$$\frac{d}{ds}(\rho U_p^2 b \sin \Psi) = b (\rho_\infty - \rho) g , \tag{22}$$

$$\frac{d}{ds}(\rho U_p^2 b \cos \Psi) = 0 , \tag{23}$$

$$\frac{d}{ds}(\rho U_p b T) = 2 \alpha \rho_\infty U_p T_\infty , \tag{24}$$

where

$$T(o) = T_o,$$
$$U_p(o) = U_{po},$$
$$b(o) = b_o, \text{ and}$$
$$\rho(s) = \rho[T(s)] .$$

$\Psi(s)$ is the angle that the plume forms with the horizontal at any location s.

Equation (21) stated in words is: the local rate of change of the plume mass equals the rate at which ambient fluid is being entrained. Equation (22) states: the local rate of change of vertical momentum equals the local buoyant force. Equation (23) implies that the horizontal momentum is constant. Equation (24) equates the local rate of change of the plume energy to the rate at which energy is carried into the plume with the entrained fluid.

The set of equations (21) through (24) is different from most plume transport analyses because the Bousinesq approximation is not used. The plume density is simply carried along as a nonlinear coefficient that depends on the local temperature.

The equations can be non-dimensionalized by defining

$$\tilde{T} = \frac{T - T_\infty}{T_o - T_\infty}$$

$$\tilde{\rho} = \rho/\rho_o$$

$$\tilde{b} = b/b_o$$

$$\tilde{U}_p = U_p/U_{po}$$

$$\tilde{s} = s/b_o$$

The conservation equations are then

$$\frac{d}{d\tilde{s}} (\tilde{\rho}\, \tilde{U}_p\, \tilde{b}) = \frac{2\, \alpha\, \rho_\infty}{\rho_o} \tilde{U}_p \tag{25}$$

$$\frac{d}{d\tilde{s}} (\tilde{\rho}\, \tilde{b}\, \tilde{U}_p^{\,2} \sin \Psi) = \frac{(\rho_\infty - \rho)\, g\, b_o}{\rho_o\, U_{po}^{\,2}} \tilde{b} \tag{26}$$

$$\frac{d}{d\tilde{s}} (\tilde{\rho}\, \tilde{b}\, \tilde{U}_p^{\,2} \cos \Psi) = 0 \tag{27}$$

$$\frac{d\tilde{T}}{d\tilde{s}} = - \frac{2\, \alpha\, \rho_\infty}{\rho_o} \frac{\tilde{T}}{\tilde{\rho}\tilde{b}} \tag{28}$$

with

$$\tilde{T}(o) = 1$$

$$\tilde{U}_p(o) = 1$$

$$\tilde{b}(o) = 1 \qquad (28a)$$

$$\Psi(o) = 0$$

$$\tilde{\rho}(o) = 1$$

Several authors[65-67] solve plume transport problems similar to equations (25) through (28) by numerically solving the full set of non-linear ODEs. An approach such as that would be prohibitively expensive for use within the PSP model. The problem becomes much simpler if a jet trajectory is known.

Such a trajectory was obtained from the work of Cederwall.[68] In his work on buoyant slot jets, the trajectory data for a wide range of jet Froude numbers were found to lie along a straight line on a log-log plot. A linear fit (on a log-log plot) to Cederwall's data produced the following equation.

$$y/b_o = 0.2356 \left(\frac{x}{b_o}\right)^{2.5779} F_j^{-2.104} \qquad (29)$$

where

$$F_j = \frac{U_{po}}{\sqrt{\frac{\rho_\infty - \rho_o}{\rho_\infty} g\, b_o}}$$

Equation (29) is a correlation for the plume trajectory y(x) as a function of the initial conditions F_j.

With the trajectory (29) known, the angle Ψ is given by

$$\Psi = \tan^{-1}\left(\frac{dy}{dx}\right) \qquad (30)$$

Since Ψ is determined, one of the equations (25) through (28) can be eliminated. Equation (26) is eliminated because it is very difficult to solve near $\Psi = o$.

The plume transport problem is now to solve equations (25), (27), (28), and (29). Equations (25) and (28) can be combined to yield

$$\frac{d\tilde{T}}{ds} = -\frac{d}{ds}\left(\tilde{\rho}\,\tilde{U}_p\,\tilde{b}\right)\frac{\tilde{T}}{\tilde{\rho}\,\tilde{U}_p\,\tilde{b}} \qquad (31)$$

The solution of (31) is

$$\tilde{T} = \frac{1}{\tilde{\rho}\,\tilde{U}_p\,\tilde{b}}\,. \qquad (32)$$

The solution of (27) is

$$\tilde{\rho}\,\tilde{b}\,\tilde{U}_p^{\,2}\cos\Psi = 1 \ . \tag{33}$$

If (32) and (33) are substituted into (28), the energy equation becomes

$$\frac{d\tilde{T}}{d\tilde{s}} = \frac{-2\,\alpha\,\rho_\infty}{\rho_o}\,\frac{\tilde{T}^3}{\cos\Psi} \ . \tag{34}$$

The plume transport problem is thus reduced to solving equations (32), (33), and (34) subject to the initial conditions (28a) and constraint (29).

A numerical solution to the problem is found by writing (34) as

$$\frac{d\tilde{T}}{d\tilde{s}} = -A(s)\,\tilde{T}^3 \tag{35}$$

where

$$A(s) \equiv \frac{2\,\alpha\,\rho_\infty}{\rho_o\cos\Psi(s)} \tag{36}$$

Equation (35) can be written as

$$\frac{d\tilde{T}}{A\tilde{T}^3} = -\,d\tilde{s} \tag{37}$$

If A is assumed to be constant over an interval $\Delta\tilde{s}$, (37) can be integrated. The integration is taken from a point $\tilde{s}$ where $T = T_i$ to $\tilde{s} + \Delta\tilde{s}$ where $\tilde{T}$ is desired. The integral is

$$\frac{1}{2A}\,\frac{1}{\tilde{T}^2}\Bigg|_{\tilde{T}_i}^{\tilde{T}} = \Delta\tilde{s} \ . \tag{38}$$

After rearranging, (38) becomes

$$\tilde{T}^2 = \frac{\tilde{T}_i^{\,2}}{1 + 2\,A\,\Delta\tilde{s}\,\tilde{T}_i^{\,2}} \ . \tag{39}$$

A solution procedure for a numerical plume transport calculation is outlined below.

1. Begin at $\tilde{s}$
2. calculate A from (36)

3. calculate $\tilde{T}(\tilde{s} + \Delta\tilde{s})$ using (39)
4. calculate $\tilde{U}_p$ and $\tilde{b}$ using (32) and (33), respectively.
5. Let $\tilde{s} = \tilde{s} + \Delta\tilde{s}$ and go to step 2.

A subroutine was written to implement the solution procedure described above from an initial condition at the T-quencher up to the surface. The subroutine is described in the next chapter.

Some typical results for the plume temperature as a function of vertical position for various Froude numbers is shown in Fig. 33. As expected, at low jet Froude numbers, the plume entrains little ambient fluid near the source ($y = 0$) and hence slightly warmer water reaches the PSP surface. The buoyancy thus dominates the flow for low F_j. As F_j is increased, more entrainment occurs in the lower part of the pool, and the plume is cooled before it reaches the water surface. Hence, for high F_j, the initial jet momentum dominates the flow.

The plume transport temperature results were found to be relatively insensitive to the vertical step size, dy/b_o. Table 1 contains temperature results at various elevations as a function of the vertical step size. As $d\tilde{y}$ was decreased by a factor of 1000 (0.4 to 0.0004), $\tilde{T}$ only changed by about 0.1% . This precision is attributed to the benefits obtained by solving most of the problem analytically.

Table 1. Sensitivity of $\tilde{T}$ to the vertical step size $d\tilde{y}$

Step size dy/b_o	$\tilde{T}\big\|_{\tilde{y}=4}$	$\tilde{T}\big\|_{\tilde{y}=8}$	$\tilde{T}\big\|_{\tilde{y}=16}$
4.0	0.41927	0.35781	0.29429
0.4	0.41190	0.35282	0.29116
0.04	0.41162	0.35261	0.29101
0.004	0.41161	0.35260	0.29100
0.0004	0.41161	0.35260	0.29100

$\tilde{y} = y/b_o$

$F_j = 5.0$

The plume transport analysis was verified by comparing the numerical results to Cederwall's experimental dilution data and the analytical dilution predictions of other experimenters.[69-71] Figure 34 is a comparison of typical results from the plume transport analysis (with $F_j = 5$) to Cederwall's experimental data and the analytical predictions of

three other experimenters. Figure 34 is identical to figure 8 in Cederwall's study, with the current results shown for comparison. The dilution was defined as

$$S_m = \frac{\rho_o - \rho_\infty}{\rho - \rho_\infty} \tag{40}$$

Equation (40) is consistent with Cederwall's definition of S_m.

The plume dilution results compare well with the other dilution predictions. The curve shape agrees with two other analysts, the curve passes through the data, and it approaches the experimental correlation of Rouse[71] for low F_j.

4. Plume Impingement Dynamics

The T-quencher is confined in the discharge bay. Obviously, for large jet Froude numbers in equation (29), the plume will hit the torus wall. Figure 35 illustrates the wall impingement problem. When the impingement occurs, the plume will turn upward and move vertically to the surface. At impingement, the angle Ψ will be changed abruptly from its value before impingement to about $\Psi = 90°$. From that point upward, the plume transport model using the trajectory (29) is invalid. The following model is proposed for determining the plume transport after impingement.

With sin $\Psi = 1$ at impingement, equation (26) becomes

$$\frac{d}{ds}(\tilde{\rho}\,\tilde{b}\,\tilde{U}_p^2) = \frac{(\rho_\infty - \rho)}{\rho_o}\,\frac{g\,b_o}{U_{po}^2}\,\tilde{b} \tag{41}$$

If the inertial part of the jet Froude number is strong enough to force wall impingement, it is assumed that the right hand side of (41) can be neglected. This assumption in effect neglects the buoyant force after wall impingement, and holds the total vertical momentum after impingement constant. This is an assumption common to almost all isothermal jet analyses.[72] Hence (41) becomes

$$\frac{d}{ds}(\tilde{\rho}\,\tilde{b}\,\tilde{U}_p^2) = 0 \tag{42}$$

or

$$\begin{aligned} \tilde{\rho}\,\tilde{b}\,\tilde{U}_p^2 &= \text{constant} \\ &= \tilde{\rho}\,\tilde{b}\,\tilde{U}_p^2 \Big|_{\text{impingement}} \end{aligned} \tag{43}$$

The plume transport problem after wall impingement is to solve equations

(43), (32), and (28) beginning with the initial conditions

$$\begin{aligned} \tilde{T} &= \tilde{T}\Big|_{\text{impingement}} \\ \tilde{b} &= \tilde{b}\Big|_{\text{impingement}} \\ \tilde{U} &= \tilde{U}\Big|_{\text{impingement}} \end{aligned} \tag{44}$$

Equations (43) and (32) can be combined to yield

$$\tilde{U} = \tilde{T}\,(\tilde{\rho}\,\tilde{b}\,\tilde{U}_p^{\,2})\Big|_{\text{impingement}} = \tilde{T}\,K_1\,, \tag{45}$$

after jet impingement. With equation (45) and (32), equation (28) becomes

$$\frac{d\tilde{T}}{ds} = \frac{-2\,\alpha\,\rho_\infty}{\rho_o}\,K_1\,\tilde{T}^3 \tag{46}$$

Equation (46) is almost identical to equation (34). The only difference is that the $1/\cos\Psi$ term in (34) is replaced by K_1 in (46). The same solution procedure can be used for solving (46) by redefining the constant A in (36), i.e.,

$$A(\tilde{s})\Big|_{\text{after impingement}} \equiv \frac{2\,\alpha\,\rho_\infty}{\rho_o}\,K_1\,. \tag{47}$$

A solution procedure for the plume transport after wall impingement is outlined below.

1. Start at the point of wall impingement. Use $\tilde{T}$, $\tilde{u}$, $\tilde{b}$ at that point as initial conditions.
2. calculate A from (47)
3. calculate $\tilde{T}(\tilde{s} + \Delta\tilde{s})$ using (39)
4. calculate $\tilde{U}_p$ using (45)
5. calculate $\tilde{b}$ using (32)
6. let $\tilde{s} = \tilde{s} + \Delta\tilde{s}$ and go to step 2.

The same subroutine that was used to implement the plume transport solution of the previous section contains the above procedure for the transport after impingement. The subroutine is described in the next chapter.

5. Merging Plume Dynamics

If the T-quencher discharge has very low initial momentum, the plumes formed on each side of the quencher will merge directly above the quencher to form a single plume. Figure 36 illustrates the merging plume problem. This flow regime can occur for low steam flow condensation inside the quencher.

Liseth[73] has studied the merging plume problem for buoyant jets issuing from a diffuser manifold. The pictures in his report indicate that the merging point is about one pipe diameter above the diffuser. The merged plume transport analysis will apply from this point upward to the surface of the pool.

From the merge point upward, the merged plume transport analysis is analogous to the wall impingement treatment of Part 4; except in this case the buoyant force is the dominant mechanism for plume mixing instead of the initial momentum.

The vertical momentum equation, (41), the energy equation, (28), and the conservation relation, (32), will be used to model the vertical transport. If (32) is substituted into (41), the result is

$$\frac{d}{d\tilde{s}} \left(\frac{\tilde{U}_p}{\tilde{T}} \right) = \frac{(\rho_\infty - \rho)}{\rho_o} \frac{g\, b_o}{U_{po}^2} \tilde{b} \,. \tag{48}$$

Equation (28) can be written as

$$\frac{d\tilde{T}}{d\tilde{s}} = \frac{-2\, \alpha\, \rho_\infty}{\rho_o} \tilde{U}_p\, \tilde{T}^2 \,. \tag{49}$$

The merged plume transport problem is essentially to solve (48), (49), and (32) subject to the initial conditions (28a).

If the right hand side of (48) is assumed constant over a small step $\Delta\tilde{s}$, (48) can be solved for $\tilde{U}_p/\tilde{T}$. The result of integrating (48) from $\tilde{s}$ to $\tilde{s} + \Delta\tilde{s}$ is

$$\frac{\tilde{U}_p}{\tilde{T}} = \frac{(\rho_\infty - \rho)}{\rho_o} \frac{g\, b_o}{U_{p\phi}^2} \tilde{b} \Bigg|_{\tilde{s}} \Delta\tilde{s} + \frac{\tilde{U}_p}{\tilde{T}} \Bigg|_{\tilde{s}} \tag{50}$$

$$= K_2(\tilde{s})$$

or

$$\tilde{U}_p \Big|_{\tilde{s}+\Delta\tilde{s}} = K_2(\tilde{s})\, \tilde{T} \Big|_{(\tilde{s} + \Delta\tilde{s})} \tag{51}$$

If (51) is substituted into (49),

$$\frac{d\tilde{T}}{d\tilde{s}} = \frac{-2\, \alpha\, \rho_\infty}{\rho_o} K_2\, \tilde{T}^3 \,. \tag{52}$$

Equation (52) has the same form as (46) and (34) . Only the constant has changed. Therefore, the same general equation [equation (39)] can be used for the solution, and the same subroutine can be used for implementation. The subroutine is described in the next chapter. The solution method is outlined below.

1. Begin at the point of plume merging. $\tilde{T}$, $\tilde{u}$, $\tilde{b} = 1$.
2. Calculate K_2 using (50).
3. Calculate $\tilde{T}$ $(\tilde{s}+\Delta\tilde{s})$ using (39), where A in equation (39) is replaced by K_2.
4. Calculate $\tilde{U}_p$ using (51) .
5. Calculate $\tilde{b}$ using (32) .
6. Let $\tilde{s} = \tilde{s} + \Delta\tilde{s}$ and go to step 2 to move another step along the trajectory.

6. Surface Spreading Models

The surface spreading zone is defined as the part of the near field that extends from the surface of the pool downward to the point where the plume flow starts changing into a complicated 3D surface impingement. Figure 37 illustrates the surface spreading region.

The purpose of the surface spreading model is to obtain an estimate of the hot water layer thickness and an average horizontal velocity that models the near field/far field interchange.

In the surface spreading model, the near field outflow is treated as a density current, as described in Chapter 2. The density current is assumed to be of uniform thickness h_d. The driving force for the gravity current is the density difference between the discharge bay, ρ_1, and the interior of the far field, ρ_2. A reasonable choice for ρ_2 is the average density of the entire far field region. The density current model is illustrated in Fig. 38.

The surface spreading problem in the PSP is unlike any of the classical problems involving turbulent, buoyant convection from a source in a confined region.[74-76] In the classic treatment, all of the vertical momentum in the discharge bay is directed outward after the surface impingement. The result is a supercritical flow in a small layer immediately outside the surface impingement followed by an internal hydraulic jump (sometimes called a density jump) to subcritical flow in the far field. The jump can be stable or unstable; criteria exist for predicting the stability.[77] The internal hydraulic jump treatment is inappropriate for the surface spreading problem because most of the momentum is reflected off the surface and causes a recirculation flow in the discharge bay that feeds the steam condensation and the plume entrainment.

At the ends of the T-quencher, there is a small contribution to the outflow from the vertical momentum of the plumes. However, for the most part, the exchange between the near field and the far field is governed by the pressure difference created by the horizontal density gradient.

A cross section of a circular channel is shown in Fig. 39. For any level z, the cross sectional area below z is

$$A = (\pi - \alpha_p + \frac{1}{2} \sin 2\,\alpha_p)\, a^2 , \qquad (53)$$

where

$$\alpha_p = \cos^{-1}\left(\frac{z - a}{a}\right) .$$

In Fig. 38, a steady state mass balance written between section 1 (at the discharge bay) and section 2 (far downstream) yields

$$\rho_1 U_1 (A_1 - A_2) = \rho_2 U_2 A_2 , \tag{54}$$

where

A_1 = the area below z = D
A_2 = the area below z = D - h_d.

In equation (54) the velocities are assumed constant over their respective areas. Equation (54) simply states that the outflow equals the inflow at section 1.

Equation (54) is rewritten as

$$\frac{U_2}{U_1} = \frac{\rho_1}{\rho_2} \left(\frac{A_1}{A_2} - 1 \right) \tag{55}$$

The PSP surface spreading problem is similar in many respects to a lock exchange problem.[78-80] For those problems, and with a rectangular cross section, Turner[80] gives U_2 as

$$U_2 = 0.47 \sqrt{g' d} \tag{56}$$

where

$$g' = \frac{(\rho_2 - \rho_1)}{\rho_1} g$$

d = a characteristic length .

He gives U_1 as

$$U_1 = 0.59 \sqrt{g' d} \tag{57}$$

thus, the ratio U_2/U_1 equals about 0.80 .

The same velocity ratio is assumed to hold for the PSP flow, i.e.,

$$\frac{U_2}{U_1} \equiv 0.80 \tag{58}$$

With equation (58), equation (55) becomes

$$\frac{A_2}{A_1} = \frac{1}{1 + (0.8) \frac{\rho_2}{\rho_1}} \tag{59}$$

Using equation (53)

$$\frac{A_2}{A_1} = \frac{A\ (z = D - h)}{A\ (z = D)} = \frac{\pi - \alpha_p + \frac{1}{2} \sin 2\ \alpha_p}{\pi - \alpha_D + \frac{1}{2} \sin 2\ \alpha_D} , \qquad (60)$$

where

$$\alpha_D = \cos^{-1}\left(\frac{D - a}{a}\right)$$

Given the pool depth, D, the torus minor radius, a, and the ratio ρ_2/ρ_1, equations (59) and (60) can be solved for α_p. The layer thickness, h_d, is then found by substituting $z = D - h_d$ into the expression for α_p.

Equations (59) and (60) were solved for various ratios ρ_2/ρ_1 and D/a. The results are presented in Fig. 40 in the form of h_d/D versus ρ_2/ρ_1 for various D/a. The results in Fig. 40 are correlated by

$$h_d/D = C_1 + C_2 \frac{\rho_2}{\rho_1} , \qquad (61)$$

where

$$C_1 = 0.141 + 0.117\left(\frac{D}{a}\right) + 0.0281\left(\frac{D}{a}\right)^2 ,$$

$$C_2 = 0.1915 + 0.0112\left(\frac{D}{a}\right) - 0.0032\left(\frac{D}{a}\right)^2 .$$

Equation (57) is used to obtain the velocity at section 1. Benjamin[81] and Lamb[82] give the proper depth scale for pipe flow as

$$d = \frac{\text{area}}{\text{section width}}$$

or,

$$d = \frac{(\pi - \alpha_p + \frac{1}{2} \sin 2\ \alpha_p)\ a^2}{2\sqrt{2\ a\ D - D^2}} . \qquad (62)$$

Substituting (62) into (57) and rearranging gives

$$\frac{U_1}{\sqrt{g\ D}} = 0.59\ \frac{\rho_2}{\rho_1} - 1 \sqrt{\frac{(\pi - \alpha_p + \frac{1}{2} \sin 2\ \alpha_p)(a/D)^2}{2\sqrt{2\ (a/D) - 1}}} \qquad (63)$$

The left hand side of (63) is the characteristic Froude number of unconfined, free surface flow. If (63) is plotted on log - log paper versus $(\rho_2/\rho_1 - 1)$ for various D/a, the resulting straight lines can be written as

$$F \equiv \frac{U_1}{\sqrt{g\ D}} = C_3\left(\frac{\rho_2}{\rho_1} - 1\right)^{0.4934} , \qquad (64)$$

where

$$C_3 = 0.3658 - 0.0299\ (D/a) + 0.0418\ (D/a)^2 \ .$$

The surface spreading model is summarized in two steps:

1. Given ρ_2/ρ_1 and D/a, calculate h_d/D using equation (61),
2. calculate U_1 using equation (64).

The model is implemented in subroutine LAMBDA, which is described in Chapter five.

7. Local Recirculation Model

The local recirculation flow consists of the hot water that flows downward in the discharge bay to feed the steam condensation and plume entrainment. The recirculation flow is created by the upward-moving plume flow as it impinges on the free surface from below. A small part of the plume momentum is dissipated in the turbulence of the surface zone, a small part of the momentum causes a slight surface swell, and the largest part is reflected downward to create the local recirculation flow.

The model for the recirculation flow in Bay D is based on a simple application of conservation of mass. The amount of Bay D recirculation equals the sum of the vertical upflow of the plumes minus the total outflow in the surface spreading zone, i.e.,

$$W_{rec} = W_{p\ell} - W_1 \ , \tag{65}$$

where

W_{rec} = recirculation flow in Bay D,
$W_{p\ell}$ = total upflow from all plumes created by the T-quencher,
W_1 = portion of the Bay D outflow that leaves the surface spreading region.

8. Near Field Energy Balances

The purpose of the near field energy balances is to provide the energy source distribution for the large, lumped nodes that overlap Bay D in the thermal model of the whole pool. The source distribution is used to create the S_i's in equation (2).

Bay D is divided into three parts, as shown in Fig. 41. The plume zone in Fig. 41 contains the steam condensation zone that was described earlier in this chapter. The T-quencher energy source for the entire PSP model appears in the plume zone as the total enthalpy of the steam. The steam mixes with the entrained water, W_{ent}, and appears at the entrance to the surface zone as the total plume flow, $W_{p\ell}$, at the plume terminal temperature, $T_{p\ell}$. The entrainment flow includes the

plume entrainment and the water that feeds the steam condensation. W_{rec} is the recirculation flow, $W_{p\ell}$ is the plume flow into the surface zone, W_1 is the flow from the surface zone to the far field, W_2 is the flow from the recirculation zone to the far field, and W_{in} is the flow from the far field into the recirculation zone. The dashed lines in Fig. 41 correspond to the z levels of the cells that contain Bay D in the model of the whole pool. A pool model with four z levels is depicted in Fig. 41.

An energy balance written on the recirculation region is

$$\frac{d\,T_R}{dt} = \frac{W_{rec}}{M_R}\,T_s + \frac{W_{in}}{M_R}\,T_{in} - \left(\frac{W_{ent} + W_2}{M_R}\right) T_R \,, \qquad (66)$$

where

T_R = temperature of the recirculation region,
T_s = temperature of the surface region,
T_{in} = average temperature of the far field nodes that feed the lower part of Bay D,
M_R = mass of the recirculation region.

An energy balance on the surface region is

$$\frac{d\,T_s}{dt} = \frac{W_{p\ell}}{M_s}\,T_{p\ell} - \frac{(W_1 + W_{rec})}{M_s}\,T_s \,, \qquad (67)$$

where

M_s = mass of the surface region,
$T_{p\ell}$ = average temperature of the plumes at the top of the plume zone,

The specific heat is assumed to be constant in the above equations.

In equations (66) and (67) there are two unknowns: T_s and T_R. The plume terminal temperature, $T_{p\ell}$, is determined by the plume transport analyses, and T_{in} is known from the thermal model of the whole pool. The plume flow, $W_{p\ell}$, and entrainment, W_{ent}, are known from the plume transport analyses. The near field/far field exchange flows (W_{in}, W_1, and W_2) are determined by coupling the surface spreading analysis and the far field analysis.

Initial conditions for equations (66) and (67) are

$$T_R(0) = T_{Ro}$$

$$T_s(0) = T_{so} \qquad (68)$$

The analytical solution to equations (66) and (67) is

$$T_s(t) = T_{so}\, e^{a_1 t} + T_{p\ell}\,(1 - e^{a_1 t}) \,, \tag{69}$$

$$T_R(t) = \left(\frac{a_2}{a_1 - a_3}\right)(e^{a_1 t} - e^{a_3 t})\,(T_{so} - T_{p\ell}) \tag{70}$$

$$+ T_{Ro}\, e^{a_3 t} - (1 - e^{a_3 t})\left[\frac{a_2}{a_3} T_{p\ell} - \left(1 + \frac{a_2}{a_3}\right) T_{in}\right] ,$$

where

$$a_1 = -W_{p\ell}/M_s \,,$$

$$a_2 = (W_{ent} - W_1)/M_R \,,$$

$$a_3 = -(W_{ent} + W_2)/M_R \,.$$

The above solution applies in general for any time, t, for which the flows (W_{ent}, $W_{p\ell}$, etc.) and the temperatures ($T_{p\ell}$, T_{in}) remain constant. Over the time step of the temperature calculations for the whole pool, the above solutions will provide an estimate of the new surface and recirculation zone temperatures.

The new near field zonal temperatures can be used to create effective sources for the large nodes that represent Bay D by examining only the net energy transfer between the near field regions. For example, the energy deposited in the surface region (exclusive of the near field/far field exchange flows) is

$$E_s = W_{p\ell}\, T_{p\ell} - W_R T_s \,. \tag{71}$$

Similarly, the net energy deposited to the recirculation region is

$$E_R = W_R T_s - W_{ent}\, T_R \,. \tag{72}$$

The energy deposited to the plume zone is

$$E_p = W_{ent}\, T_R - W_{p\ell}\, T_{p\ell} + W_{st} h_{st} \,, \tag{73}$$

where

W_{st} = steam flow through the T-quencher,
h_{st} = enthalpy of the steam.

The total energy deposited within the near field is the sum of equations (71) through (73), or

$$E_s + E_R + E_p = W_{st} h_{st} . \tag{74}$$

Thus, the energy transfers between the near field regions are elaborate mechanisms for distributing the T-quencher energy, $W_{st}\ h_{st}$, within the near field.

This energy distribution can be mimicked in the equations for the whole pool by introducing the following uniform extraneous sources.

$$S_{up} = E_s/M_s$$

$$= \frac{W_{p\ell}\ T_{p\ell} - W_R\ T_s}{M_s} , \tag{75}$$

$$S_{low} = \frac{W_{st}\ h_{st} - E_s}{M_D - M_s} , \tag{76}$$

where

M_D = total mass of Bay D.

S_{up} is the uniform extraneous source to be added to the nodes that overlap the surface zone. S_{low} is the uniform extraneous source to be added to the nodes below the surface zone.

The near field energy balances and the effective near field source model are implemented in subroutine QNCELL, which is described in Chapter five.

D. THERMAL CONVECTION CELL MODEL--FAR FIELD ANALYSIS

1. Description of the Far Field Region

The far field region is the portion of the PSP located away from the discharging T-quencher. For example, if a single T-quencher were discharging into the PSP, the far field would include 15 of the 16 bays.

The purpose of the far field analysis is to determine the fluid velocities in the far field region, and to use that velocity distribution to construct the mass flows that cross the boundaries of each node in the time dependent thermal model of the PSP.

The flow in the far field can be considered to be two dimensional. The two dimensions are z, the elevation, and θ, the circumferential distance around the pool. The far field velocities to be determined are the horizontal (i.e., circumferential) velocity, $u(z,\theta)$,

and the vertical velocity, $w(z,\theta)$. The unknown velocities and the problem geometry are shown in Fig. 42. The domain is bounded on the left by the near field / far field interface, on the right by a symmetry plane, above by the water surface, and below by the torus floor.

The third dimension is x, the distance across the pool. This dimension would be into the page in Fig. 42. The far field velocities, temperature, and density are assumed to be constant with respect to x. This assumption is justified by the following reasons. First, there are no external momentum sources forcing the fluid in the x direction. Second, the only significant force in the x direction is due to the centrifugal acceleration. This acceleration, u^2/r, is small because: u is expected to be small, and r, the radial distance from the torus center, is large. Third, based on the Monticello data,[83] the stratification in the z direction is very strong. This tends to retard any motion in the x direction by eliminating any vertical flow at the torus wall that must accompany any significant flow in the x direction.

The flow in the far field is assumed to be steady over the time step of the temperature calculations for the whole pool. Although the flow is actually time dependent, changes in the far field velocities are expected to occur slowly because the near field / far field density difference that drives the circulation changes slowly. The far field velocities are assumed to change instantaneously at the beginning of the time step, and to remain constant over the time step. The implications of this assumption are discussed in Appendix B.

The approach used to determine the far field velocity distribution is outlined in the steps below.

1. Begin with the two dimensional equations of continuity and momentum for the torus.
2. Eliminate the pressure terms by integrating the z momentum equation from arbitrary z up to the water surface. This produces the pressure, P. Form $\partial P/\partial\theta$, and substitute this into the θ momentum equation. The result is an integro-differential equation for $u(z,\theta)$, $w(z,\theta)$ and $D(\theta)$, the pool depth.
3. Assume that a z level, h, exists such that above h, all the water moves away from Bay D, and below h, all the water moves toward Bay D. $z = h$ is the plane of zero horizontal velocity.
4. Integrate the equations from $z = h$ up to D.
5. Assume a shape for the z dependence of $u(z,\theta)$ and for $w(z,\theta)$ based on the boundary conditions of the problem.
6. Solve the resulting ODEs using the approximate method described in part 4 of this section.

The development and solution of the far field equations (as outlined in the above steps) is detailed in parts 2 and 4 of this section, respectively. Part 3 describes the near field / far field interface, and part 5 describes the method of calculating the nodal mass flows given the velocity field.

2. The Far Field Equations

The development of the far field equations begins with the coupled, steady state equations for conservation of mass and momentum in the torus. The equations for the torus are written in the modified cylindrical coordinate system shown in Fig. 43. The vertical dimension from the torus floor is z, while θ is the circumferential angle measured from a reference plane $\theta = 0°$.

The equations are

$$f(z)\,\frac{\partial u}{\partial \theta} + \frac{\partial w}{\partial z} = 0, \tag{77}$$

$$f(z)\,u\,\frac{\partial u}{\partial \theta} + w\,\frac{\partial u}{\partial z} = \frac{-f(z)}{\rho_o}\,\frac{\partial P}{\partial \theta} + \frac{1}{\rho_o}\,\frac{\partial}{\partial z}\,(\tau_{\theta z}) \tag{78}$$

$$f(z)\,u\,\frac{\partial w}{\partial \theta} + w\,\frac{\partial w}{\partial z} = -\frac{1}{\rho}\,\frac{\partial P}{\partial z} - g\ , \tag{79}$$

where

$u = u(z,\theta)$, the circumferential fluid velocity,
$w = w(z,\theta)$, the vertical fluid velocity,
$P = P(z,\theta)$, the pressure,
$\tau_{\theta z} = \tau_{\theta z}(z,\theta)$, the circumferential shear stress,
$\rho = \rho(z,\theta)$, the fluid density,
ρo = a reference density,
$f(z)$ = torus function derived in Appendix A.

The boundary conditions for the problem are

$u = 0$ at the symmetry plane and on the bottom of the pool,

$w = 0$ at the surface and bottom of the pool,

$\frac{\partial u}{\partial z} = 0$ at the surface,

$\frac{\partial w}{\partial \theta} = 0$ at the symmetry plane,

$P = P_o$ at the surface,

$\frac{\partial p}{\partial \theta} = 0$ at the symmetry plane.

In addition, $\tau_{\theta z}$ is a known function of u, and $\rho(z,\theta)$ is given as a function of the current pool temperature distribution.

Equations (77) to (79) are obtained from the standard equations for conservation of mass and momentum in three dimensional cylindrical coordinates. The details of the development are in Appendix A.

The development in Appendix A begins by assuming the water can be treated as incompressible. The equations (in a r-θ-z coordinate system) are reduced by neglecting the radial velocities and radial gradients. This is the 2D assumption that is based on the Monticello data and on a study of the phenomena. However, after neglecting the radial velocities and gradients, 1/r remains with each θ-derivative. This term is eliminated by integrating across the torus in the radial direction. The integration produces f(z), the torus function in equations (77) through (79). f(z) takes into account the z variation of the torus width, and the 1/r term in front of $\partial/\partial\theta$.

The basic equations in Appendix A were further reduced by assuming that the shear stresses in the z direction are negligible, and that the dominant viscous term is $\tau_{\theta z}$ in the θ momentum equation. This assumption is less restrictive than what has been used in the past by many researchers in hydraulic channel theory.[84-86] The standard assumption is that the horizontal velocities (u) are much larger than the vertical velocities (w), and that the vertical gradients ($\partial/\partial z$) are much larger than the horizontal gradients ($\partial/\partial\theta$). Their assumption would produce equations (77) and (78), but the left hand side of equation (79) would be neglected. The standard assumption in effect restricts the analysis to very long hydraulic channels in which the pressure variation can be assumed to be hydrostatic.

Unfortunately, the standard assumptions for hydraulic channel theory are not applicable to the PSP because it behaves as a short hydraulic channel. The density currents that move outward from the discharge bay meet head-on at the symmetry plane between the two discharging T-quenchers. The collision of the density currents cannot be modeled using theory that neglects the left hand side of equation (79). Therefore, the standard assumption is invalid, and the entire left hand side of the z momentum equation is retained in equation (79).

The Bousinesq approximation has been applied to the development of equations (77) through (79). This assumption is frequently used in modeling density driven flows. It involves ignoring the z and θ variation of the density in the theta momentum equation, but retaining the variation in the z equation. Thus, ρ_o appears in equation (78) and ρ in equation (79).

Equation (79) is integrated from arbitrary z up to D(θ), where D is the depth of the pool as a function of θ:

$$\int_z^{D(\theta)} \frac{\partial P}{\partial z}\, dz = -\int_z^{D(\theta)} \rho f(z)\, u\, \frac{\partial w}{\partial \theta}\, dz - \int_z^{D(\theta)} \frac{\rho}{2}\, \frac{\partial}{\partial z}(w^2)\, dz - \int_z^{D(\theta)} \rho g dz \,. \qquad (80)$$

In equation (80), if $\rho(z,\theta)$ is assumed to be $\bar{\rho}(\theta)$, the average density

as a function of θ, equation (80) becomes

$$P_o - P(z,\theta) = -\bar{\rho}(\theta) \int_z^D f(z)\, u\, \frac{\partial w}{\partial \theta}\, dz - \frac{\bar{\rho}(\theta)}{2} \int_z^D \frac{\partial}{\partial z}(w^2)\, dz - \bar{\rho}(\theta) g \int_z^D dz \,, \tag{81}$$

or

$$P(z,\theta) - P_o = \bar{\rho}(\theta) \int_z^D f(z)\, u\, \frac{\partial w}{\partial \theta}\, dz - \frac{\bar{\rho}(\theta)}{2} w^2(z,\theta) + \bar{\rho}\, g\, (D - z) \,, \tag{82}$$

where P_o is the pressure at the surface.

Equation (82) can be differentiated with respect to theta to form $\partial P/\partial\theta$, which is substituted into equation (78):

$$f(z)\, u \frac{\partial u}{\partial \theta} + w \frac{\partial u}{\partial z} = -\frac{f(z)}{\rho_o} \frac{\partial}{\partial \theta} \left\{ \bar{\rho} \int_z^D f(z)\, u \frac{\partial w}{\partial \theta}\, dz \right\} + \frac{f(z)}{2\rho_o} \frac{\partial}{\partial \theta}(\bar{\rho} w^2) - \frac{f(z)}{\rho_o} \frac{\partial}{\partial \theta}(\rho\, g(D - z)) + \frac{1}{\rho_o} \frac{\partial \tau_{\theta z}}{\partial z} \tag{83}$$

The left hand side (LHS) of equation (83) can be rewritten as

$$\text{LHS} = f(z) \frac{\partial}{\partial \theta}(u^2) + \frac{\partial}{\partial z}(uw). \tag{84}$$

A z level, $z = h$, is assumed to exist such that above h, $u(z,\theta)$ is positive (directed away from the near field), and below h, $u(z,\theta)$ is negative (directed toward the near field). This idealization of the far field is shown in Fig. 44. The plane $z = h$ is the plane of zero horizontal velocity. Assuming that h is constant effectively treats the far field flow as if a hot water layer of thickness $(D - h)$ were moving out away from the near field and a cold water layer of thickness h were moving countercurrently back toward the near field.

The constant layer thickness assumption has been used by some researchers in their models of countercurrent hydraulic channel flow.[86,87] The difference between the method used here to represent the torus flows and what has been done in the past involves the difficulty associated with the torus function $f(z)$, and in the full treatment of $\partial P/\partial\theta$ in equation (83).

Equation (83) is integrated from z = h, to z = D . If λ is defined as

$$\lambda = h/D \tag{85}$$

the integrals become

$$\int_{\lambda D}^{D} f(z)\,\frac{\partial}{\partial\theta}(u^2)\,dz + \int_{\lambda D}^{D}\frac{\partial}{\partial z}(uw)\,dz =$$

$$\int_{\lambda D}^{D} -\frac{f(z)}{\rho_o}\,\frac{\partial}{\partial\theta}\left\{\bar{\rho}\int_{z}^{D} f(z')\,u\,\frac{\partial w}{\partial\theta}\,dz'\right\}\,dz + \int_{\lambda D}^{D}\frac{f(z)d}{2\rho_o d\theta}\,(\bar{\rho}w^2)\,dz$$

$$+\int_{\lambda D}^{D} -\frac{f(z)}{\rho_o}\,\frac{\partial}{\partial\theta}\,[\bar{\rho}g\,(D-z)]\,dz + \int_{\lambda D}^{D}\frac{1}{\rho_o}\,\frac{\partial\tau_{\theta z}}{\partial z}\,dz\ . \tag{86}$$

The second integral on the left hand side of equation (86) is identically zero because w is zero at z = D , and u is zero at z = h .

At this point, this discussion of the development of the far field equations will pause so that derivation of the vertical profiles of $u(z,\theta)$ and $w(z,\theta)$ can be presented.

It is assumed that the theta and z velocities can be separated into a z-dependent shape function (dimensionless) and a θ-dependent amplitude function (dimensional), i.e.,

$$u(z,\theta) = U(z)\,U_s(\theta)\ , \tag{87}$$

$$w(z,\theta) = W(z)\,W_m(\theta)\ . \tag{88}$$

The z-dependent shape functions, U(z) and W(z), were developed by a method very similar to the Karman - Pohlhausen technique for boundary layer analysis. In that technique, the velocity profile is assumed to be a fourth order polynomial in η ($\eta = z/D$) with the surface velocity, $U_s(\theta)$, the level of zero horizontal velocity, z = h, and the depth, $D(\theta)$, taken as parameters of the profile.

As an example of the Karman - Pohlhausen technique, consider countercurrent, 2 layer flow in a uniform cross section channel. At the channel bottom, U = 0. At the water surface, $U = U_s$ and $\partial U/\partial z = 0$. At z = h, U = 0. Also, the total outflow above z = h is assumed equal to the inflow below z = h. The fourth order polynomial is

$$\frac{u}{U_s} = a + b\eta + c\eta^2 + d\eta^3 + e\eta^4\ . \tag{89}$$

with the boundary constraints

$$\frac{u}{U_s} = 0 \qquad \text{at} \quad \eta = 0\ , \tag{90}$$

$$\frac{u}{U_s} = 0 \ \text{at} \quad \eta = \frac{h}{D} = \lambda\ , \tag{91}$$

$$\frac{u}{U_s} = 1 \qquad \text{at} \quad \eta = 1 , \tag{92}$$

$$\frac{\partial}{\partial \eta}\left(\frac{u}{U_s}\right) = 0 \quad \text{at} \quad \eta = 1 , \tag{93}$$

$$\int_0^1 \left(\frac{u}{U_s}\right) d\eta = 0 . \tag{94}$$

The boundary constraints [equations (90) through (94)] are sufficient to determine the constants a through e in equation (89). The z-profile of the horizontal velocity is then known and can be substituted into an equation for the variation of U_s down the channel [an equation similar to equation (86)].

The example presented above is the theory developed by Sturm[88] in his dissertation on the flow of density currents in the sidearms of cooling ponds. It produces the profile shown in Fig. 45. The Sturm approach was attempted for use in the PSP far field model, modified by multiplying the velocity in equation (94) by the torus width as a function of η; all other boundary constraints were the same.

The results of using Sturm's vertical profile for the torus velocities were good over a limited range of λ. $\lambda = 0.5$ to about $\lambda = 0.62$ produced reasonable velocity profiles. However, if λ was increased any further, the resulting velocity profiles had nonphysical positive parts for $z < \lambda$. The velocity profiles still fit the boundary constraints, except nonphysical wiggles appeared in the profile for small z.

To eliminate the wiggles in the velocity profiles, and to allow for a generally broad range of λ, Sturm's profile was modified for application to flow in a circular cross section with arbitrary λ.

Instead of a fourth order polynomial over all η, the velocities were assumed to be piecewise continuous cubics. The derivative is allowed to be discontinuous where the two polynomials join. One third order polynomial applies for $0 \leq \eta \leq \lambda$, and another third order polynomial applies for $\lambda \leq \eta \leq 1$. The profiles are

$$\frac{u}{U_s} = a + b\eta + c\eta^2 + d\eta^3, \quad 0 \leq \eta \leq \lambda , \tag{95}$$

$$\frac{u}{U_s} = e + f\eta + g\eta^2 + h\eta^3, \quad \lambda \leq \eta \leq 1 . \tag{96}$$

The boundary constraints for u/U_s are

$$\frac{u}{U_s} = 0 \qquad \text{at } \eta = 0 , \tag{97}$$

$$\frac{u}{U_s} = 0 \qquad \text{at} \quad \eta = \lambda , \tag{98}$$

$$\frac{d^2}{d\eta^2}\left(\frac{u}{U_s}\right) = 0 \qquad \text{at} \quad \eta = \lambda , \tag{99}$$

$$\int_0^{\lambda} \left(\frac{u}{U_s}\right)_1 F_1(\eta)d\eta = -\int_{\lambda}^{1} \left(\frac{u}{U_s}\right)_2 F_1(\eta)d\eta \ , \tag{100}$$

where

$\left(\frac{u}{U_s}\right)_1 = \frac{u}{U_s}$ using equation (95),

$\left(\frac{u}{U_s}\right)_2 = \frac{u}{U_s}$ using equation (96),

$F_1(\eta) = 2D\sqrt{2\alpha\eta-\eta^2}$,

α = (torus minor radius)/D .

The boundary constraints for $\lambda \leq \eta \leq 1$ are

$$\frac{u}{U_s} = 0 \qquad \text{at} \quad \eta = \lambda \ , \tag{101}$$

$$\frac{u}{U_s} = 1 \qquad \text{at} \quad \eta = 1, \tag{102}$$

$$\frac{d}{d\eta}\left(\frac{u}{U_s}\right) = 0 \qquad \text{at} \quad \eta = 1 \ , \tag{103}$$

$$\frac{d^2}{d\eta^2}\left(\frac{u}{U_s}\right) = 0 \qquad \text{at} \quad \eta = 1 \ . \tag{104}$$

The constraints, equations (97) through (104), are sufficient to produce the constants a through h. The calculation of the constants a through h is programmed into subroutine VELCON, as described in the next chapter. Typical profiles for various λ are shown in Fig. 46. For very large λ, the sharp discontinuous derivative between the upper flow and the lower flow is apparent. However, in the range where Sturm's fourth order polynomial was successful, the derivative changes rather smoothly between the upper and the lower flow.

A similar approach was adopted for determining the vertical profile of $w(z,\theta)$. The z-dependent shape of $w(z,\theta)$, $W(z)$, is written as

$$\frac{w}{W_m} = \omega_a + \omega_b\eta + \omega_c\eta^2 + \omega_d\eta^3, \quad 0 \leq \eta \leq \lambda \ , \tag{105}$$

$$\frac{w}{W_m} = \omega_e + \omega_f\eta + \omega_g\eta^2 + \omega_h\eta^3, \quad \lambda \leq \eta \leq 1 \ . \tag{106}$$

The boundary constraints for $0 \leq \eta \leq \lambda$ are

$$\frac{w}{W_m} = 0 \qquad \text{at} \quad \eta = 0 , \tag{107}$$

$$\frac{d}{d\eta}\left(\frac{w}{W_m}\right) = 0 \qquad \text{at} \quad \eta = \lambda , \tag{108}$$

$$\frac{w}{W_m} = -1 \qquad \text{at} \quad \eta = \lambda , \tag{109}$$

$$\int_0^{\lambda} \left(\frac{w}{W_m}\right)_1 \left(\frac{u}{U_s}\right)_1 F_1(\eta)d\eta = -\int_{\lambda}^{1} \left(\frac{w}{W_m}\right)_2 \left(\frac{u}{U_s}\right)_2 F_1(\eta)d\eta , \tag{110}$$

where

$\left(\frac{w}{W_m}\right)_1 = \frac{w}{W_m}$ using equation (105),

$\left(\frac{w}{W_m}\right)_2 = \frac{w}{W_m}$ using equation (106).

The boundary constraints for $\lambda \leq \eta \leq 1$ are

$$\frac{w}{W_m} = 0 \qquad \text{at} \quad \eta = 1 , \tag{111}$$

$$\frac{w}{W_m} = -1 \qquad \text{at} \quad \eta = \lambda , \tag{112}$$

$$\frac{d}{d\eta}\left(\frac{w}{W_m}\right) = 0 \qquad \text{at} \quad \eta = \lambda , \tag{113}$$

$$\frac{d^2}{d\eta^2}\left(\frac{w}{W_m}\right) = 0 \qquad \text{at} \quad \eta = 1 . \tag{114}$$

Equation (110) insures that the net vertical momentum convected into the system above λ matches the net vertical momentum convected out below λ.

The constraint equations (107) through (114) are sufficient to determine the constants ω_a through ω_h. The calculation of the constants ω_a through ω_h is also programmed into subroutine VELCON as described in the next chapter.

Typical vertical velocity profiles in the z-direction are shown in Fig. 47. The vertical velocity is maximum at $\eta = \lambda$, and zero at the water surface ($\eta = 1$) and torus floor ($\eta = 0$). For the vertical velocity profiles, there were no problems in matching the two cubics and their derivatives at $\eta = \lambda$ as occurred with the horizontal velocity profiles.

At this point, the vertical profiles U(z) and W(z) are known, and we return to the development of the far field equations. Substituting

equations (87) and (88) into equation (86) yields

$$\int_\lambda^1 f(\eta)\,\frac{dU_s^2}{d\theta}\,U^2(\eta)\,D\,d\eta =$$

$$\int_\lambda^1 -\frac{f(\eta)}{\rho_o}\,\frac{d}{d\theta}\left\{\bar{\rho}\int_\eta^1 f(\eta')\,U_s(\theta)\,\frac{dW_m}{d\theta}\,U(\eta')\,W(\eta')\,D\,d\eta'\right\}D\,d\eta$$

$$+\int_\lambda^1 \frac{f(\eta)}{2\rho_o}\,\frac{d}{d\theta}\,(\bar{\rho}\,W_m^2)\,W^2(\eta)\,D\,d\eta + \int_\lambda^1 -\frac{f(\eta)}{\rho_o}\,\frac{d}{d\theta}\,(\bar{\rho}\,g\,D)\,(1-\eta)\,D\,d\eta$$

$$+\int_\lambda^1 \frac{1}{\rho_o\,D}\,\frac{d}{d\eta}\,[\tau_{\theta z}(\eta)]\,D\,d\eta\,, \tag{115}$$

where the integrals over z have been written as integrals over η,

$$\eta = \frac{z}{D(\theta)}\,. \tag{116}$$

Equation (115) can be rewritten as

$$\gamma_1\,D\,\frac{d}{d\theta}\,(U_s^2) = \gamma_2\,D\,\frac{d}{d\theta}\left(\bar{\rho}\,U_s D\,\frac{dW_m}{d\theta}\right) + \gamma_3\,D\,\frac{d}{d\theta}\,(\bar{\rho}\,W_m^2)$$

$$+\,\gamma_4\,D\,\frac{d}{d\theta}\,(\bar{\rho}\,D) + \gamma_5\,\tau_{\theta z}(\lambda)\,, \tag{117}$$

where the η-dependent definite integrals have been written as γ's. Specifically,

$$\gamma_1 \equiv \int_\lambda^1 f(\eta)\,U^2(\eta)\,d\eta\,, \tag{118}$$

$$\gamma_2 \equiv \int_\lambda^1 -\frac{f(\eta)}{\rho_o}\left\{\int_\eta^1 f(\eta')\,U(\eta')\,W(\eta')\,d\eta'\right\}d\eta\,, \tag{119}$$

$$\gamma_3 \equiv \int_\lambda^1 -\frac{f(\eta)}{2\rho_o}\,W^2(\eta)\,d\eta\,, \tag{120}$$

$$\gamma_4 \equiv \int_\lambda^1 -\frac{f(\eta)}{\rho_o}\,g(1-\eta)\,d\eta\,, \tag{121}$$

$$\gamma_5 \equiv -\frac{1}{\rho_o}\,. \tag{122}$$

Given the velocity profiles $U(\eta)$ and $W(\eta)$, a reference density, ρ_o, and λ, the constants γ_1 through γ_5 can be determined. The polynomials for $f(\eta)$, $U(\eta)$, and $W(\eta)$ were substituted into the integrals (118) through (122). The detailed expressions for γ_1 through γ_5 are programmed into subroutine GAMMA, as described in Chapter five.

Essentially the same procedure that led to equation (117) is now applied to equation (77), the continuity equation. The equation is integrated from z = h to z = D.

$$\int_h^D \frac{\partial w(z,\theta)}{\partial z}\, dz = -\int_h^D f(z)\, \frac{\partial u}{\partial \theta}\, dz \ , \tag{123}$$

or,

$$w(\theta,D) - w(\theta,h) = W_m(\theta) = -\int_\lambda^1 f(\eta)\, \frac{d\, U_s}{d\theta}\, U(\eta)\, D d\eta \tag{124}$$

Equation (124) is rewritten as

$$\frac{d\, U_s}{d\theta} = -\frac{1}{\gamma_{11} D}\, W_m(\theta) \ , \tag{125}$$

where

$$\gamma_{11} \equiv \int_\lambda^1 f(\eta)\, U(\eta)\, d\eta \ . \tag{126}$$

The constant γ_{11} is programmed into subroutine GAMMA, as were γ_1 through γ_5.

Equations (117) and (125) are the far field equations. They are one dimensional versions of the theta momentum and continuity equations for the torus. These equations are sufficiently general so that any expression for the interfacial shear stress $\tau_{\theta z}$ and for the depth of the channel as a function of θ can be supplied.

In this work it is assumed that $\tau_{\theta z}(\lambda)$ is given by

$$\tau_{\theta z}(\lambda) = K \rho_o\, U_s^2(\theta) \ , \tag{127}$$

where K is an arbitrary friction factor. This type of expression is often used for the interfacial shear.[84-88] However, there is much uncertainty in the value of K. In addition, very little is known about the exact nature of $\tau_{\theta z}$ — even in an idealized two-layer flow.[89] Therefore, for the methodology developed here, K is left variable, so that K can be adjusted by the user as necessary to take into account the effect of the internal flow obstructions that exist in the PSP.

It is also assumed that the depth of the pool is constant, i.e.,

$$D(\theta) \equiv D_o \equiv \text{constant} \ . \tag{128}$$

The implications of this assumption are discussed in Appendix B.

With assumptions (127) and (128), the far field problem becomes

$$\gamma_1 \frac{d}{d\theta}\,(U_s^2) = \gamma_2\, D_o \frac{d}{d\theta}\left(\bar{\rho}\, U_s \frac{dW_m}{d\theta}\right) + \gamma_3 \frac{d}{d\theta}\,(\bar{\rho}\, W_m^2)$$

$$+ \gamma_4\, D_o \frac{d\bar{\rho}}{d\theta} - \frac{K}{D_o}\, U_s^2 \ , \tag{129}$$

$$\frac{d\,U_s}{d\theta} = -\frac{1}{\gamma_{11} D_o} W_m(\theta) \ , \tag{130}$$

with boundary conditions

$$U_s(\theta_i) = U_{so} \ , \tag{131}$$

$$U_s(\theta_f) = 0 \tag{132}$$

$$W_m(\theta_i) = 0 \ , \tag{133}$$

$$\frac{dW_m}{d\theta}(\theta_f) = 0 \ , \tag{134}$$

where

θ_i = location of the near field / far field interface,

θ_f = location of the far field symmetry plane,

$\bar{\rho}$ = vertically averaged density — supplied from the time dependent calculations of the PSP temperatures,

U_{so} = near field / far field interface velocity.

3. The Near Field / Far Field Interface

The most important boundary condition to the far field problem is equation (131), which is the initial surface velocity, U_{so}. U_{so} is determined by matching the near field outflow and the far field inflow, i.e.,

$$\left\{ \begin{array}{c} \text{near field outflow} \\ \text{above } \lambda \end{array} \right\} = \left\{ \begin{array}{c} \text{far field inflow} \\ \text{above } \lambda \end{array} \right\} \tag{135}$$

The near field outflow consists of a layer thickness, h_d, and a mean outflow velocity, U_1. The parameter λ is given by

$$\lambda = 1 - \frac{h_d}{D_o} \ . \tag{136}$$

Equation (135) is expressed mathematically as

$$U_{so} \int_\lambda^1 U(\eta)\, F_1(\eta)\, d\eta = U_1 \int_\lambda^1 F_1(\eta)\, d\eta, \tag{137}$$

where $U(\eta)$ is given by equation (95), and $F_1(\eta)$ is given in equation (100).

Everything in equation (137) (except for U_{so}) is a known function of the pool depth, the torus minor radius, the layer thickness, and U_1. Thus, U_{so} can be written as

$$U_{so} = \frac{U_1 \int_\lambda^1 F_1(\eta)\, d\eta}{\int_\lambda^1 U(\eta)\, F_1(\eta)\, d\eta} . \qquad (138)$$

The integrals in equation (138) are evaluated in subroutine VELCON, immediately after the constants in the expression for $U(\eta)$ are calculated. Thus, U_{so} is given explicitly in terms of U_1.

4. Solution of the Far Field Equations

A solution is sought to equations (129) and (130) with boundary conditions (131) through (134). Since equation (129) is highly nonlinear, a purely analytical solution is impossible. In addition, a purely numerical solution to the far field problem is unacceptable because the far field equations must be solved once for each discharging T-quencher at every time step in the PSP temperature calculations. The solution of large sets of nonlinear finite difference or finite element equations at each time step would be prohibitively expensive to run within the PSP model.

Since a purely analytical and a purely numerical solution are unattainable, a solution method is developed that is somewhere in between.

Observe the rather simple form of equation (130). In words, this equation states that the rate of change of the horizontal velocity is linearly proportional to the downflow velocity. If the downflow velocity $W_m(\theta)$ were a known function of theta, then a simple integration would yield $U_s(\theta)$.

Also observe the form of equation (129). Each term (except for the last one) is in the form of a derivative with respect to theta. The last term is a constant times U_s^2. If $U_s(\theta)$ were a known function of theta, then it could be substituted into equation (129), which could then be integrated over theta.

The observations described in the previous two paragraphs led to the approximate solution method described in the steps below.

1. Guess a polynomial form of $W_m(\theta)$ that is constrained to solve equation (130) over the θ-domain of interest.
2. Determine $U_s(\theta)$ by integrating equation (130).
3. Substitute $U_s(\theta)$ into equation (129).
4. Integrate equation (129) over the theta domain of interest to form an integral momentum constraint on the velocities. Evaluation of the integral at the θ boundaries of the domain forms an algebraic equation that must be solved if the correct velocity profiles are guessed,i.e., the left hand side of the equation must equal the right hand side or the $W_m(\theta)$ guess is wrong.

5. If the integral momentum constraint is satisfied to a desired degree of convergence, then the problem is solved. If not, then a new guess for $W_m(\theta)$ is formed and steps 2 through 4 are repeated. The iteration proceeds until the problem converges.

The polynomial guess for $W_m(\theta)$ is

$$W_m(\theta) = w_1 + w_2\theta + w_3\theta^2 + w_4\theta^3 \ . \tag{139}$$

The constants w_1, w_2, w_3, w_4 are determined from the following conditions.

$$W_m = 0 \qquad \text{at} \quad \theta = \theta_i \ , \tag{140}$$

$$W_m = W_{end} \qquad \text{at} \quad \theta = \theta_f \ , \tag{141}$$

$$\frac{dW_m}{d\theta} = 0 \qquad \text{at} \quad \theta = \theta_f \ , \tag{142}$$

$$\int_{\theta_i}^{\theta_f} W_m(\theta)d\theta) = \gamma_{11} U_{so} D_o \ , \tag{143}$$

where W_{end} is the guessed downflow velocity at the end of the far field.

Equation (143) is determined by integrating equation (130) over the entire far field, and applying equations (131) and (132) to the evaluation of the theta integral. Equation (143) states that the total downflow over the far field (at z = h) equals the inflow to far field at θ_i. The inflow at θ_i and the downflow over θ are shown in Fig. 48.

To verify that $W_m(\theta)$ satisfies the continuity equation at any θ, integrate equation (130) from θ_i to an arbitrary θ.

$$-\gamma_{11} D_o \int_{\theta_i}^{\theta} \frac{d\, U_s}{d\theta} = \int_{\theta_i}^{\theta} W_m(\theta)\, d\theta \ , \tag{144}$$

or,

$$\gamma_{11}D_oU_{so} - \gamma_{11}D_oU_s(\theta) = \int_{\theta_i}^{\theta_f} W_m d\theta - \int_{\theta}^{\theta_f} W_m d\theta \ . \tag{145}$$

In equation (145), the integral from θ_i to θ was written as the integral from θ_i to θ_f minus the integral from θ to θ_f. The first terms on each side of equation (145) cancel because of the fourth constraint on $W_m(\theta)$, [equation (143)]. Thus,

$$\gamma_{11}D_o\, U_s(\theta) = \int_{\theta}^{\theta_f} W_m(\theta)\, d\theta \tag{146}$$

Equation (146) is satisfied because it is simply equation (130) integrated from arbitrary θ to θ_f, i.e.,

$$- \gamma_{11} D_o \int_{\theta}^{\theta_f} d U_s = \int_{\theta}^{\theta_f} W_m(\theta)\, d\theta \ , \tag{147}$$

or,

$$- \gamma_{11} D_o [U_s(\theta_f) - U_s(\theta)] = \int_{\theta}^{\theta_f} W_m \, d\theta \ . \tag{148}$$

Equation (148) and (146) are identical; hence, $W_m(\theta)$ satisfies equation (130) for any θ.

If equation (139) is substituted into equation (130), and integrated from arbitrary θ to θ_f, $U_s(\theta)$ is determined.

$$U_s(\theta) = \frac{1}{\gamma_{11} D_o} \left\{ w_1(\theta_f - \theta) + \frac{w_2}{2}(\theta_f^2 - \theta^2) + \frac{w_3}{3}(\theta_f^3 - \theta^3) + \frac{w_4}{4}(\theta_f^4 - \theta^4) \right\} . \tag{149}$$

If equation (129) is integrated from θ_i to θ_f ,

$$U_s^2 \Big|_{\theta_i}^{\theta_f} = \frac{\gamma_2}{\gamma_1} D_o \bar{\rho} U_s \frac{d W_m}{d\theta} \Big|_{\theta_i}^{\theta_f} + \frac{\gamma_3}{\gamma_1} (\bar{\rho} W_m^2) \Big|_{\theta_i}^{\theta_f} + \frac{\gamma_4}{\gamma_1} D_o \rho \Big|_{\theta_i}^{\theta_f} - \frac{K}{D_o} \int_{\theta_i}^{\theta_f} U_s^2(\theta)\, d\theta \ . \tag{150}$$

For simplicity, the integral of U_s^2 in equation (150) is written as

$$\int_{\theta_i}^{\theta_f} U_s^2(\theta) d\theta \equiv I_f \Big|_{\theta_i}^{\theta_f} \ . \tag{151}$$

I_f is a ninth order polynomial in θ, because U_s is fourth order.

When the boundary conditions (131) through (134) are applied to equation (150), the resulting equation is

$$U_{so}^2 = \frac{\gamma_2}{\gamma_1} D_o \bar{\rho}(\theta_i) U_{so} \frac{d W_m}{d\theta}(\theta_i) - \frac{\gamma_3}{\gamma_1} \bar{\rho}(\theta_f) W_m^2(\theta_f) - \frac{\gamma_4}{\gamma_1} D_o [\bar{\rho}(\theta_f) - \bar{\rho}(\theta_i)] + \frac{K}{D_o} I_f \Big|_{\theta_i}^{\theta_f} \ , \tag{152}$$

where I_f = the polynomial in equation (149) squared and integrated over θ. Equation (152) is a constraint that the guessed velocity field must meet in order to satisfy the momentum equations in an integral sense over the domain.

The solution method described in steps one through five is put into practice by first guessing W_{end} in equation (141), and then calculating the constants w_1 through w_4 in equation (139). At that point W_m, U_s, and $d W_m/d\theta$ are known polynomials in θ. Since $\bar{\rho}$, U_{so}, D_o, K, and the γ's are inputs to the far field problem, every term in equation (152) is determined. The left hand side of the equation can be compared to the right hand side, and if they are equal, a solution is found. If equation (152) is not satisfied, a new guess is made for W_{end}.

Before the technique of determining a new guess for W_{end} is described, it is useful to examine some typical velocity profiles. Several horizontal velocity profiles (curves 1 through 5) are shown in Fig. 49. The curves in Fig. 49 were generated assuming a near field outflow velocity of 1 Ft/s. The profiles in Fig. 49 were produced by varying W_{end}, hence changing w_1 through w_4, and hence changing $W_m(\theta)$ and $U_s(\theta)$. If W_{end} is large, the downflow is concentrated far away from the near field, and a horizontal velocity profile like curve 1 is produced. Curve 1 would correspond to a very weak frictional term ora very strong density gradient term in equation (152). If the magnitude of the frictional term were increased, or the density gradient term decreased, the downflow would shift more toward the near field, and the curves 2, 3, 4, and 5 would be produced as progressively more friction or progressively less $\Delta\rho$ were added.

The interaction of all the terms in equation (152) determines the particular shape of the calculated velocity profiles. The initial momentum is included in the left hand side of equation (152). The length of the far field region affects the magnitude of the first two terms on the right hand side of equation (152). The density gradient and the interfacial friction are represented by the third and fourth terms on the right hand side, respectively.

To understand how the downflow profile is iteratively changed so that the integral constraint (152) is satisfied, consider a very long far field of uniform temperature. For this case, equation (152) takes the form

$$U_{so}^2 = K_1 + \frac{K}{D_o} [I_f(\theta_f) - I_f(\theta_i)] \qquad (153)$$

In equation (153), K_1 contains the first three terms of equation (152), which are very small for a long channel. If the left hand side of (153) is greater than the right hand side, the term $I_f(\theta_f)$ is much too large. $I_f(\theta_f)$ is too large because the guessed $U_s(\theta_f)$ is too large. If W_{end} is made larger, then $U_s(\theta_f)$ will be made smaller, and hence $I_f(\theta_f)$ becomes smaller. If W_{end} were moved upward by exactly the right amount, then the left side of equation (153) would equal the right side. If W_{end} were moved up too much, then the left side would become smaller than the right side.

An iterative process is thus defined in which the quantity Q, defined by

$$Q = \frac{\left\{\begin{array}{c}\text{Left hand side of} \\ \text{equation (152)}\end{array}\right\} - \left\{\begin{array}{c}\text{Right hand side} \\ \text{of equation (152)}\end{array}\right\}}{U_{so}^2} \qquad (154)$$

is made small by adjusting the guessed downflow velocity profile. In practice, a convergence limit ε is chosen such that whenever

$$|Q| < \varepsilon \ , \qquad (155)$$

the far field problem is considered solved.

The sensitivity of the downflow velocity profiles to the convergence limit was investigated by varying ε and comparing the resultant downflow profiles. The profiles changed very little as ε varied from 0.01 down to 0.0001--only the number of iterations to converge changed. A default value of $\varepsilon = 0.001$ was programmed into the PSP far field model as a suitable convergence. This ε typically takes about 10 iterations to converge.

The far field iterative solution is contained in subroutine FARFLD. The vertical velocity profiles are programmed into subroutine VELCON, and the horizontal velocity profiles are determined by subroutine DWNFLO. The far field subroutines are described in Chapter five.

5. Calculation of Nodal Mass Flows

The objective of calculating the fluid velocities in the far field is to determine the mass flows that cross the faces of the nodes in the time dependent temperature calculations in the PSP.

When the far field velocity calculation has converged, the circumferential velocity, $u(z,\theta)$, is known. $U_s(\theta)$ gives the amplitude of the velocity as a function of theta and $U(z)$ gives the shape of the velocity as a function of z . For any cell i in the domain, the velocity distribution across the left face of the cell is given by $U_s(\theta_1)U(z)$, and the velocity distribution across the right face of the cell is given by $U_s(\theta_2)U(z)$, where θ_1 and θ_2 are the left and right theta locations of the cell faces, respectively. The velocity distributions at postions θ_1 and θ_2 are shown schematically in Fig. 50.

The calculation of the mass flow across a vertical face of any cell i is a simple matter of integrating the velocity profile. For example, the mass flow across the left face of cell i in Fig. 50 is given by

$$FOL_i = \rho_o \, U_s(\theta_1) \int_{z_0}^{z_1} F_1(z) \, U(z) \, dz \ , \qquad (156)$$

where

FOL_i = flow out the left face of cell i,

ρ = a representative density for cell i,

$U_s(\theta_l)$ = the theta velocity amplitude along the left face,

$F_l(z)$ = width of the torus as a function of z,

z_0, z_l = bottom and top locations of the horizontal faces of node i, respectively,

$U(z)$ = the horizontal velocity as a function of z, given by equations (95) and (96).

The calculation of the flow across the top and bottom faces of the cells is performed by utilizing a mass balance at each stack of the nodes. In Fig. 50, for the bottom node i, the flow into the top face is given by

$$FIT_i = FOL_i - FIR_i \ , \tag{157}$$

where FIR_i = flow into the right face of cell i . For node i+1, located immediately above node i, the mass balance yields

$$FIT_{i+1} = FOB_{i+1} + FOL_{i+1} - FIR_{i+1} \tag{158}$$

where FOB_{i+1} = flow out of the bottom face of cell i+1 . However, $FOB_{i+1} = FIT_i$, which was just determined by equation (157). Hence, FIT_{i+1} can be determined.

Thus, a series of mass balances which starts at the bottom node and marches to the top of the domain yields the vertical mass flows at each theta position in the system.

The mass flows in the PSP are symmetric about the centerline of the discharging T-quencher, as shown in Fig. 51. The mass flows are calculated for the part of the far field on only one side of the T-quencher and the mass flows on the other side are formed as the mirror image of the first side.

The calculations of the mass flows is performed in subroutine FARFLD, and the formation of the symmetrical flow field around the T-quencher centerline is performed in subroutine PDRIVR; both of these subroutines are described in Chapter five.

E. THERMAL STRATIFICATION MODEL

The previous sections of this chapter have dealt with the thermal convection cell model, which is designed to model the PSP response during periods when steam is being discharged through T-quenchers. The objective of this section is to describe a completely different model for the flow in the PSP--the thermal stratification model.

The purpose of the thermal stratification model is to estimate the fluid flow that occurs in the PSP immediately following closure of the SRVs. As discussed in Chapter two, a stable thermal stratification is created in the pool through a very complicated series of internal wave motions. Very little is known about the thermal mixing characteristics

of this type of flow--especially in the area of describing the dynamic characteristics of the flow.

A very simple model for the transient thermal stratification is proposed to describe the flow in the PSP immediately following SRV closure. The model is based in part on the dynamics of thermals, and in part on the dynamics of density currents.

The model for the transient thermal stratification consists of producing an equal and opposite mass flow between adjacent nodes that is proportional to the square root of the density difference between the nodes. The length scale for the motion was chosen as the height of the given fluid layer in which the nodes are located. The flow area was chosen as one half of the cross sectional area of the nodes. The adjacent nodes and the mass flows are shown in Fig. 52.

The model for the mass flow between adjacent nodes is

$$\dot{M}_{STR} = \rho_H A_{flo} \sqrt{2\Delta_z \frac{\Delta\rho}{\rho_H} g} \qquad (159)$$

where

$\dot{M}_{STR}$ = the stratification flow,
ρ_H = the average density of the two nodes,
A_{flo} = one half the cross sectional area,
Δ_z = the height of the nodes,
$\Delta\rho$ = the density difference between the nodes.

Although equation (159) is a very crude model of a very complex phenomenon, it models the transient thermal stratification flow quite well, as described in Chapter six.

Within the transient thermal mixing model of the PSP, equation (159) is applied to each node in the system to produce a series of horizontal flows for each layer. The model is implemented in subroutine QNHOFF, as described in Chapter five.

F. BULK POOL CIRCULATION MODEL

The bulk pool circulation model was designed for transients in which the PSP water is forced to move at a high velocity (bulk pool velocities ~3-5 Ft/s) in the circumferential direction. Discharge of water into the PSP from the residual heat removal (RHR) system would produce such a flow.

The effect of a large circumferential velocity is to thoroughly mix the PSP water in the vertical direction. If there are no sources of energy in the PSP, a large circumferential velocity will also thoroughly mix the water in the theta direction. If there are sources of energy in the PSP (such as discharging T-quenchers), then a large circumferential velocity will simply carry the energy around the PSP at the bulk pool velocity.

The bulk pool circulation model involves specifying the PSP velocity field as follows.

$$W(z,\theta) = 0, \text{ everywhere} ,$$

and

$$U(z,\theta) = U_{BP}, \text{ everywhere} , \tag{161}$$

where

U_{BP} = the bulk pool velocity.

In addition, the bulk pool circulation model allows only a one dimensional variation of the temperature, i.e.,

$$T(z,\theta) \equiv T(\theta) . \tag{162}$$

Equation (162) is enforced in the two dimensional, z-θ noding of the PSP by averaging the temperatures at each stack of theta nodes throughout the domain. The averaging is performed at the beginning of the time step in which the bulk pool circulation model is used.

The bulk pool circulation model is implemented in subroutine RHR, as described in Chapter five.

G. WELL MIXED POOL MODEL

The well mixed pool model was designed for transients in which the PSP can be treated as a large, well mixed pot of water. This approach saves computer time and is the only option available in existing codes. The well mixed pool model is quite simply,

$$T(z,\theta) = T_b, \text{ everywhere} . \tag{163}$$

The bulk pool temperature, T_b, is determined by solving

$$\frac{d}{dt} (M_p C_p T_b) = S_{tot} , \tag{164}$$

where

S_{tot} = the total energy per unit time added to the PSP,
M_p = the mass of water in the PSP.

For a constant energy source, equation (164) can be solved to yield

$$T_b^{t+\Delta t} = \frac{(M_p C_p T_b)^t + S_{tot}\Delta t}{(M_p C_p)^{t+\Delta t}} . \tag{165}$$

The well mixed pool model is implemented in subroutine WELMIX, as described in Chapter five.

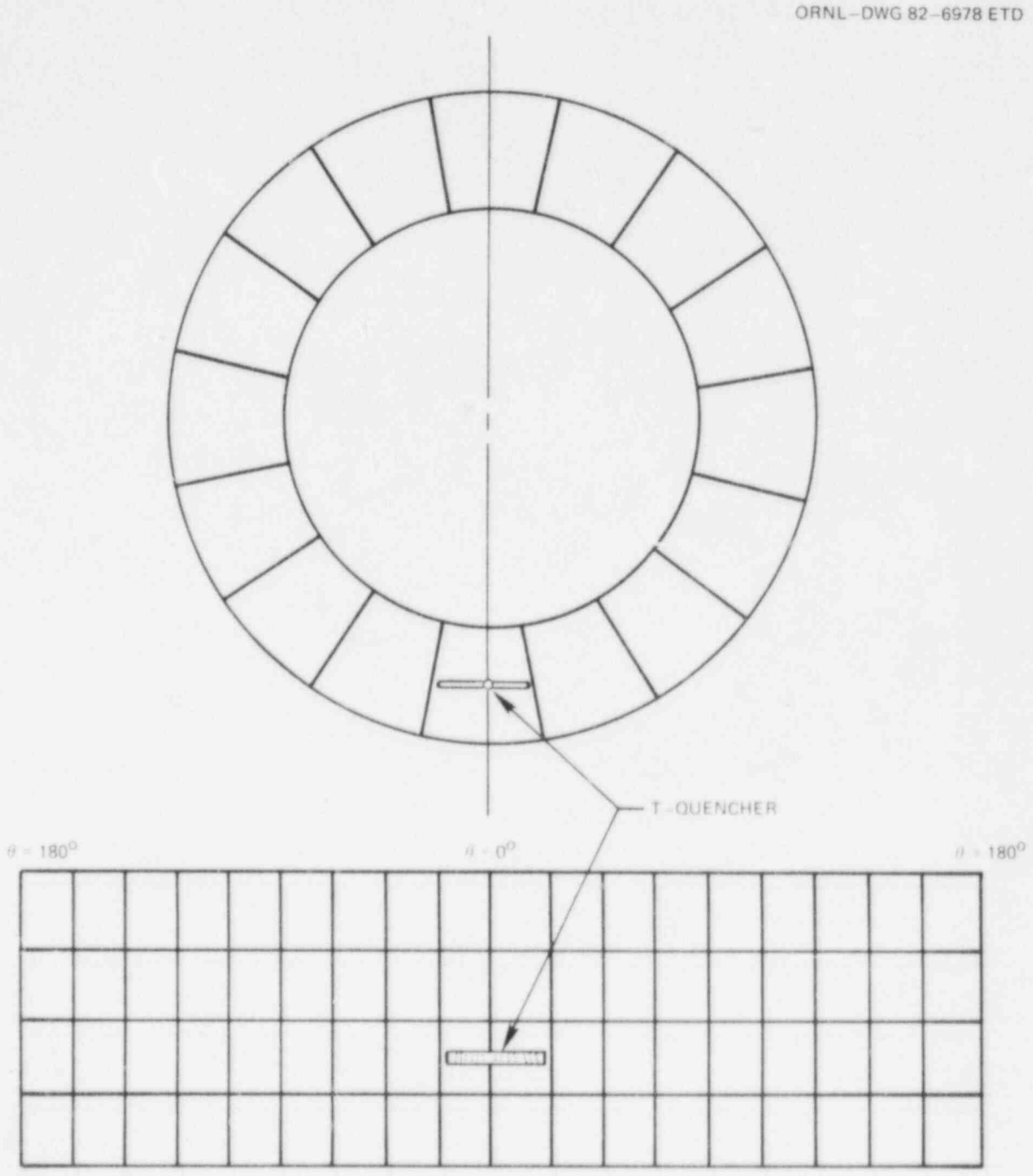

Fig. 16. Two dimensional PSP thermal model.

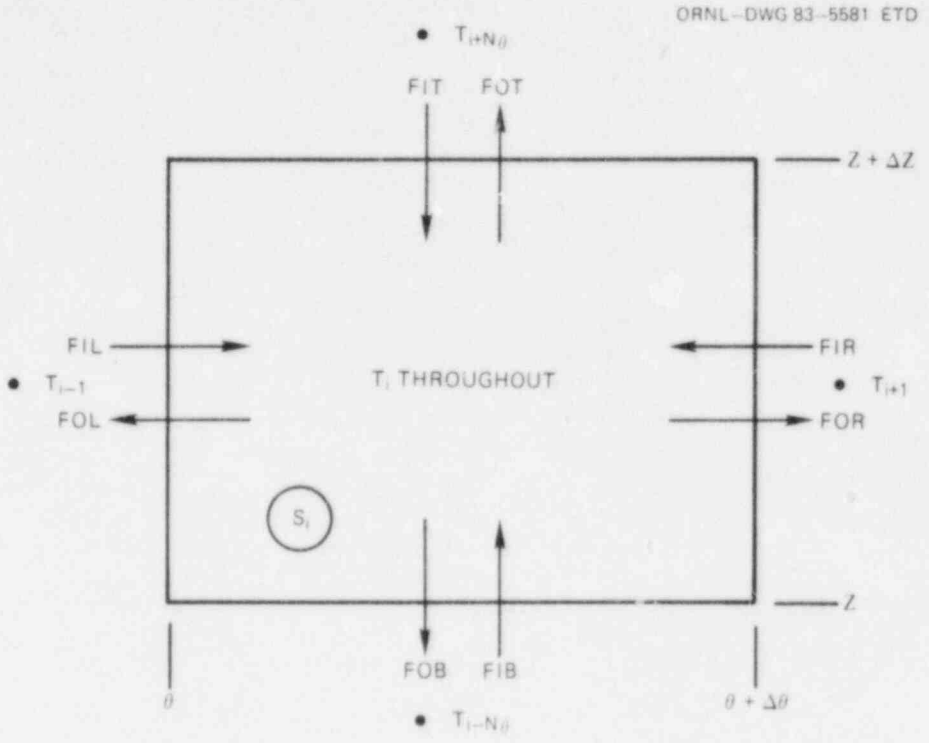

Fig. 17. General node energy balance.

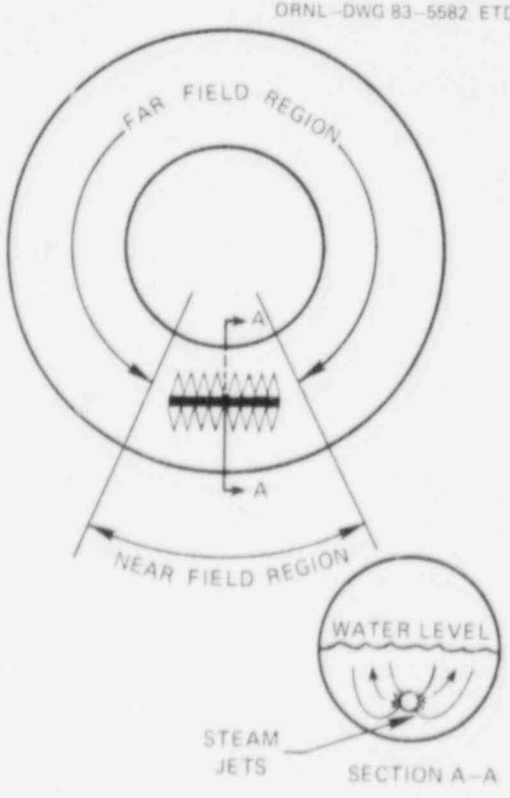

Fig. 18. Near field and far field regions.

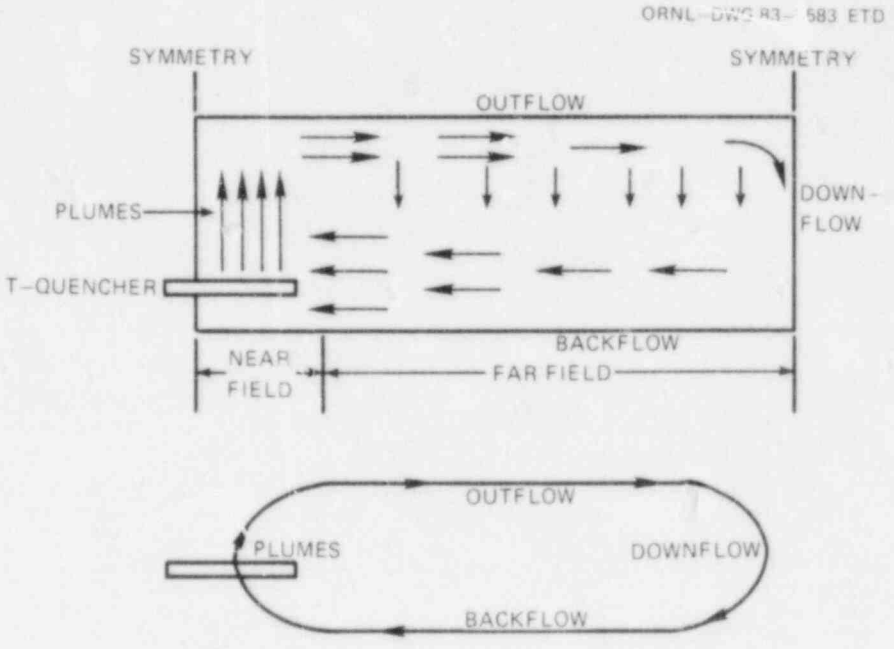

Fig. 19. Effective convection cell behavior of PSP.

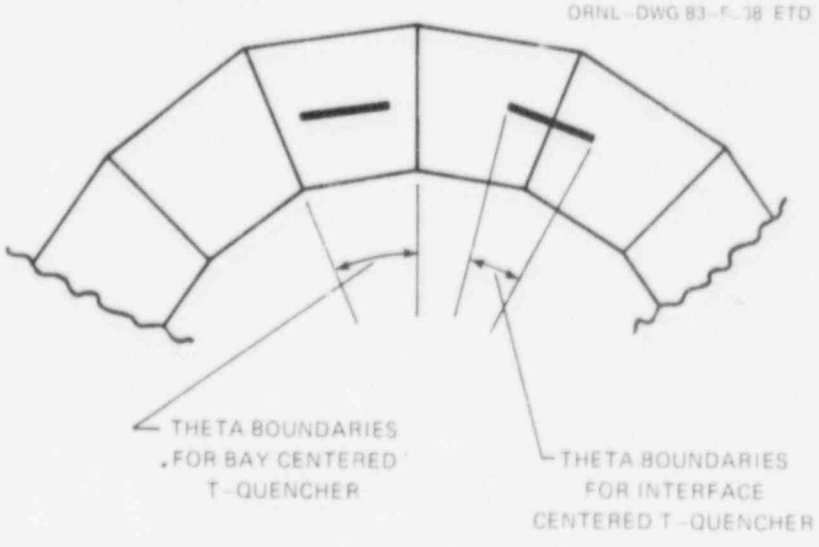

Fig. 20. Theta boundaries of the near field.

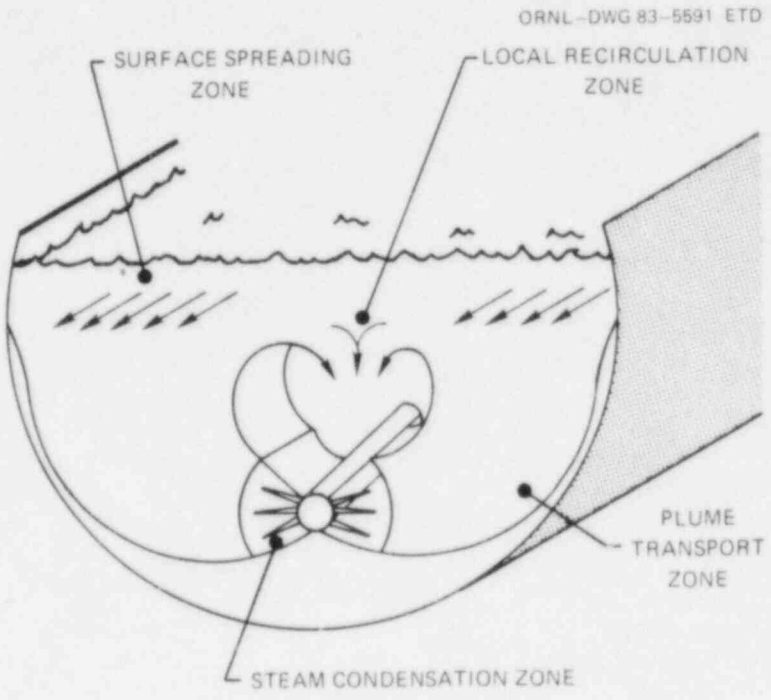

Fig. 21. Near field analysis zones.

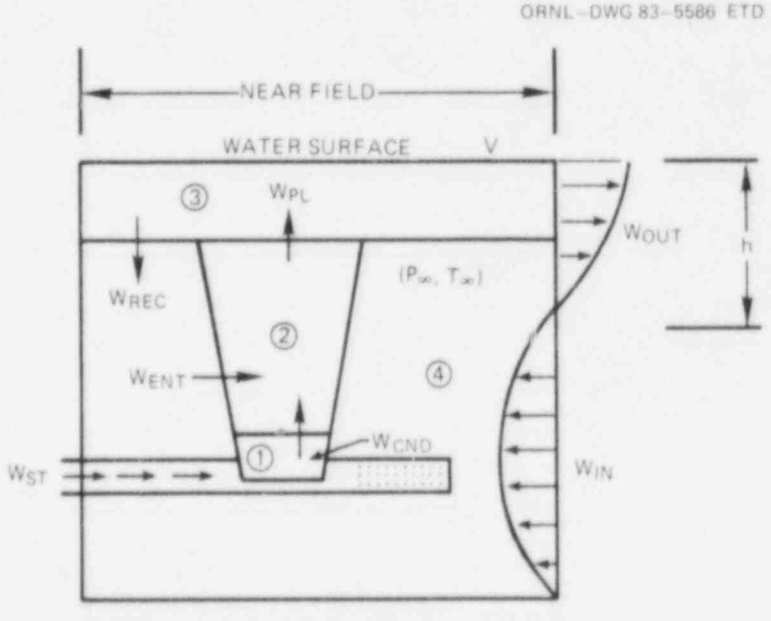

① STEAM CONDENSATION ZONE

② PLUME TRANSPORT ZONE

③ SURFACE SPREADING ZONE

④ LOCAL RECIRCULATION ZONE

Fig. 22. Lumped near field zones.

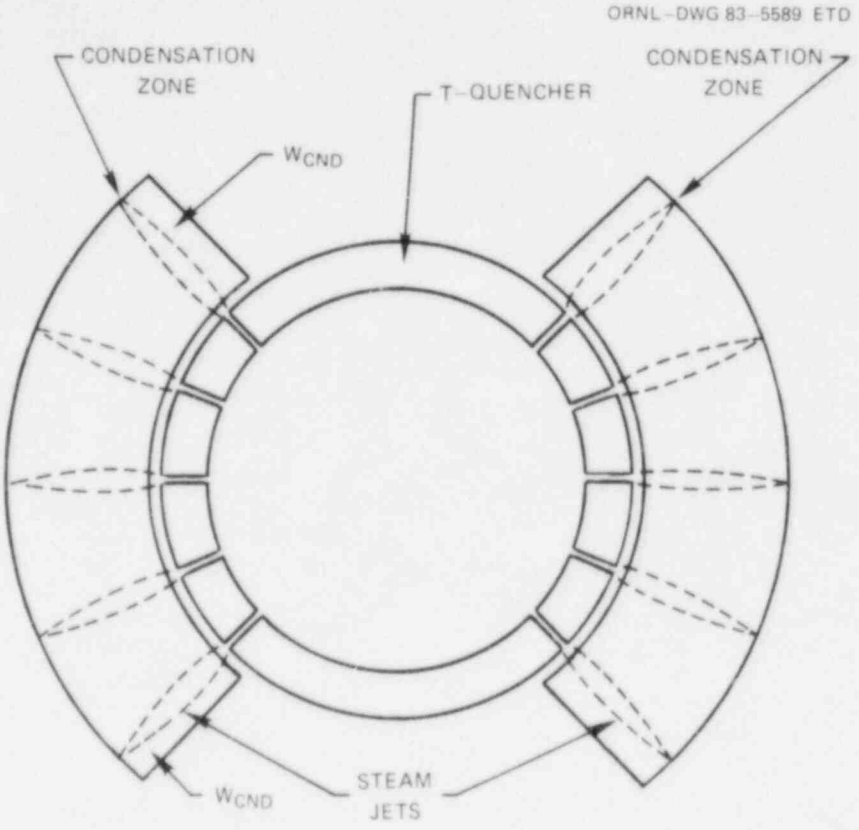

Fig. 23. Steam condensation zone.

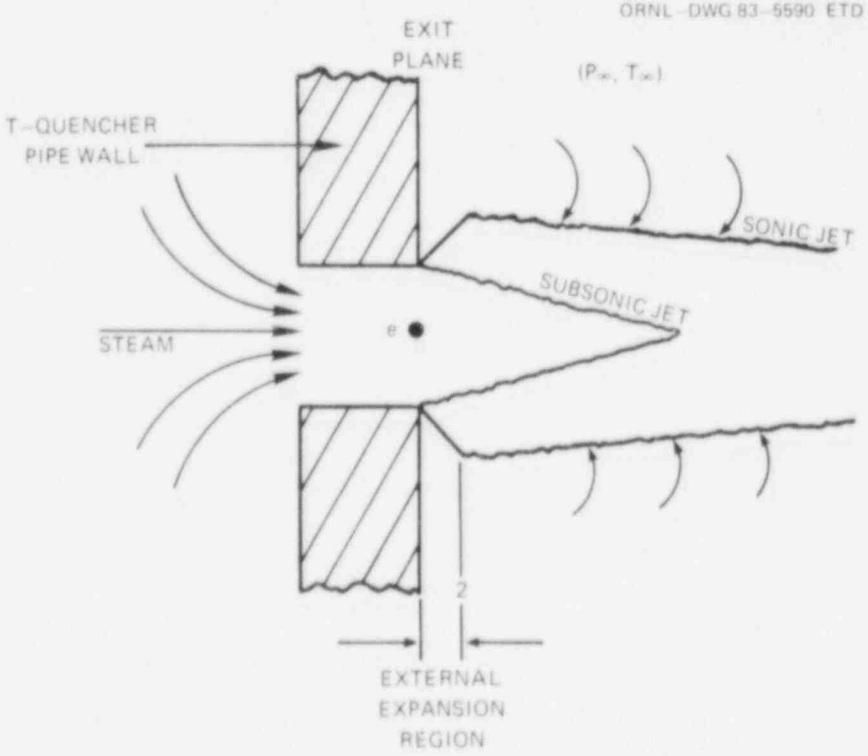

Fig. 24. Typical T-quencher hole.

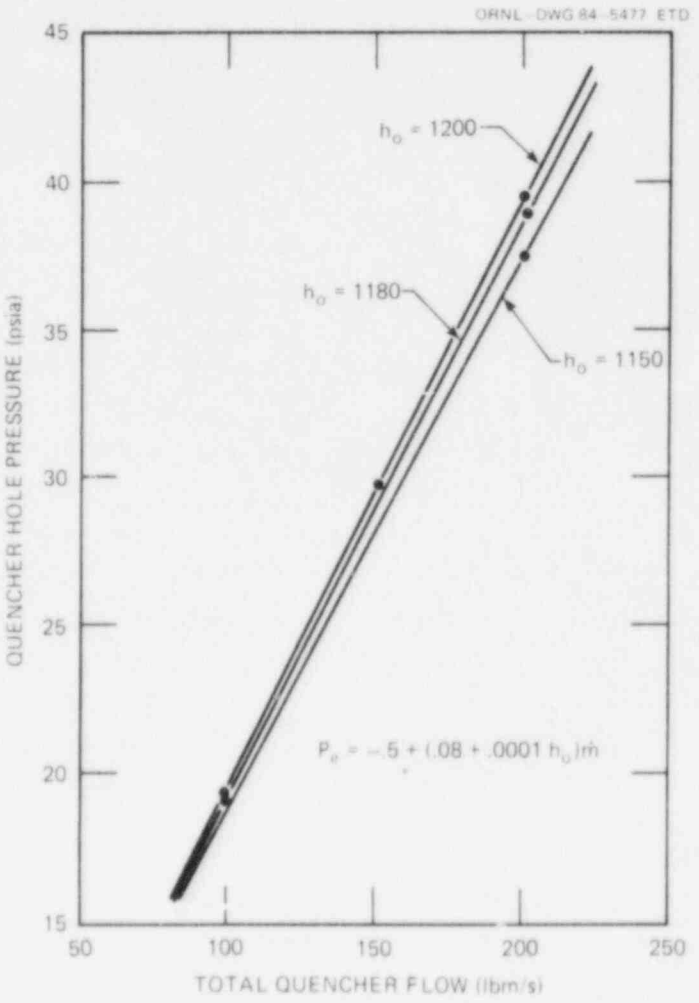

Fig. 25. Choked exit plane pressure versus quencher flow.

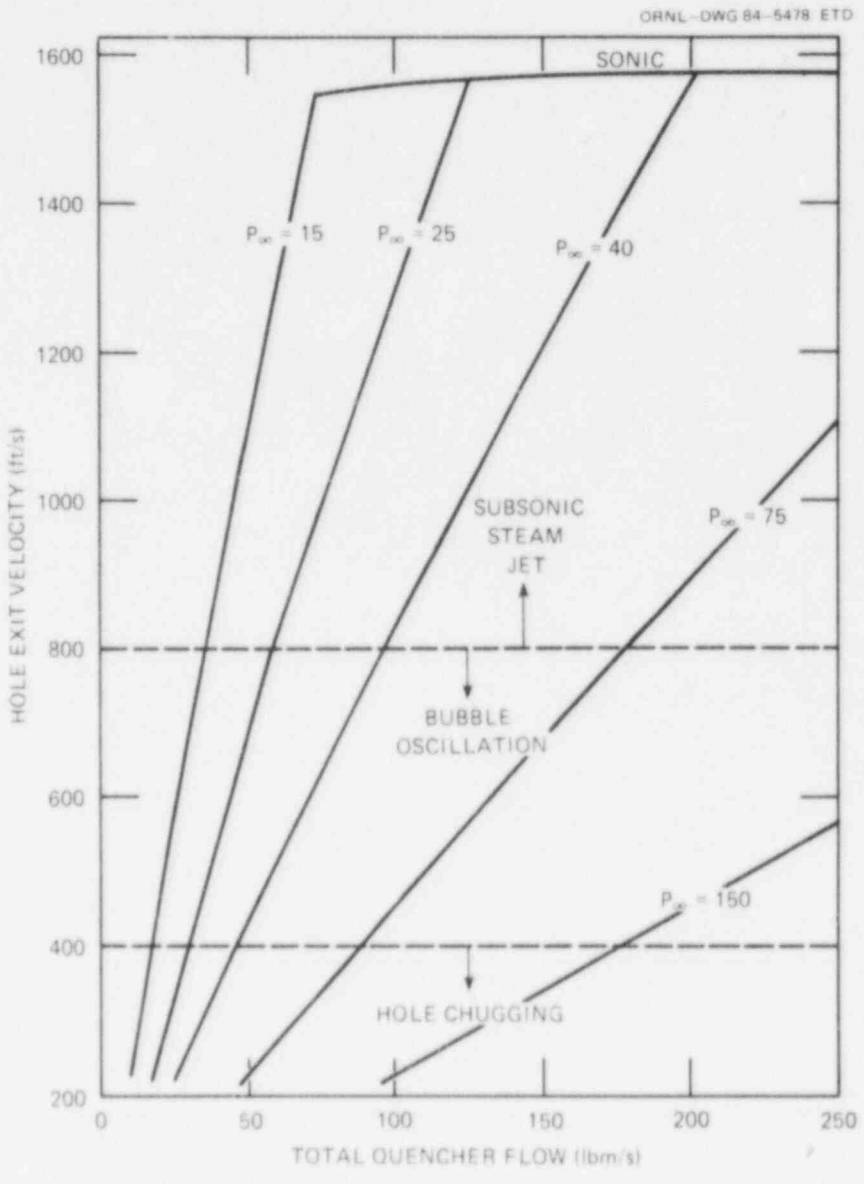

Fig. 26. Subsonic hole exit velocity versus quencher flow.

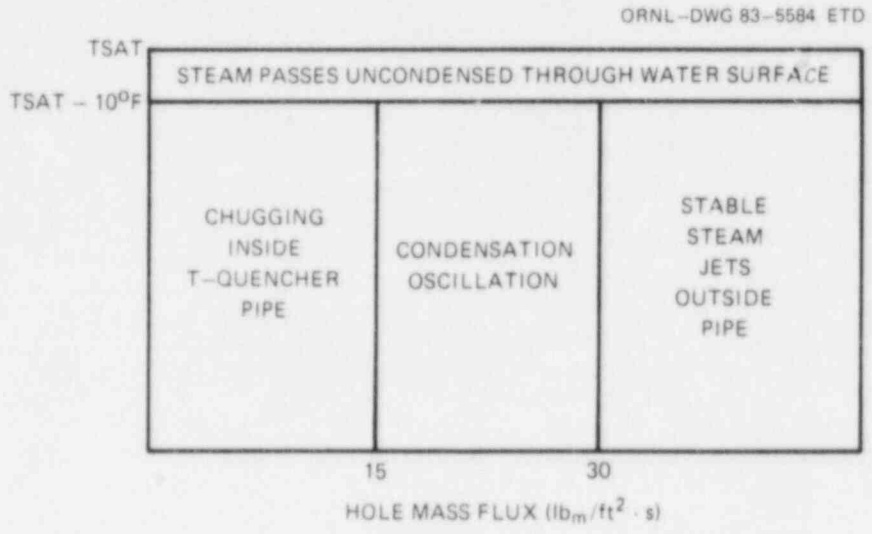

Fig. 27. Flow regime map for single jet at atmospheric pressure.

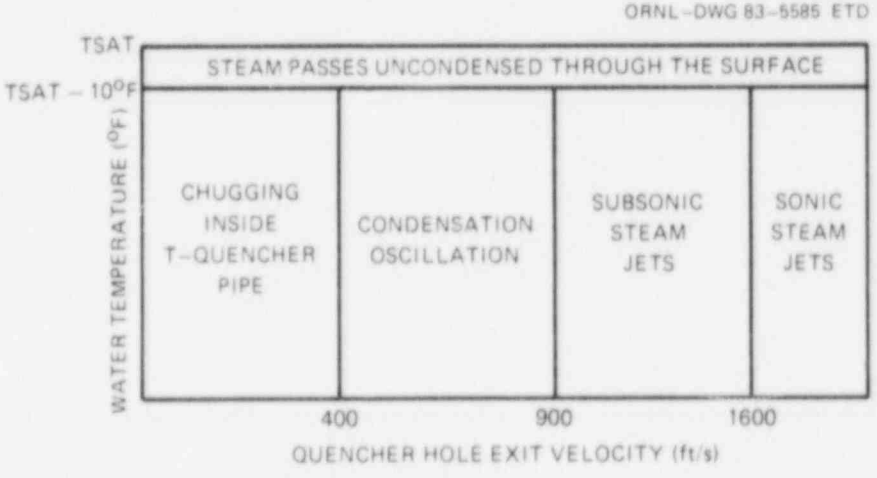

Fig. 28. Approximate flow regime map for arbitrary pressure.

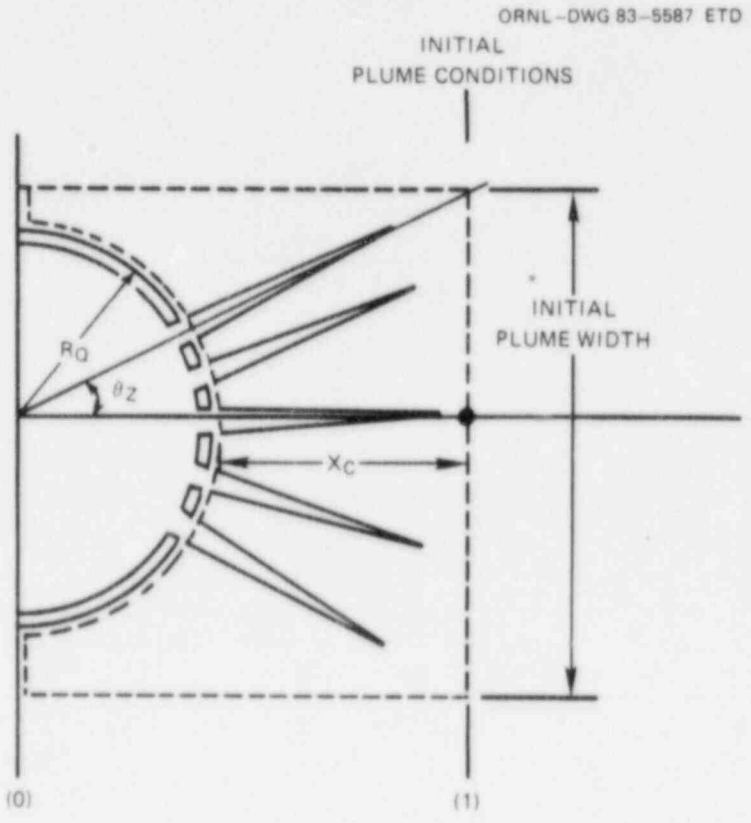

Fig. 29. Boundaries for momentum and energy balances on condensation zone.

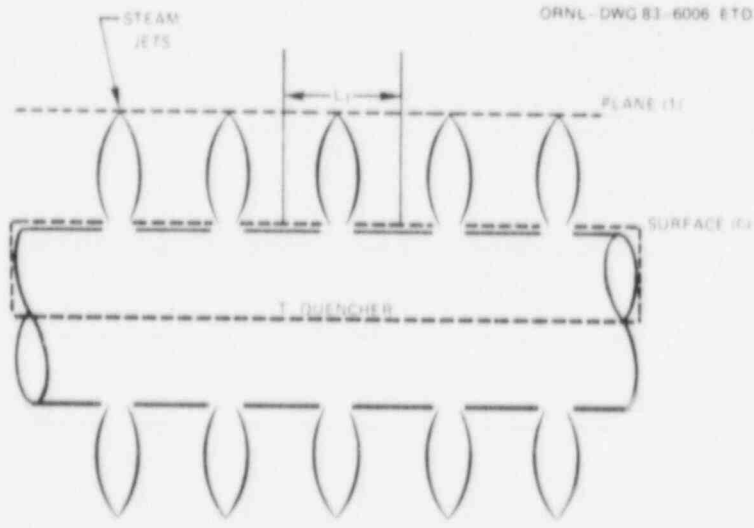

Fig. 30. Top view of steam condensation zone.

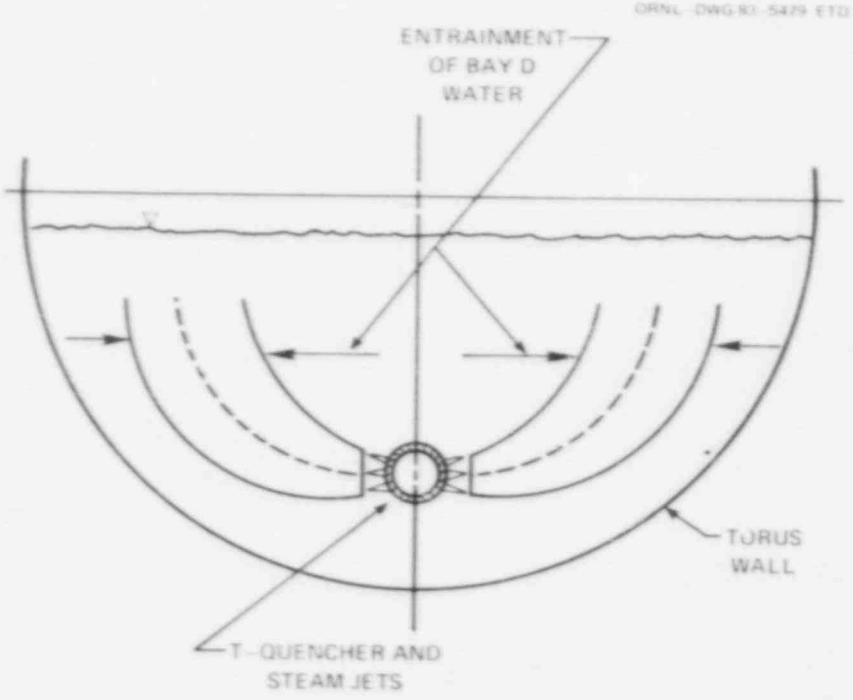

Fig. 31. Plume transport region.

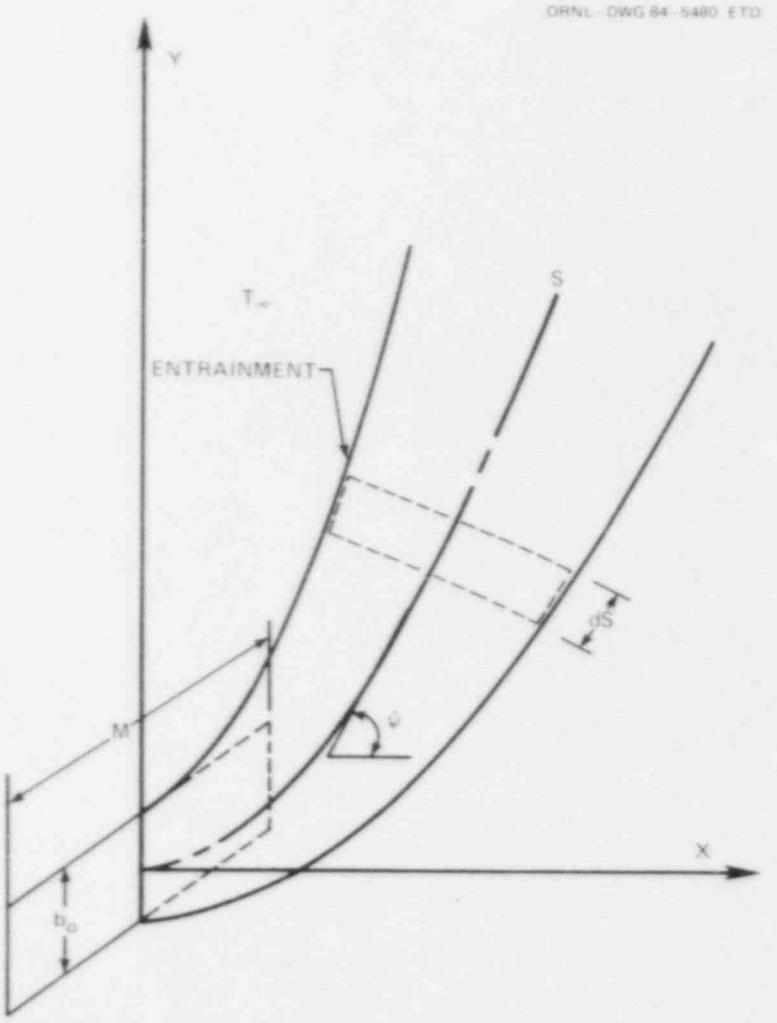

Fig. 32. Plume transport analysis coordinate system.

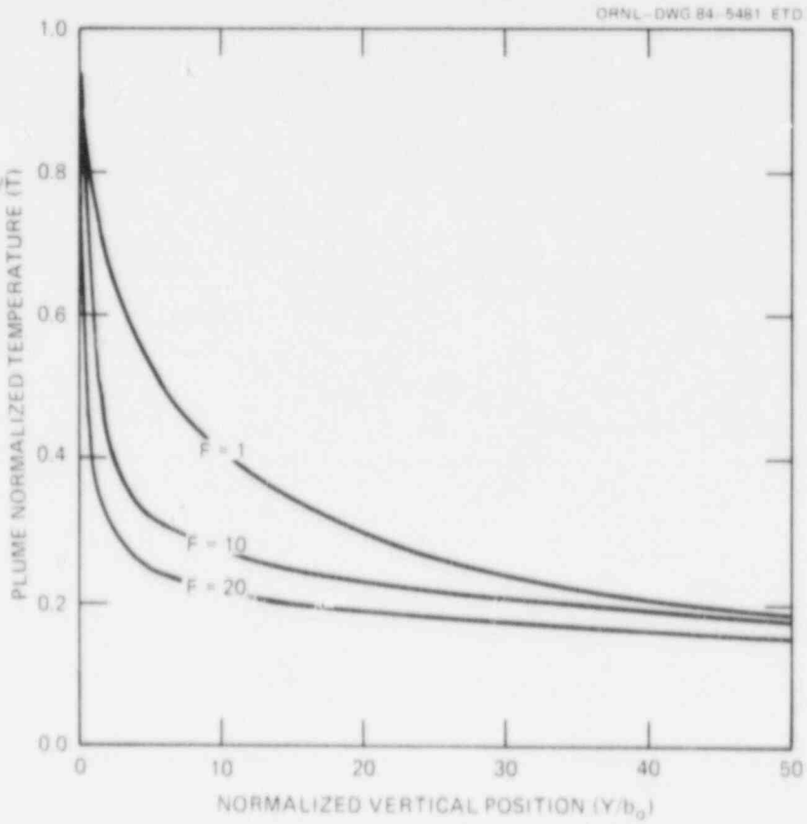

Fig. 33. Typical plume temperature results.

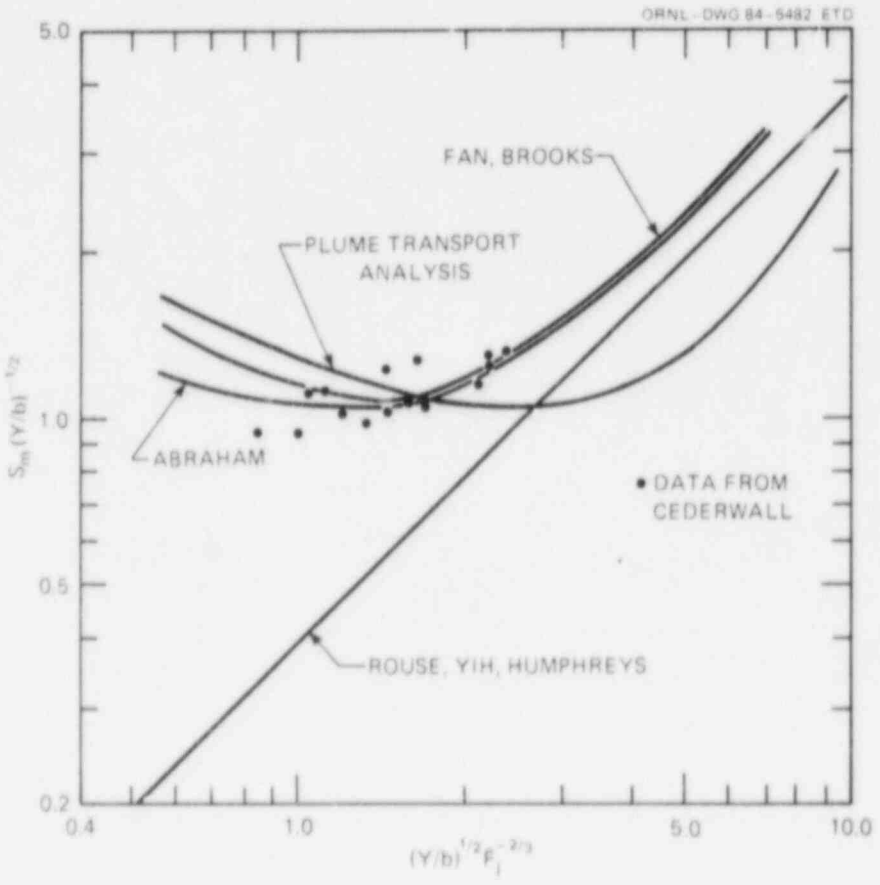

Fig. 34. Plume transport results.

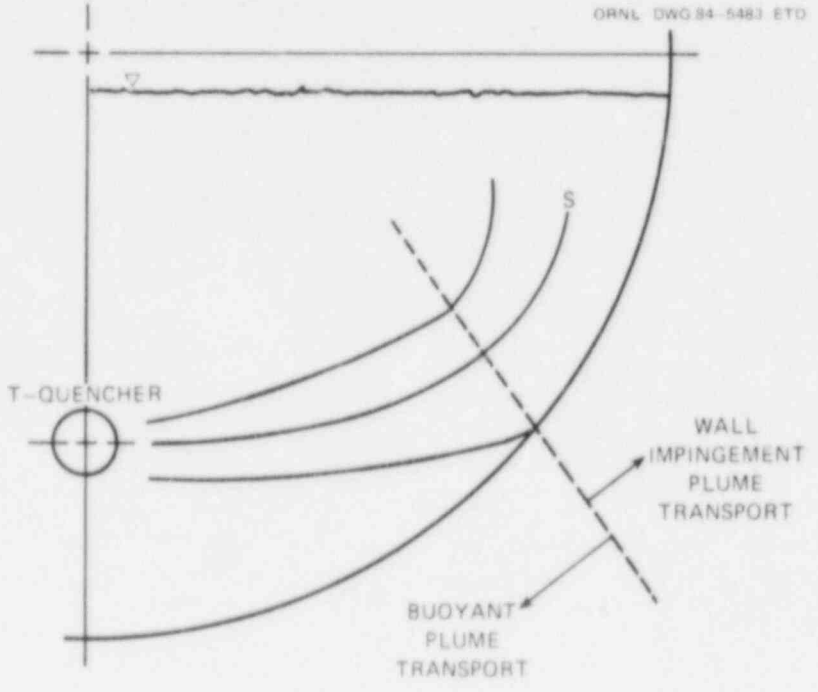

Fig. 35. Torus wall impingement problem.

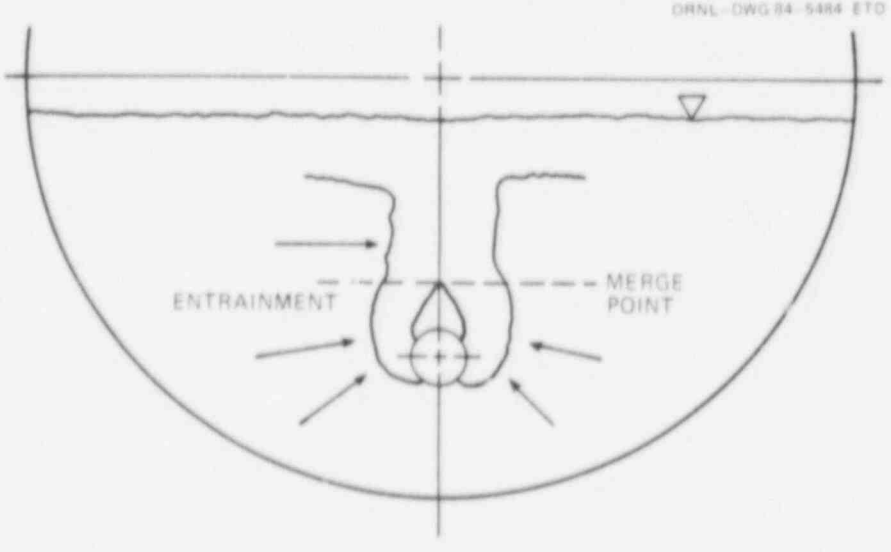

Fig. 36. Merging plumes.

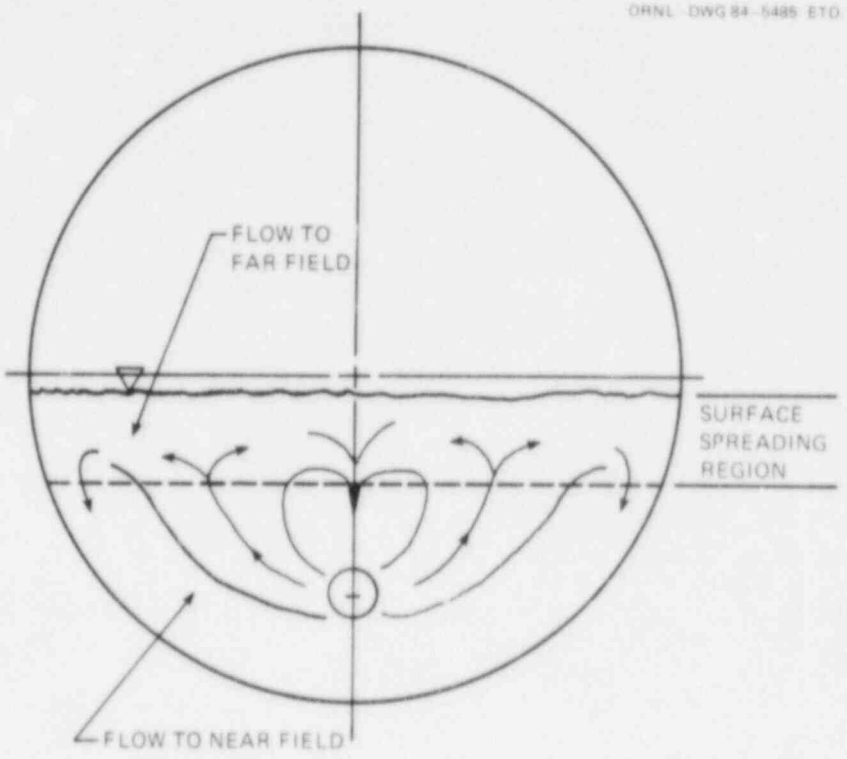

Fig. 37. Surface spreading region.

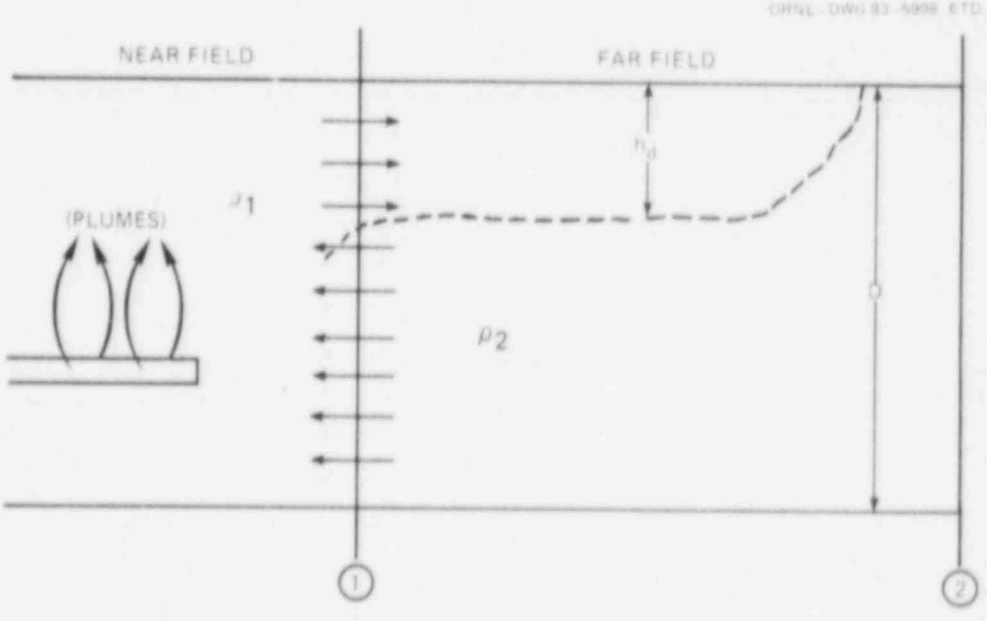

Fig. 38. Density current model of the surface spread

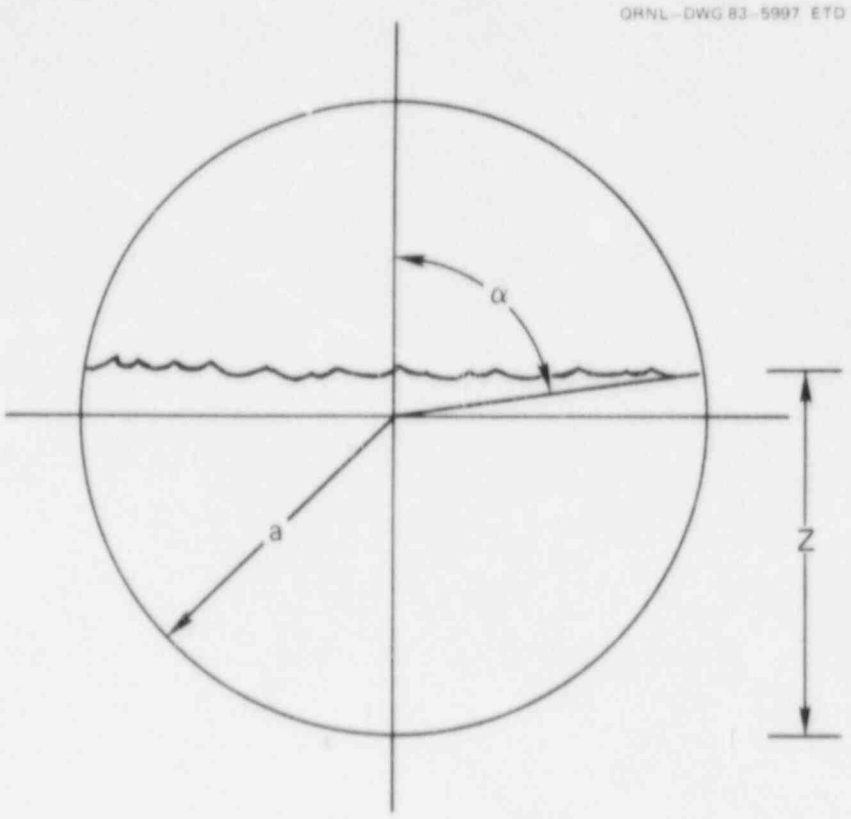

Fig. 39. PSP flow areas.

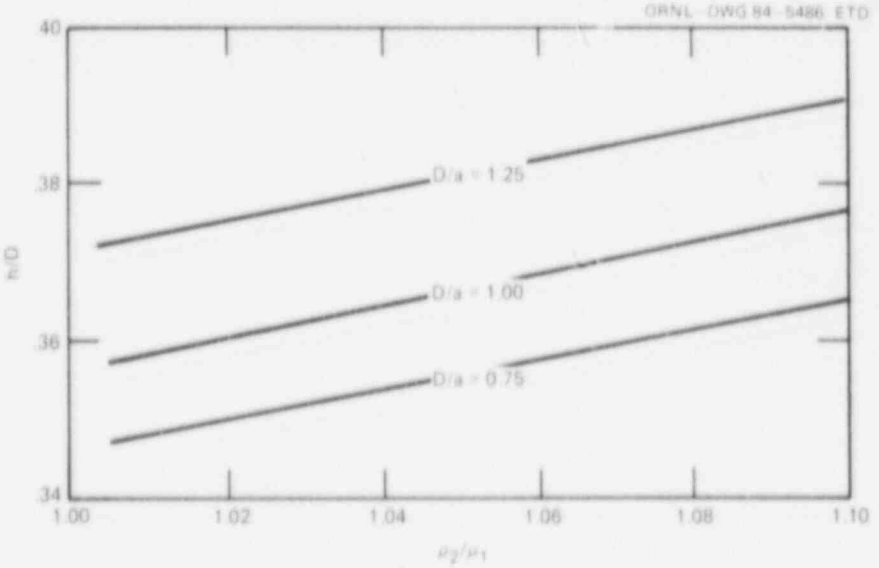

Fig. 40. Density current thickness.

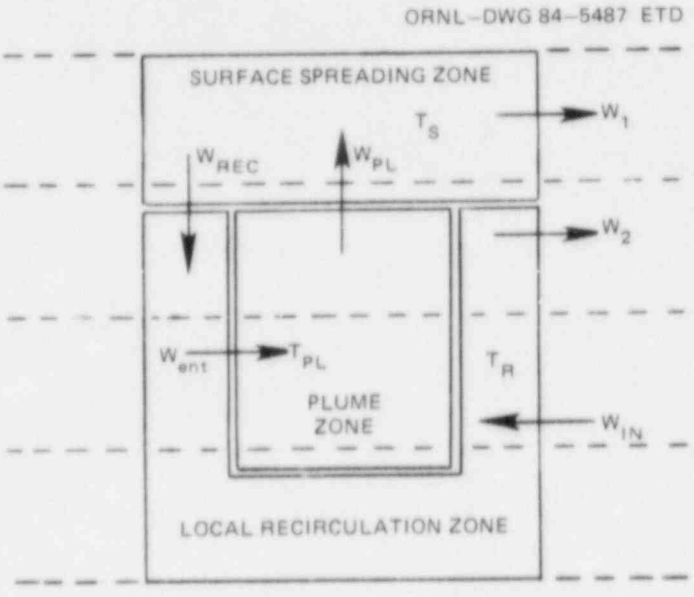

Fig. 41. Nodes for near field energy balances.

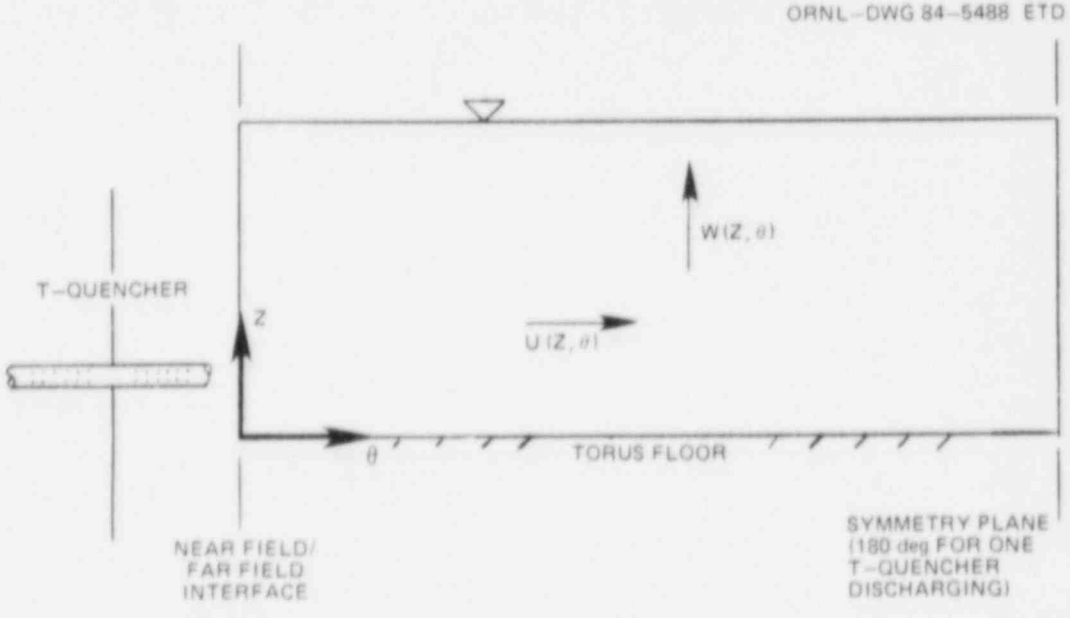

Fig. 42. Far field problem geometry.

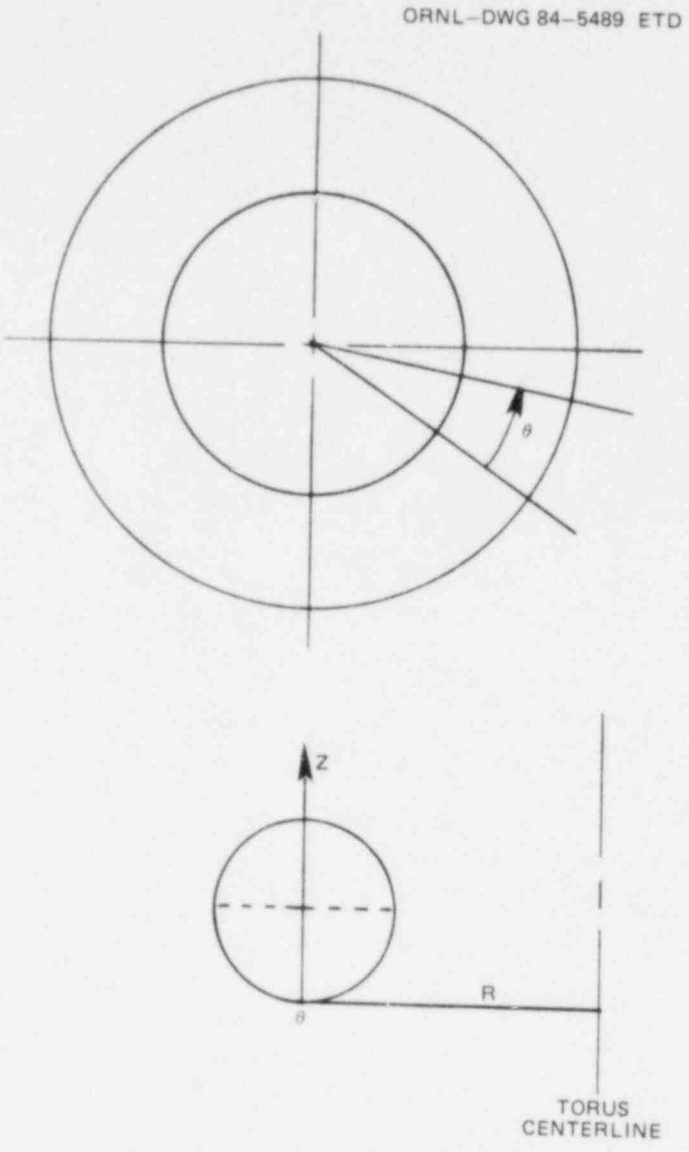

Fig. 43. Modified cylindrical coordinate system.

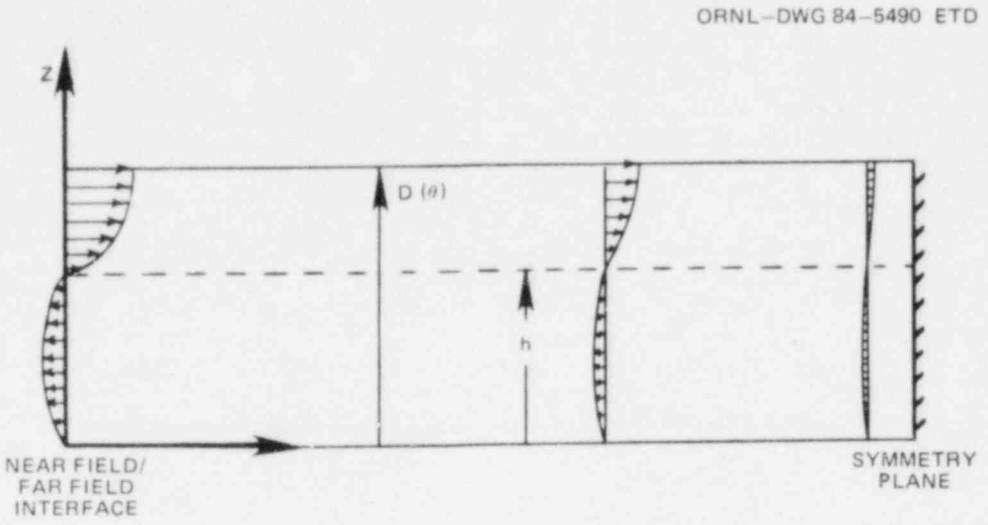

Fig. 44. Constant layer thickness model of the far field.

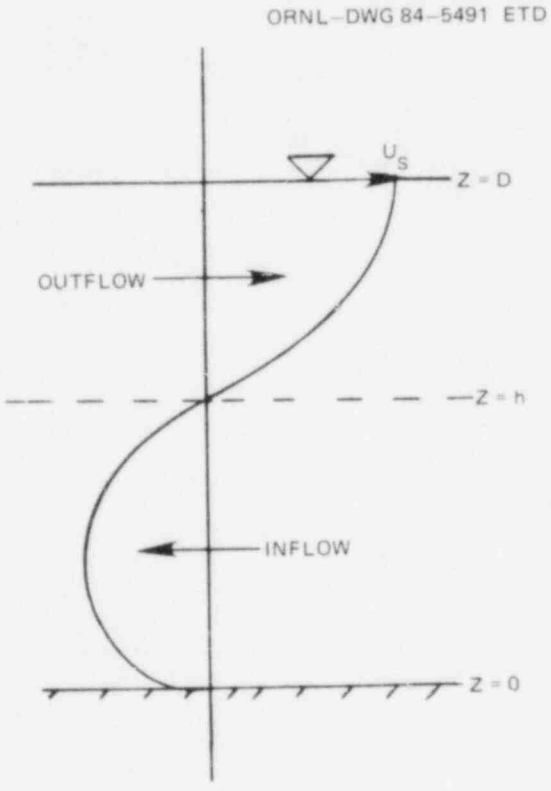

Fig. 45. Velocity profile for uniform cross section channel.

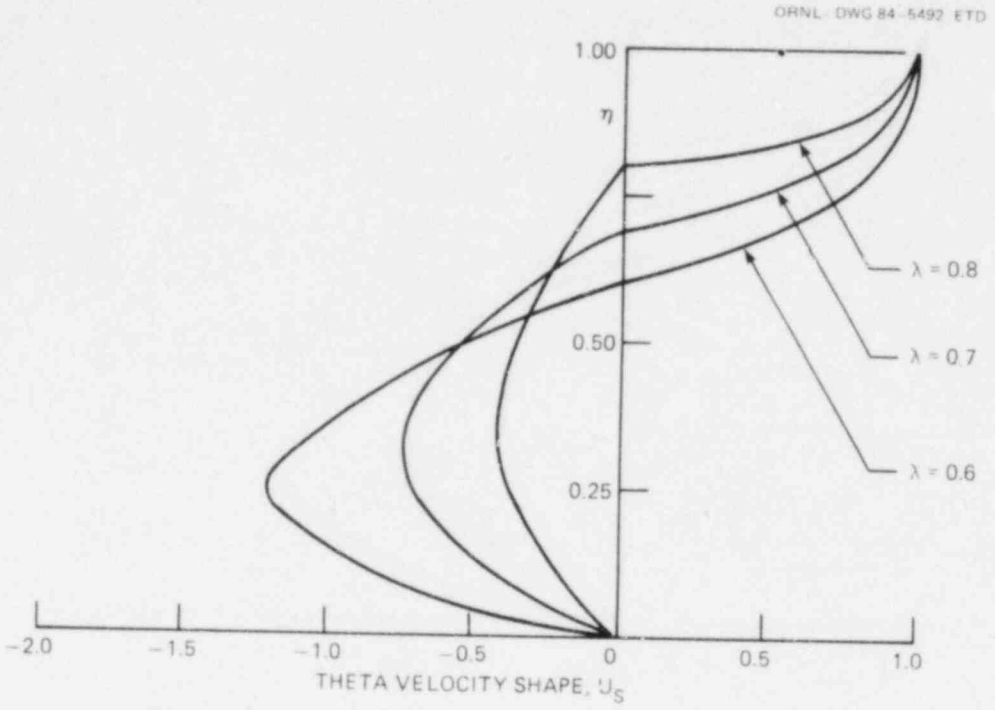

Fig. 46. Typical PSP theta velocity profiles.

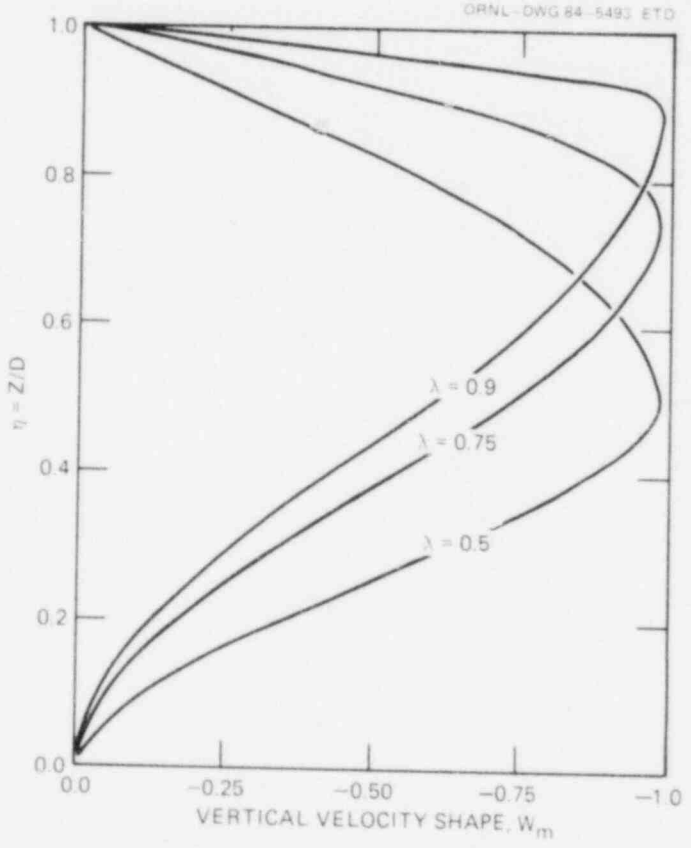

Fig. 47. Typical PSP vertical velocity profiles.

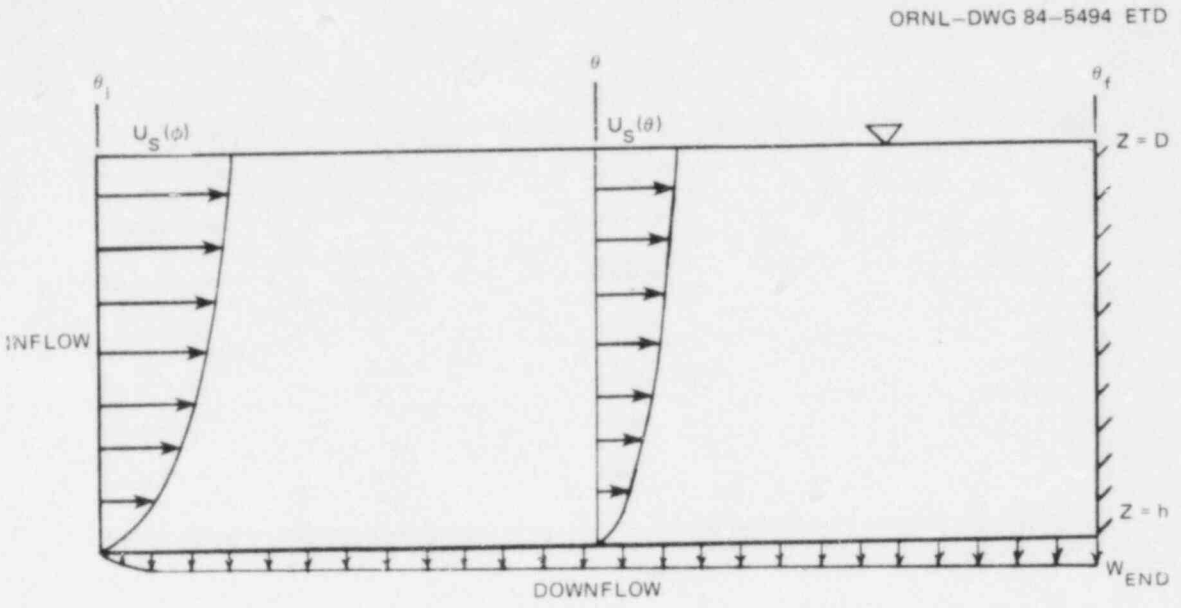

Fig. 48. Inflow from near field and downflow over far field.

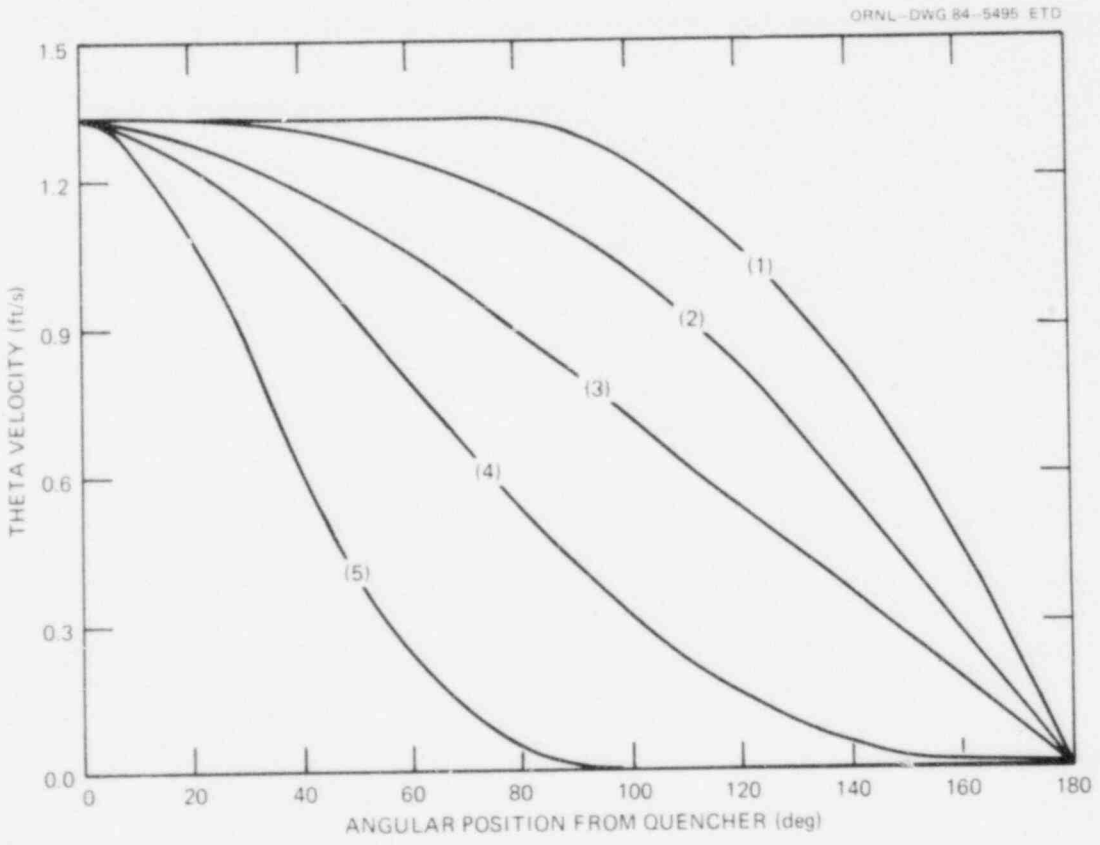

Fig. 49. Typical theta velocity distributions.

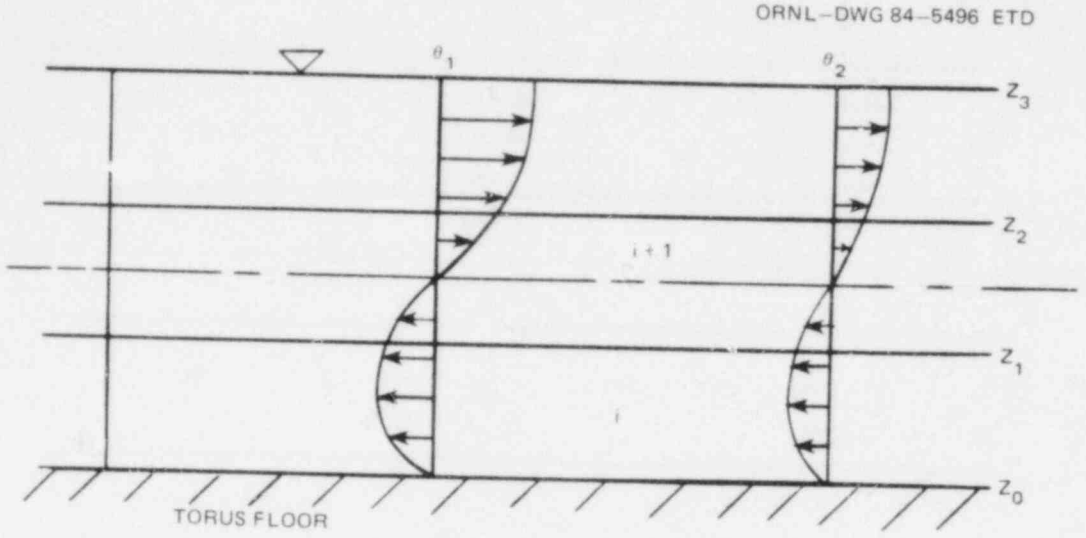

Fig. 50. Calculation of nodal mass flows.

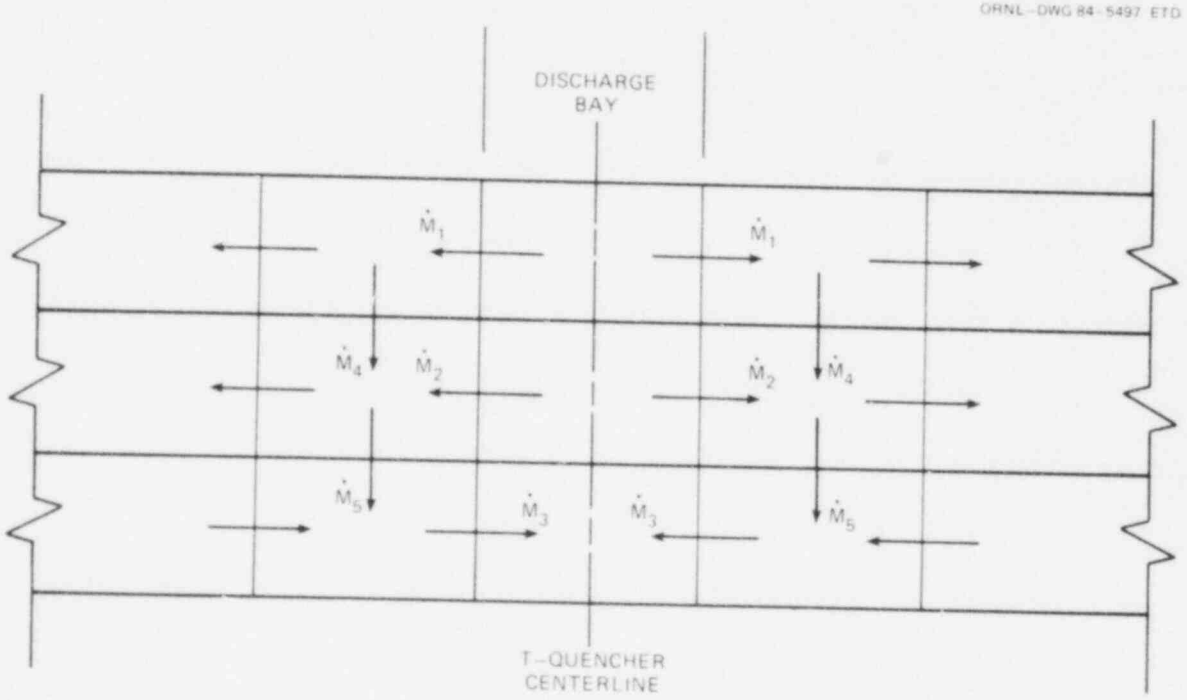

Fig. 51. Symmetry of PSP mass flows.

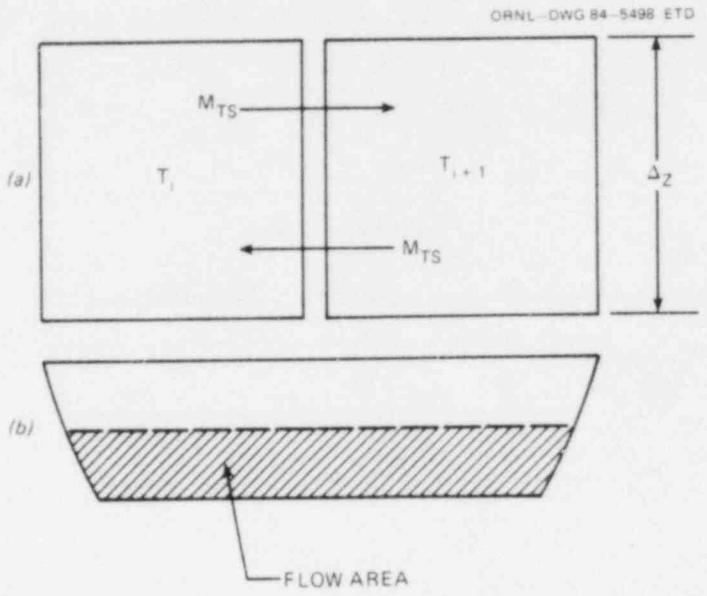

Fig. 52. Thermal stratification model.

CHAPTER V

SOLUTION OF THE MODEL EQUATIONS

A. ORGANIZATION OF THE MODEL SOLUTIONS

All of the models described in chapter four have been implemented in a computer program designed for use in the numerical simulation of the response of BWR Mark I pressure suppression pools to accident situations.

The PSP code was written as a large subroutine that could be used in conjunction with other computer models that describe the BWR primary and secondary containment systems. The PSP code can also be used in a stand-alone mode by writing a small program to call the PSP subroutine at each time step. Detailed recommendations for use of the PSP models are described in Appendix C, and detailed instructions for use of the code (including input description and sample output) are described in Appendix D.

The PSP code is structured as shown in Fig. 53. The main driver subroutine for the code is PDRIVR, which implements the steps shown in Fig. 53 by calling other subroutines. PDRIVR receives input from the calling program, and depending on the value of input parameter IMODEL, determines the PSP flow field using the T-quencher thermal convection cell model (IMODEL=1), the thermal stratification model (IMODEL=2), the bulk pool circulation model (IMODEL=3), or the well mixed pool model (IMODEL=4). If IMODEL equals 1,2,or 3, PDRIVR will call subroutine POOL, which sets up and solves equation (1) for every node in the PSP. The nodal temperature calculations are described in section D of this chapter. If IMODEL equals 4, subroutine PDRIVR avoids the computational cost of solving the N coupled ODEs by setting every temperature in the domain equal to the bulk pool temperature.

After the new temperatures are determined, subroutine PDRIVR calls subroutine VOLUME, which is designed to adjust the PSP water level to account for the net mass gain or loss due to water entering and leaving the PSP during the time step. The water level calculation is described in section E.

B. THERMAL CONVECTION CELL MODEL SOLUTIONS

1. Introduction

The T-quencher thermal convection cell model is implemented in subroutine QNCELL. QNCELL is divided into two major parts: the near field subroutines, which implement the near field analysis, and the far field subroutines, which implement the far field analysis. The input to QNCELL is the T-quencher steam flow and enthalpy, the PSP overpressure, and the theta boundaries of the far field. The output of QNCELL is the

nodal mass flow distribution and the discharge bay energy source distribution. The organization of QNCELL is shown in Fig. 54.

The remaining parts of this section describe the subroutines that implement the near field and the far field analyses.

2. Steam Condensation

The T-quencher steam condensation model is implemented in subroutine CONDNS. Input to CONDNS consists of the T-quencher steam flow and enthalpy, the local pressure, and the discharge bay average temperature. The output of CONDNS is a set of four plume initial conditions consisting of a hot water jet temperature, velocity, width, and Froude number. The set of four corresponds to the four zones of holes on the standard General Electric Company T-quencher.

CONDNS uses the model for the thermodynamic conditions in a typical T-quencher hole, determines the condensation regime using the simple map developed in Chapter four, and then solves the coupled conservation of energy and momentum equations, equations (13) and (14), for a typical column of holes on the T-quencher to produce the plume initial conditions.

3. Plume Transport

The plume transport dynamics are calculated in subroutine PLUME. PLUME is designed to follow a turbulent, buoyant plume from the T-quencher upward to the PSP surface. PLUME takes into account the possibility of torus wall impingement and plume merging directly above the T-quencher.

Input to PLUME consists of the set of four plume initial conditions from subroutine CONDNS. The output of PLUME consists of the total entrainment of Bay D water (from all four plumes) and the average plume temperature near the PSP surface.

4. Near Field Energy Balances

The near field energy balances are performed in subroutine QNCELL. The energy balances use the analytical solutions for the temperatures of the surface and recirculation regions (equations (69) and (70) , respectively) to determine the T-quencher source distribution (equations (75) and (76)). The sources are applied to the nodes that overlap the discharge bay in the thermal model of the whole pool.

Input to the energy balances consists of the total plume flow near the PSP surface, the average plume terminal temperature, the recirculation flow (defined by equation (65)), and the near field / far field interface flow.

5. Near Field / Far Field Interface

The near field / far field interface is determined in subroutine LAMBDA, using the surface spreading model described in Chapter four.

The average velocity of the hot water that flows out of the near field into the far field is calculated using equation (64). The thickness of the hot water layer is determined using equation (61).

6. Far Field Velocity Profiles

The far field theory described in Chapter four is implemented in subroutine FARFLD. The organization of subroutine FARFLD is shown in Fig. 55. The vertical profiles of $u(z,\theta)$ and $w(z,\theta)$ are determined in subroutine VELCON. The gammas, which are defined by equations (118) through (122) and (126) are determined in subroutine GAMMA. The downflow velocity profile, $W_m(\theta)$, is determined in subroutine DWNFLO.

In each of the three subroutines that deal with velocity profiles (VELCON,GAMMA,and DWNFLO), the expressions for each particular set of constants have been determined analytically and are programmed into the subroutines. The subroutines simply perform polynomial evaluation. For example, in the expression for γ_1,

$$\gamma_1 = \int_{\lambda}^{1} f(\eta)\, U^2(\eta)\, d\eta ,$$

the second order polynomial $f(\eta)$ and the third order polynomial $U(\eta)$ are known functions of η, but they contain arbitrary constants. The polynomials were multiplied, integrated, and then programmed into subroutine GAMMA for evaluation with the arbitrary constants and λ as input.

7. Iterative Determination of the Velocity Field

The iterative process for determining the far field velocities $u(z,\theta)$ and $w(z,\theta)$ is implemented in subroutine FARFLD. The first guess for $W_m(\theta)$ is always constrained to $W_{end} = 0$, as shown by curve (1) in Fig. 56. Then, depending on the sign of Q (given by equation (154)), the downflow is moved either more toward θ_f, as shown by curve (2) in Fig. 56, or more toward θ, as shown by curve (3) in Fig. 56. In either case, the downflow is moved until a sign change occurs in Q. At that point, the correct downflow profile is trapped, and the iteration proceeds rapidly to a solution where $|Q|$ is small.

The iterative technique used to converge on Q is simple interval halving until Q becomes small ($Q \sim 0.1$) then a Newton's method iteration is used to converge quickly to $|Q| < \varepsilon$.

C. OTHER MODEL SOLUTIONS

The previous section described the implementation of the T-quencher thermal convection cell model. The purpose of this section is to describe the implementation of the thermal stratification model, the bulk pool circulation model, and the well mixed pool model.

The thermal stratification model is implemented in subroutine QNHOFF. The input to QNHOFF is the PSP temperature distribution at the current time. QNHOFF produces an equal and opposite mass flow between

adjacent nodes using equation (159). There is no flow in the vertical direction using the thermal stratification model.

The bulk pool circulation model is implemented in subroutine RHR. Subroutine RHR in essence circulates the water in the PSP at the bulk velocity that is input by the code user. This subroutine will function either with T-quenchers discharging steam into the pool, or without any discharging T-quenchers. If T-quenchers are discharging, RHR will create a uniform energy source in Bay D.

The well mixed pool model is implemented in subroutine WELMIX. WELMIX calculates a bulk pool temperature, T_b, using equation (165), and sets every nodal temperature in the PSP equal to T_b.

D. PSP TEMPERATURE CALCULATIONS

The goal of the PSP models is to produce the pool temperature distribution, $\underset{\sim}{T}$ at the new time $t+\Delta t$. Therefore,

$$\frac{d\underset{\sim}{T}}{dt} = A\underset{\sim}{T} + \underset{\sim}{S} \tag{166}$$

must be solved at each time step to produce $\underset{\sim}{T}$ at the new time. The initial conditions are

$$\underset{\sim}{T}(0) = \underset{\sim}{T}_i \tag{167}$$

There are two options available for solving equations (166) in the PSP code. If input parameter METHOD is zero, then a Crank-Nicholsen solution method is used. If METHOD is not zero, then an ODE solver that is user supplied must be used.

The Crank-Nicholsen scheme is to approximate equation (166) by

$$\underset{\sim}{T}^{t+\Delta t} = \underset{\sim}{T}^{t} + \frac{\Delta t}{2}\left[A\ \underset{\sim}{T}^{t+\Delta t}\right] + \frac{\Delta t}{2}\left[A\ \underset{\sim}{T}^{t}\right] + \Delta t\underset{\sim}{S}^{t}\ , \tag{168}$$

where the superscripts indicate the time level at which the dependent variables are to be evaluated. Equation (168) can be rearranged in the form

$$A'\underset{\sim}{T}^{t+\Delta t} = S'\ , \tag{169}$$

where

$$A' = I - \frac{\Delta t}{2}A\ ,$$

$$S' = \underset{\sim}{T}^{t} + \frac{\Delta t}{2}A\ \underset{\sim}{T}^{t} + \Delta t\ \underset{\sim}{S}\ .$$

Equation (169) is then solved for $T^{t+\Delta t}$ using standard Gaussian elimination. Equation (169) is formed in subroutine POOL, and the solution is found using subroutine DSOLVR, which is a subroutine to solve N linear equations in N unknowns.

If parameter METHOD is input different from zero, a subroutine to solve equation (166) must be supplied, as described in Appendix D. An example of this option is provided in the sample problem input in Appendix D, where the user supplied ODE solver is LSODE.[90] All of the results presented in Chapter six were generated using LSODE because it is a state of the art ODE solver, and it is much more economical to run than the Crank-Nicolson scheme.

E. PSP WATER LEVEL CALCULATION

After each temperature calculation, the water level of the PSP is adjusted to account for two effects: (1) the mass of the system has been changed by water flowing into or out of the system, and (2) the nodal masses have changed because the nodal densities have changed with temperature.

The water level adjustment is performed in subroutine VOLUME. Since the new mass of the PSP, M_n, is known, i.e.,

$$M_n = M_o + M_{add} \quad , \tag{170}$$

where

M_n = total mass of the PSP at $t+\Delta t$,
M_o = total mass of the PSP at t,
M_{add} = net mass of water added,

the water level can be adjusted to make the PSP mass at the new time solve equation (170). An iterative procedure for adjusting the PSP water level, ZLVL, is outlined in the steps below.

1. Guess a new ZLVL.
2. Calculate the mass of the pool below the upper layer, BLOMAS, as

$$\text{BLOMAS} = \sum_i \rho_i(T_i)\, V_i \quad , \tag{171}$$

where T_i are the new PSP temperatures, ρ_i are the new PSP densities, and V_i are the fixed PSP nodal volumes below the upper layer. The index i includes all the nodes except those in the upper layer.

3. Calculate the new upper layer cell volumes based on the guessed ZLVL.
4. Form the new upper layer mass, UPRMAS , as

$$\text{UPRMAS} = \sum_i \rho_i(T_i)\, V_i \quad , \tag{172}$$

where the index i includes only the upper layer nodes.

5. Compare M_n to BLOMAS + UPRMAS. If

$$ERR = |M_n - BLOMAS - UPRMAS| < \varepsilon ,$$

then the new level is known. If not, then change ZLVL and go to step 2. In subroutine VOLUME, a value of $\varepsilon = 1.0$ was used (this corresponds to about one pound of water error in the entire PSP). The water level iteration typically takes about 3 iterations to converge.

F. EXTENSIONS OF THE PSP MODELS

1. Multiple Discharging T-Quenchers

The thermal convection cell model of the PSP was originally developed for only one discharging T-quencher.

Subsequently, the model was extended to include an arbitrary number of discharging T-quenchers by assuming that between any two discharging T-quenchers, the flow field is symmetric. Figure 57 illustrates the PSP model for two discharging T-quenchers, one at $\theta = 0°$, and the other at $\theta = 100°$.

For the example shown in Fig. 57, the multiple discharging T-quencher model assumes that symmetric, alternating convection cells would be created between $\theta = 0°$ and $\theta = 100°$, and between $\theta = 100°$ and $\theta = 360°$.

The multiple discharging T-quencher model is implemented in subroutine PDRIVR. The vector of T-quencher switches, NONON, is searched to determine which quenchers the user has turned on. The convection cell model is then called to solve the near field and the far field problems between the two discharging T-quencher locations. The model is called once for each T-quencher that is on.

2. PSP Bypass

The PSP models were originally designed to calculate the PSP thermal mixing from a well mixed initial condition to a point in time when the water near the T-quencher becomes saturated.

These models have been extended to permit recognition that steam might pass uncondensed into the PSP airspace when the Bay D water becomes very hot--an event termed PSP bypass. PSP bypass occurs when the Bay D water that surrounds the discharging T-quencher is at or near the saturation temperature. The near field--far field recirculation still continues; but, since the Bay D water is so hot, the steam is all or partially uncondensed.

The utility of allowing PSP bypass is that it is necessary to provide an estimate of the PSP temperature distribution after Bay D saturates. With bypass, the model can run until the containment model predicts drywell failure due to overpressurization.

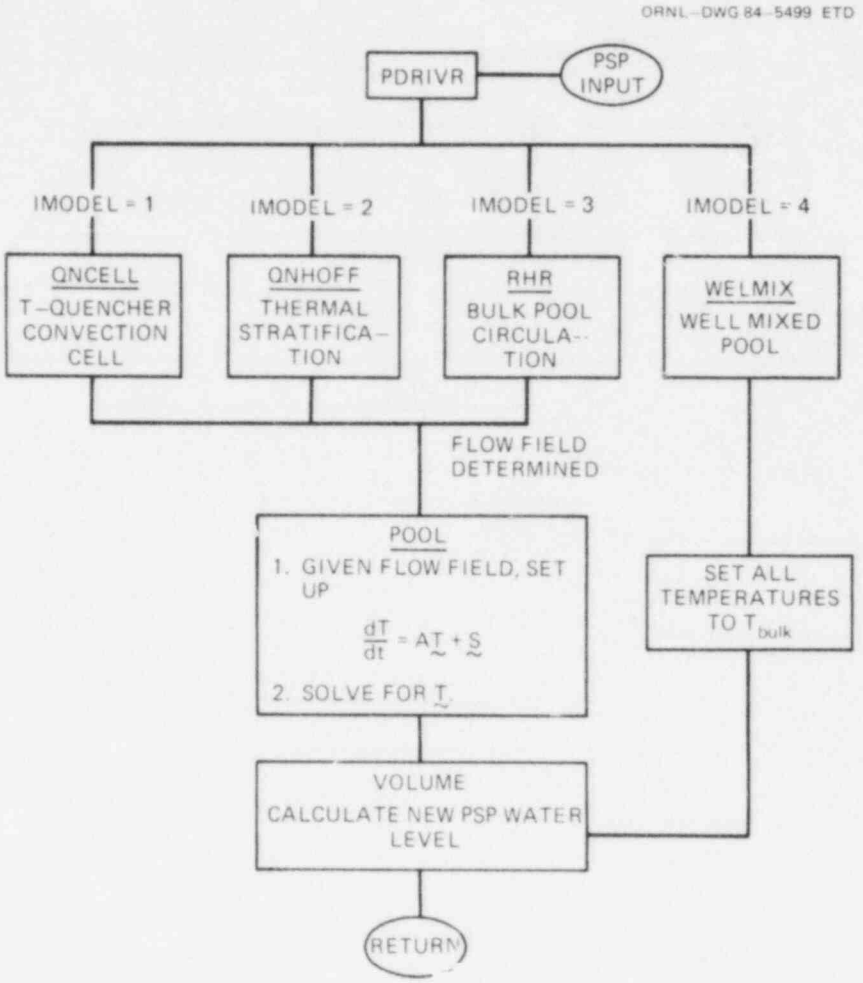

Fig. 53. PSP code organization.

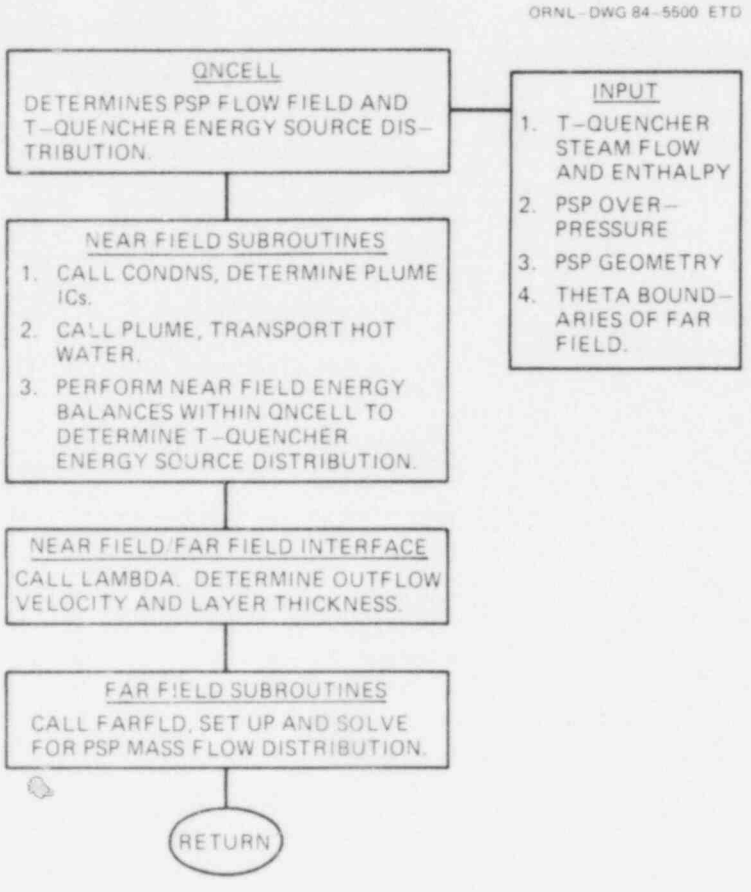

Fig. 54. QNCELL organization.

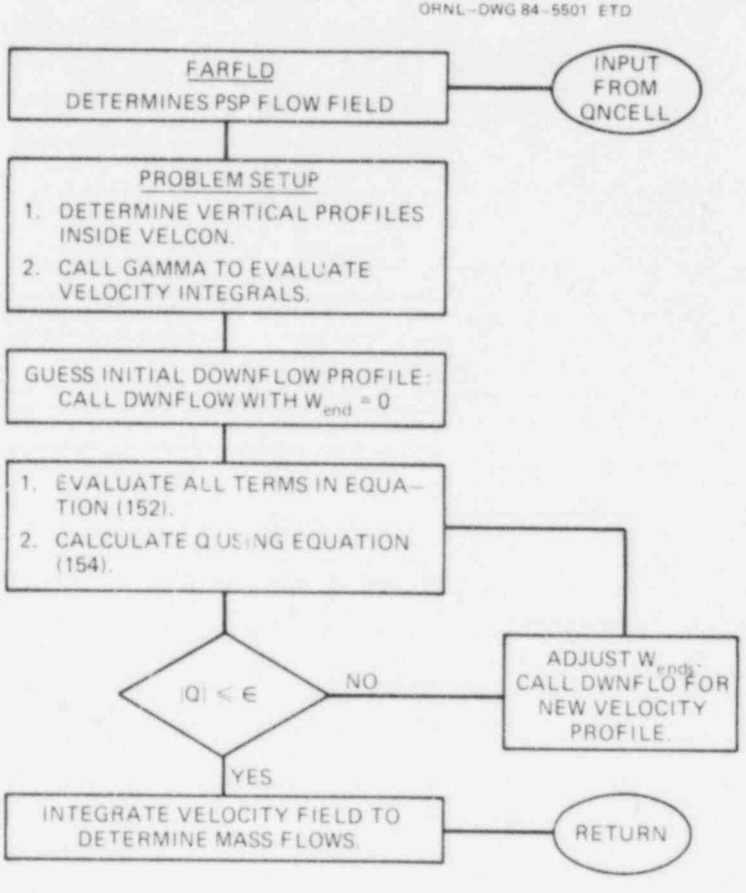

Fig. 55. FARFLD organization.

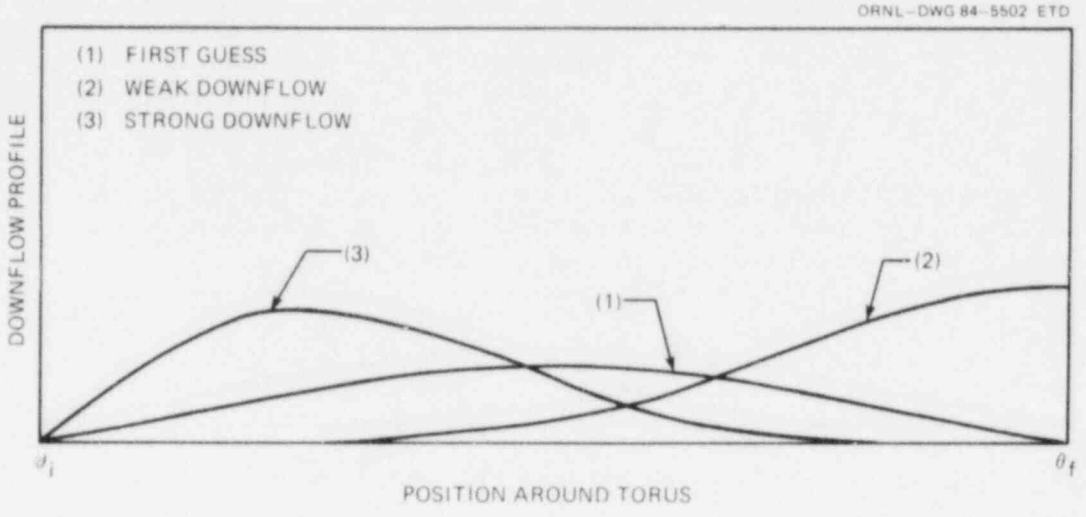

Fig. 56. Downflow profile guessing scheme.

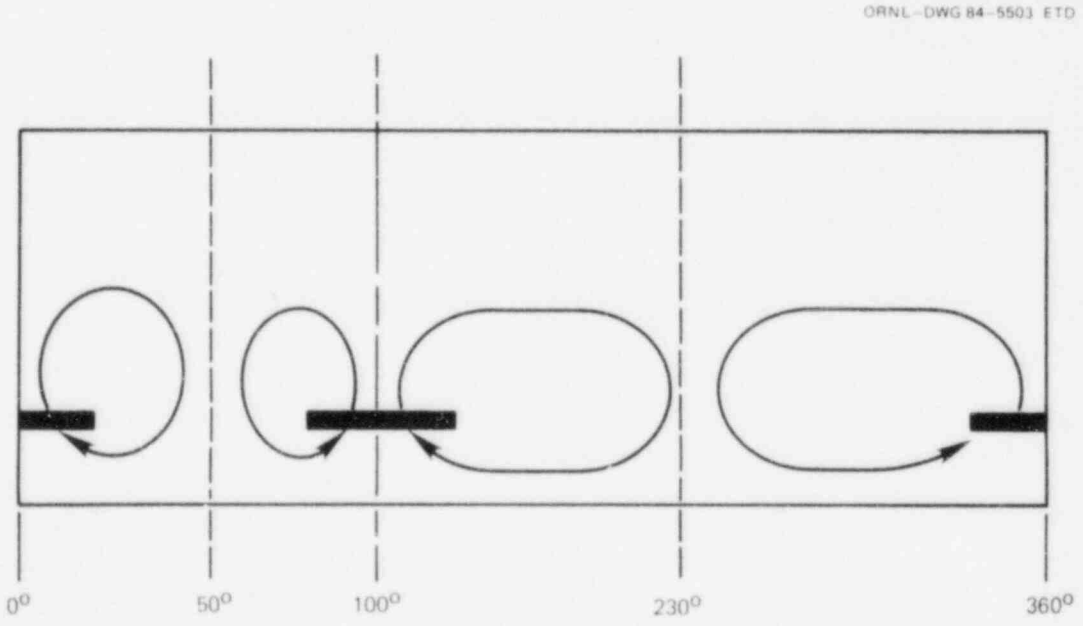

Fig. 57. Convection cells for two T-quenchers.

CHAPTER VI

OVERALL MODEL VERIFICATION: COMPARISON WITH EXPERIMENT

A. INTRODUCTION

The purpose of this chapter is to verify the PSP thermal mixing model by comparing PSP temperature distributions predicted by the model with PSP temperature distributions experimentally measured in an operating BWR suppression pool. The experimental data are the results of the Monticello T-quencher thermal mixing test[83] that was performed in November, 1978 at the Monticello Nuclear Generating Station. A description of the Monticello experiments is provided in Sect. B of this chapter.

There are four models for the flow field in the PSP. Thus, four model verifications are presented in section C. The thermal convection cell and thermal stratification models are verified by comparison to the Monticello T-quencher test that had no RHR system discharge to the pool. The bulk pool circulation model is verified by comparison to the Monticello T-quencher test that had a RHR-induced bulk circulation of the PSP. Finally, the well mixed pool model is verified by comparison to the bulk pool average temperatures measured during the Monticello test without RHR.

In section D, a comparison is made between the current PSP model and a preliminary PSP model that was developed during the early stages of this dissertation.

The sensitivity of the temperature results to various modeling parameters is presented in section E. The sensitivity analyses were performed by varying the modeling parameters and comparing the temperature results to the T-quencher discharge portion of the Monticello test without RHR discharge to the pool.

B. DESCRIPTION OF THE MONTICELLO DATA

1. T-Quencher Thermal Mixing Without RHR-Induced Pool Circulation

An in-plant test was performed by the General Electric Company to evaluate the thermal mixing characteristics of a modified T-quencher design. The modified T-quencher consisted of the standard T-quencher as shown in Fig. 3, Page 11, with 40 holes from one arm relocated to the endcap of the T-quencher.

The Monticello test procedure was to open a single SRV and discharge steam through the T-quencher to an initially stagnant PSP that was at an approximately uniform initial temperature of 52.1 F. The SRV was held open for about 11 minutes by the reactor operator, and then it was closed.

During the steam discharge, temperature data were recorded from 23 temperature sensors installed at selected locations around the PSP. The circumferential locations of the temperature sensors are shown in Fig. 58. Except for the discharge bay, there were 3 temperature sensors at each theta location. The sensors were distributed unevenly over the depth of the pool.

Following the SRV closure, the temperatures were recorded for an additional 60 minutes to measure the thermal stratification of the pool.

The transient PSP temperature distribution measured during the T-quencher discharge is shown in Fig. 59. Figure 59 is a reproduction of figure 5-9 from reference 83; however, the abcissa is presented in terms of theta instead of distance from the Bay D centerline (as the abcissa was in reference 83). Each curve in Fig. 59 is a plot of the bay average temperature versus angular position from the discharging T-quencher centerline. The 3 curves are temperature distributions at 15 seconds, 3 minutes, and 11 minutes after the SRV was opened.

The purpose of the T-quencher endcap holes was to induce a small amount of bulk pool circulation. A principal observation of the experiment was that the endcap holes did induce some pool circulation to enhance the PSP thermal mixing. However, the circulation was so small that the test results were only slightly perturbed from the temperature distribution expected to be induced by a standard T-quencher. The perturbation consists of a 5° skew of the peak of the temperature distribution from the Bay D centerline, as shown in Fig. 59. The distribution is skewed in the direction of the endcap hole discharge.

Since the endcap hole perturbation to the temperature distribution is small, the data recorded during the SRV discharge through the modified T-quencher will be used to verify the PSP model results. Only the Monticello data from the downstream half of the temperature distribution will be used to compare with the symmetric distribution predicted by the PSP model. The effects of the experimental non-symmetry are minimized by only using the downstream temperatures for model verification. Unfortunately, experimental data of this type with a standard T-quencher are not available for the Mark I geometry.

The thermal convection cell model will be compared to the experimental data from this test for the time period from 0.0 to 11.0 minutes, and the thermal stratification model will be compared to the data from 11.0 to 30.0 minutes.

2. T-Quencher Thermal Mixing With RHR-Induced Pool Circulation

A second in-plant test was performed at Monticello to evaluate the thermal mixing characteristics of the modified T-quencher with one of the RHR systems operating in the recirculation mode. During the test, the RHR system discharged water to a point located 180° from Bay D at a rate of about 10,000 gpm.

Before the test, the PSP was cooled to about 53.2 F using the RHR discharge. The SRV was then opened for about 12 minutes, and data were recorded from the 23 temperature sensors located around the PSP. Following closure of the valve, data were recorded for an additional 45 minutes.

The results of the T-quencher test with RHR circulation will be compared to temperatures predicted using the bulk pool circulation model.

C. COMPARISON OF THE PSP MODEL RESULTS TO THE MONTICELLO TEST DATA

1. SRV Discharge and Thermal Stratification

The purpose of this section is to present a comparison of the Monticello data for the 11.0 minutes of T-quencher discharge to the PSP thermal mixing results using the thermal convection cell flow model for 11.0 minutes. In addition, the thermal stratification data that were recorded immediately after the SRV was closed will be compared to the PSP model results using the thermal stratification flow model from 11.0 minutes to 30.0 minutes.

The Monticello comparisons will be presented in four groups. Each group consists of three plots. The four groups correspond to the four positions around the circumference of the Monticello PSP where temperature sensors were located. These locations were designated as Monticello Bays D,C,B, and H. The three plots in each group correspond to the three z levels at which the temperature sensors were located.

The PSP model was run using an input torus major radius of 49.0 Ft, and a minor radius of 13.83 Ft. The initial pool level and temperature were 10.95 Ft and 52.1 F, respectively. The steam flow and enthalpy were assumed constant over the 11.0 minutes of steam discharge; 208.5 Lbm/s of steam was input with a stagnation enthalpy of 1193.6 Btu/Lbm. A constant pool overpressure of 15.0 psia was input, and evaporation from the PSP surface was neglected.

The model input parameters for the Monticello run are contained in the sample driver program and input data file presented in Appendix D.

The model was run with a noding that consisted of eight levels in the z-direction and one node per bay of the PSP in the theta direction. This noding yields a total of 128 nodes for the Monticello PSP model. A far field friction factor of 0.10 was used. The ODEs for the nodal temperatures were solved using LSODE[90], with the Adams predictor-corrector method chosen for a solution scheme, and an absolute error control parameter of 1.0×10^{-6}. The integration time step in LSODE is selected automatically based on this absolute error control parameter. The time step between LSODE edits (which is the time step between changes in the flow field) was 5.0 seconds.

The Monticello discharge bay (Bay D) model predictions and experimental data are shown in Figs. 60, 61, and 62.

Figure 60 is a comparison of the upper level experimental temperature in Bay D to the corresponding node in the PSP model. The maximum error between model and experiment for this location was about 33%, and occurred at 1.0 minute after the SRV was opened. As shown in Fig. 60, the model prediction matched the data very closely from about 4 to 30 minutes with a maximum error of 6% . The thermal stratification model performed very well at this location: it closely predicted the shape

and amplitude of the temperature response after SRV closure. The thermal stratification model predicted a layer average that was within 1% of the experimental surface temperature over the time interval from 15 to 30 minutes.

Figures 61 and 62 are comparisons of the experimental temperatures to the PSP model predictions for the middle and lower level sensor locations in Bay D, respectively. The thermal convection cell model performed poorly for these locations with errors of between 30% and 40% during most of the T-quencher discharge. However, the thermal stratification model performed well, correctly predicting the local temperatures late in the transient to within 2% .

A possible explanation for the large difference between the predicted and the experimental temperatures in the lower portions of Bay D is that the Monticello temperature sensors were located directly in the T-quencher plumes. The point sensors would thus record only the high plume temperatures. Since the PSP model predicts only layer average temperatures, the high plume temperatures would be lumped with the adjacent cold water temperatures in Bay D to produce a layer average that is much lower than the point sensor.

The Monticello Bay C model predictions and experimental data are shown in Figs. 63, 64, and 65. Bay C is located 45° from Bay D.

Figure 63 is a comparison of the Bay C upper level experimental temperature to the PSP model prediction. Both the convection cell and thermal stratification models closely predicted the experimental data for this location, with a maximum error of 2% over the time interval from 5 to 30 minutes. A maximum error of 14% occurred early in the transient at 3 minutes after the SRV opened.

Figures 64 and 65 are comparisons of the experimental temperatures to the PSP model predictions for the middle and lower level sensor locations in Bay C, respectively. As shown in Fig. 64, the thermal convection cell model predictions for the middle level are quite poor, with about 50% error during the time between 5 and 11 minutes. However, the thermal stratification model correctly predicted the middle sensor data from 15 to 30 minutes with an error of between 5% and 10% over that time interval.

Both the thermal convection cell and thermal stratification model predictions for the lower sensor location in Bay C are reasonable estimates of the lower sensor temperature response, as shown in Fig. 65. Both models predicted temperatures for these locations to within 15% over the entire transient.

The Monticello Bay B model predictions and experimental data are shown in Figs. 66, 67, and 68. Bay B is located 90° from Bay D.

Figure 66 is a comparison of the Bay B upper level experimental temperatures to the PSP model prediction. Both the convection cell and thermal stratification models predicted the data for this location to within 2% over the time interval from 7 to 30 minutes.

Figures 67 and 68 are comparisons of the experimental temperatures to the PSP model predictions for the middle and lower sensor locations in Bay B, respectively. As shown in Fig. 67, the thermal convection

cell model did a much better job of predicting the middle layer temperatures for this location than it did for Bay C. The predicted temperatures are generally closer to the experimental data during the steam discharge.

The Monticello Bay H model predictions and experimental data are shown in Figs. 69, 70, and 71. Bay H is located 180° from Bay D.

Figure 69 is a comparison of the upper level experimental temperatures in Bay H to the PSP model prediction. The convection cell model performed well for this location by providing an estimate of the local temperature response that was within a maximum error of about 20%. The convection cell model did a good job of predicting the Bay H time constant: at about 5 minutes, the Bay H sensors responded to the steam discharge with a rapid temperature increase. The PSP model correctly predicted this effect, as shown in Fig. 69.

The convection cell and thermal stratification models did a good job of predicting the Bay H transient temperatures for the middle sensor location, with errors of less than 5% , as shown in Fig. 70. The models performed poorly for the lower location, as shown in Fig. 71.

2. SRV Discharge With RHR System Pool Circulation

The purpose of this section is to present a comparison of the data from the Monticello T-quencher thermal mixing test with RHR-induced pool circulation to the PSP model predictions using the bulk pool circulation flow model.

The bulk pool circulation model was run for comparison to the Monticello data using almost the same input data and geometry information as the T-quencher thermal convection cell runs. Only the initial PSP temperature and T-quencher discharge time were different. These input parameters were 53.2 F, and 12.0 minutes, respectively.

Only one of the four RHR systems was discharging water to the PSP during the test. Thus, a relatively low bulk pool circulation velocity of 1.0 Ft/s was input to the model.

Figure 72 is a comparison of the PSP bay average temperature results to the Monticello data at 3 minutes after the SRV was opened. Overall, the bulk pool circulation model did a relatively poor job of predicting the local bay average temperatures at 3 minutes. An error of about 17% occurred in the Bay D predicted temperature at this point in time.

Figures 73 and 74 are comparisons of the bulk pool circulation model results to the Monticello data at 7 and 12 minutes, respectively. As shown by these figures, the model did a good job of predicting the experimental data at times farther into the transient. The model predictions for the discharge bay sensors located in bays C, B, and H were predicted to within a maximum error of about 6% for times greater than 7 minutes. The model predictions at 7 and 12 minutes were worse for the upstream half of the PSP, as shown in Figs. 73 and 74. The maximum error between model and experiment was about 20%; this error occurred at a theta location of about -90° for times greater than 7 minutes.

3. Well Mixed Pool

The well mixed pool model was verified by running the model for the Monticello T-quencher test without RHR circulation, and comparing the predicted bulk pool temperatures to the experimentally measured bulk pool temperatures.

A comparison of the measured and calculated bulk pool temperatures is shown in Fig. 75. The well mixed pool model closely predicts the measured bulk pool temperatures throughout the T-quencher discharge indicating that the Monticello bulk pool temperature measurements are correct.

D. COMPARISON OF THE PSP MODEL TO OTHER MODELS

At the beginning of this dissertation effort, no model existed in the open literature for calculating detailed PSP thermal mixing. Since then, results from a preliminary version of the PSP model presented in Chapt. 4 have been published.[92]

The preliminary PSP model consisted of essentially the same two dimensional, lumped treatment of the temperature calculations presented in this dissertation. In addition, the same thermal stratification model was used. However, the thermal convection cell model that is presented here was not in existence. In the preliminary PSP model, the flow field during T-quencher discharge was "specified" based on an assumption of uniform downflow in the far field and a near field / far field exchange flow that consisted of just enough cold water from the lower layers of the PSP to condense the steam.

Although the preliminary model for the PSP flow was relatively crude, and relied mostly on engineering judgment, it produced a reasonable estimate of the PSP thermal mixing.

A comparison of the results of the preliminary PSP model to the results of the current PSP model is presented in Fig. 76. Figure 76 is a plot of the Monticello Bay C surface temperature and the two PSP model predictions for the T-quencher test without RHR circulation.

As shown in Fig. 76, the current model of the PSP flow (which is based on a detailed calculation of the flow instead of engineering judgment) produces a better estimate of the Monticello surface temperatures.

E. SENSITIVITY OF THE TEMPERATURE RESULTS TO VARIOUS MODELING PARAMETERS

1. Far Field Interfacial Friction Factor

The sensitivity of the PSP model temperature results to the far field friction factor, K, was investigated by varying K from a best estimate of K = 0.10 and comparing the resultant temperature response to the Monticello T-quencher test without RHR. An objective of the

friction factor study was to determine if an optimum K exists for use in the PSP model.*

The friction factor was varied over the range from K = 0.08 to K = 0.15. This range of K was identified by a study of the literature on density current flow. For each K, the thermal convection cell model was run for 11.0 minutes and the results were compared to the Monticello data. The model was run with a fixed time step of 5.0 seconds, and a noding that consisted of eight layers in the z-direction and one node per bay in the theta direction.

The results of the friction factor study are summarized by two plots. The first plot is a comparison of the Monticello Bay H surface temperature to the corresponding nodal response calculated with the PSP model. The first plot is shown in Fig. 77. The second plot is a comparison of the Monticello Bay B middle temperature to the corresponding nodal response calculated with the PSP model. The second plot is shown in Fig. 78.

The results presented in Fig. 77 can be considered an indication of how sensitive the temperature of the PSP regions located far away from the discharge bay are to the interfacial friction factor. As shown in Fig. 77, the temperature results indicated a predictably strong sensitivity to K. For large K (K=0.15), the water that is moving out from the discharge bay is dragged downward by the interfacial friction into the regions of the PSP near Bay D. As a result, little hot water reaches Bay H, and the resultant surface temperature increase is small relative to the Monticello Bay H temperature. For small K (K=0.08), less fluid is dragged down in the regions of the PSP near Bay D. More hot water reaches Bay H, and the surface temperature responds with a large and rapid temperature increase.

The results presented in Fig. 78 can be considered an indication of how sensitive the interior regions of the PSP are to the interfacial friction factor. For large K (K=0.15), much of the hot water that is moving out across the surface of the PSP is dragged down near Bay D. The strong downflow yields a temperature response that is comparable to the Monticello temperature at this location. For small K (K=0.08), less energy is deposited close to Bay D, and the resultant temperature increase is small compared to the Monticello response for that location.

The optimum number to use for K is about K = 0.10 . A value of K larger than 0.10 produced Bay B results that were better, however, the Bay H results were poor. A value of K smaller than 0.10 produced better Bay H results, however, the Bay B results were poor.

The value of K that was chosen as a best estimate turned out to be the optimum value of K in terms of providing the best overall agreement to the Monticello experimental data.

---

*The best estimate of K was determined by an engineering judgement of the various K's reported in the density current literature.[84-89] Most of the K's were for rectangular cross sections. Some of the K's were for river flow and others were for the flow in lakes and oceans. None of the K's was for suppression pools (a half-filled torus with internal flow obstructions).

2. Number of Nodes in the Vertical Direction

The sensitivity of the PSP model temperature results to the number of nodes in the vertical direction was investigated by varying the number of equally spaced layers in the z-direction and comparing the resultant temperature response to the Monticello surface temperature.

The number of levels (NLVL) that were distributed over the PSP depth was varied over the range from NLVL = 2 to NLVL = 20 . For each NLVL, the thermal convection cell model was run for 11.0 minutes, and the model results were compared to the Monticello data from the T-quencher test without RHR. The model was run with a fixed time step of 5.0 seconds, a fixed noding in the theta direction of one node per bay, and a fixed K of 0.10 .

The results of the layer study are shown in Fig. 79, which is a plot of the PSP surface average temperature at the time of SRV closure versus the number of layers in the z-direction. Each point on the curve in Fig. 79 was produced by forming a numerical average of the 16 surface nodal temperatures at time = 660.0 seconds. The data in Fig. 79 show that as the number of levels is increased, the surface temperature predicted by the PSP model asymptotically approaches the measured surface temperature from below. This trend is correct, because with a small number of layers, cold water from below is averaged with the hot water from above the centerline of each node to produce a layer average temperature that is lower than the measured surface temperature.

3. Number of Nodes in the Circumferential Direction

The sensitivity of the PSP temperature results to the number of nodes in the theta direction was investigated by doubling the number of theta nodes and comparing the temperature response predicted by the PSP model to the temperatures measured during the Monticello test without RHR.

The PSP model was run with the number of theta nodes, NTHETA, equal to 16 (1 node per bay) and with NTHETA equal to 32 (2 nodes per bay). For each run, the number of levels in the model was fixed at 8, the time step was 5.0 seconds, and K was 0.10 . The PSP model was run for 11.0 minutes, and the surface temperature profiles at the end of the run were compared to the Monticello surface temperatures at that time.

A comparison of the Monticello surface temperature profile at 660.0 seconds to the PSP model prediction at that time is shown in Fig. 80 for the 1 node per bay and the 2 node per bay cases. As shown in Fig. 80, there is very little difference between the profiles predicted with 1 or 2 nodes per bay. The 2 node per bay case merely provides more detail between the 1 node per bay temperatures. Thus, 1 node per bay of the PSP is sufficient to provide enough detail to model the energy transport in the theta direction.

4. Time Step

The sensitivity of the PSP model temperature results to the time step between flow field calculations was investigated by varying the

time step and comparing the resultant temperature distributions to the Monticello data from the T-quencher test without RHR.

The time step was varied over the range from 0.5 to 20.0 seconds. For each run in the time step study, the thermal convection cell model was run for 11.0 minutes, and the transient temperatures predicted by the PSP model were compared to the Monticello data. The model was run with a fixed noding of eight levels in the z-direction and one node per bay in the theta direction. A friction factor of K = 0.10 was used for all the runs.

The temperatures predicted by the PSP model showed an insensitivity to the time step over the time step range from 0.5 to 20.0 seconds. The results of the study are represented by the data presented in table 2. Table 2 contains the percent error of the Bay H surface node at different points in time as a function of the time step between temperature calculations. The change in the percent errors observed by moving vertically down any column in table 2 is very small; a maximum of 0.05% difference between Δt = 20.0 seconds and Δt = 0.5 seconds occurred at time = 8 minutes.

Table 2. Bay H local temperature percent errors at various times as a function of the time step

Time step (sec)	Minutes				
	t = 4	t = 6	t = 8	t = 10	t = 11
20	-2.51	9.63	17.05	16.35	16.99
10	-2.47	9.67	17.08	16.36	17.00
5	-2.47	9.69	17.08	16.36	17.00
2	-2.47	9.70	17.09	16.37	17.00
1	-2.48	9.70	17.10	16.37	17.00
0.5	-2.48	9.70	17.10	16.38	17.00

The other nodal temperatures predicted by the model responded similar to the Bay H surface temperature that is presented in table 2. There were very small changes in the predicted temperatures due to a change in the time step.

The insensitivity of the temperature results to the time step size is an indication that the quasistatic treatment of the PSP is a good assumption. If the quasistatic assumption was not appropriate, then lowering the time step size would have shown a change in the temperature distribution due to the nonlinear feedback between the fluid flow and the thermodynamics. In the quasistatic assumption, the fluid velocities are treated as constants over the time step of the temperature calculations. This permits two simplifications: the energy equation for the

water is decoupled from the momentum equations, and the fluid dynamics is rendered a steady state problem instead of a transient problem.

The slow change of the PSP velocities is characterized by a plot of the average near field outflow velocity versus time, as shown in Fig. 81. The near field outflow velocity is the velocity that is produced by the surface spreading part of the near field theory; it forms the velocity boundary condition between the near field and the far field.

The near field outflow velocities from four of the time step study calculations (time steps of 0.5, 1.0, 5.0, and 10.0 seconds) are presented in Fig. 81. From about 1.0 minute after the SRV was opened until the SRV was closed at 11.0 minutes, the near field outflow velocity changed very slowly from 0.42 Ft/s to 0.35 Ft/s, respectively. During that time period, the quasistatic assumption is considered a good model of the PSP fluid dynamics. The flow field is determined by the temperature distribution, and the temperature distribution slowly changes due to the energy carried by the flow.

From 0.0 to 1.0 minutes, the plots in figure 81 show that for time steps larger than about 5.0 seconds, the quasistatic assumption is a poor representation of the PSP flow field. Thus, for transients in which SRVs are rapidly cycled on and off, the PSP model predictions may be inaccurate for large time steps due to the approximate nature of the fluid dynamics.

F. DISCUSSION OF THE PSP MODEL PERFORMANCE

In assessing whether the PSP model is "good" or "bad", the very difficult model verification procedure must be considered: the average temperatures predicted for large nodal volumes of water were compared to experimental data recorded at specific points in the domain. Large errors between the point data and the nodal averages are to be expected.

A large error (~20%) between the point data and the nodal average temperature does not necessarily mean the nodal temperature is wrong; it could mean that the nodal average temperature is not representative of all temperatures at a point in that zone. This was the case with the lower layer Bay D nodal temperatures shown in Figs. 61 and 62: the point data compared poorly with the nodal average, however, the point data were affected by the plumes, which is a three dimensional effect not treated in the two dimensional model of the PSP.

Overall, the thermal convection cell model did a good job of predicting PSP surface temperatures. Thus, the PSP model is well suited for the task of providing the input to a drywell pressurization calculation. In addition, the model correctly predicted the strength to the far field convection cell as evidenced by the correct time delay in the response of the Bay H nodes. Thus, the model is well suited for the task of analyzing the overall thermal mixing in the PSP, i.e., the model can predict how the entire PSP interacts with the discharge bay when an isolated T-quencher is discharging. The model did a relatively poor job of predicting the temperatures of the nodes in the interior of the PSP. In addition, the model performed poorly for some of the nodes located in the lower layers of the PSP. Thus, the model may not be well

suited for the task of verifying or predicting the response of point temperatures in the PSP.

Overall, the thermal stratification model predicted the layer average temperatures very well. The predicted layer average was within 2% of the experimental data for the surface temperatures, and within 5% for many of the middle and lower layer sensor locations.

The bulk pool circulation model predicted the bay average temperatures recorded during the RHR circulation test quite well. The shape of the curve agrees with the experimental data, and the Bay D average temperature (which is often the effect of interest in this type of transient) was closely predicted.

The well mixed pool model correctly predicted the bulk pool temperatures measured during the Monticello test, thus verifying this model.

A typical run of the PSP code (with 128 nodes and using the thermal convection cell model, which is the most detailed model) took about 0.3 seconds of CPU time per time step to run on an IBM-3033. Thus, the models performed well in terms of computational costs.

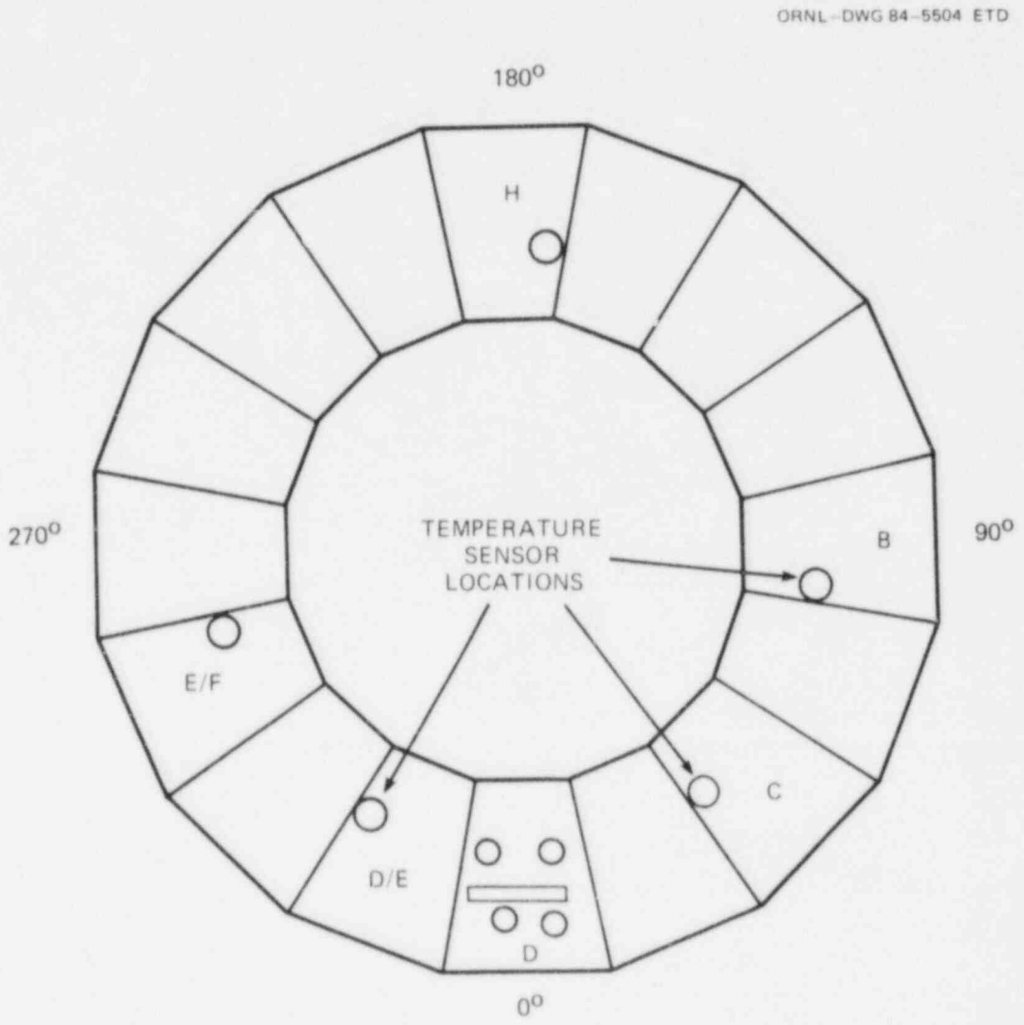

Fig. 58. Temperature sensor locations.

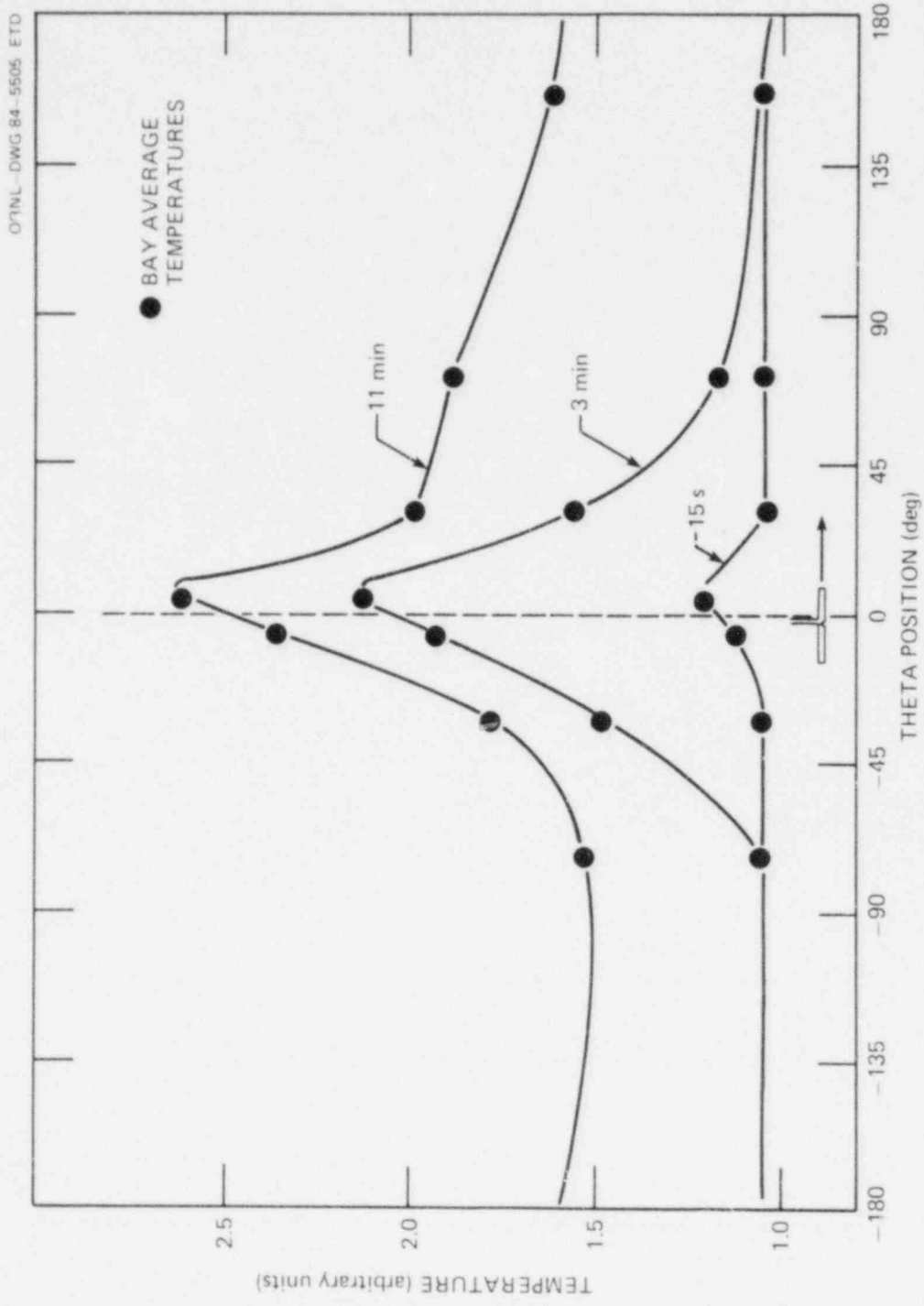

Fig. 59. Bay average temperature distributions.

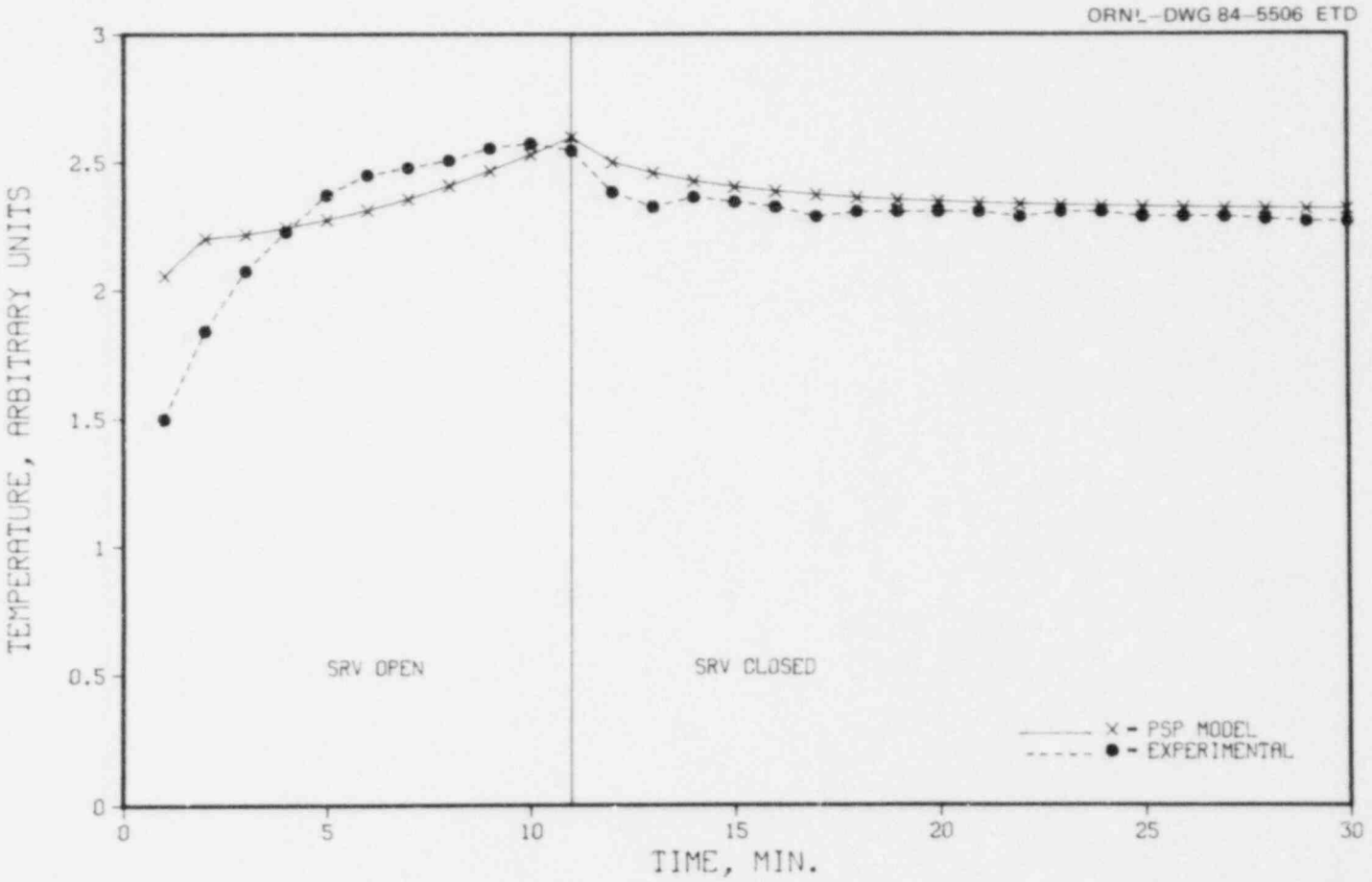

Fig. 60. Bay D upper sensor temperatures.

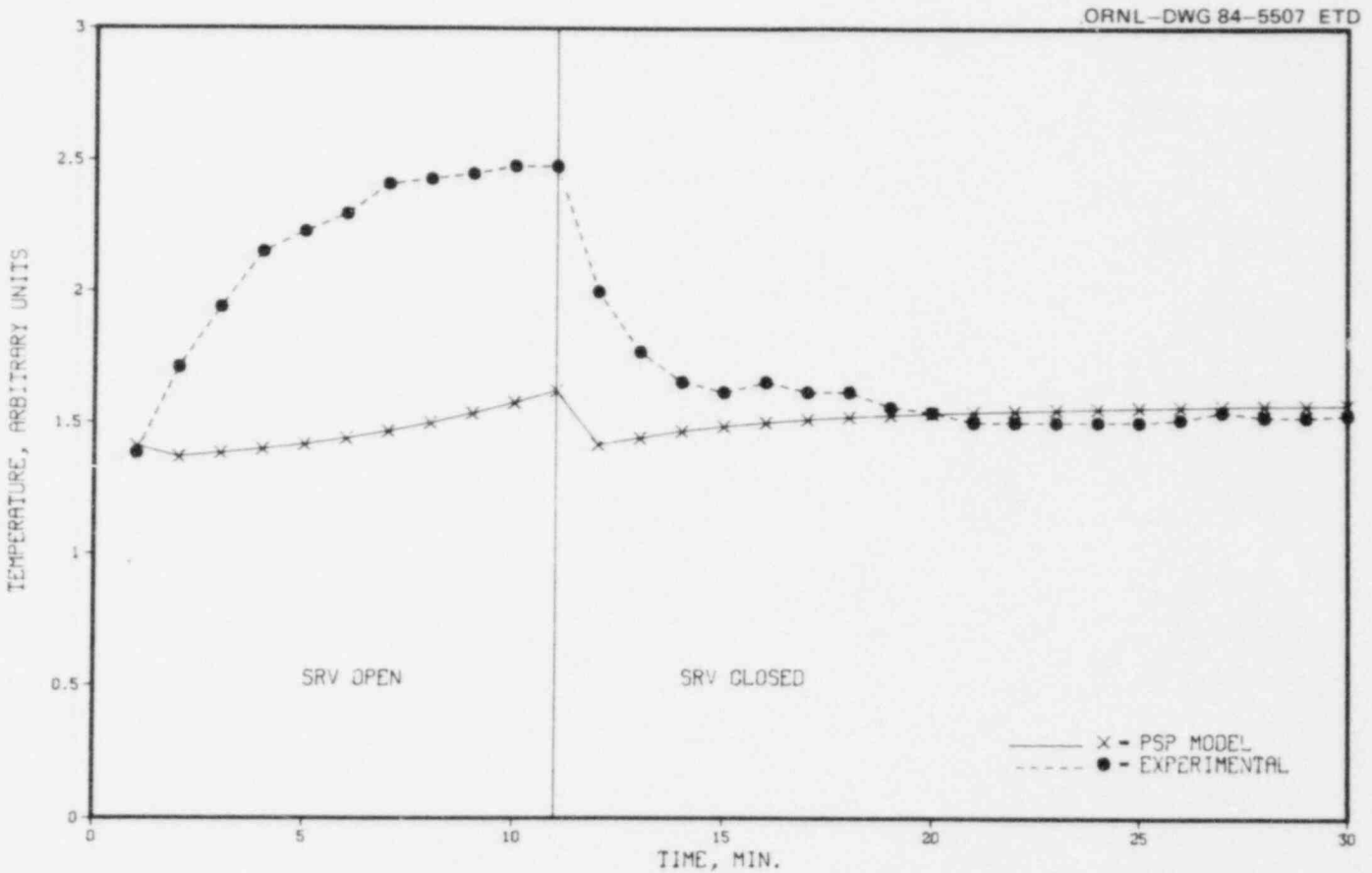

Fig. 61. Bay D middle sensor temperatures.

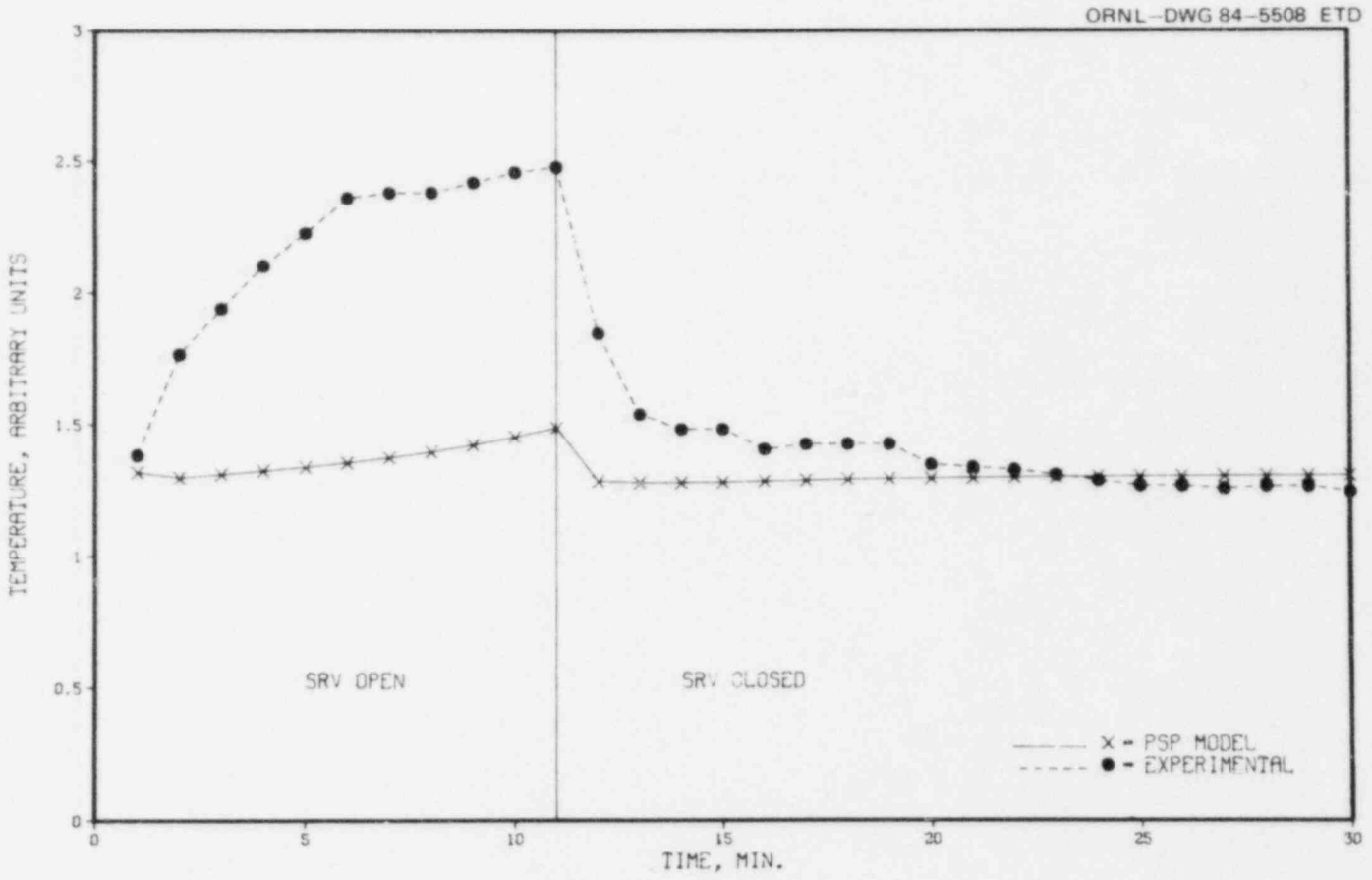

Fig. 62. Bay D lower sensor temperatures.

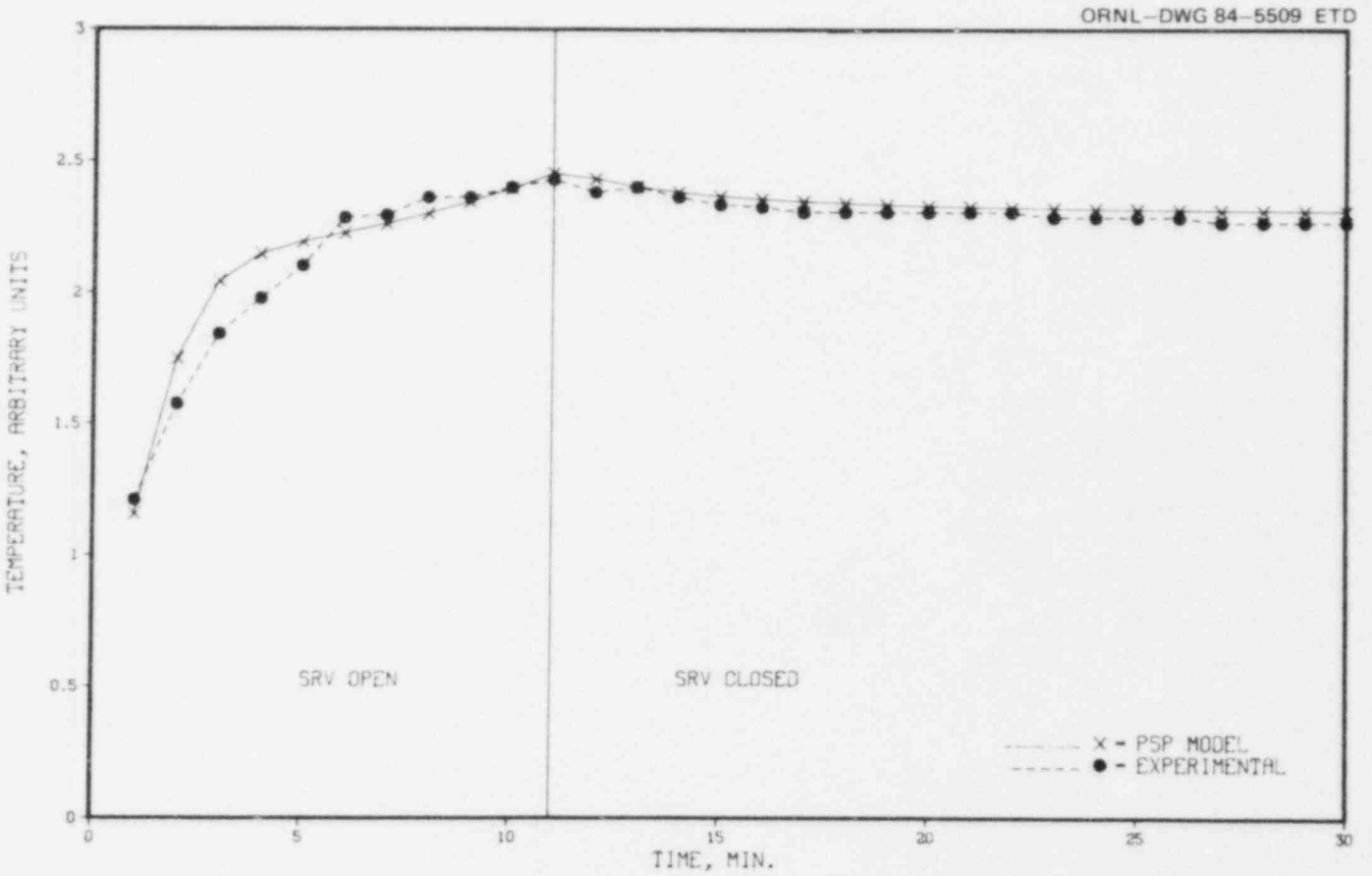

Fig. 63. Bay C upper sensor temperatures.

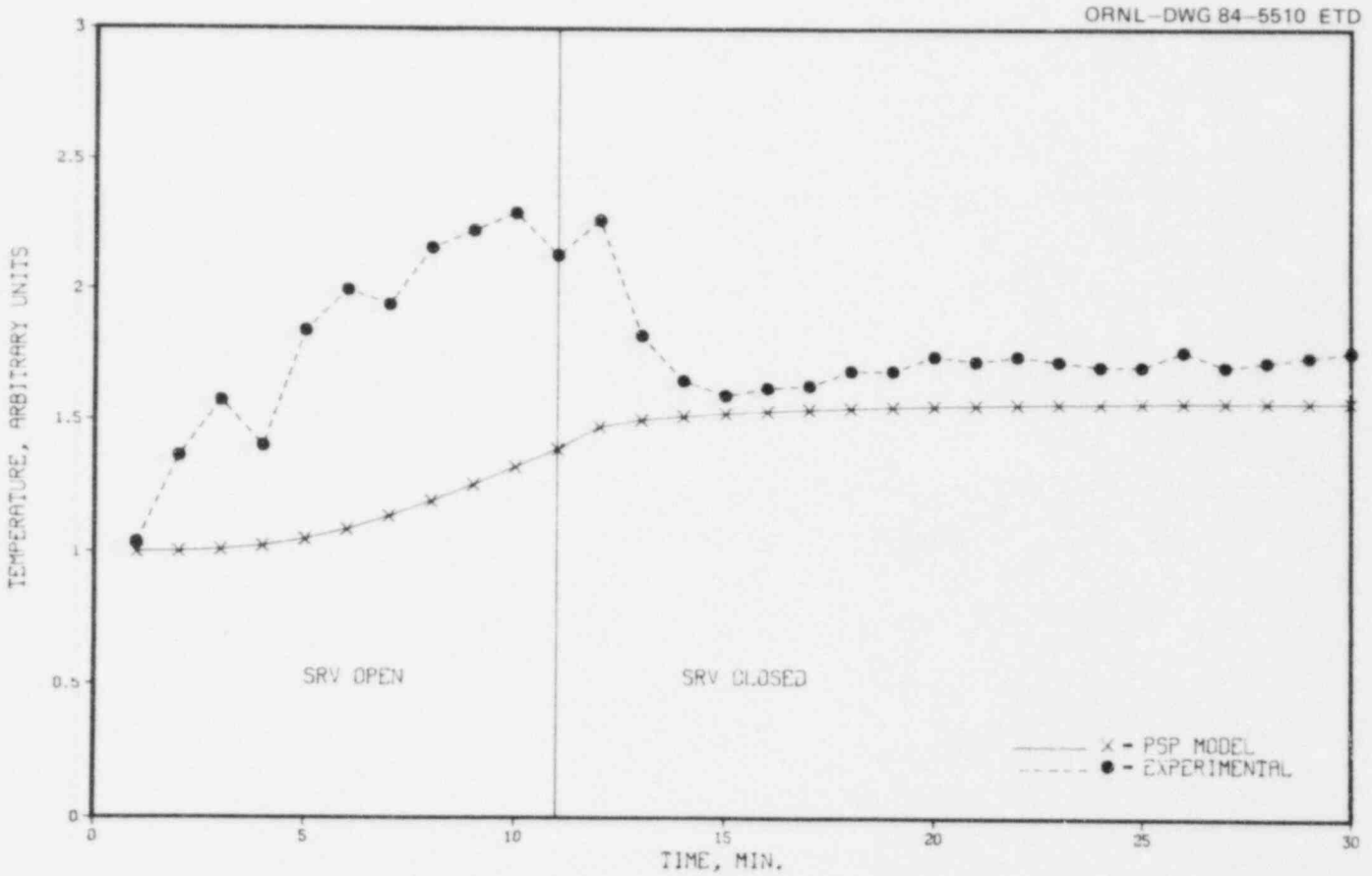

Fig. 64. Bay C middle sensor temperatures.

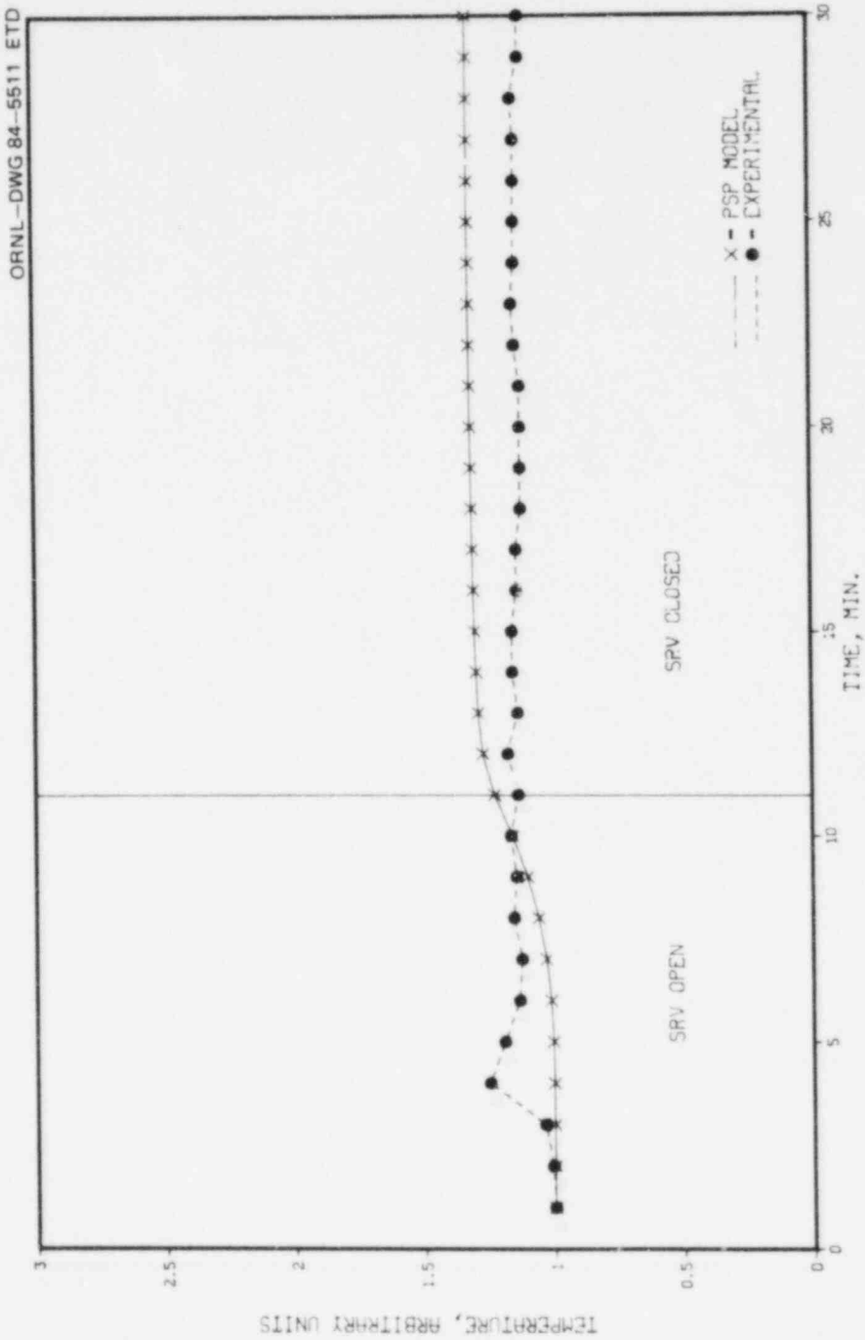

Fig. 65. Bay C lower sensor temperatures.

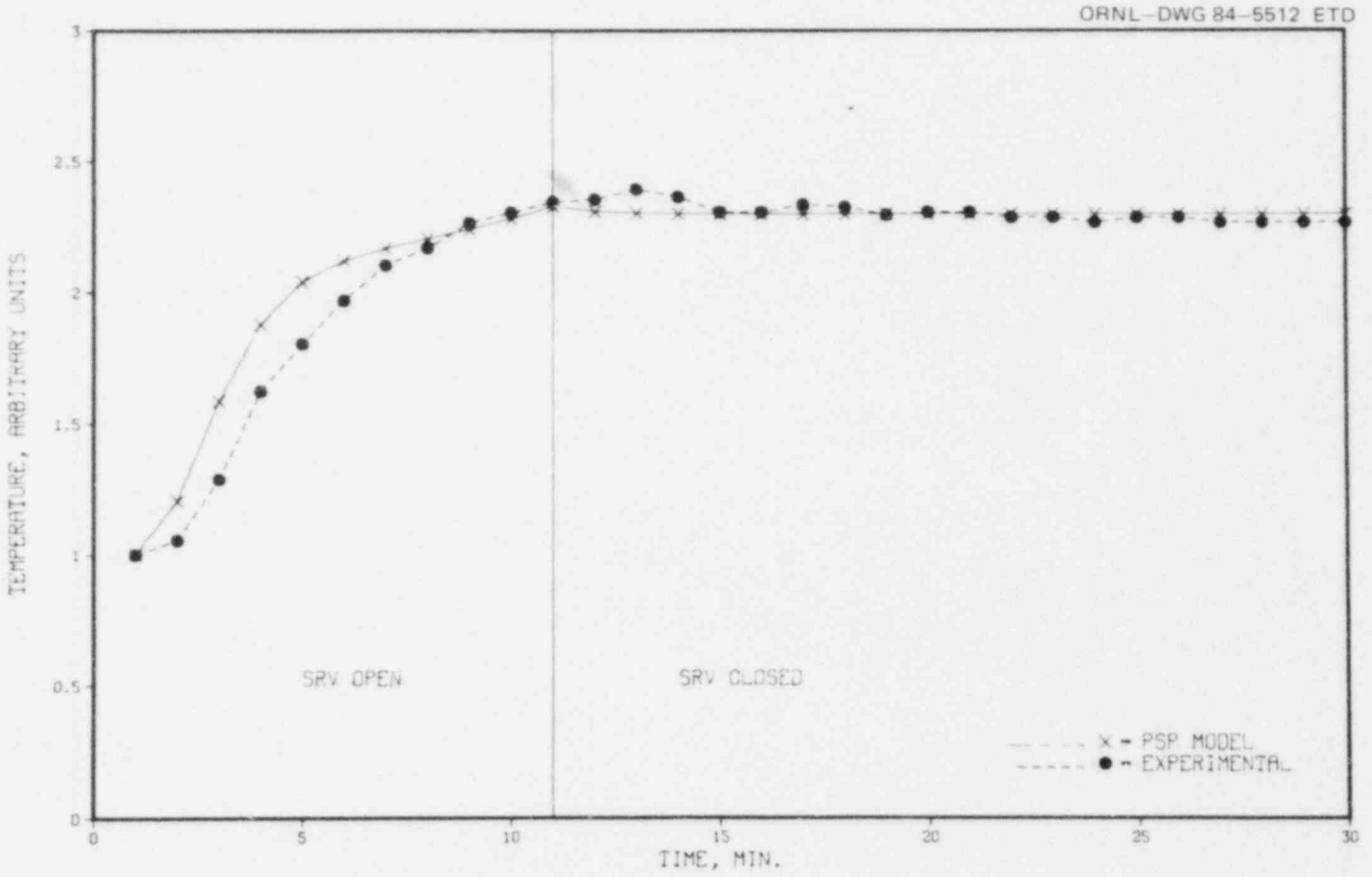

Fig. 66. Bay B upper sensor temperatures.

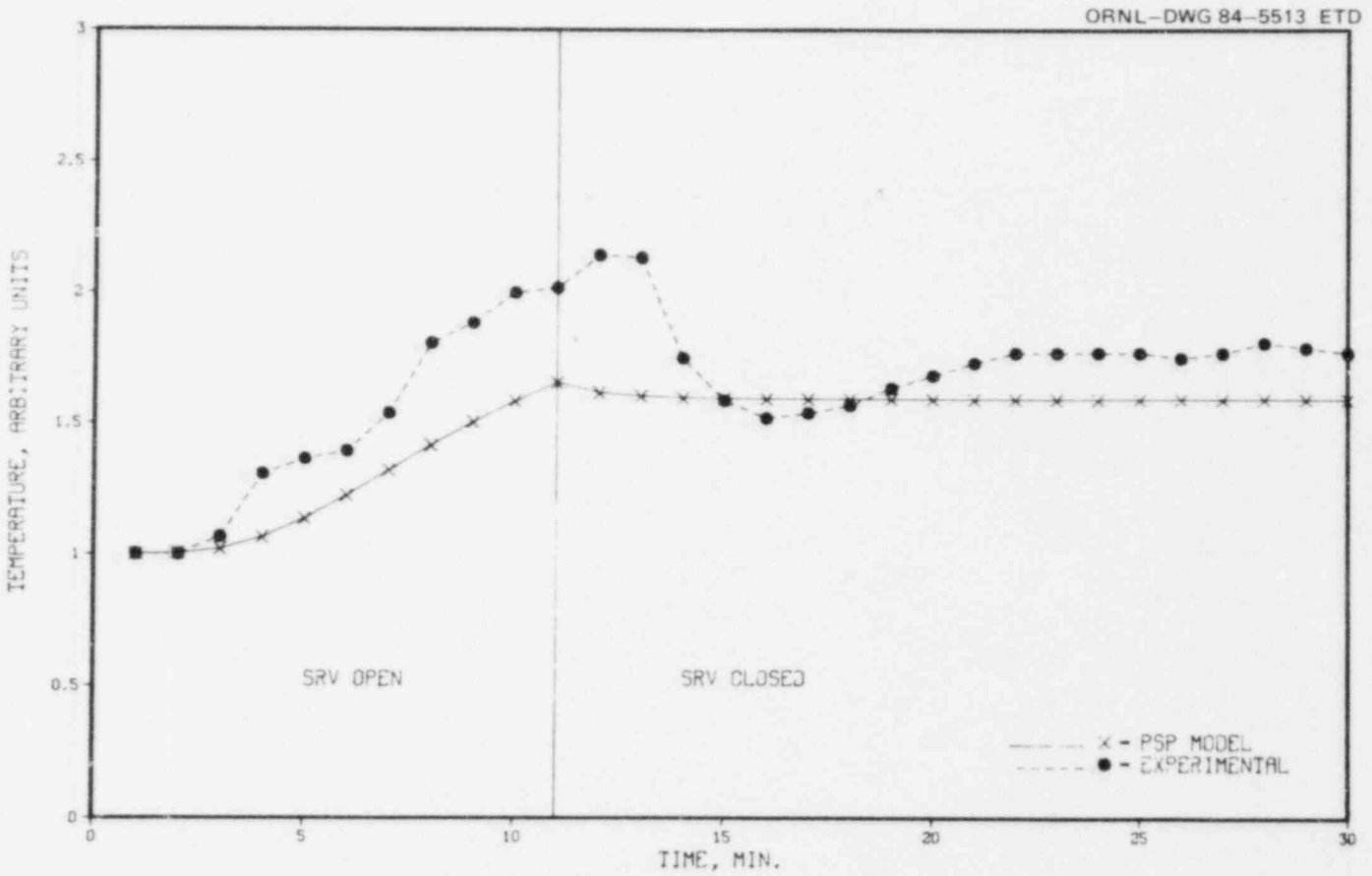

Fig. 67. Bay B middle sensor temperatures.

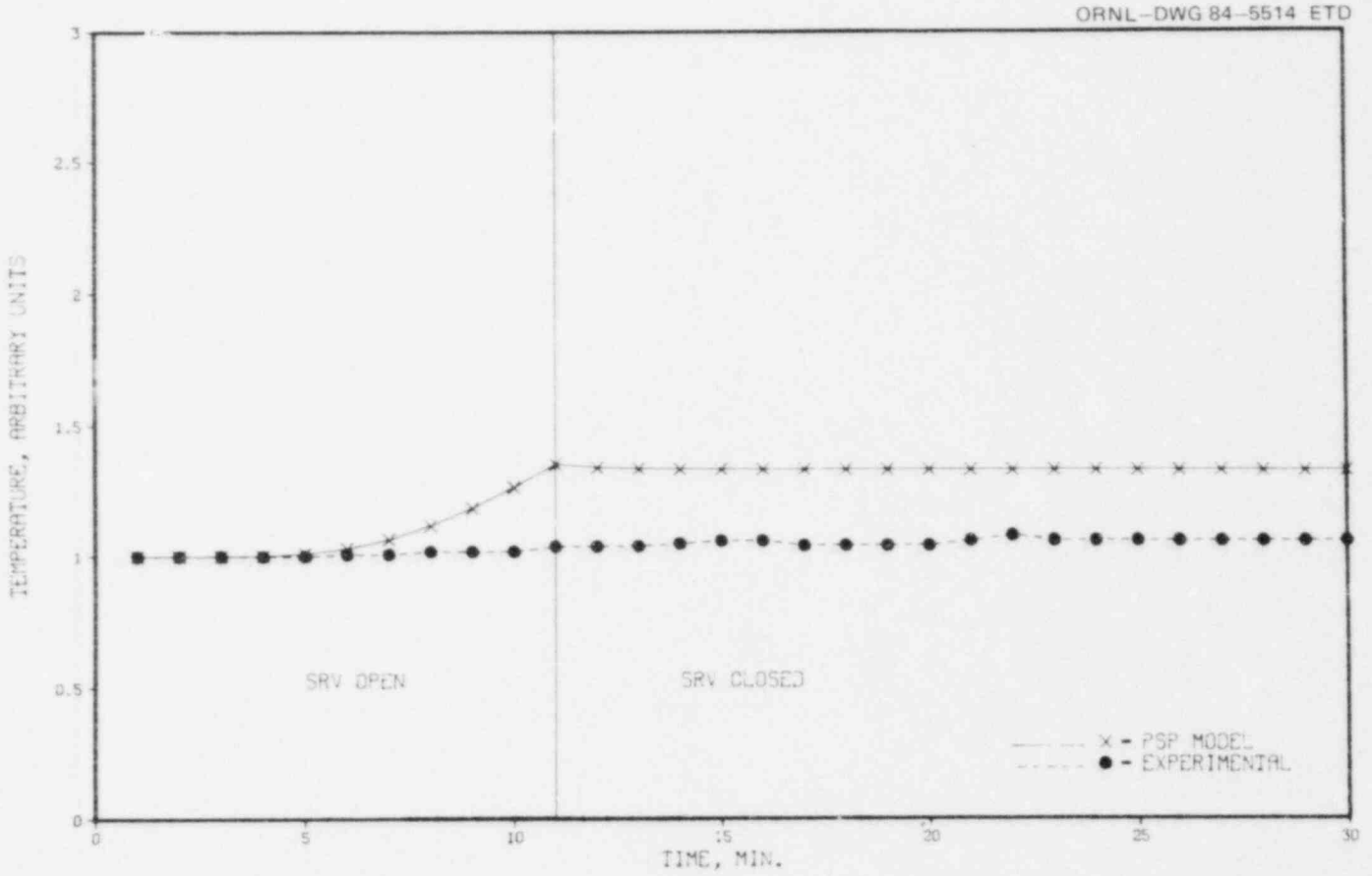

Fig. 68. Bay B lower sensor temperatures.

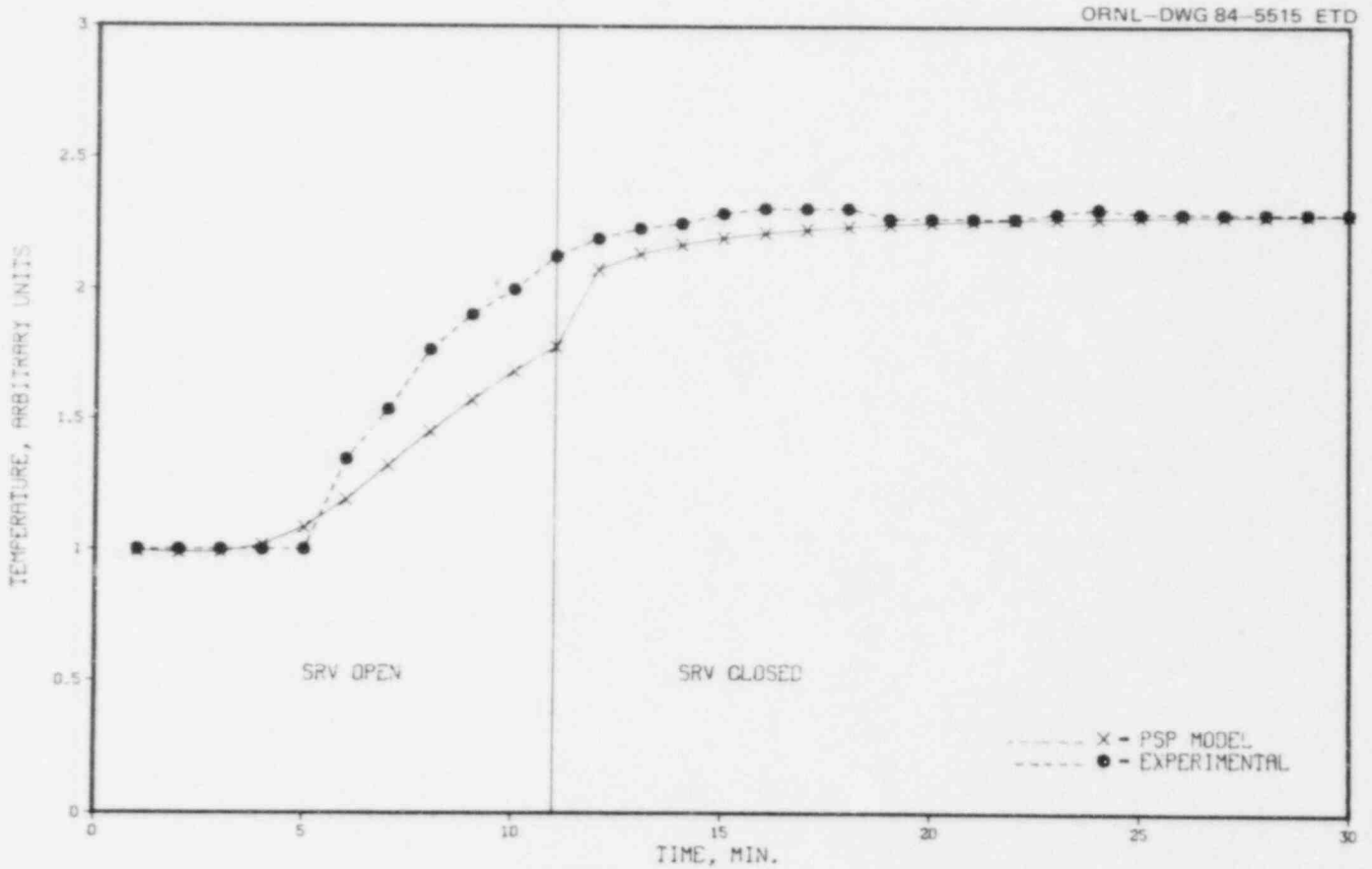

Fig. 69. Bay H upper sensor temperatures.

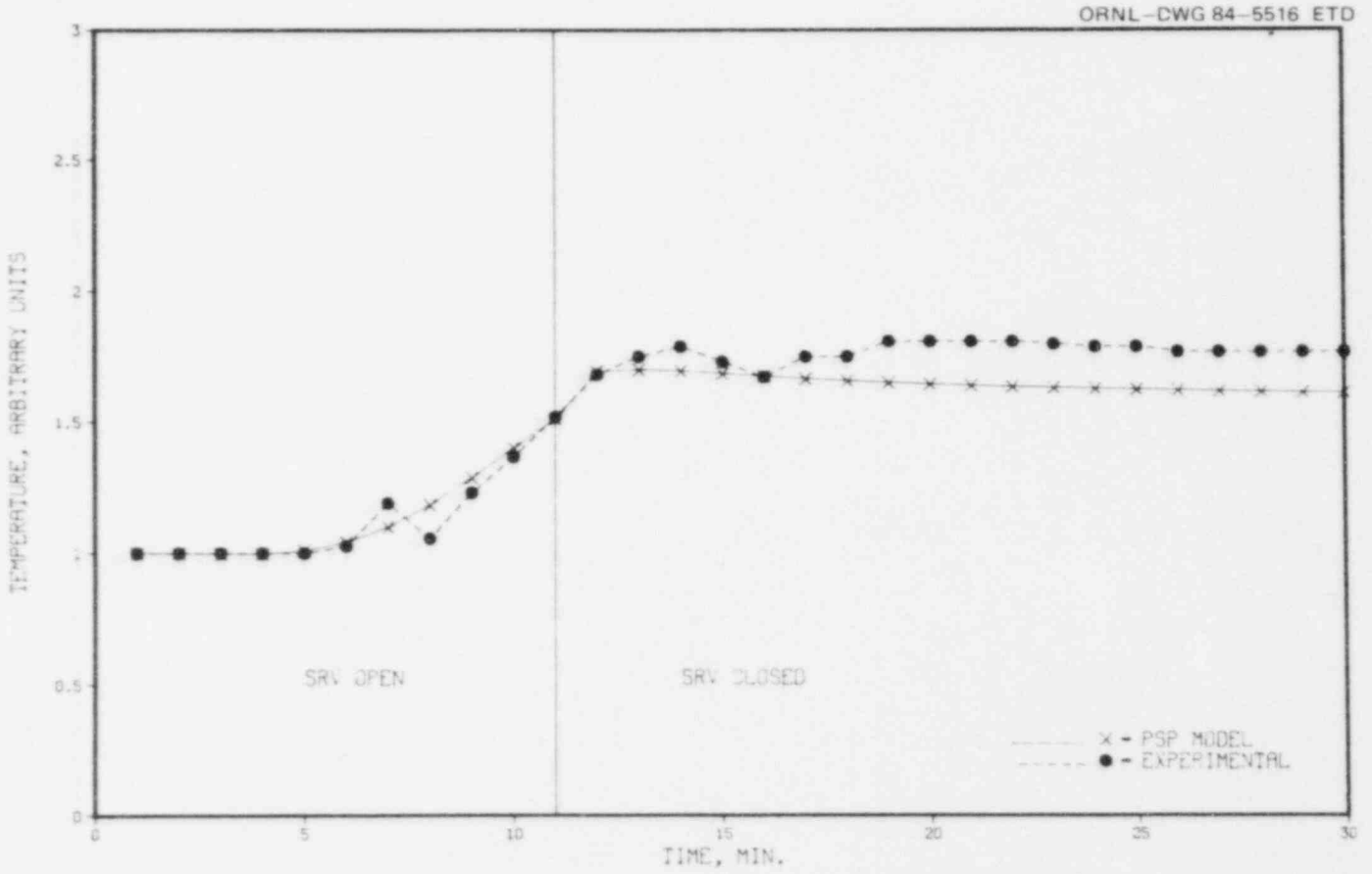

Fig. 70. Bay H middle sensor temperatures.

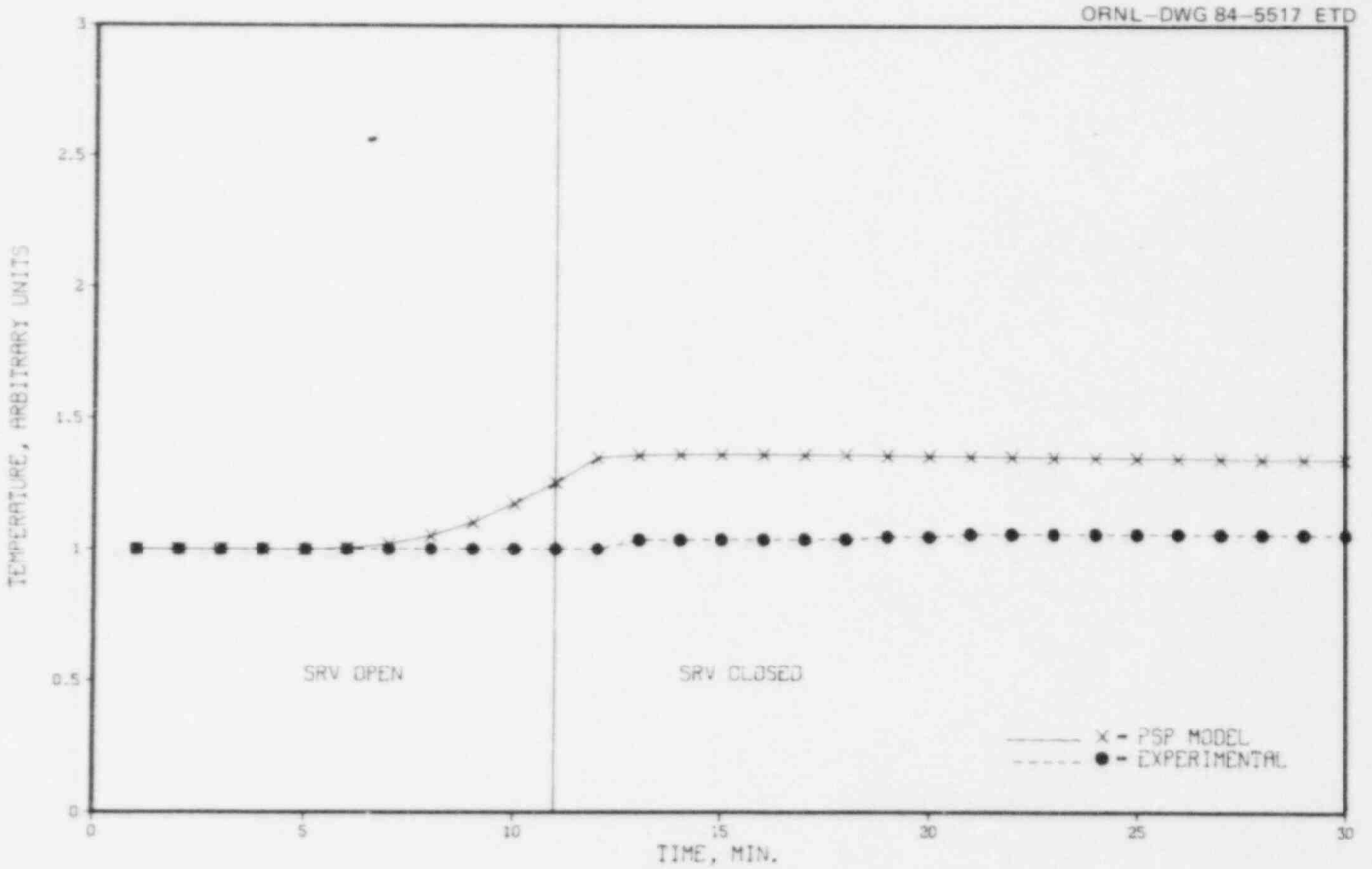

Fig. 71. Bay H lower sensor temperatures.

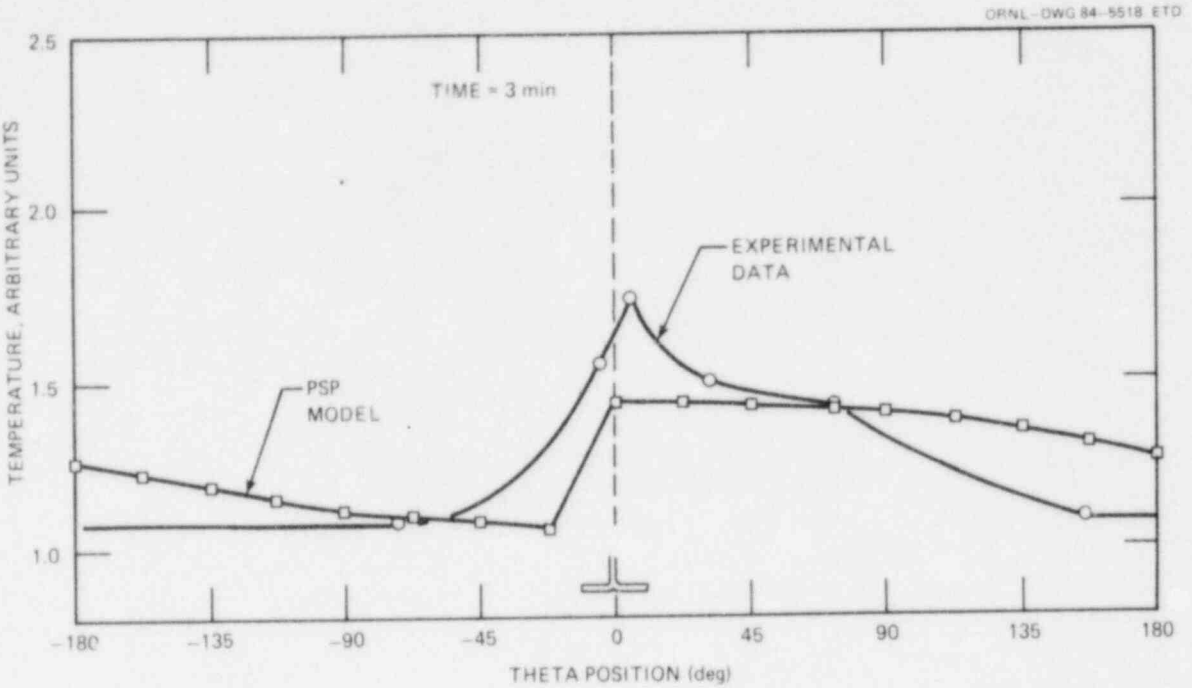

Fig. 72. Bay average temperature distribution with RHR, 3 min.

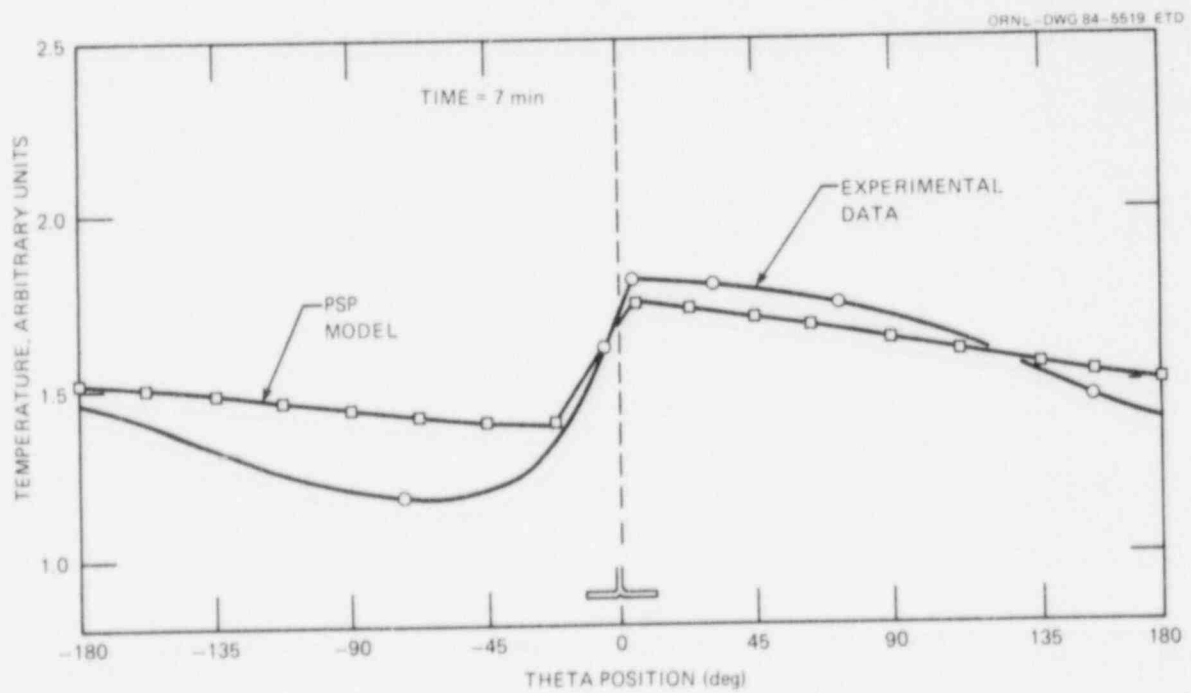

Fig. 73. Bay average temperature distribution with RHR, 7 min.

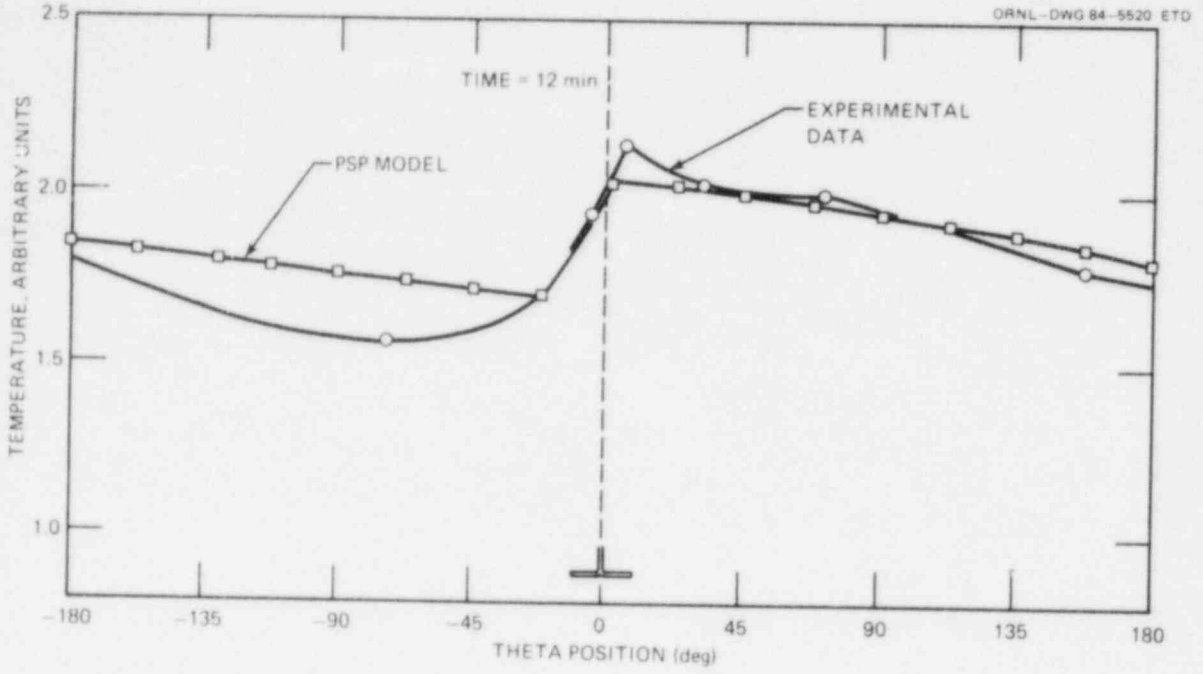

Fig. 74. Bay average temperature distribution with RHR, 12 min.

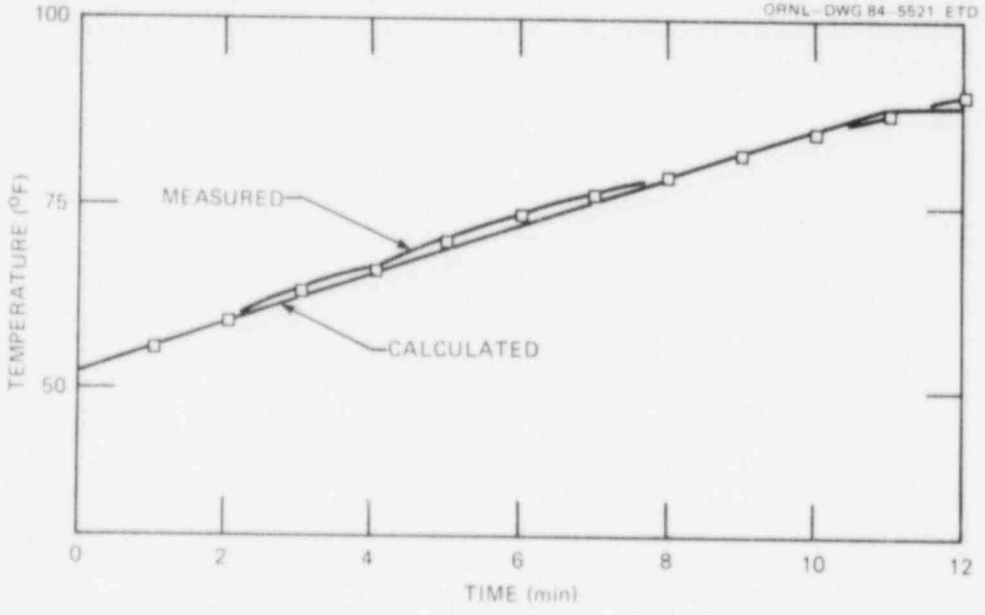

Fig. 75. Measured versus calculated bulk pool temperatures.

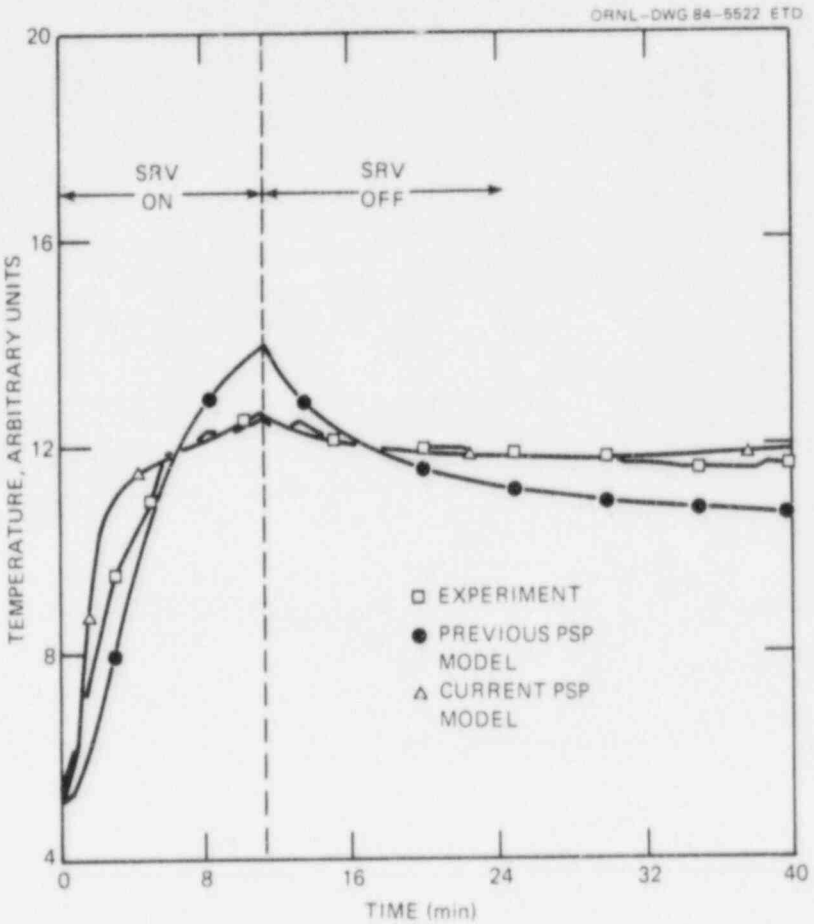

Fig. 76. Comparison of preliminary and current PSP models.

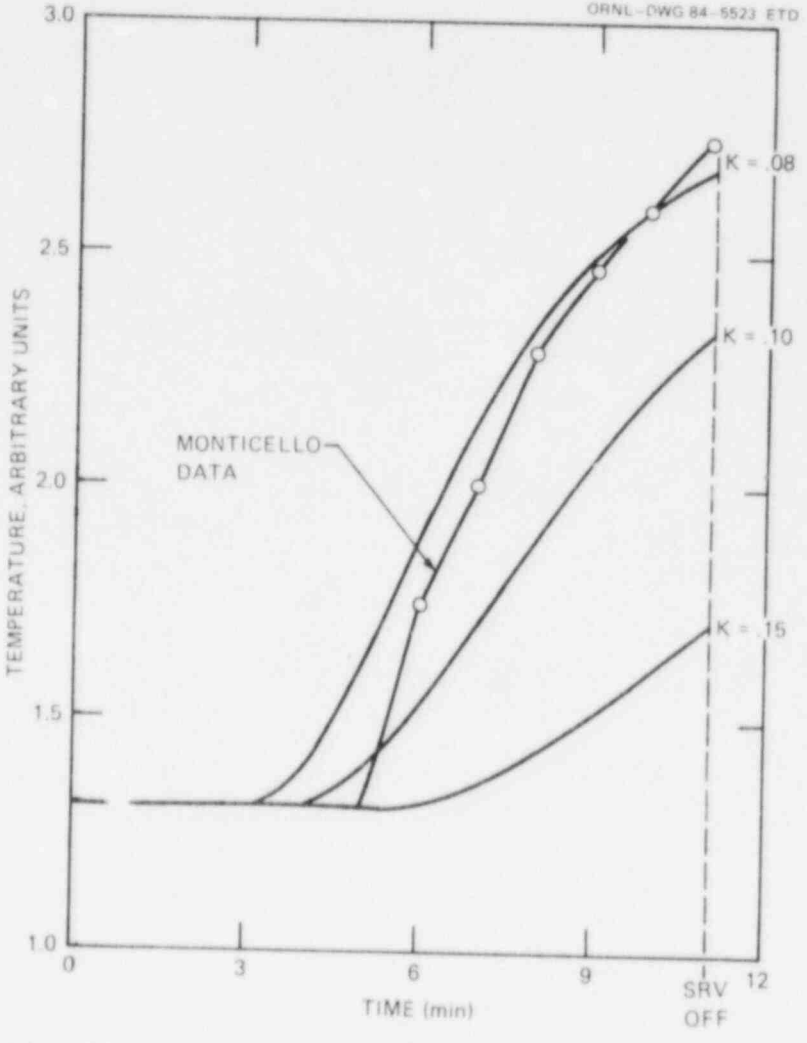

Fig. 77. Sensitivity of nodal temperatures to K.

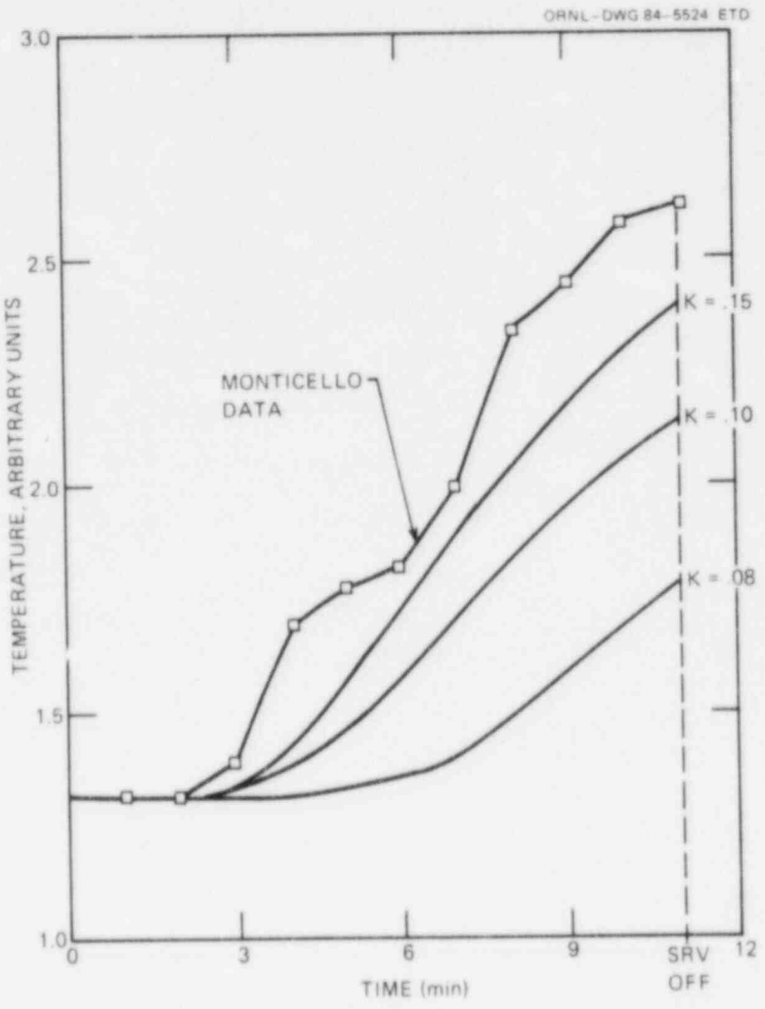

Fig. 78. Sensitivity of nodal temperatures to K — interior.

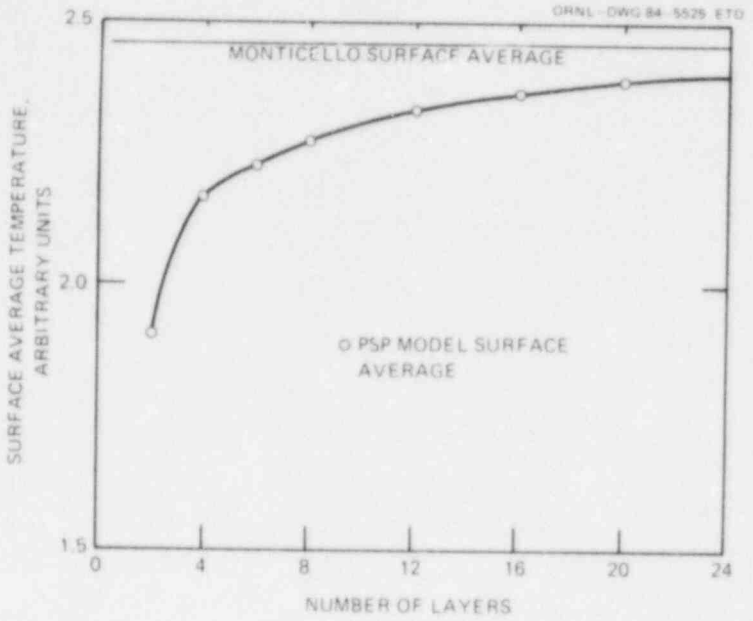

Fig. 79. Sensitivity of nodal temperatures to the number of layers.

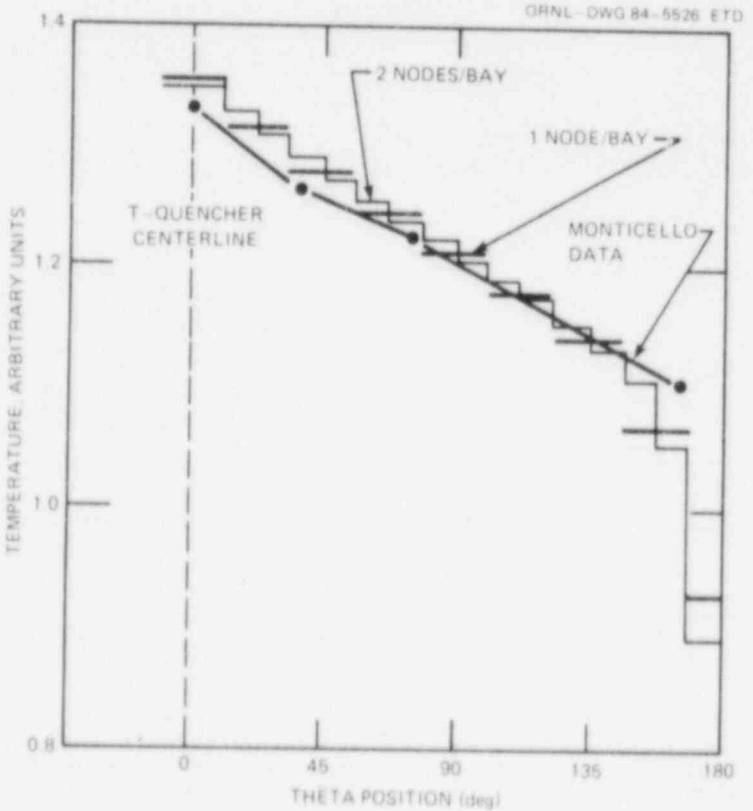

Fig. 80. Sensitivity of nodal temperatures to the number of theta nodes.

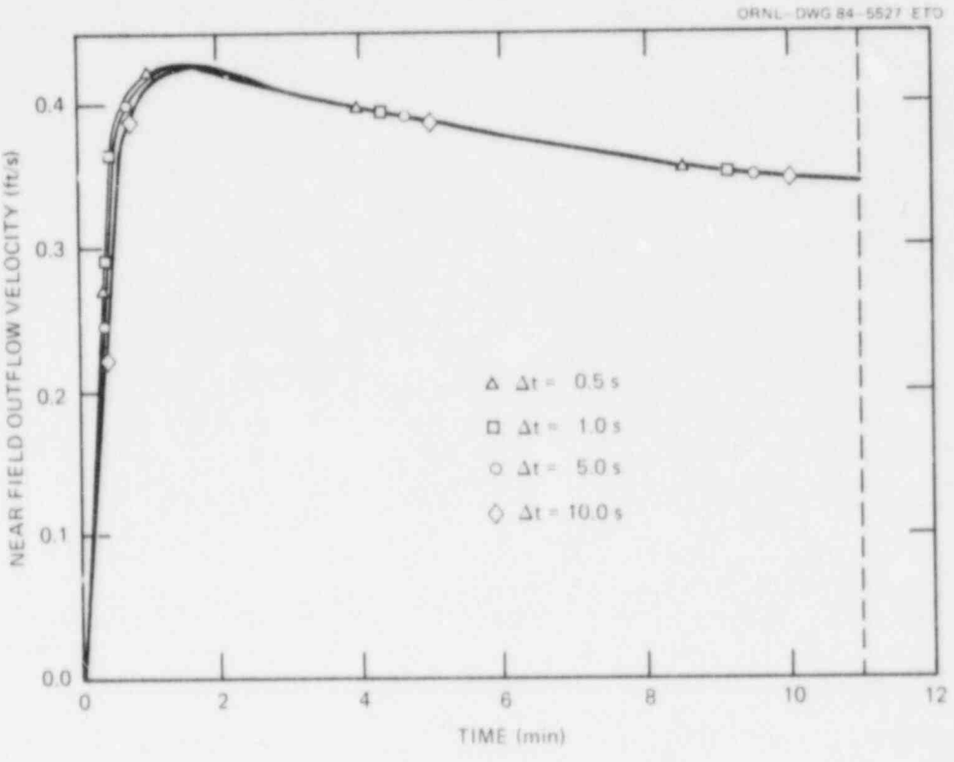

Fig. 81. Sensitivity of the near field outflow to the time step.

CHAPTER VII

APPLICATIONS TO SOME BOILING WATER REACTOR SAFETY STUDIES

A. SINGLE SRV: TIME TO SATURATE AT FULL FLOW

An important BWR reactor safety question is: given that a single SRV is discharging steam into the PSP at full flow, how much time does the reactor operator have before the PSP water is saturated in the vicinity of the T-quencher?

This problem was addressed using the PSP model by simply extending the Monticello T-quencher discharge transient in time. Instead of closing the SRV at 11.0 minutes, the valve was left open for 60.0 minutes. As in Chapter six, eight layers and one node per bay were used to model the PSP. The pressure of the suppression pool atmosphere was assumed constant at atmospheric pressure during the runs.

The discharge bay local temperature results predicted by the PSP model are represented by Fig. 82. Figure 82 is a plot of the local subcooling versus time after SRV opening. The subcoolings for the PSP surface layer and the layer that contains the T-quencher are shown in Fig. 82.

The PSP model predicts that the Bay D surface nodes will saturate at about 35.0 minutes into the transient. The bulk pool temperature at this point in time was 161.8 F, which is very close to the 160.0 F bulk pool temperature limit for suppression pools.

Even though the surface layer is near saturation, the lower layers of the PSP are still quite cold, as evidenced by the 80 F subcooling at the quencher level at 35.0 minutes.

As shown in Fig. 82, about 10.0 additional minutes of SRV discharge time are required to completely saturate the discharge bay. At 48.0 minutes, the PSP model predicted total Bay D saturation. The bulk pool temperature at this point in time was 197.8 F.

B. SINGLE SRV: TEMPERATURE RESPONSE TO REACTOR VESSEL BLOWDOWN

During steam discharge to the PSP, the reactor vessel pressure usually decreases very rapidly. Since the SRV flow is determined by the reactor pressure, the steam flow will also decrease. Thus, instead of a SRV continually discharging steam at full flow into the PSP, a transient that is more probable to occur in an operating BWR is for the steam flow to begin at a high rate, and then decay with time as the reactor vessel pressure decreases. This type of transient is the stuck open relief valve (SORV) case.

A plot of steam flow versus time for a SORV event is shown in Fig. 83. The steam flows and enthalpys for this SORV transient were supplied by the General Electric Company. There is an abrupt change in the depressurization rate at 20.0 minutes.

The PSP model with Monticello geometry as input was run with the input steam flow shown in Fig. 83. As in Chapter six, the model was run with eight layers in the vertical direction and one node per bay in the theta direction.

The Bay D surface temperature results for the SORV event are presented in Fig. 84. The SORV caused a rapid local temperature increase from 0.0 to 22.0 minutes. With the decrease in steam flow at 20.0 minutes, the Bay D surface temperature decreased. This is a correct trend because the energy addition to the near field is suddenly lowered, while at the same time, the near field / far field recirculation flow is held fairly constant.

C. SINGLE SRV: OPERATOR ROTATION OF VALVES

In an operating BWR, if manual SRV actuation is needed, the operating procedures require the reactor operator to sequentially open SRVs that discharge to T-quenchers located at different points around the PSP. In this manner, the energy is distributed as uniformly as possible around the PSP.

The case of operator rotation of SRVs was investigated by performing the full flow stuck open relief valve analysis that was described in Section A of this chapter--with the exception that the theta location of the discharging T-quencher was changed every two minutes. In other words, valve no. 1 located at 0° was opened for 2.0 minutes, then valve no. 2 located at 180° was opened for 2.0 minutes, then valve no. 3 located at 90.0° was opened for 2.0 minutes, etc. , until a total of 13 SRVs were sequentially opened. At 26.0 minutes, when all 13 valves had been opened, the valve rotation cycle was repeated.

The steam flow for this case, as with earlier transients, was 208.5 Lbm/s. The transient was run for 60.0 minutes and with the same noding (eight z levels and one node per bay) as before.

The results of the operator rotation of valves problem are presented in Fig. 85 in the form of minimum PSP subcooling versus time. The minimum subcooling from the single SRV analysis (as was presented in Fig. 82) is shown in Fig. 85 for comparison.

Very early in the transient, from 0.0 to 10.0 minutes, operator rotation of the valves had a significant impact on the minimum PSP subcooling. The sucooling was raised by rotation of the valves by about 10 F at several times during the first 10.0 minutes.

From 10.0 to about 26.0 minutes, the effect of valve rotation on the minimum PSP subcooling was very small.

At 26.0 minutes, the valve rotation cycle started over. From that time until about 30.0 minutes, there was an increase in the PSP subcooling. This anomaly is due to the particular valve locations and rotation scheme chosen for study. During the last 10.0 minutes of the first rotation, five SRVs with T-quenchers located in one half of the PSP were opened. T-quenchers at 135°, 292.5°, 112.5°, 247.5°, and 225.0° were opened (in order) from 16.0 to 26.0 minutes. Thus more energy was deposited in one half of the PSP. This effectively separated the PSP into a "hot" and a "cold" half. When the valve rotation cycle started over,

the discharge location was switched to 0.0 degrees, which was a T-quencher located in the middle of the colder half of the PSP. The peak PSP surface temperature decreased, and the corresponding subcooling increased, as shown in Fig. 85.

Operator rotation of the valves shifted the time of PSP surface saturation from about 35.0 minutes (with a single T-quencher discharge location) to about 50.0 minutes (with operator rotation of the valves every 2.0 minutes). These results apply only to the particular PSP geometry modeled here. For a different T-quencher configuration and valve rotation scheme, the plot of minimum subcooling versus time will be different.

The PSP model should be run for the plant-specific geometry and operating procedures to evaluate the effect of operator rotation of the valves at a particular BWR PSP.

For this particular geometry, operator rotation of the valves was beneficial. However, for other plants, these results do not apply.

D. MULTIPLE SRVS: TEMPERATURE RESPONSE

The purpose of this section is to demonstrate the capability of the PSP model to accomodate multiple discharging SRVs.

The PSP thermal convection cell model was run for 10.0 minutes with two T-quenchers discharging steam to the PSP. The steam flow was 208.5 Lbm/s; and as before, a noding of eight z layers and one node per bay were used to calculate the PSP temperature distribution. The two T-quenchers were located at 0° and 180°, respectively.

The PSP surface temperature distributions versus time are shown in Fig. 86. Temperature distributions at 1.0, 6.0, and 10.0 minutes are presented. As they should be, the surface temperature distributions between the two T-quenchers (in either direction) are symmetric.

Although only a two valve case is presented, the PSP convection cell model will accomodate up to four discharging T-quenchers. For more than four quenchers, the code automatically switches to the well mixed pool model, because the PSP behaves as a well mixed pot of water with many discharging T-quenchers.

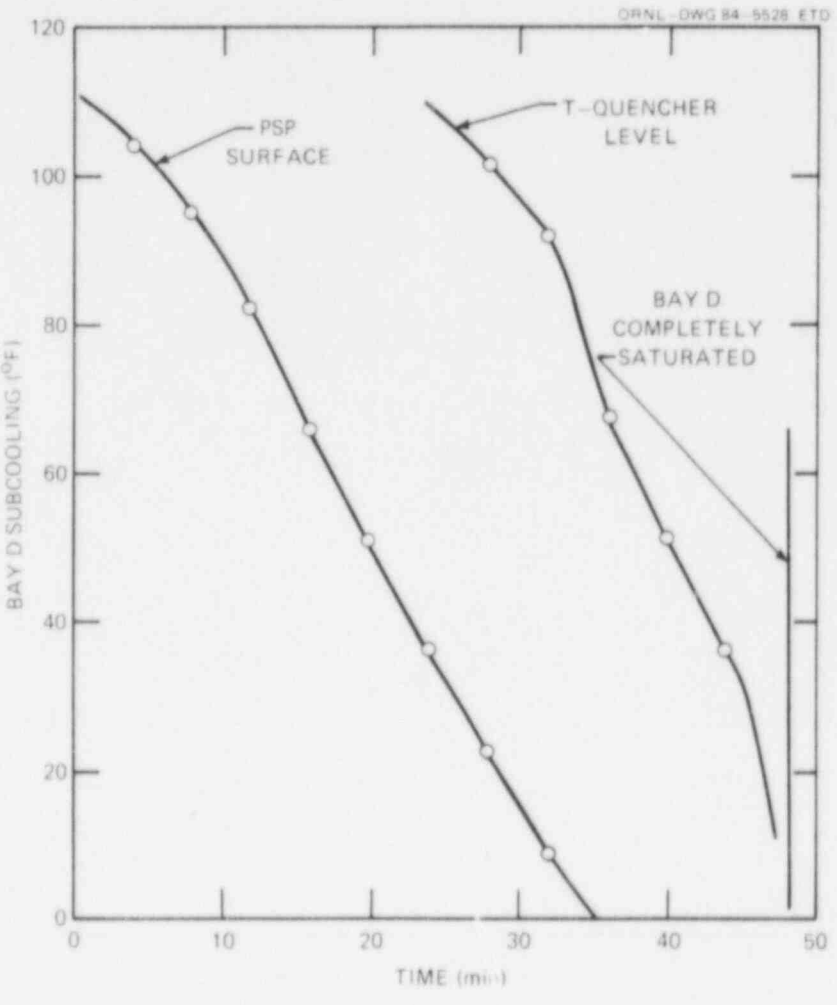

Fig. 82. Local subcooling versus time.

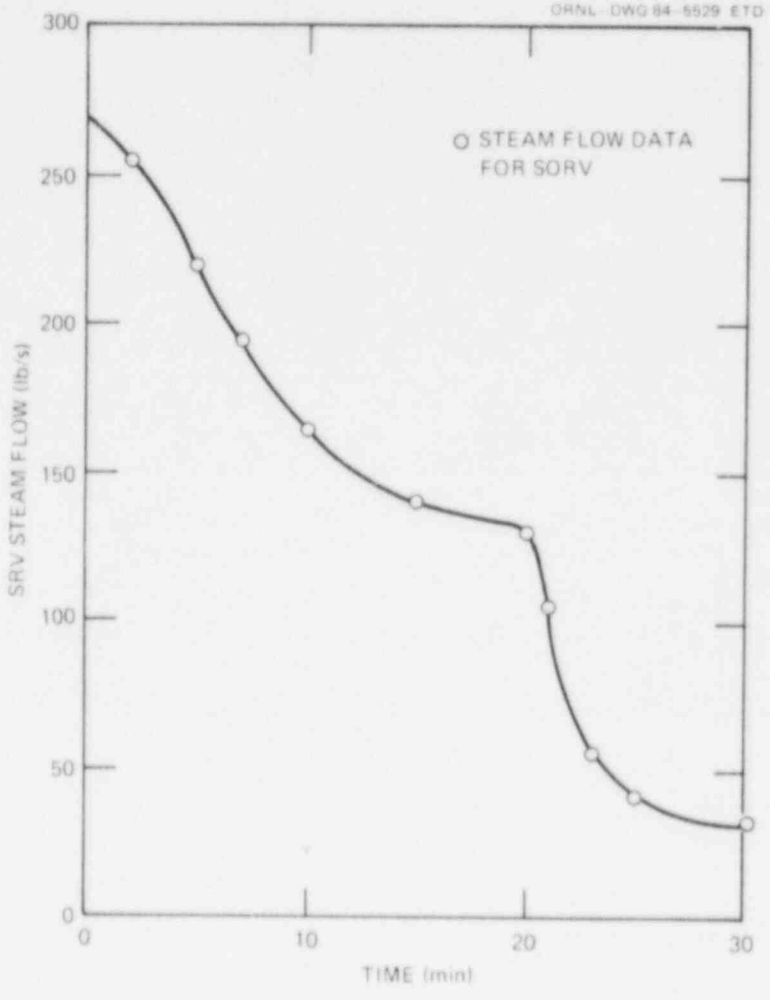

Fig. 83. SORV steam flow versus time.

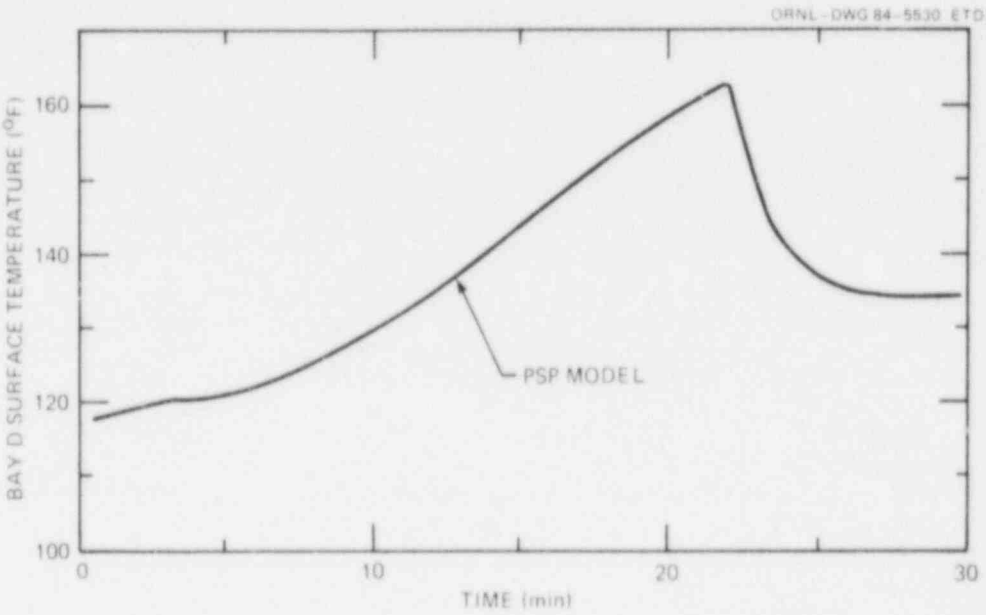

Fig. 84. Bay D surface temperature versus time.

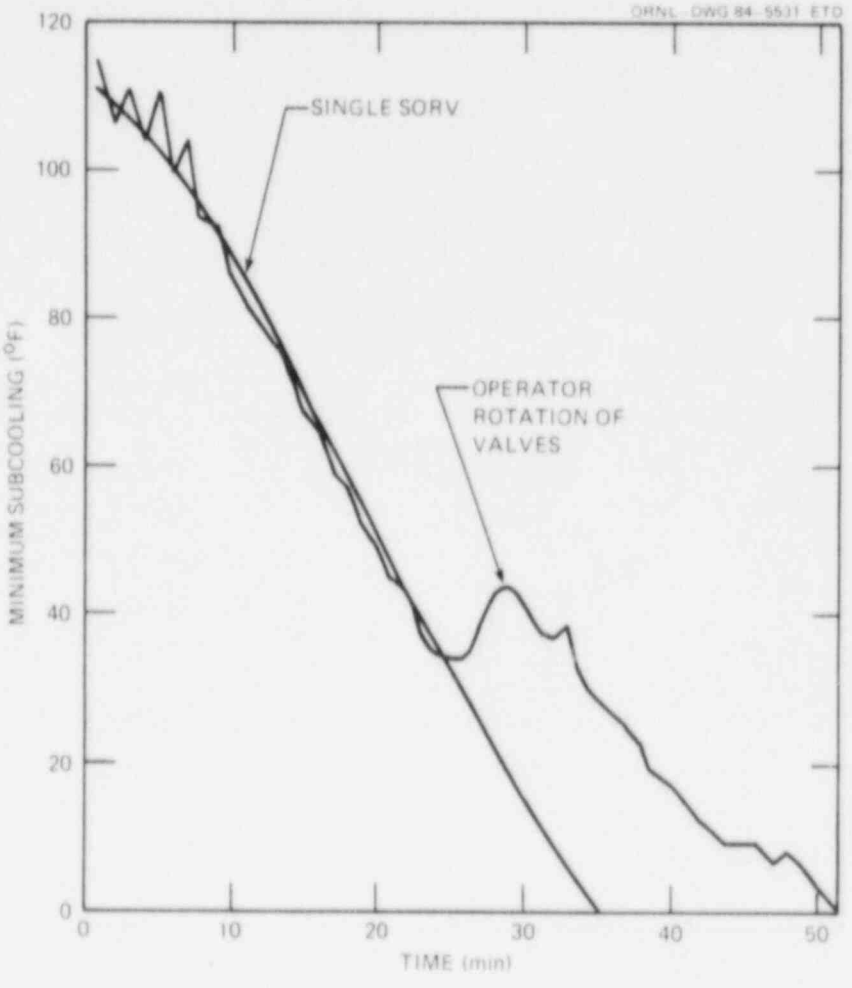

Fig. 85. Minimum subcooling versus time for operator rotation of valves.

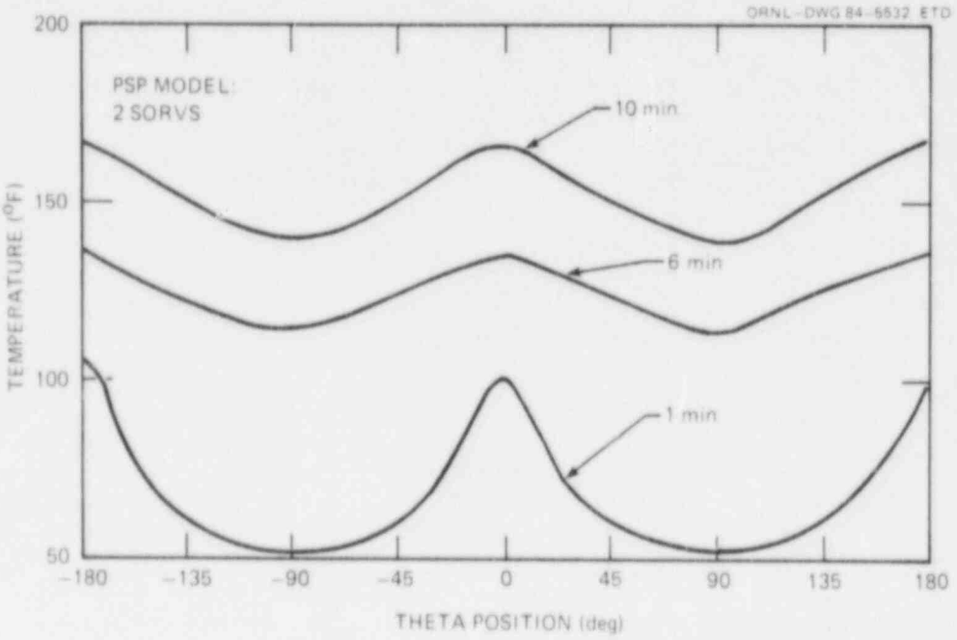

Fig. 86. Bay D surface temperature versus time: two SRVs.

CHAPTER VIII

CONCLUSIONS AND RECOMMENDATIONS FOR FUTURE STUDY

A. SUMMARY AND CONCLUSIONS

The primary objective of this study was to develop and verify a pressure suppression pool (PSP) thermal mixing model for a single T-quencher discharging steam to the pool. A goal of the model was to predict the temperature distribution throughout the PSP water during T-quencher discharge. Toward that end, a two dimensional model of the PSP was developed based on lumped parameter energy balances applied to many large fluid nodes in the pool. The nodes that subdivide the PSP were defined by a grid in the vertical and circumferential directions.

The coefficients of the coupled ordinary differential equations that comprise the thermal mixing model are determined by the flow field in the PSP.

Several models were developed to describe the flow field in the PSP. Each model is designed to predict the flow field due to a particular group of dominating phenomena. The four flow models are described below.

1. The T-quencher thermal convection cell model was developed to predict the PSP flow field due to a single discharging T-quencher. The model consists of several near field models that describe the fluid flow in the vicinity of the T-quencher, and a far field model that describes the fluid flow in the region of the PSP located away from the T-quencher.
2. The thermal stratification model was developed to predict the PSP flow field immediately following the safety relief valve closure. This model is based on a very simplified treatment of the internal density wave flow in the PSP.
3. The bulk pool circulation model was developed to extend the thermal mixing model to include the possibility of RHR-system circulation of the PSP. This model consists of imposing a specified circumferential velocity on the PSP.
4. The well mixed pool model was developed to extend the thermal mixing model to include the possibility of a well mixed PSP. This model consists of distributing the PSP energy uniformly throughout the pool.

The PSP thermal mixing model was verified by comparing temperatures predicted by the model to temperatures that were measured during experiments in an operating BWR suppression pool. Overall, each of the models provided reasonably good agreement with the experimental temperatures.

The PSP thermal mixing model was extended to facilitate the modeling of multiple discharging T-quenchers. The flow field was assumed symmetric between each two discharging T-quenchers. Thus, the thermal convection cell model for a single T-quencher can be applied to the case

of an arbitrary number of T-quenchers by simply changing the length of the far field region, and then using the model N times, where N is the number of discharging T-quenchers.

The thermal mixing model was extended to include the capability of modeling PSP bypass. PSP bypass was defined as steam flowing through saturated water near a T-quencher and passing uncondensed into the PSP airspace. This extension of the model permits the PSP computer code to continue predicting the PSP temperatures past the point in time when the water near the T-quencher becomes saturated.

There are two major conclusions that can be drawn from the PSP thermal mixing model development effort:

1. The PSP thermal mixing behavior during T-quencher discharge is identified as being characterized by plume transport dynamics in the near field and density current flow in the far field. Immediately following SRV closure, thermal stratification is created in the pool by a series of internal wave motions.
2. A two dimensional model of the PSP thermal mixing was developed and verified. The model adequately predicts BWR, MK I pressure suppression pool behavior for transients involving SRV discharge.

B. RECOMMENDATIONS FOR FUTURE STUDY

There are many areas for future study that have been identified by this work. The areas are roughly divided into two categories: specific PSP studies and fundamental research.

There are two specific PSP studies that should be performed. These are (1) an experimental study of T-quencher dynamics, and (2) a modeling study that would focus on PSP thermal mixing when a T-quencher is discharging steam in the presence of a small bulk pool circulation. The T-quencher dynamics study should focus on identifying the T-quencher flow regimes and studying the interactions of the many steam jets that exit the T-quencher with the surrounding water. The modeling study of PSP thermal mixing in the presence of a small bulk pool circulation should focus on the interactions of the bulk pool circulation with the far field density current.

There is much fundamental thermal-hydraulic research that should be performed to aid future PSP studies. There are 3 areas that need particular attention: the areas of condensing steam jets, thermal stratification, and density current interfaces.

A steam jet study should be performed that would identify some parameters of use to a PSP modeler. Three of these parameters include the steam jet entrainment, the hot water velocity distribution downstream of the condensing jet, and the effect of noncondensibles on the steam jet behavior.

A thermal stratification study should be performed that would identify the internal wave motions in the PSP. Parameters such as internal density wave height, wave velocity, and effective hot water layer entrainment should be investigated.

An experimental study should be performed to identify the characteristics of the density current interface. This interface separates the hot water layer that moves in the horizontal direction from the cold water layer that moves countercurrently underneath the hot layer. Emphasis in the study should be on identifying the upper layer entrainment and the interfacial friction.

When further in-plant testing such as the Monticello T-quencher thermal mixing study is performed, the PSP should be instrumented with many more temperature sensors than were installed at the Monticello tests. These additional temperature sensors would provide more information about the PSP thermal mixing and they would provide more temperatures for the verification of this and any future PSP analyses.

LIST OF REFERENCES

1. T. M. Su, "Suppression Pool Temperature Limits for BWR Containments," NUREG-0783, November, 1981.

2. W. J. Bilanin, "The General Electric Pressure Suppression Containment System Analytical Model," NEDO-20533, 1975.

3. D. Brosche, "A Model for the Calculation of Vent Clearing Transients in Pressure Suppression Systems," Nucl. Engr. Des., 38, pp.131-141, 1976.

4. H. Nariai, et al, "Thermo-Hydraulic Behavior in a Model Pressure Suppression Containment During Blowdown," Topics in Two-Phase Heat Transfer and Flow, Winter ASME Meeting, 1978.

5. D. H. Cook, et al, "Station Blackout at Browns Ferry Unit One-Accident Sequence Analysis," NUREG/CR-2182, November, 1981.

6. D. H. Cook, et al, "Loss of DHR Sequences at Browns Ferry Unit One-Accident Sequence Analysis," NUREG/CR-2973, May, 1983.

7. F. J. Moody, "Pressure Suppression Containment Thermal-Hydraulics State of the Art," Proceedings of the ANS/ASME/NRC International Topical Meeting on Nuclear Reactor Thermal-Hydraulics, Saratoga Springs, N.Y., October, 1980.

8. Safety Evaluation Report - Mark I Containment Long-Term Program, NUREG-0661, July 1980.

9. Three Dimensional Pool Swell Modeling of a Mark I Suppression System, EPRI NP-906, October, 1978.

10. H. Nariai, et al, "Thermo-Hydraulic Behavior in a Model Pressure Suppression Containment During Blowdown," Topics in Two-Phase Heat Transfer and Flow, Winter ASME Meeting, 1978.

11. W. G. Anderson, et al, "Small Scale Modeling of Hydrodynamic Forces in Pressure Suppression Systems," NUREG/CR-003, 1978.

12. B. D. Nichols, et al, "Numerical Simulation of Boiling Water Reactor Vent-Clearing Hydrodynamics," Nucl. Sci. Engr., 73, pp.196-209, 1976.

13. D. Brosche, "Model for the Calculation of Vent Clearing Transients in Pressure Suppression System," Nucl. Engr. Des., 38, pp.131-141, 1976.

14. K. W. Wong, H. S. Yao, "Mark I Containment Program Downcomer Submergence Functional Assessment Report," NEDO-21885, 1978.

15. J. S. Marks, G. B. Andeen, "Chugging and Condensation Oscillation Tests," EPRI NP-1167, September, 1979.

16. J. Collen, "Analysis of Pressure Oscillations and Pressure Spikes in the Marviken Pressure Suppression Containment," Proceedings of International Specialists Meeting on BWR - Pressure Suppression Containment Technology, Geesthacht, Federal Rep. of Germany, June, 1981.

17. M. Okazaki, "Analysis for Pressure Oscillation Phenomena Induced by Steam Condensation in Containment with Pressure Suppression System," Nucl. Sci. and Tech., 16, pp. 30-42, January, 1979.

18. J. S. Marks, G. B. Andeen, "Chugging and Condensation Oscillation," Condensation Heat Transfer, pp.93-102, 18th National Heat Transfer Conference, San Diego, CA., 1979.

19. P. A. Sargis, et al, "A Fundamental Thermal Hydraulic Model to Predict Steam Chugging Phenomena," Topics in Two-Phase Heat Transfer and Flow, pp.123-133, Winter ASME Meeting, 1978.

20. P. A. Sargis, et al, "Analysis of Steam Chugging Phenomena, Vol. 1," EPRI NP-1305, January, 1981.

21. R. Fiebig, "Dynamics of the Water Movement at the Chugging Process in Wide Pipes (Theory)," Proceedings of International Specialists Meeting on BWR-Pressure Suppression Containment Technology, Geesthacht, Federal Rep. of Germany, June, 1981.

22. P. Valandani, "Safety Relief Valve Discharge Analytical Models," NEDO-20942, May 1975.

23. P. Valandani, et al, "Comparison of Safety Relief Valve Model Predictions with Test Data," NEDO-21062, July 1975.

24. F. T. Dodge, "Analytical Models for T-Quencher Water Jet Loads on Submerged Structures," NEDO-25090, May 1979.

25. B. J. Patterson, "Mark I Containment Program: Monticello T-Quencher Thermal Mixing Test Final Report," NEDO-24542, 1979.

26. J. S. Turner, "Buoyant Plumes and Thermals," Annual Review of Fluid Mechanics, Vol. I, 1969.

27. B. R. Morton, "Forced Plumes," J. Fluid Mech., 2, pp.151-163, 1959.

28. B. R. Morton, G. Taylor, J. S. Turner, "Turbulent Gravitational Convection from Maintained and Instantaneous Sources," Proc. Roy. Soc. A, 234, pp.1-23, 1955.

29. W. D. Baines, J. S. Turner, "Turbulent Buoyant Convection from a Source in a confined Region," J. Fluid Mech., 37, pp.51-80, 1969.

30. P. C. Manins, "Turbulent Buoyant Convection from a Source in a Confined Region," J. Fluid Mech., 91, pp.765-781, 1978.

31. G. H. Jirka, "Multiport Diffusers for Heat Disposal," J. of Hyd. Div., ASCE, 106, No. HY12, pp.1425-1468, 1982.

32. A. Kudo, "Basic Study on Vapor Suppression," Fifth Int. Heat Transfer Conference, Tokoyo, 1974.

33. Y. I. Balakleyevskiy, "Experimental Study of Condensation of a Submerged Steam Jet," Heat Transfer - Soviet Research, 12, pp.124-130, 1980.

34. C. P. Greef, "A Study of the Condensation of Vapor Jets Injected Into Subcooled Liquid Pools," General Electricity Generating Board, Berkeley Nuc. Labs, RD/B/N3262, 1975.

35. L. E. Stanford, C. C. Webster, "Energy Suppression and Fission Product Transport in Pressure Suppression Pools," ORNL/TM/3448, 1975.

36. J. C. Weimer, et al, "Penetration of Vapor Jets Submerged in Subcooled Liquids," AIChE Journal, 19, pp.552-558, 1973.

37. P. J. Kerney, "Characteristics of a Submerged Steam Jet," Ph.D. Dissertation, Penn. State Univ., 1970.

38. M. E. Simpson, C. K. Chan, "Hydrodynamics of a Subsonic Vapor Jet in Subcooled Liquid," Sixth Internaltional Heat Transfer Conf., Toronto, 1978.

39. I. Catton, et al, "Hydrodynamics of a Vapor Jet in Subcooled Liquid," NUREG/CR-1632, 1980.

40. T. Von Karman, "The Engineer Grapples With Nonlinear Problems," Bull. Am. Math. Soc., 46, pp.615-660, 1940.

41. T. B. Benjamin, "Gravity Currents and Related Phenomena," J. Fluid Mech., 31, pp.209-248, 1967.

42. D. N. Brocard, D. F. Harleman, "Two-Layer Model for Shallow Horizontal Convective Circulation," J. Fluid Mech., 100, pp.129-146, 1980.

43. G. H. Jirka, "Thermal Structure of Cooling Ponds," J. of the Hyd. Div., ASCE, 106, No. HY5, pp.701-715, 1980.

44. G. L. Bata, "Recirculation of Cooling Water in Rivers and Canals," J. of the Hyd. Div., ASCE, 83, No. HY3, pp. 1265-1 to 1265-27, 1957.

45. T. W. Sturm, "An Analytical and Experimental Investigation of Density Currents in Sidearms of Cooling Ponds," Ph.D. Dissertation, Univ. of Iowa, 1976.

46. T. W. Sturm, "Heat Loss From Sidearms of Cooling Lakes," J. of the Hyd. Div., ASCE, 106, No. HY5, pp.783-804, 1980.

47. I. G. Currie, Fundamental Mechanics of Fluids, McGraw Hill Book Co., New York, N.Y., 1974, p.302.

48. J. S. Turner, Buoyancy Effects in Fluids, Cambridge Univ. Press, Cambridge, U.K., 1973, Ch. 10.

49. V. L. Streeter, Handbook of Fluid Dynamics, McGraw Hill, 1962.

50. R. R. Long, "A Theory of Turbulence in Stratified Fluids," J. Fluid Mech., 42, pp.349-365, 1970.

51. A. D. McEwan, "The Kinematics of Stratified Mixing Through Internal Wavebreaking," J. Fluid Mech., 128, pp.47-57, 1983.

52. L. R. Wyatt, "The Entrainment Interface in a Stratified Fluid," J. Fluid Mech., 86, pp.293-311, 1978.

53. T. H. Ellison, J. S. Turner, "Turbulent Entrainment in Stratified Flows," J. Fluid Mech., 6, pp423-448, 1960.

54. J. S. Turner, "The Influence of Molecular Diffusivity on Turbulent Entrainment Across a Density Interface," J. Fluid Mech., 33, pp.639-656, 1968.

55. B. J. Patterson, "Mark I Containment Program: Monticello T-Quencher Thermal Mixing Test Final Report," NEDO-24542, 1979.

56. P. J. Kerney, "Characteristics of a Submerged Steam Jet," Ph.D. Dissertation, Penn. State Univ., 1970.

57. C. K. Chan, et al, "Studies of Dynamic Loads in Pressure Suppression Containment," Sixth Water Reactor Safety Information Meeting, Gaithersburg, Md., November, 1978.

58. P. Liseth, "Mixing of Merging Buoyant Jets from a Manifold in Stagnant Receiving Water of Uniform Density," Univ. of Calif. Report HEL 23-1, 1970.

59. B. R. Morton, "Forced Plumes," J. Fluid Mech., 2, pp.151-163, 1959.

60. B. R. Morton, G. Taylor, J. S. Turner, "Turbulent Gravitational Convection from Maintained and Instantaneous Sources," Proc. Roy. Soc. A, 234, pp.1-23, 1955.

61. W. D. Baines, J. S. Turner, "Turbulent Buoyant Convection from a Source in a confined Region," J. Fluid Mech., 37, pp.51-80, 1969.

62. F. P. Ricou, D. B. Spalding, "Measurements of Entrainment by Axisymmetric Turbulent Jets," J. Fluid Mech., 2, pp.21-32, 1961.

63. J. S. Turner, "Buoyant Plumes and Thermals," Annual Review of Fluid Mechanics, Vol. I, 1969.

64. J. S. Turner, Buoyancy Effects in Fluids, Cambridge Univ. Press, Cambridge, U.K., 1973, Ch. 10.

65. J. B. Riester, et al, "Effects of Water Temperature and Salt Concentration on the Characteristics of Horizontal Buoyant Submerged Jets," J. Heat Transfer, 102, pp.557-562, 1980.

66. R. C. Y. Koh, L. N. Fan, "Mathematical Models for the Prediction of Temperature Distributions Resulting from the Discharge of Heated Water Into Large Bodies of Water," WPCR-PB-208-034, 1970.

67. S. Satyanarayana, "A Study of Laminar Buoyant Jets Discharged at an Inclination to the Vertical Buoyancy Force," Int. J. of Heat and Mass Transfer, 25, pp.1569-1577, 1982.

68. K. Cederwall, "Buoyant Slot Jets Into Stagnant or Flowing Environments," Calif. Inst. of Tech. Report PB-228-385, 1971.

69. L. N. Fan, N. H. Brooks, "Numerical Solution of Turbulent Buoyant Jet Problems," W. M. Keck Lab., Calif. Inst of Tech. Report KH-R-18, 1969.

70. G. Abraham, "The Flor of Round Buoyant Jets Issuing Into Ambient Fluid Flowing in a Horizontal Direction," Fifth Int. Water Poll. Res. Conf., San Francisco, 1970.

71. H. Rouse, et al, "Gravitational Convection From a Boundary Source," Tellus, 1, pp. 201-210, 1952.

72. G. N. Abramovich, The Theory of Turbulent Jets, M.I.T. Press, Cambridge, Mass., 1963.

73. P. Liseth, "Mixing of Merging Buoyant Jets from a Manifold in Stagnant Receiving Water of Uniform Density," Univ. of Calif. Report HEL 23-1, 1970.

74. W. D. Baines, J. S. Turner, "Turbulent Buoyant Convection from a Source in a confined Region," J. Fluid Mech., 37, pp.51-80, 1969.

75. J. J. Lorenz, et al, "Entrainment by a Jet at a Density Interface in a Thermally Stratified Vessel," Trans. ASME. 101, pp. 538-542, 1979.

76. G. H. Jirka, "Stability and Mixing of a Vertical Plane Buoyant Jet in Confined Depth," J. Fluid Mech., 94, pp.275-304, 1979.

77. G. H. Jirka, "Multiport Diffusers for Heat Disposal," J. of Hyd. Div., ASCE, 106, No. HY12, pp.1425-1468, 1982.

78. D. I. H. Barr, "Densimetric Exchange Flow in Rectangular Channels," La Houille Blanche, 22, pp.619-632, 1967.

79. R. E. Bakkour, "Turbulent Underflow in a Short Channel of Limited Depth," J. of the Hyd. Div., ASCE, 109, No. 5, 1983.

80. J. S. Turner, Buoyancy Effects in Fluids, Cambridge Univ. Press, Cambridge, U.K., 1973, Ch. 10.

81. T. B. Benjamin, "Gravity Currents and Related Phenomena," J. Fluid Mech., 31, pp.209-248, 1967.

82. H. Lamb, Hydrodynamics, Sixth Ed., Cambridge Univ. Press., 1945.

83. B. J. Patterson, "Mark I Containment Program: Monticello T-Quencher Thermal Mixing Test Final Report," NEDO-24542, 1979.

84. D. N. Brocard, D. F. Harleman, "Two-Layer Model for Shallow Horizontal Convective Circulation," J. Fluid Mech., 100, pp.129-146, 1980.

85. T. W. Sturm, J. F. Kennedy, "Heat Loss From Sidearms of Cooling Lakes," J. of the Hyd. Div., ASCE, 106, No. HY5, pp. 783-804, 1980.

86. S. C. Jain, "Buoyancy Driven Circulation in Free Surface Channels," J. Fluid Mech., 122, pp. 1-12, 1982.

87. G. H. Jirka, "Thermal Structure of Cooling Ponds," J. of the Hyd. Div., ASCE, 83, No. HY3, pp.701-715, 1980.

88. T. W. Sturm, "An Analytical and Experimental Investigation of Density Currents in Sidearms of Cooling Ponds," Ph.D. Dissertation, Univ. of Iowa, 1976.

89. K. Lofquist, "Flow and Stress Near an Interface Between Stratified Liquids," Phys. Fluids, 3, pp.158-175, 1960.

90. A. C. Hindmarsh, "LSODE and LSODI, Two New Initial Value Ordinary Differential Equation Solvers," ACM-SIGNUM Newsletter, 15, No. 4, pp10-11, 1980.

91. B. J. Patterson, "Mark I Containment Program: Monticello T-Quencher Thermal Mixing Test Final Report," NEDO-24542, 1979.

92. D. H. Cook, H. L. Dodds, "Localized Heating Model for BWR Pressure Suppression Pools," Proc. ANS Winter Meeting, Detroit, March, 1983.

93. R. B. Bird, W. E. Stewart, E. N. Lightfoot, Transport Phenomena, 7th Ed. , Wiley, 1966.

APPENDIXES

APPENDIX A

FAR FIELD THEORY: DEVELOPMENT OF EQUATIONS

The three dimensional steady flow equations for conservation of mass and momentum in a cylindrical coordinate system are[93]

$$\frac{1}{r}\frac{\partial}{\partial r}(\rho r v_r) + \frac{1}{r}\frac{\partial}{\partial \theta}(\rho v_\theta) + \frac{\partial}{\partial z}(\rho v_z) = 0 \qquad \text{A.1}$$

$$\rho\left(v_r\frac{\partial v_r}{\partial r} + \frac{v_\theta}{r}\frac{\partial v_r}{\partial \theta} - \frac{v_\theta^2}{r} + v_z\frac{\partial v_r}{\partial z}\right) = -\frac{\partial P}{\partial r} + \left(\frac{1}{r}\frac{\partial}{\partial r}(r\tau_{rr}) + \frac{1}{r}\frac{\partial \tau_{r\theta}}{\partial \theta} - \frac{\tau_{\theta\theta}}{r} + \frac{\partial \tau_{rz}}{\partial z}\right) \qquad \text{A.2}$$

$$\rho\left(v_r\frac{\partial v_\theta}{\partial r} + \frac{v_\theta}{r}\frac{\partial v_\theta}{\partial \theta} + \frac{v_r v_\theta}{r} + v_z\frac{\partial v_\theta}{\partial z}\right) = -\frac{1}{r}\frac{\partial P}{\partial \theta} + \left(\frac{1}{r^2}\frac{\partial}{\partial r}(r^2\tau_{r\theta}) + \frac{1}{r}\frac{\partial \tau_{\theta\theta}}{\partial \theta} + \frac{\partial \tau_{\theta z}}{\partial z}\right) \qquad \text{A.3}$$

$$\rho\left(v_r\frac{\partial v_z}{\partial r} + \frac{v_\theta}{r}\frac{\partial v_z}{\partial \theta} + v_z\frac{\partial v_z}{\partial z}\right) = -\frac{\partial P}{\partial z} + \left(\frac{1}{r}\frac{\partial}{\partial r}(r\tau_{rz}) + \frac{1}{r}\frac{\partial \tau_{\theta z}}{\partial \theta} + \frac{\partial \tau_{zz}}{\partial z}\right) - \rho g \qquad \text{A.4}$$

where v_r = the radial velocity,
v_θ = the circumferential velocity, and
v_z = the vertical velocity.

The origin of the coordinate system is located at the center of the torus, as shown in Fig. 87.

The radial velocities and gradients in equations A.1 through A.4 are neglected (this is equivalent to assuming uniformity in the radial direction). Furthermore, the suppression pool water is assumed incompressible. With these two assumptions, the governing equations for the PSP fluid dynamics become

$$\frac{1}{r}\frac{\partial v_\theta}{\partial \theta} + \frac{\partial v_z}{\partial z} = 0 \qquad \text{A.5}$$

$$\rho\left(\frac{v_\theta}{r}\frac{\partial v_\theta}{\partial \theta} + v_z\frac{\partial v_\theta}{\partial z}\right) = -\frac{1}{r}\frac{\partial P}{\partial \theta} + \left(\frac{1}{r}\frac{\partial \tau_{\theta\theta}}{\partial \theta} + \frac{\partial \tau_{\theta z}}{\partial z}\right) \qquad \text{A.6}$$

$$\rho\left(\frac{v_\theta}{r}\frac{\partial v_z}{\partial \theta} + v_z\frac{\partial v_z}{\partial z}\right) = -\frac{\partial P}{\partial z} + \left(\frac{1}{r}\frac{\partial \tau_{\theta z}}{\partial \theta} + \frac{\partial \tau_{zz}}{\partial z}\right) - \rho g \qquad \text{A.7}$$

The stresses in the vertical direction and the normal stress term in the circumferential direction are neglected. This approximation is consistent with past analyses of hydraulic channel flow.[84-87] Thus, the only frictional term of importance is $\tau_{\theta z}$.

A change of variable is performed that moves the origin of the coordinate system from r = 0 out to r = R, where R is the major radius of the torus. Let

$$r = R + x \ , \qquad \text{A.8}$$

where x is the distance across the body of the torus, as shown in Fig. 87.

If v_θ is replace by the variable u, and v_z is replaced by w, equations A.5 through A.7 become

$$\frac{1}{R + x} \frac{\partial u}{\partial \theta} + \frac{\partial w}{\partial z} = 0 \ , \qquad \text{A.9}$$

$$\frac{1}{R + x} u \frac{\partial u}{\partial \theta} + w \frac{\partial u}{\partial z} = \frac{-1}{(R + x)} \frac{1}{\rho_o} \frac{\partial P}{\partial \theta} + \frac{1}{\rho_o} \frac{\partial}{\partial z} (\tau_{\theta z}) \qquad \text{A.10}$$

$$\frac{1}{R + x} u \frac{\partial w}{\partial \theta} + w \frac{\partial w}{\partial z} = - \frac{1}{\rho} \frac{\partial P}{\partial z} - g \ , \qquad \text{A.11}$$

In the above equations the Boussinesq approximation has been applied by treating the fluid density as a constant in the θ-momentum equation.

The functions of x in the above equations are eliminated by integrating across the torus in the x-direction from

$$x = -\sqrt{\alpha^2 - (\alpha - z)^2} = a(z) \qquad \text{A.12}$$

to

$$x = \sqrt{\alpha^2 - (\alpha - z)^2} = b(z) \ , \qquad \text{A.13}$$

where α is the torus minor radius.

All terms in equations A.9 through A.11 that are without any x-dependence gain the following coefficient as a result of the x-integration.

$$\int_a^b dx = 2\sqrt{\alpha^2 - (\alpha - z)^2} = F_1(z) \qquad \text{A.14}$$

All terms in equations A.9 through A.11 with a 1/(R+x) dependence gain the following coefficient.

$$\int_a^b \frac{dx}{R + x} = \ln \left\{ \frac{R + \frac{F_1}{2}}{R - \frac{F_1}{2}} \right\} = F_2(z) \qquad \text{A.15}$$

If the resulting set of equations are divided by $F_1(z)$, each term that contains a theta derivative will have a multiplier of the form

$$\frac{F_2(z)}{F_1(z)} = f(z) \ . \qquad \text{A.16}$$

Thus, the equations for the fluid flow in the torus become

$$f(z) \frac{\partial u}{\partial \theta} + \frac{\partial w}{\partial z} = 0 \ , \qquad \text{A.17}$$

$$f(z)\ u \frac{\partial u}{\partial \theta} + w \frac{\partial u}{\partial z} = \frac{-f(z)}{\rho_o} \frac{\partial P}{\partial \theta} + \frac{1}{\rho_o} \frac{\partial}{\partial z} (\tau_{\theta z}) \qquad \text{A.18}$$

$$f(z)\ u \frac{\partial w}{\partial \theta} + w \frac{\partial w}{\partial z} = - \frac{1}{\rho} \frac{\partial P}{\partial z} - g \ , \qquad \text{A.19}$$

These equations are used as a starting point for the analysis presented in Chapter four.

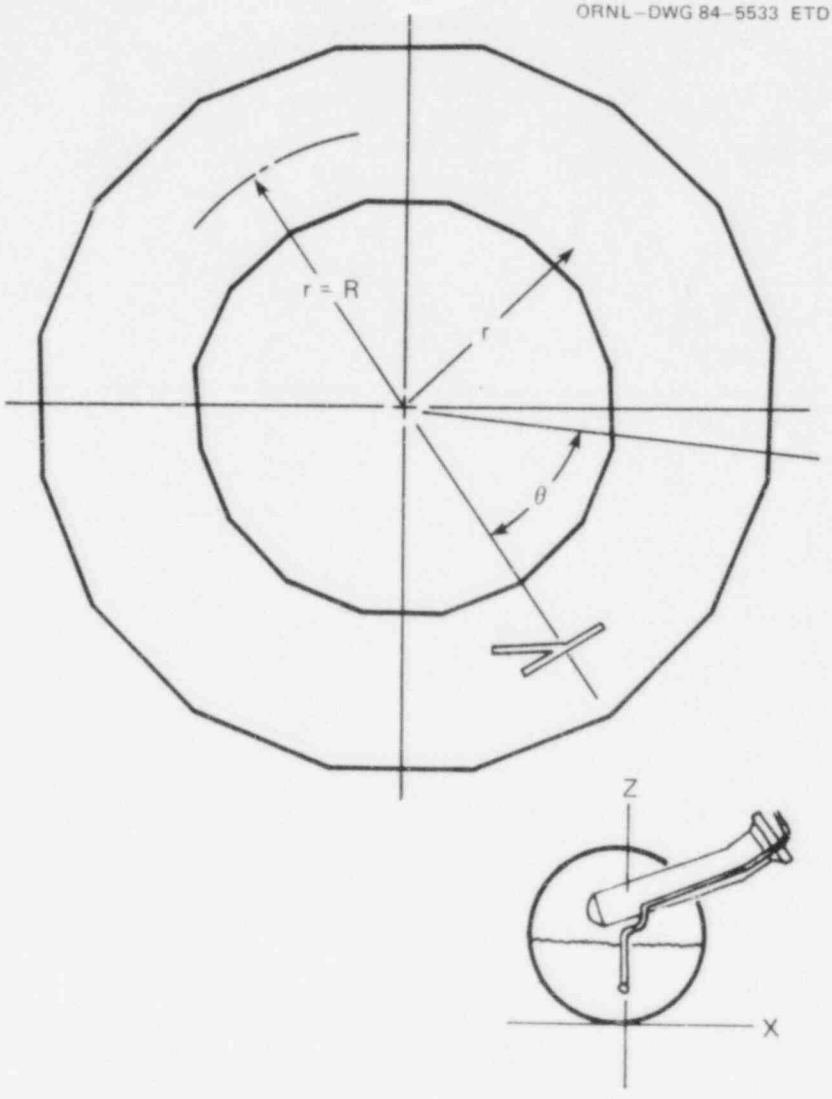

Fig. 87. General cylindrical coordinate system for the torus.

APPENDIX B

DISCUSSION OF MODELING UNCERTAINTIES

A. INTRODUCTION

The broad scope of this dissertation necessitated many approximations so that a complete PSP thermal mixing model could be developed. The purpose of this Appendix is to present and discuss some of the major assumptions.

B. UNCERTAINTY IN THE TEMPERATURE CALCULATIONS

1. Two Dimensional Approximation of the PSP

The thermal mixing model of the PSP is a two dimensional approximation to the three dimensional energy transport equation in the torus. This approach is primarily based on a study of the Monticello data, which showed an overall two dimensional variation in temperatures during and after the T-quencher discharge.

In the far field, the two dimensional approximation is justified because there are no forces other than the centrifigul force to cause the fluid to flow in the radial direction. The theta velocities are usually small; hence the centrifigul acceleration is small. Furthermore, the buoyancy force tends to retard any downflow at the outer wall that must accompany any significant radial fluid velocity. If the three dimensional flow in the far field were modeled, it is expected that the full three dimensional treatment would induce a slight tilt of the horizontal surfaces of constant density.

In the near field, the two dimensional approximation is a poor assumption because the fluid momentum source is directed primarily in the radial direction. The detailed near field models for plume transport, surface spread, and local recirculation are attempts to compensate for the three dimensionality of the T-quencher source within the two dimensional model of the whole pool.

2. Lumped Treatment of the Temperature Calculations

An assumption in the PSP thermal mixing model is that each node in the domain behaves as a well mixed pot of water. The water temperature everywhere within the node is a constant (at the current time step), and the temperature of the fluid leaving the node is equal to the temperature within the node.

Obviously, temperature gradients would exist within the nodes for any real fluid. Clearly, the lumped treatment of the temperature calculations introduces error into the solution. With a more detailed numerical approximation to the energy equation, such as a two dimensional finite difference or finite element approach, the temperature results would probably be more accurate. However, the detailed approaches would involve more computational cost. It is doubtful that a detailed approach would be affordable to implement in a PSP model--especially if the PSP model is required to couple to other system models and to run for a long time.

3. Quasistatic Treatment of the Flow Field

One of the most important assumptions in the PSP analysis is the quasistatic assumption, i.e., that over the time step the velocity field is constant. The computational benefit of this assumption is that the fluid momentum and continuity equations are reduced to second order PDEs in space only—the first order time derivatives are neglected. Of course, computational error is also introduced with this assumption because the time derivatives are neglected.

The sensitivity study of Chapter six showed that after a SRV discharge time of about one minute, the quasistatic assumption is justified because of the slowly changing nature of the flow field. However, for short times after the SRV opens, small time steps (about 0.5 to 1.0 sec.) are advised.

The assumption of an instantaneous change of the PSP velocity at the time of SRV opening was made primarily to simplify the modeling effort. However, the air clearing event that accompanies each opening of a SRV supports this assumption because the air bubble flow, the pool swell, and the small surface waves that are created by the air clearing event act together to impulsively start the PSP motion before any steam is condensed and before any density current flow begins.

C. UNCERTAINTY IN THE THERMAL CONVECTION CELL MODEL

1. Near Field Models

There are separate near field models for the T-quencher steam condensation, the plume transport, and the surface spreading. The uncertainties in each of these areas will be discussed separately.

The T-quencher steam condensation model has uncertainties in the steam jet initial conditions, the water jet initial conditions, and in the flow regime map. However, the most severe uncertainty in the steam condensation model is in neglecting the effect of the noncondensibles on the steam condensation. Improvements in the steam condensation model can be made when more research is performed on the basic phenomena involved in the noncondensible gas effects on condensation.

The plume transport model has uncertainties in the areas of torus wall impingement and in merging plume dynamics. The basic model for the

isolated, buoyant plume was verified in Chapter four. However, the extensions to wall impingement and plume merging were made without verification.

The surface spreading model has an uncertainty in the constant that was used for the ratio between the near field outflow and inflow. This constant (equal to 0.8) was based on the exchange in rectangular channels, and was used for the curved, circular channel that forms the PSP. Improvement in the surface spreading model can be made when fundamental research is performed in this area.

2. Far Field Model

The far field model contains many uncertanties. However, there are three major assumptions that will be discussed here. These are the constant hot water layer thickness assumption, the constant pool depth assumption, and the far field solution scheme.

The constant hot water layer thickness assumption was based on similar assumptions made by other researchers, and on studies of the density current phenomenon. In cases where the layer thickness was calculated as a function of distance down the channel, overall changes were very small. This assumption can be improved when more research is performed on the nature of the density current interface.

The constant PSP depth assumption was based primarily on the need to simplify the far field problem. The constant depth assumption has been used by other researchers. However, some researchers retain the depth as a dependent variable. In the early stages of the far field theory development, a variable PSP depth was included. But several modeling failures prompted the constant PSP depth assumption.

To facilitate improvement on the constant depth assumption, the far field equations were developed with a variable D, and the constant D assumption was made at the last part of the theoretical development.

The far field solution scheme is an approximate method of solving the fluid equations in the PSP. The approximation is that momentum conservation is quaranteed in an integral sense over the entire domain. Locally, conservation of momentum, but not conservation of mass, may be violated.

An improved solution method for the nonlinear, second order far field problem would improve the accuracy of the far field velocity distribution. However, care must be taken to insure that a model that is developed is affordable for running within the PSP code.

APPENDIX C

RECOMMENDATIONS FOR USE OF THE PSP MODEL

A. CHOICE OF A FLOW MODEL

The PSP model contains four options for calculating the flow in the suppression pool. The four flow models are the thermal convection cell model, the thermal stratification model, the bulk pool circulation model, and the well mixed pool model. The models can be used in any order to move the PSP forward in time from one time step to another. The flexibility of using the flow models in any order allows a broad range of transients to be modeled. The following example illustrates the use of the four models.

Consider a hypothetical BWR accident sequence that begins with a reactor scram and the coincident actuation of the 6 SRVs in the automatic depressurization system (ADS). Assume 4 of the 6 SRVs close after 30.0 seconds of operation--2 of the valves remain stuck open. Assume one of the stuck open SRVs closes after 2.0 minutes and the other valve closes after 10.0 minutes of discharge. Assume that after both stuck open valves are closed, the reactor operator decides to turn on the RHR system. Assume that 20.0 minutes are required to start the RHR system. During the 20.0 minutes between closure of all the valves and the start of the RHR system, the PSP will stratify. After starting, assume that the RHR system is operated for 20.0 minutes in order to thoroughly mix the PSP.

The scenario described above can be modeled with the PSP code by using the well mixed pool model from 0.0 to 0.5 minutes (during the ADS blowdown), the thermal convection cell model with 2 discharging SRVs from 0.5 to 2.5 minutes (during the 2 stuck open SRV discharge), the thermal convection cell model with 1 discharging SRV from 2.5 to 10.5 minutes (during the 1 stuck open SRV discharge), the thermal stratification model from 10.5 to 30.5 minutes (during the RHR sytem startup), and the bulk pool circulation model from 30.5 to 50.5 minutes (during the RHR system discharge).

In general, the particular transient to be modeled will clearly determine the flow model to use. However, there are situations in which two of the models could be used for the same transient. For example, if an anticipated transient without scram (ATWS) accident sequence involved 4 SRVs discharging steam to the PSP, either the thermal convection cell model or the well mixed pool model could be used to calculate the PSP temperature distribution versus time.

In modeling an ATWS sequence, if more than 4 SRVs are discharging steam to the PSP, it is recommended that the PSP be modeled as a well mixed pool. The division of the PSP modeling between a well mixed pool and distinct convection cells at 4 SRVs is based on a consideration of the limited size of the PSP relative to the number of convection cells that must be created by the far field model. With 5 or more discharging SRVs, the size of the individual far field convection cells would be

limited to about 1 bay of the PSP. The assumptions used in developing the far field model would break down for such a short far field.

B. CHOICE OF MODELING PARAMETERS

The choice of modeling parameters for a particular transient depends on the type of transient and the effect of interest desired from the calculation. The modeling parameters that significantly affect the PSP temperature results were identified in the sensitivity analysis in Chapter six. Those parameters were the far field interfacial friction factor, the number of levels in the z-direction, the number of nodes in the theta direction, and the time step.

The sensitivity study identified $K = 0.10$ as a best estimate of the friction factor; this value of K is programmed into the PSP code as a default value.

The sensitivity study showed that one node per bay in the theta direction (a total of 16 theta nodes) was sufficient to model the circumferential transport.

The sensitivity study showed an insensitivity to the time step over the range from 0.5 to 20.0 seconds. A time step of 5.0 seconds is recommended.

If detailed surface temperature distributions versus time are needed for a T-quencher discharge transient, then many z-levels should be used (8 layers was sufficient to model the Monticello transient). However, as few as 4 layers can give a reasonable estimate of the temperature distribution in the vertical direction.

APPENDIX D

INSTRUCTIONS FOR USE OF THE PSP CODE

A. PSP CODE INPUT

The PSP code is designed to be fed all the appropriate information about the PSP geometry, the number of T-quenchers that are discharging, and the flow model to be used. There are two types of required input to the model: a geometry and modeling information data file, and the subroutine calling variables.

A data file must be supplied with the subroutine that will be read on the first call and ignored on subsequent calls. The data file contains the following information.

Input Variable	Function
TWSPAV	Initial bulk pool temperature
B	Torus minor radius
R	Torus major radius
ZLVLO	Initial PSP water level
QLVL	T-quencher centerline level
NLVL	Number of layers desired in the model
NPERBA	Number of theta nodes per bay of the PSP
DCLVL	Level of the bottom of the downcomers
QLOCN(I)	Location in degrees of the T-quencher centerlines around the torus

The subroutine calling variables are listed below.

Calling Variable Definitions

IMODEL = The flow model for the pool.
1 => Thermal convection cell model
2 => Thermal stratification
3 => Bulk Pool circulation
4 => Well Mixed pool

NQNCHR = The number of T-quenchers in the PSP.

NQNON(I) = A vector of switches that tells the code which T-quenchers are on. 1 => quencher(I) is on, 0 => it is off. ($1 \leq I \leq 13$)

TIM = The current time, seconds. Used for printout.

TIMSTP = The time step, seconds

WSSV = Steam flow, Lbm/s, through each T-quencher.

HST = Steam total enthalpy, Btu/Lbm.

PTSPG = Total pressure at the PSP surface, psia.

WTESPW = Total evaporation rate, Lbm/s, from the PSP surface.

ASSPW = Area of the PSP surface, Ft**2 (output).

TWSPAV = Bulk average PSP temperature, F, input on the first call, output thereafter.
TWSSP = Average temperature of the PSP surface, F. (output)
TWBSP = Average temperature of the PSP bottom layer, F. (output)
TWMXSP = Maximum nodal temperature, F. (output)
VWSP = Volume of water in the PSP, FT**3
IPR = Print option flag. 1 => short print, 0 => details.
IPLOT = Plot output option flag. 0 => no plot data output, 1 => plot data written to For08.
METHOD = Solution method for the ODEs that describe the PSP nodal temperatures. 0 => Crank Nicholsen, 1 => an ODE solver that is user input is applied. For the results presented in Chapter six, the solver was LSODE.
WBIPAS = Total steam flow not condensed, Lbm/s.
URHR = The bulk pool circumferential velocity for IMODEL=3.

Sample input for the PSP code is shown in Table 3. This is the calling program for the Monticello T-quencher verification presented in Chapter six.

B. PSP CODE OUTPUT

There are three types of output generated by the PSP code. The simplest output is the return variables in the calling statement. The PSP code will return TWSPAV (the new PSP bulk temperature), TWSSP (the average temperature of the surface nodes), TWBSP (the average temperature of the bottom layer of nodes), TWMXSP (the maximum nodal temperature in the PSP), and VWSP (the volume of water in the PSP) on each call to the program.

Each time the code is called, output is written to FOR06. If input parameter IPR is zero, then a detailed listing of the PSP temperature distribution will be output. If IPR is one, then an abbreviated set of temperatures will be output.

If input parameter IPLOT is one, selected temperatures will be output to FOR08 for use by a plotting routine. If IPLOT is zero, no plotting information will be output.

A sample of the PSP code output is shown below as Table 4.

Table 3. Sample PSP Model Input

```
      DOUBLE PRECISION TIM,TIMSTP,WSSV,HST,PTSPG,WTESPW,
     1 ASSPW,TWSPAV,TWSSP,TWBSP,TWMXSP,VWSP,CHK,WBIPAS,URHR
      INTEGER IMODEL,NQVCHR,NQNON(13),IPR,IPLOT,METHOD
CC
CC
      IMODEL=1
      NQNCHR=13
      DO 5 I=1,13
5     NQNON(I)=0
      NQNON(7)=1
      TIM=0.000
      TIMSTP=5.000
      WSSV=208.500
      HST=1193.600
      PTSPG=15.000
      WTESPW=0.000
      IPR=0
      URHR=2.000
CCCCCCCCCCCCCCCC        1=>   LSODE
CCCCCCCCCCCCCC          0=>  CRANK NICHOLSEN
      METHOD=1
      IPLOT=0
CC
CC
      DO 100 I=1,132
      IPR=1
      TIM=DFLOAT(I)*TIMSTP
      JJ=IDINT((TIM+0.001D0)/60.000)
      CHK=DABS(TIM-DFLOAT(JJ)*60.000)
      IF(CHK.LT.1.0D-03) IPR=0
      IF(TIM.GT.660.000) IMODEL=2
      IF(TIM.GT.660.000) WSSV=0.000
      IF(TIM.GT.660.000) NQVQN(7)=0
      IF(TIM.GT.660.000) NQNON(2)=0
C
      CALL PUREVR(IMODEL,NQNCHR,NQNON,TIM,TIMSTP,WSSV,HST,PTSPG,
     1 WTESPW,ASSPW,TWSPAV,TWSSP,TWBSP,TWMXSP,VWSP,IPR,IPLOT,METHOD,
     1 WBIPAS,URHR)
C
C
      WRITE(6,50) TIM,TWSPAV,TWSSP,TWMXSP,WBIPAS
50    FORMAT(' TIM=',F10.2,' TWSPAV=',F10.4,' TWSSP=',F10.4,
     1 ' TWMXSP=',F10.4,' WBIPAS=',F8.2)
C
C
100   CONTINUE
      STOP
      END

//
```

Table 4. Sample PSP Model Output

```
PIP 0.6588D+01DELD ZLVL= 0.1785D+02 TSAT= 0.2215D+03 PTSPG= 0.1500D+02
IMODEL=   1
QUENCHER #   7 IS ON. CENTERLINE AT 180.000
NEXT QUENCHER ON IS #   7 AT 180.000 DEGREES
INDX= 10 NEAR= 16 THATP=   168.750 NT=  7
TBAYD=   97.289 TFAR=   87.934 TWSPAV=   88.549
 ##### LAMBDA= 0.65111 DI=  0.3069 #######
-------------------------------------------------------------------------------
UBAR=  0.30691546 THATP=168.75000000 THATI=  0.0        DTHETA= 22.50000000
ROBR1= 62.0306 ROBR2= 62.1394 RONOT= 62.1327 FRK=  0.10000
USZERO=     0.404711085
-------------------------------------------------------------------------------
IN   7 ITERATIONS: WEND=  0.1958175650390-01 THZ=   0.2375000+02
THI=  0.0            THP=  0.1687500D+03 DOWNFLC CHECK=   2
-------------------------------------------------------------------------------
 THETA              WM                          US
-------------------------------------------------------------------------------
  1   0.0      0.0                      0.4047110846000+00
  2  22.50     0.0                      0.4047110846000+00
  3  45.00     0.1220244559560-02       0.4020837676050+00
  4  67.50     0.4365031384590-02       0.3850326365020+00
  5  90.00     0.8631248846140-02       0.3439046560890+00
  6 112.50     0.1309811635710-01       0.2745576327360+00
  7 135.00     0.1692485333120-01       0.1783275487250+00
  8 157.50     0.1925067918250-01       0.6203656225030-01
SORFAK(   1)=  0.6711047089990+00
SORFAK(   2)=  0.6711047089990+00
SORFAK(   3)=  0.6711047089990+00
SORFAK(   4)=  0.6711047089990+00
SORFAK(   5)=  0.6711047089990+00
SORFAK(   6)=  0.9638894298720+00
SORFAK(   7)=  0.1225961236860+01
SORFAK(   8)=  0.1225961236860+01
::::::::::::::::::::: INSIDE POOL. TIME=         660.00    :::::::
::::::::::::::::::::: INSIDE POOL. TIME=         660.00    :::::::
BAY T  1=  78.769 BAY T  2=  89.384 BAY T  3=  92.823 BAY T  4=  92.123
BAY T  5=  89.786 BAY T  6=  87.190 BAY T  7=  85.534 BAY T  8=  85.336
BAY T  9=  97.500 BAY T 10=  85.336 BAY T 11=  85.534 BAY T 12=  87.190
BAY T 13=  89.786 BAY T 14=  92.123 BAY T 15=  92.823 BAY T 16=  89.384
-------------------------------------------------------------------------------
```

Table 4 (continued)

LEVEL 1	LEVEL 2	LEVEL 3	LEVEL 4	LEVEL 5	LEVEL 6	LEVEL 7	LEVEL 8
CELL 1	CELL 17	CELL 33	CELL 49	CELL 65	CELL 81	CELL 97	CELL 113
52.7809	55.8346	60.9978	66.8136	72.7557	78.9460	84.8936	87.6332
CELL 2	CELL 18	CELL 34	CELL 50	CELL 66	CELL 82	CELL 98	CELL 114
53.3886	56.5176	66.9856	76.3772	85.2918	93.0462	99.2025	103.5250
CELL 3	CELL 19	CELL 35	CELL 51	CELL 67	CELL 83	CELL 99	CELL 115
53.4150	59.0413	68.7204	79.6572	89.7868	97.6923	104.1157	111.9134
CELL 4	CELL 20	CELL 36	CELL 52	CELL 68	CELL 84	CELL 100	CELL 116
53.1596	58.4364	67.9569	78.5980	87.7907	94.5640	103.3246	115.8622
CELL 5	CELL 21	CELL 37	CELL 53	CELL 69	CELL 85	CELL 101	CELL 117
52.8027	57.2187	65.7442	75.0839	82.3871	88.0244	101.4796	118.8838
CELL 6	CELL 22	CELL 38	CELL 54	CELL 70	CELL 86	CELL 102	CELL 118
52.4834	55.8269	62.9414	70.5827	75.7122	81.5814	100.3686	121.7748
CELL 7	CELL 23	CELL 39	CELL 55	CELL 71	CELL 87	CELL 103	CELL 119
52.2742	54.5977	60.2157	66.1292	68.8010	79.9017	100.8053	124.8034
CELL 8	CELL 24	CELL 40	CELL 56	CELL 72	CELL 88	CELL 104	CELL 120
52.1721	53.6999	57.9540	62.2906	62.7202	84.3912	102.6690	126.0987
CELL 9	CELL 25	CELL 41	CELL 57	CELL 73	CELL 89	CELL 105	CELL 121
86.4010	76.2391	75.5443	78.0286	82.0030	91.4597	105.0769	131.6895
CELL 10	CELL 26	CELL 42	CELL 58	CELL 74	CELL 90	CELL 106	CELL 122
52.1721	53.6999	57.9540	62.2906	62.7202	84.3912	102.6690	126.0987
CELL 11	CELL 27	CELL 43	CELL 59	CELL 75	CELL 91	CELL 107	CELL 123
52.2742	54.5977	60.2157	66.1292	68.8010	79.9017	100.8053	124.8034
CELL 12	CELL 28	CELL 44	CELL 60	CELL 76	CELL 92	CELL 108	CELL 124
52.4834	55.8269	62.9414	70.5827	75.7122	81.5814	100.3686	121.7748
CELL 13	CELL 29	CELL 45	CELL 61	CELL 77	CELL 93	CELL 109	CELL 125
52.8027	57.2187	65.7442	75.0839	82.3871	88.0244	101.4796	118.8838
CELL 14	CELL 30	CELL 46	CELL 62	CELL 78	CELL 94	CELL 110	CELL 126
53.1596	58.4364	67.9569	78.5980	87.7907	94.5640	103.3246	115.8622
CELL 15	CELL 31	CELL 47	CELL 63	CELL 79	CELL 95	CELL 111	CELL 127
53.4150	59.0413	68.7204	79.6572	89.7868	97.6923	104.1157	111.9134
CELL 16	CELL 32	CELL 48	CELL 64	CELL 80	CELL 96	CELL 112	CELL 128
53.3886	56.5176	66.9856	76.3772	85.2918	93.0462	99.2025	103.5250

NUREG/CR-3471
ORNL/TM-8906
Dist. Category RX, 1S

Internal Distribution

1. S. J. Ball
2. T. E. Cole
3. S. D. Clinton
4-7. D. H. Cook
8-9. H. L. Dodds
10. S. R. Greene
11. D. Griffith
12-13. R. M. Harrington
14-15. S. A. Hodge
16. C. R. Hyman
17. J. E. Jones, Jr.
18. T. S. Kress
19. A. P. Malinauskas
20. L. J. Ott
21. H. E. Trammell
22. R. P. Wichner
23. A. L. Wright
24. Patent Office
25. Central Research Library
26. Document Reference Section
27-28. Laboratory Records Department
29. Laboratory Records (RC)

External Distribution

30-31. Director, Division of Accident Evaluation, Nuclear Regulatory Commission, Washington, DC 20555
32-33. Chief, Containment Systems Research Branch, Nuclear Regulatory Commission, Washington, DC 20555
34. Office of Assistant Manager for Energy Research and Development, DOE, ORO, Oak Ridge, TN 37830
35-39. Director, Reactor Safety Research Coordination Office, DOE, Washington, DC 20555
40. R. Deams, New York Power Authority, 123 Main Street, White Plains, NY, 10601
41-42. L. D. Proctor, Tennessee Valley Authority, W10D199 C-K, 400 West Summit Hill, Knoxville, TN 37902
43. J. D. Woolcott, Engineering Section, Browns Ferry Nuclear Plant, Decatur, AL, 35602
44. Wang Lau, Tennessee Valley Authority, W10C126 C-K, 400 West Summit Hill, Knoxville, TN 37902
45. R. F. Christie, Tennessee Valley Authority, W10C125 C-K, 400 West Summit Hill, Knoxville, TN 37902
46. J. A. Raulston, Tennessee Valley Authority, W10C126 C-K, 400 West Summit Hill, Knoxville, TN 37902
47. H. L. Jones, Tennessee Valley Authority, W10A17 C-K, 400 West Summit Hill, Knoxville, TN 37902
48. F. J. Moody, General Electric Company, 175 Curtner Avenue, San Jose, CA 95215
49. Z. R. Rosztoczy, Research and Standards Coordination Branch, Office of Nuclear Reactor Regulation, U.S. Nuclear Regulatory Commission, Washington, DC 20555

50. K. W. Holtzclaw, General Electric Company 175 Curtner Avenue, San Jose, CA 95125
51-52. Technical Information Center, DOE Oak Ridge, TN 37830
53-577. Given distribution as shown under categories RX, 1S (NTIS-10)

☆ U.S. GOVERNMENT PRINTING OFFICE: 1984-746-067:4153

NRC FORM 335 (2-84) NRCM 1102 3201, 3202

U.S. NUCLEAR REGULATORY COMMISSION

BIBLIOGRAPHIC DATA SHEET

SEE INSTRUCTIONS ON THE REVERSE

1. REPORT NUMBER (Assigned by TIDC, add Vol. No., if any)
NUREG/CR-3471
ORNL/TM-8906

2. TITLE AND SUBTITLE
Pressure Suppression Pool Thermal Mixing

3. LEAVE BLANK

4. DATE REPORT COMPLETED
MONTH: August
YEAR: 1984

5. AUTHOR(S)
D. H. Cook

6. DATE REPORT ISSUED
MONTH: September
YEAR: 1984

7. PERFORMING ORGANIZATION NAME AND MAILING ADDRESS (Include Zip Code)
Oak Ridge National Laboratory
P.O. Box X
Oak Ridge, Tennessee 37831

8. PROJECT/TASK/WORK UNIT NUMBER

9. FIN OR GRANT NUMBER
B0452

10. SPONSORING ORGANIZATION NAME AND MAILING ADDRESS (Include Zip Code)
Division of Accident Evaluation
Office of Nuclear Regulatory Research
U.S. Nuclear Regulatory Commission
Washington, DC 20555

11a. TYPE OF REPORT
Topical

b. PERIOD COVERED (Inclusive dates)

12. SUPPLEMENTARY NOTES

13. ABSTRACT (200 words or less)

A model is developed and verified to describe the thermal mixing that occurs in the pressure suppression pool (PSP) of a commercial BWR. The model is designed specifically for a Mark-I containment and is intended for use in severe accident sequence analyses. The model developed in this work produces space and time dependent temperature results throughout the PSP and is useful for evaluating the bulk PSP thermal mixing, the condensation effectiveness of the PSP, and the long-term containment integrity. The model is designed to accommodate single or multiple discharging T-quenchers, a PSP circumferential circulation induced by the residue heat removal system discharge, and the thermal stratification of the pool that occurs immediately after the relief valves close.

The PSP thermal mixing model is verified by comparing the model-predicted temperatures to experimental temperatures that were measured in an operating BWR suppression pool. The model is then used to investigate several PSP thermal mixing problems that include the time to saturate at full relief valve flow, the temperature response to a typical stuck open relief valve scenario, and the effect of operator rotation of the relief valve discharge point.

14. DOCUMENT ANALYSIS - KEY WORDS/DESCRIPTORS
SRV
BWR
Severe Accident Analyses
ATWS
Pressure Suppression Pool

15. IDENTIFIERS/OPEN-ENDED TERMS

16. AVAILABILITY STATEMENT
Unlimited

17. SECURITY CLASSIFICATION
(This page) Unclassified
(This report) Unclassified

18. NUMBER OF PAGES

19. PRICE

120555078877 1 1AN1RX11S
US NRC
ADM-DIV OF TIDC
POLICY & PUB MGT BR-PDR NUREG
W-501
WASHINGTON DC 20555

105